Fall 12-17-2014

Heme-dependent Tryptophan Oxidation: Mechanistic Studies on Tryptophan 2,3-Dioxygenase and MauG

Jiafeng Geng

HEME-DEPENDENT TRYPTOPHAN OXIDATION: MECHANISTIC STUDIES ON TRYPTOPHAN 2,3-DIOXYGENASE AND MAUG

by

JIAFENG GENG

Under the Direction of Aimin Liu

ABSTRACT

Hemoenzymes are prevalent in nature and participate in a wide range of biological activities. Frequently, high-valence iron intermediates are involved in the catalytic events of these enzymes, especially when the activation of peroxide or dioxygen is involved. Building on the fundamental framework of iron-oxygen chemistry, the mechanistic understandings of these enzymes and their reactive intermediates constantly attract attention from the enzymology community.

This dissertation work focused on the mechanistic studies on two hemoenzymes, tryptophan 2,3-dioxygenase (TDO) and MauG, both of which catalyze unique chemical transformations, *i.e.*, tryptophan oxidation. TDO and MauG are structurally distinct from each other; they catalyze different types of oxidization reactions on tryptophan via diverse strategies. TDO catalyzes the ring-cleavage dioxygenation reaction of free L-tryptophan, incorporating both oxygen atoms from dioxygen into the substrate. MauG uses hydrogen peroxide as the oxidant to catalyze a complex posttranslational-modification reaction on two tryptophan residues from a

protein substrate. It utilizes radical chemistry to perform a 40-Å long-range catalytic event. Despite the differences in their catalytic behavior, both enzymes are suggested to employ high-valence iron intermediates in their reactions.

A collection of biochemical and spectroscopic approaches was employed to obtain detailed insight into the electronic and structural contributions to the formation and stabilization of high-valence iron intermediates, and into the heme-dependent tryptophan-oxidation mechanisms. In the study of TDO, we solved the long-standing mystery of how the active Fe(II) enzyme is generated from the resting Fe(III) form by hydrogen peroxide. A peroxide-driven reactivation mechanism was established based on the identification of a compound ES-type ferryl intermediate. Additional efforts were dedicated to clarify the controversy in the literature regarding the catalytic roles of a distal histidine residue. Chemical-rescue approaches were used to specify the catalytic contributions of the target residue. In the study of MauG, we discovered an unprecedented tryptophan-mediated charge-resonance phenomenon in the *bis*-Fe(IV) redox state. This discovery provides the molecular basis for the chemical reactivity of the catalytically competent *bis*-Fe(IV) intermediate. Together with our collaborators, we also outlined the mechanism of the MauG-mediated long-range catalysis by identifying the catalytic functions of several important residues along the reaction pathway.

INDEX WORDS: High-valence iron, Chemical rescue, Electron paramagnetic resonance, Posttranslational modification, Radical enzymology, Electron transfer, Electron hopping, Charge resonance, Long-range catalysis

HEME-DEPENDENT TRYPTOPHAN OXIDATION: MECHANISTIC STUDIES ON TRYPTOPHAN 2,3-DIOXYGENASE AND MAUG

by

JIAFENG GENG

A Dissertation Submitted in Partial Fulfillment of the Requirements for the Degree of

Doctor of Philosophy

in the College of Arts and Sciences

Georgia State University

2014

HEME-DEPENDENT TRYPTOPHAN OXIDATION: MECHANISTIC STUDIES ON TWO CASE ENZYMES, TRYPTOPHAN 2,3-DIOXYGENASE AND MAUG

by

JIAFENG GENG

Committee Chair: Aimin Liu

Committee: Ivaylo Ivanov

Jun Yin

Electronic Version Approved:

Office of Graduate Studies

College of Arts and Sciences

Georgia State University

December 2014

DEDICATION

This dissertation is dedicated to my beloved mother, Yanqing Zhang, in Heaven. Her unconditional and measureless love is the treasure of my life.

ACKNOWLEDGEMENTS

Five years has passed since August 2009 when I first arrived at Atlanta to pursue my graduate career. During my stay in this beautiful city, I have been extremely lucky to meet and spend time with many wonderful people. Their help, support, care, and love have made me to believe that life is truly a journey to embrace, enjoy, treasure, and appreciate.

First and foremost, I would like to thank my research advisor, Prof. Aimin Liu, who picked me up in person at the Hartsfield-Jackson Airport five years ago when I stepped onto American soil. He introduced me to the amazing world of Biochemistry. Over the years, I have benefited greatly in scientific training from his guidance, criticisms, and encouragements, as well as the superb research opportunities and resources that he provided to me.

I wish to express my gratitude to my dissertation committee members, Drs. Ivaylo Ivanov and Jun Yin, for their valuable comments and suggestions on my dissertation. I am grateful to Drs. Jenny Yang and Zhi-Ren Liu for their advice and encouragements on my research presentations during the joint group meetings. I wish to thank Dr. Dabney Dixon for her guidance on my presentation skills at the graduate research seminars. Also, I thank the rest of the faculty members in the Chemistry Department, especially Drs. Binghe Wang, Giovanni Gadda, and Al Baumstark, who taught me a lot of knowledge and lessons that are helpful for not only my scientific research but also other aspects of my life.

I sincerely appreciate all the help and support from the past and current Liu Lab members and will cherish the terrific moments that we have shared together. I am indebted to Dr. Rong Fu, who devoted a lot of time and effort on the initial characterizations of TDO and MauG. When I first started, it was through reading her dissertation that I quickly became familiar with my research projects. I thank Dr. Sunil Naik, our former postdoctoral associate, for teaching me

Mössbauer spectroscopy and rapid freeze-quench techniques. The homemade chipati-curry meal that he brought to share is the most delicious Indian food that I have ever tasted. I thank my buddy in the lab, Kednerlin Dornevil, who worked with me together on the mechanistic studies of TDO and MauG. Through this team work, I harvested both high-quality scientific publications and a lifetime friendship. I thank Ian Davis for being such a responsible lab manager. His brilliant suggestions on my projects and valuable comments on my manuscripts helped to boost my research productivity significantly. I thank Lu Huo for being a trustworthy friend not only inside but also outside the lab. Every time I had to leave my car for my wife, I would call her to ask for a ride. I thank Ryan Gumpper, Shingo Esaki, and Ross Terrell for their assistance and support during our internal collaborations. I am grateful to all the other lab members who had helped me in my graduate study.

I wish to thank all my collaborators for giving me the opportunity to work on the exciting and fruitful projects. I am extremely grateful to Dr. Victor Davidson from University of Central Florida for providing us with the purified MauG proteins for EPR characterizations and the expression systems of MauG and preMADH for our own research purposes. His guidance and scientific attitude deeply affected me and helped me to become a better scientist. I thank Dr. Zehava Eichenbaum and her graduate student, Ankita Sachla, from the Biology Department for collaborating with us on the interesting heme oxygenase, HupZ. I have also enjoyed the collaboration with Dr. Gangli Wang and his graduate students, Zhenghua Tang and Dengchao Wang, on the spectroscopic studies of gold nanoclusters. All these collaborations have broadened my vision on chemical and biological research, and equipped me with a diverse collection of knowledge and experience.

I acknowledge the generous financial support from the Molecular Basis of Disease Program of Georgia State University. The graduate fellowship, travel awards, and seed grant allowed me to pay my monthly bills, travel to several eye-opening scientific conferences, and participate in the fascinating interdisciplinary research.

The biggest fortune that I gained during the past five years is my incredible friends. They are always ready to help and listen to me. Although a lot of them have left Atlanta to pursue their dreams, I will always treasure the beautiful memories that we share together in the rest of my life. I own my gratitude to Chen (Alice) Zhang and Xiaojun (Max) Xu for taking care of me all these years and encouraging me during the dark times. I thank Yanqing Zhou and Kun Wang for accommodating me when I was new to the states. I thank my former roommate, Dr. Qichun Zhang, for everything that she taught me especially in being a solid and responsible individual. I thank the folks from the GSU and Emory soccer clubs. I had a lot of fun playing soccer with them on weekends. I am always grateful for their help and care when I was severely injured on the soccer field in 2010.

Special thanks to Dr. Liang Li, my former instructor in high school and good friend ever since, for her encouragements and inspirations to me to study aboard and experience a different life.

Finally, to my family, their unconditional love is the power source for me to overcome the obstacles in life. I am deeply indebted to my wife, Dan Cui, who made a huge sacrifice in her career for our family reunion. It is after she came to the states that I started to focus on what I should focus and take more responsibilities for the family. The happy and stable married life is the key for my success in academics.

TABLE OF CONTENTS

LIST OF TABLES

LIST OF FIGURES

1 INTRODUCTION

(This chapter is modified from the following two review articles that JG coauthored: 1. Geng J, Davis I, Liu F, and Liu A (2014) *Bis*-Fe(IV): Nature's sniper for long-range oxidation. ***J. Biol. Inorg. Chem.***, in press (DOI 10.1007/ s00775-014-1123-8); 2. Geng J, and Liu A (2014) Heme-dependent dioxygenases in tryptophan oxidation. ***Arch. Biochem. Biophys.***, 544, 18-26.)

1.1 General introduction: From transition metals in biology to hemoproteins

Transition metals are widespread in the biosphere and often encountered as an integral component to proteins. Their coordination chemistry play important structural and functional roles in metalloproteins, and this connection builds on the fundamental framework of bioinorganic chemistry. Among all the transition metals in biological systems, iron is the most widely used, mainly because of its high abundance in the biosphere, the ability to access multiple oxidation states under physiologically relevant conditions, and the rich and diverse redox chemistry. One of the most common existing forms of iron ions in metalloproteins is heme. Heme is an iron-porphyrin complex with the iron ion coordinated by the four N atoms from the tetrapyrrole moiety, leaving two axial positions open for additional ligands (Figure 1.1.1).

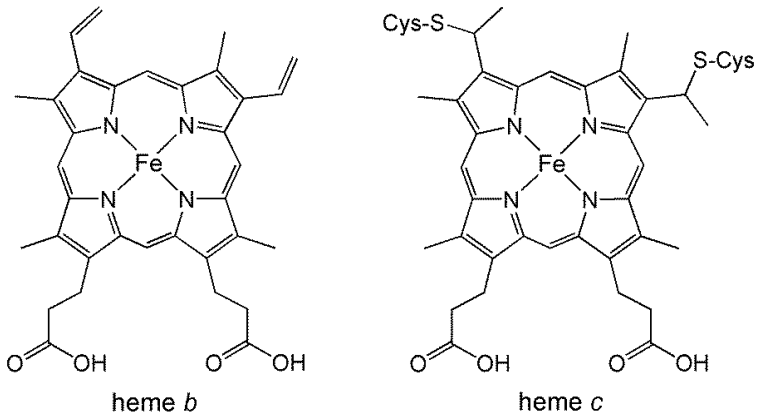

Figure 1.1.1 Chemical structures of heme *b* and *c*.

There are multiple types of heme in biological systems, and they differ in the substitution groups on the porphyrin ring. The most common and abundant type is heme *b*, also known as

protoporphyrin IX (Figure 1.1.1). Heme *b* is present as a prosthetic group in a wide range of proteins, including hemoglobin, myoglobin, peroxidases, and cytochrome P450 oxygenases. It is usually non-covalently attached to the protein matrix through the axial coordination from the side chain of a certain amino acid residue as well as some weak interactions between the protoporphyrin ring and the nearby protein environment. In some less common cases, *bis*-axial coordination can occur, resulting in a hexacoordinated, rather than pentacoordinated, heme iron ion. It is believed that other types of heme are derived from heme *b* [1,2]. A common modification is covalently attaching heme *b* to the protein, thereby generating heme *c* (Figure 1.1.1). In heme *c*, two thioether bonds are formed between the two heme peripheral vinyl groups and two specific cysteine residues from a unique CXXCH motif.

Hemoproteins participate in a wide variety of biological functions, including oxygen transport and storage (*e.g.*, hemoglobin and myoglobin), electron transfer (ET) and gas sensing (*e.g.*, some cytochrome *c* proteins), and chemical catalysis (*e.g.*, peroxidases, catalases, P450 monooxygenases). The enzymatic role of hemeoproteins was revealed more than one century ago when the study of horseradish peroxidase was initiated in 1903 [3]. Over the years, hemoenzymes are found to be extremely versatile, and a rich array of chemical transformations are identified to be catalyzed by hemoenzymes [3-5]. These transformations cover both reductive and oxidative chemistry; they can be as simple as the detoxification of peroxide and superoxide, the reactions catalyzed by catalase and superoxide dismutase, respectively, or can be as complex as the multi-step posttranslational modification involved in tryptophan tryptophylquinone (TTQ) biosynthesis, a process catalyzed by a di-heme enzyme, MauG [6].

Such a diverse collection of biological functions of hemoenzymes and hemoproteins is mainly attributed to the fact that the heme redox level can be tuned to a wide range by different

protein matrices. The major tuning effect originates from the axial heme ligands, which set a primary range of the heme redox potential. Proteins can provide axial ligands to the heme via amino acid residues that contain oxygen (*e.g.*, tyrosine), nitrogen (*e.g.*, histidine), or sulfur (*e.g.*, cysteine and methionine) atoms in their side chains. Each side chain group has a specific heme-binding affinity, which can affect the stability of the cofactor-bound protein [7-9]. Moreover, each ligand has diverse affinities for different redox states, which can influence the heme electrochemistry [9,10]. Other factors, such as the intricate weak-interaction network in the heme-binding pocket, add on a secondary layer of control on the heme redox level. These weak interactions often play additional important roles, such as facilitating the binding of substrates or other small molecules, activating or stabilizing exogenous bound molecules, and tuning the activities of catalytic intermediates. All the factors and principles mentioned above were taken into consideration throughout the pursuit of our research objectives.

1.2 Overview of the model systems and research objectives

This dissertation study aims to investigate the molecular biochemistry and mechanistic enzymology of two structurally diverse heme-dependent enzymes that perform oxidation reactions on tryptophan, either free tryptophan or protein-based tryptophan residues. The first enzyme, tryptophan 2,3-dioxygenase (TDO) utilize a ferrous heme *b* to insert both oxygen atoms from molecular oxygen into L-tryptophan (L-Trp), converting it to *N*-formylkynurenine (NFK) [11] (Figure 1.2.1). TDO makes possible a ring-opening, four-electron oxidation process, a dioxygenation reaction rarely performed by hemoenzymes. The second enzyme, MauG, is a *c*-type di-heme enzyme that participates in the final steps of the maturation of methylamine dehydrogenase (MADH) [12,13]. This maturation process involves the formation of a TTQ cofactor from two protein-based tryptophan residues in a precursor protein called preMADH

(Figure 1.2.2). The MauG-catalyzed reaction is a six-electron long-range oxidation event, in which three eq. of H_2O_2 is used as the oxidant to remotely extract electrons from the protein substrate. Notably, novel high-valence iron intermediates have been either proposed or identified in the catalytic reactions of TDO and MauG.

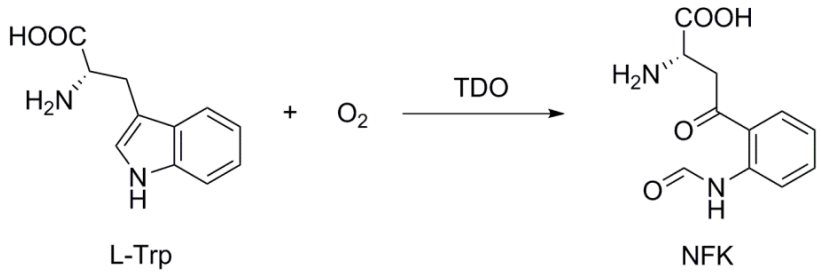

Figure 1.2.1 Chemical reaction catalyzed by TDO.

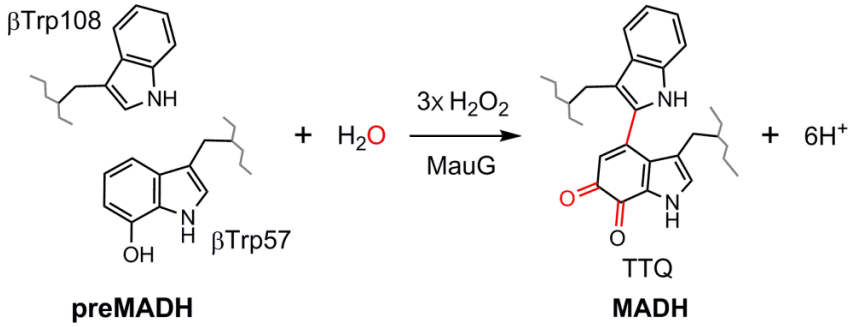

Figure 1.2.2 MauG-catalyzed TTQ biosynthesis. Posttranslational modifications of the MADH precursor, preMADH, are shown in red. H_2O_2 serves as a co-substrate to provide oxidizing equivalents.

A thorough study on these two enzyme systems can provide original chemical knowledge in many aspects of iron-oxygen chemistry and heme enzymology, including the heme-dependent tryptophan oxidizing mechanisms with comparisons to other hemoenzymes and even non-heme catalysis as well as a better definition of the molecular and structural requirements needed to attain high-valence intermediates and control their activity. The following list is the research objectives of this dissertation work. Each objective was addressed in detail by an individual chapter.

For TDO-catalyzed L-Trp dioxygenation:

(a) Elucidate the peroxide-driven reactivation mechanism, by which the catalytically active Fe(II) enzyme is formed from the resting ferric state in the presence of peroxide (Chapter 2);

(b) Investigate the catalytic roles of a conserved distal histidine using chemical-rescue approaches, and evaluate the proposed ferryl-dependent catalytic mechanism of TDO (Chapter 3).

For MauG-catalyzed TTQ biosynthesis:

(c) Determine the contributions of a tyrosine heme ligand to the formation and stabilization of the catalytically competent *bis*-Fe(IV) intermediate of MauG (Chapter 4);

(d) Uncover the long-range ET mechanism between the protein substrate and the *bis*-Fe(IV) intermediate of MauG (Chapter 5);

(e) Probe the chemical nature of the *bis*-Fe(IV) redox state by determining the electronic interactions between the hemes and the molecular basis for the chemical reactivity of the *bis*-Fe(IV) species (Chapter 6 and 7).

1.3 A literature review on tryptophan 2,3-dioxygenase

L-Tryptophan is an essential amino acid for mammals. It is utilized not only for protein synthesis but also for the biosynthesis of serotonin and melatonin by the serotonin pathway as well as nicotinamide adenine dinucleotide (NAD) by the kynurenine pathway. Although the kynurenine pathway is responsible for the catabolism of over 90% of L-tryptophan in the mammalian intracellular and extracellular pools, the scientific field was dominated in the last century by studies of the serotonin pathway, due to the physiological significance of the latter's

catabolic intermediates and products. However, in the past decade, the focus gradually reversed as the link between the kynurenine pathway and various neurodegenerative disorders and immune diseases is increasingly highlighted. Notably, the first step of this pathway, which is catalyzed by heme-dependent dioxygenases, has been proven to be a potential target for immune regulation and cancer treatment. A thorough understanding of the intriguing chemistry of the heme-dependent dioxygenases may yield profound insights for drug discovery. In this section, we survey those enzymatic and mechanistic studies, initially started by Kotake and Masayama over 70 years ago [14], on the heme-dependent tryptophan dioxygenation reactions.

1.3.1 Tryptophan 2,3-dioxygenase and indoleamine 2,3-dioxygenase

The utilization of heme iron for dioxygen activation and oxygen insertion into organic substrates is prevalent in nature, with the most well-known examples being the heme-dependent monooxygenation reactions catalyzed by cytochrome P450s. Notably, hemoproteins rarely express a dioxygenase activity as the native biological function. Thus far, only a few examples have been identified in lipid metabolism (*e.g.*, fatty acid α-dioxygenase, prostaglandin H synthase, and linoleate diol synthase), tryptophan oxidation (*e.g.*, TDO), and natural rubber degradation (*e.g.*, rubber oxygenase). Heme-dependent dioxygenases are distinctive members of the dioxygenase family in that they typically utilize a histidine-coordinated heme rather than a non-heme metal to facilitate dioxygen activation and oxygen insertion in this type of reactions.

TDO is the first functionally defined heme-dependent dioxygenase [14-16]. It was initially referred to by several different names: tryptophan peroxidase-oxidase, tryptophan pyrrolase, and tryptophan oxygenase. TDO employs a *b*-type ferrous heme to catalyze the oxidative cleavage of the indole ring of L-Trp, converting it to NFK (Figure 1.2.1). In mammals, TDO is mainly a hepatic enzyme that participates in the initial and rate-limiting step of the kynurenine pathway, which is the primary route of L-Trp degradation [17-22]. The kynurenine

pathway constitutes the major part of the *de novo* biosynthesis of NAD, an essential life-sustaining redox cofactor, in eukaryotic organisms and in some bacterial species [23,24]. In addition to mammals, TDO was found in other sources such as insects and bacteria [16,24-27].

In 1967, Hayaishi *et al*. discovered an isozyme of TDO [28,29]. This enzyme is named indoleamine 2,3-dioxygenase (IDO) because it exhibits a broader substrate-specificity than TDO. While TDO is highly specific for L-Trp, IDO can tolerate a collection of indoleamine derivatives, including D-Trp, tryptamine, and serotonin [4,30-33]. IDO participates only in the kynurenine pathway of mammals and is ubiquitously distributed in all tissues except the liver [4,33,34]. Although TDO and IDO were identified decades ago, their crystal structures were not solved until recently [27,35-37]. IDO is crystallized as a dimer with a disulfide bond connecting the two monomers [35], whereas TDO consists of four subunits arranged in a dimer of dimer quaternary structure [27,36,37] (Figure 1.3.1). The two enzymes share only ~10% sequence identity but exhibit similar active-site architectures [27,35-37]. Recently, a potential TDO/IDO superfamily has been proposed upon incorporating another heme-dependent tryptophan-utilizing enzyme, PrnB, which possesses a common structural core as those of TDO and IDO [38].

During the past decade, TDO and IDO have attracted enormous attention because of their physiological importance. IDO is inducible by interferon-γ as a result of inflammation and thus is highly related to immune functions [39-41]. It is proposed that local depletion of cellular L-Trp by IDO inhibits the growth of certain pathogens, contributing to innate host immune response [39-42]. However, in contrast, a growing body of evidence demonstrates that increased expression of IDO frequently links to host immunosuppression. It can promote immune tolerance under various physiological and pathophysiological conditions, thereby causing serious problems including maternal fetal tolerance and immune escape of cancer [33,39,41-48]. In recent years, TDO has been found to be expressed in tumor cells, and the expression of TDO has been shown

to play an immune-regulatory role in many cancer systems via preventing tumor rejection, much like the reports for IDO [48,49]. These findings make it extremely beneficial to characterize the biochemical properties and elucidate the catalytic mechanisms of TDO and IDO for inhibitor design and drug discovery.

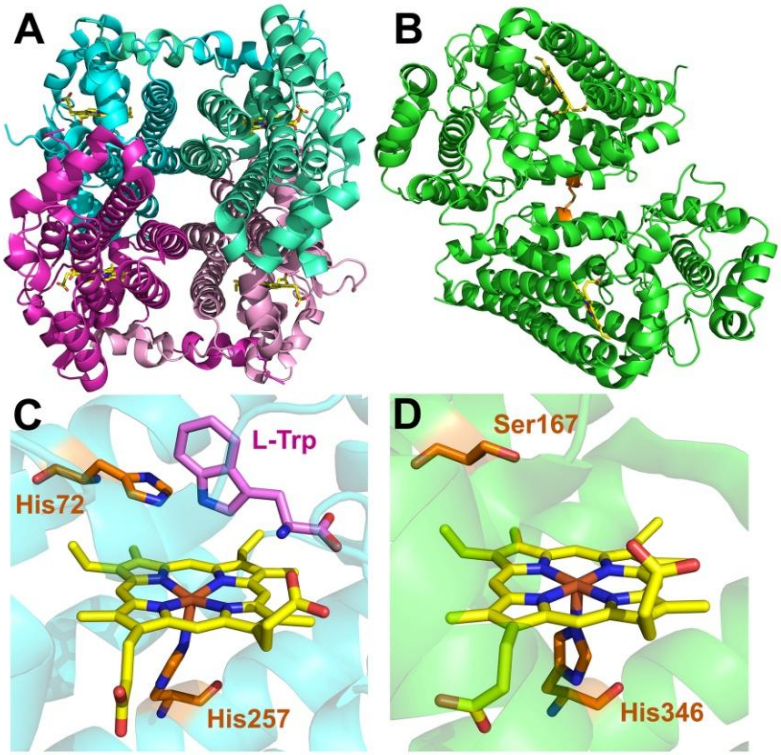

Figure 1.3.1 Crystal structures of TDO and IDO. (A) The quaternary structure of TDO is tetrameric, arranged in a dimer of dimer pattern (Protein Data Bank (PDB) entry: 2NOX). Each subunit contains a *b*-type heme that is labeled in yellow. (B) IDO is crystallized as a dimer with a disulfide bond connecting the two subunits (PDB entry: 2DOT). The hemes are labeled in yellow and the two cysteine residues of the disulfide bond are labeled in orange. (C) The active-site architecture of substrate-bound TDO (PDB entry: 2NW8). The heme center is coordinated by a proximal histidine residue (His257 in *Cupriavidus metallidurans* TDO (cmTDO) amino acid numbering). The enzyme-bound L-Trp (labeled in pink) is H-bonded to a distal histidine residue (His72 in cmTDO amino acid numbering). (D) The active-site architecture of substrate-free IDO (PDB entry: 2DOT). The distal histidine residue present in TDO is replaced by a serine residue (Ser167) in IDO.

1.3.2 Dioxygenase mechanism of TDO and IDO

The catalytic mechanism of oxygen activation and insertion for P450-type monooxygenases is well studied. It features a compound I intermediate, which is an oxo-ferryl species (Fe(IV)=O) coupled with a cation porphyrin radical [4,50]. The compound I intermediate is a catalytically competent oxidant and is able to insert the iron-bound oxygen into organic substrates [51]. It should be noted, however, heme-dependent monooxygenation consumes electrons (from NADH/NADPH) and protons with one of the oxygen atoms of O_2 being reduced to water. In contrast, the TDO/IDO reaction does not consume any electrons or protons from external sources. Thus, the dioxygenation reaction is fundamentally distinct from those monooxygenation reactions in terms of oxygen reduction.

Despite accelerated efforts to investigate the mechanisms of TDO and IDO, the strategies by which oxygen is activated and inserted to L-Trp is not yet definitively established. This conundrum is mainly due to a lack of direct and solid experimental evidence for the chemical identities of key catalytic intermediates. Nonetheless, recent crystallographic, spectroscopic, and computational studies have provided researchers with a diverse collection of information to draw a general picture of the reaction pathway and comment on several long-debated issues regarding the dioxygenase mechanisms. These issues are related to the following topics: (a) the formation of the catalytic ternary complex, (b) the involvement of an acid-base catalyst for reaction initiation, (c) the existence of high-valence ferryl species in the reaction cycle.

(a) The catalytic ternary complex of TDO and IDO

A ternary complex of Fe(II)-O_2-Trp is regarded as the starting point of the dioxygenase reactions of TDO and IDO (Figure 1.3.2). In this complex, the ferrous heme is coordinated by O_2 with the substrate L-Trp binding nearby. The direct coordination of O_2 to the heme iron plays an essential role for activation of the dioxygen molecule in a previously proposed base-dependent

mechanism [4,35,37,52-55] (Figure 1.3.2_A) and a recently proposed ferryl-dependent mechanism [54-60] (Figure 1.3.2_B). In the former mechanism, the direct coordination significantly increases the electron-deficiency of the distal oxygen atom with the heme iron withdrawing a great portion of electron density from the dioxygen molecule. This facilitates an effective nucleophilic attack by the electron-rich C3 of the substrate after deprotonation of the indole NH group (Figure 1.3.2_A). In the latter mechanism, the direct coordination enhances the radical feature of the distal oxygen atom with the heme-bound O_2 possessing superoxide characteristics, enabling a direct radical addition of the distal oxygen to the C2 position of the substrate without deprotonation of the indole moiety (Figure 1.3.2_B).

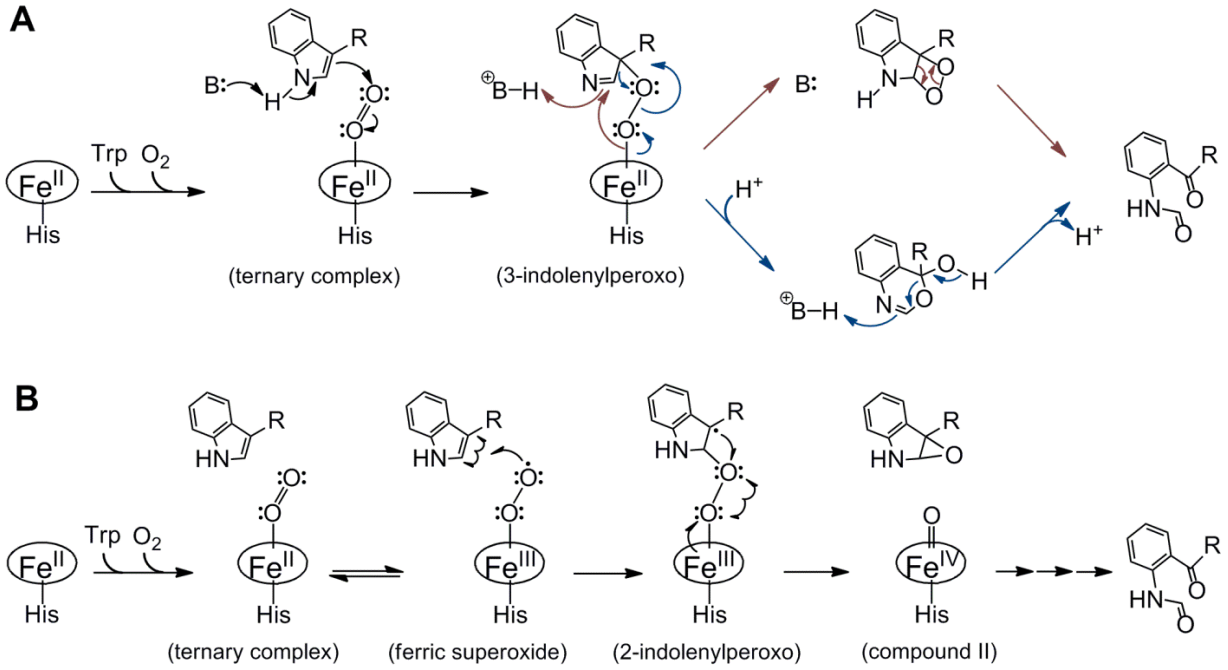

Figure 1.3.2 Representative catalytic mechanisms of TDO and IDO. (A) A previously proposed base-dependent mechanism. This mechanism is branched at the 3-indolenylperoxo intermediate, which is proposed to be decomposed via either a dioxetane pathway (red, upper branch) or a Criegee rearrangement pathway (blue, bottom branch). (B) A recently proposed ferryl-dependent mechanism, in which direct radical addition of the ferric superoxide to the indole C2 position is proposed. The catalytic steps connecting the compound II intermediate and the final product is still under development.

Spectroscopic and computational studies have shown that the conformation of the ternary Michaelis complex of TDO is tuned by the protein matrix via intricate hydrophobic and hydrogen-bonding (H-bonding) interactions for efficient catalysis [36,59-63]. Structural comparisons show that most of the hydrophobic interactions between L-Trp and the substrate-binding pocket of TDO are conserved in IDO [27,35-37,63]. However, due to substitutions of active-site residues, several important H-bonding interactions in the TDO ternary complex are inevitably missing or altered in IDO. They are believed to be the key factors that differentiate the reactivities and substrate selectivity between these two isozymes. For example, an H-bonding interaction between the amine group of L-Trp and the side chain hydroxyl of a distal threonine residue was suggested to be responsible for the strict substrate L-stereoselectivity of TDO [64,65]. Compared to the TDO ternary complex, the IDO ternary complex displays a higher degree of conformational freedom [60-62]. This is consistent with the relaxed substrate specificity of IDO. The elevated structural flexibility destabilizes the IDO ternary complex, making it susceptible to autoxidation [4].

Interestingly, an emerging body of evidence indicates that the assembly processes of the ternary complex in TDO and IDO differ (Figure 1.3.3). In TDO, the binding of the primary-substrate (L-Trp) is believed to precede the binding of the secondary-substrate (O_2) [4] (Figure 1.3.3_A). This notion was initially evidenced from a pioneer rapid-kinetic study by Hayaishi and coworkers [66]. They showed that accumulation of the oxy-ferrous complex of TDO can be observed only in the presence of L-Trp, and that in the absence of L-Trp, the ferrous heme does not readily bind O_2 although is eventually oxidized to the ferric state by O_2 [66]. An induced-fit behavior occurs in TDO upon L-Trp binding, as revealed from the crystal structures of substrate-free and substrate-bound *Xanthomonas campestris* TDO (xcTDO) [36] as well as a recent modeling study based on the crystal structure of *Drosophila melanogaster* TDO (dmTDO) [27].

L-Trp recognition can establish a complex and extensive network of substrate-enzyme interactions, which stabilizes the active-site region and completely shields it from the solvent by switching from an open conformation to a closed conformation through loop movements [36]. Thus, the Trp-TDO binary complex represents an intermediate stage in the formation process of the ternary Michaelis complex of TDO. On the contrary, IDO is generally believed to bind O_2 prior to L-Trp [67,68] (Figure 1.3.3_B), despite the existence of different opinions in the early literature [4]. This assembly mode of the ternary Michaelis complex is proposed based on a collection of interesting and consistent observations. Unlike TDO, IDO can form its oxy-ferrous adduct regardless of L-Trp [69]. The rate constants for O_2 and CO binding to the heme center of ferrous IDO are not significantly perturbed by L-Trp [69]. In addition, Yeh *et al.* showed that conversion of ferric IDO to the ferryl form via peroxide oxidation significantly facilitates L-Trp binding [70]. Combining this phenomenon with a previous observation that cyanide-bound ferric IDO has a much higher affinity towards L-Trp than the ligand-free ferric enzyme [67,71], it is suggested that regardless of the heme redox state, ligand binding to the heme iron of IDO can introduce conformational changes that are in favor of L-Trp binding [70]. Moreover, since the early studies of IDO, inhibition of the dioxygenase activity at high L-Trp concentrations was noted [28,72]. A recent mechanistic study by Raven and colleagues on the substrate-inhibition effect revealed that this phenomenon can be accounted for by the sequential and ordered binding of O_2 and L-Trp [68]. At low concentrations of L-Trp, O_2 binds first followed by the binding of L-Trp; at higher concentrations of L-Trp, the order of binding events is reversed, and L-Trp binding disfavors the subsequent O_2 binding step, diminishing the catalytic activity [68]. Overall, the proposed mechanisms of Michaelis complex assembly for TDO and IDO are in accordance with the results of steady-state kinetic studies. In TDO, the K_m value of L-Trp is larger than the K_d value of L-Trp for the ligand-free ferrous enzyme [73]. However, in IDO the K_m value of L-

Trp is much smaller than the K_d value of L-Trp for the ligand-free ferrous enzyme, while the K_m value of O_2 is similar to the K_d value of O_2 for the ligand-free ferrous enzyme [67,71,74].

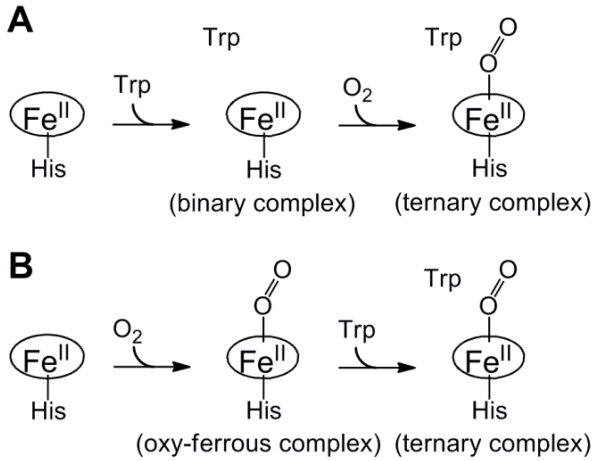

Figure 1.3.3 Assembly modes of the ternary Michaelis complex in TDO (A) and IDO (B).

The preferential binding of the primary substrate prior to O_2 binding is prevalent in iron-dependent oxygenases and has been shown to be beneficial in many cases, including cytochrome P450s and α-KG dependent non-heme oxygenases [4,75]. Recognition of the primary substrate usually triggers alterations in the microenvironment of the metal center and thereby facilitates the subsequent O_2 binding by expelling solvent molecules from the active site to increase O_2 affinity or removing solvent-derived ligands from the metal center to generate a coordination vacancy [4,75]. This substrate-binding strategy is also considered an *in vivo* protection mechanism, as retarding O_2 binding in the absence of the primary substrate can prevent oxidative damages to the metal center and avoid the release of reactive oxygen species [76]. In addition to the abovementioned benefits, in P450s, binding of the primary substrate increases the heme redox potential, which facilitates heme reduction by associated electron donors [4]. Similarly, it was shown in xcTDO that L-Trp binding causes a significant positive shift in the redox potential of the heme iron [36]. Thus, the preferential binding of L-Trp in TDO may play an additional physiological role to keep the heme iron from being oxidized. In contrast, the sequential binding

of O_2 and L-Trp in IDO is unique, and little is known about the physiological significance of this seemingly irrational design. Plausibly, the distinctive assembly mode of the IDO ternary complex is important for ensuring enzyme turnover under substrate-deficient conditions [70].

(b) Involvement of an active-site base in the first step of catalysis

Since the initial proposal by Hamilton [52], it was generally believed that TDO and IDO begin the catalytic cycle with proton abstraction from the indole NH group of L-Trp by an active-site base [4,35,37,53,61,74,77,78] (Figure 1.3.2_A). Deprotonation of the indole group can generate an electron-rich environment at the indole C3 position and thus stimulate a nucleophilic attack at the distal oxygen of the heme-bound O_2. An intermediate, 3-indolenylperoxo, is generated as a result of the nucleophilic attack (Figure 1.3.2_A). This proposal was supported by a few pieces of experimental evidence, including a solvent kinetic isotope effect study on TDO, which revealed that a proton-transfer step is partially rate-limiting in the catalytic cycle [53]. In line with this proposal, a 3-indolenylhydroperoxo intermediate was identified during the oxidation of L-Trp by a singlet O_2 from an enzyme-free reaction system [79,80]. Despite a much lower specificity, decomposition of this intermediate was shown to yield NFK with both oxygen atoms from the singlet O_2 conserved in the product [79,80].

In TDO, the distal His72 residue was regarded as the acid-base catalyst, as suggested by the crystal structure of the binary complex of xcTDO and L-Trp, which shows that the corresponding histidine residue is H-bonded to the indole NH group of L-Trp [36] (Figure 1.3.1_C). In IDO, there is no apparent active-site residue candidate that plays such a role. Instead, it was proposed that the heme-bound O_2 functions as the acid-base catalyst [35,61,74,81]. By using CO as an O_2 surrogate, resonance Raman (RR) studies by Yeh and coworkers supported the aforementioned assignments of the acid-base catalyst, with the distal histidine for TDO [61,63] and the heme-bound O_2 for IDO [81].

In the recent years, more and more studies have cast serious doubt on the base-dependent catalytic mechanism. Firstly, the indole NH group has a very high pK_a value at *ca.* 17 [82], so it would be extremely difficult for weak bases such as the imidazole moiety of His72 and the heme-bound O_2 to abstract a proton from it. Recent computational studies, including density functional theory (DFT), molecular dynamics (MD), quantum mechanics/molecular mechanics (QM/MM) and ONIOM calculations, also disfavored the involvement of an acid-base catalyst by demonstrating that the base-catalyzed deprotonation of the indole group is not energetically favorable, compared to the direct addition of the heme-bound O_2 [56-60]. Moreover, replacement of the distal histidine residue in TDO failed to shut down the enzyme, and the distal histidine mutants from different sources all exhibited a detectable activity [61,73,78,83,84], suggesting that deprotonation of the indole group is not critical for catalysis in TDO. In a spectroscopic study on the cryoreduced ternary complex of xcTDO, Davydov *et al.* showed that mutation of the distal histidine or methylation of the indole nitrogen of L-Trp had no observable effect on the spectroscopic properties of the oxy heme moiety or its annealing behavior, arguing against proton abstraction of the indole group as the initial catalytic step in TDO [62].

The most solid evidence against the base-dependent mechanism is the observation that 1-methyl-L-tryptophan (1-Me-L-Trp) is a substrate for IDO, cmTDO, and the distal histidine variants of hTDO and xcTDO [84,85]. Thus, substrate deprotonation is not an inevitable course; instead, direct addition of the heme-bound O_2 is more likely to occur in the first step.

(c) Ferryl species of TDO and IDO

Regardless of whether deprotonation of the indole NH group occurs or not, an indolenylperoxo-type intermediate, in which the heme iron and L-Trp are linked by dioxygen, is generated upon the addition of the distal oxygen to L-Trp (Figure 1.3.2). However, the protonation state of the indole moiety can affect the addition position of the distal oxygen on the

indole ring and further influence the manner of O-O bond cleavage. In the base-dependent mechanism, nucleophilic attack by the indole C3 at the distal oxygen yields a 3-indolenylperoxo intermediate (Figure 1.3.2_A). Subsequently, the O-O bond is cleaved heterolytically and the two oxygen atoms are inserted into L-Trp via either a Criegee rearrangement pathway or a dioxetane pathway (Figure 1.3.2_A). Notably, there is no high-valence heme species involved in this mechanism. As the base-catalyzed proton abstraction process is disproved by a large body of experimental and computational results, an alternative catalytic mechanism has received general recognition in the field [54-60,68,84] (Figure 1.3.2_B). In this mechanism, the oxy-ferrous heme adduct possesses ferric superoxide characteristics, and direct radical attack at the indole C2 position by the distal oxygen occurs (Figure 1.3.2_B). As a result, a 2-indolenylperoxo intermediate is generated. This intermediate is decomposed through homolytic O-O bond cleavage, generating a compound II-type ferryl species plus a monooxygenated form of L-Trp as an epoxide intermediate, which subsequently recombine to generate NFK (Figure 1.3.2_B).

The ferryl-dependent dioxygenase mechanism is supported by recent computational calculations [57-60] and experimental results [59,86-88], as well as some indirect evidence from the early studies of IDO. Notably, a unique "superoxide shunt" pathway was previously identified in IDO, in which ferric IDO can utilize superoxide (O_2^-) as a co-substrate to catalyze the dioxygenase reaction of L-Trp both *in vitro* and *in vivo* [4,89-92] (Figure 1.3.4). Spectroscopic studies revealed that ferric IDO can bind to and react with O_2^- to yield the oxy-ferrous complex [69,89,93,94], which can be also generated by addition of O_2 to the ferrous enzyme as shown in Figure 1.3.3 and 1.3.4. Moreover, it was reported that the oxy-ferrous complex of IDO readily oxidizes itself to the ferric state by releasing O_2 as O_2^-, regardless of whether L-Trp is present or not [4,59,69,72]. Taken together, one can conclude that regardless of L-Trp, the oxy-ferrous adduct of IDO is in equilibrium with the corresponding ferric superoxide

complex, which is the reactive species responsible for direct radical addition to L-Trp (Figure 1.3.4). In fact, RR characterization of the ternary Michaelis complex of IDO proved that the heme-bound O_2 exhibits superoxide characteristics [59]. A significant progress in the mechanistic studies of TDO and IDO came in 2009 when the proposed compound II-type ferryl intermediate was trapped and characterized in IDO by Yeh *et al.* [59]. This observation was later confirmed by independent work from others [86,88]. Soon afterwards, the existence of the epoxide intermediate of L-Trp in the reaction cycle was inferred by a mass spectrometry (MS) study from the Raven laboratory, in which a side product of monooxygenated L-Trp was detected from the dioxygenase reaction of IDO, xcTDO, and hTDO [87].

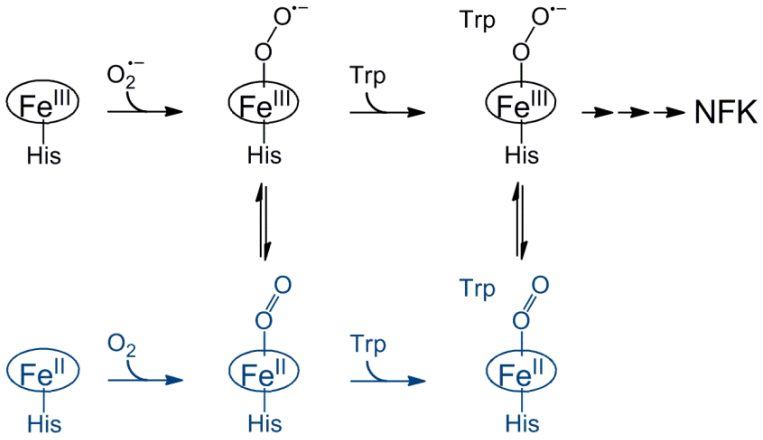

Figure 1.3.4 The "superoxide shunt" pathway in IDO. The bottom branch in blue shows the native O_2-dependent pathway. The oxy-ferrous adducts are in equilibrium with the corresponding ferric superoxide complexes regardless of the presence of L-Trp, connecting the two pathways.

Despite intensive efforts from different groups, the proposed ferryl intermediate has not yet been captured in the dioxygenase reaction of TDO. The ferryl intermediate observed in IDO was reported in a low occupancy [59,88] and lacked additional support and further characterization from different spectroscopic methods. To obtain detailed information on the chemical properties of the ferryl species in TDO and IDO, we and others have adopted an alternative pathway to produce the ferryl species in high yields via reactions with H_2O_2

[70,84,95,96]. In TDO, a compound ES-type ferryl species was generated by reacting ferric TDO with H_2O_2 and characterized by optical, EPR, and Mössbauer spectroscopy [84,96]. In Chapter 2 and 3, the detailed chemical and physical properties of this high-valence intermediate will be discussed in detail. In IDO, Lu and Yeh reported that a compound II-type ferryl species was produced upon the addition of H_2O_2 to ferric IDO [70]. This high-valence species is capable of oxidizing peroxidases substrates such as ABTS, but not L-Trp [70], which is consistent with a previous report that by using H_2O_2 as a co-substrate, IDO converts some L-Trp catabolites including melatonin, serotonin, and tryptamine, but not L-Trp, to oxygenated products [97]. The poor reactivity of the ferryl species towards L-Trp also explains why the H_2O_2-mediated reactivation pathway is not present in IDO.

1.3.3 Concluding remarks

Unexpectedly, TDO and IDO appear to employ a catalytic strategy that is highly reminiscent of those in some non-heme iron-containing oxygenases and oxidases, such as α-KG-dependent oxygenases, pterin-dependent oxygenases, isopenicilin *N* synthase (IPNS), and CloR. These enzymes utilize a ferric superoxide species, to claim the electrons needed for hemolytic cleavage of the O-O bond of O_2 from the substrates or co-substrates [75,98]. This course of action provides the catalytic driving force for substrate activation and ensures that all the oxidizing equivalents from O_2 can be properly transferred into the substrates and co-substrates, avoiding the incorporation of electron donors and associated mediators to the reaction cycle. The ferric superoxide species and subsequent ferryl intermediates allow the enzymes to sequentially target two positions of the substrates, making possible a collection of difficult reactions. In TDO and IDO, the utilization of ferric superoxide as an oxidant for substrate activation is unprecedented in heme-containing oxygenases. A recent computational study by Lai and Shaik revealed the origin of the different activities of the superoxo species between P450s and

TDO/IDO, and the axial heme ligand was suggested to be the major determinant [99]. Moreover, direct oxygen insertion performed by a compound II-type ferryl species is also exceptional in heme chemistry. Compound II complexes are usually considered languid oxidants compared to Compound I complexes. This demanding task is achieved by the TDO/IDO compound II species, mostly because the other reactant, *i.e.*, the putative epoxide intermediate of L-Trp, is already activated and fairly reactive. Currently, a detailed mechanism of the second oxygen insertion step mediated by the TDO/IDO compound II intermediate is under development, and the hypotheses from computational studies await confirmation by experimental results [57,58]. Nonetheless, the tryptophan oxidation reactions catalyzed by TDO and IDO have proven to be a distinctive prototype of heme-dependent reactions. The valuable information obtained by a collective effort from the field of enzymology has again demonstrated the remarkable catalytic versatility of hemoproteins and is inspiring to a broad science community.

1.4 A literature review on the MauG-catalyzed TTQ biosynthesis

In recent years, it has come to light that many crucial biological processes are mediated by some of the same culprits which have been implicated in aging and oxidative stress, *i.e.*, activated oxygen species and free radicals. The dual role of these reactive species as both the leading cause of non-specific cell damage and as useful catalytic intermediates necessitates that their use in biochemical reactions should be highly specific and strictly controlled. In particular, radical generation and long-range electron transfer as a means to utilize chemical power is increasingly recognized as an effective strategy for biological systems to perform demanding redox reactions [100-103]. One such example is the biosynthesis of TTQ, a protein-derived cofactor that functions as the catalytic center of MADH [104]. MADH catalyzes the oxidative deamination of methylamine to formaldehyde and ammonia, a process which allows the host

bacterium to rely on methylamine to survive [105]. It possesses an $\alpha_2\beta_2$ structure with each smaller β subunit possessing a TTQ cofactor [106].

TTQ is formed through posttranslational modification on a precursor protein, preMADH. A periplasmic enzyme, MauG, employs two *c*-type hemes to mediate this cofactor-maturation process via the oxidation of a tryptophan residue (Trp108) and a mono-hydroxylated tryptophan residue (Trp57-OH) in the β subunit of preMADH [12,13]. The latter tryptopha residue is hydroxylated through an uncharacterized mechanism prior to catalytic processing by MauG. The MauG-catalyzed reaction is a three-step, six-electron oxidation process, consisting of cross-link formation between βTrp108 and βTrp57-OH, hydroxylation of cross-linked βTrp108-βTrp57-OH, and quinol-to-quinone oxidation [107] (Figure 1.2.2). Each step requires one eq. of H_2O_2 as the oxidant [108]. Alternatively, dioxygen can substitute H_2O_2 as the oxidant in the presence of electron donors such as ascorbate and NADH, yet with a lower catalytic efficiency [108].

Rarely does a hemoenzyme catalyze such a complicated reaction. The involvement of MauG in posttranslational modification of a large protein substrate contradicts our conventional knowledge of the functional behavior of hemoenzymes, which are typically adapted to accommodate the substrates into a heme-binding pocket to facilitate catalysis. Insight into the catalytic strategy employed by MauG began to be revealed by a ground-breaking finding, namely that the MauG-catalyzed reaction proceeds via an unprecedented high-valence *bis*-Fe(IV) intermediate [109]. This section is dedicated to discussing our current understanding of this intriguing intermediate and the novel radical chemistry that it orchestrates.

1.4.1 MauG, a di-heme enzyme involved in protein maturation

The biosynthesis of MADH and its accessory proteins requires a gene cluster named methylamine utilization (*mau*) cluster [110]. The gene that encodes MauG, *mauG*, is located in this cluster. Inactivation of *mauG* in vivo results in the production of an inactive tetrameric $\alpha_2\beta_2$

protein precursor of MADH, preMADH, which contains incompletely synthesized TTQ with mono-hydroxylated βTrp57 and unmodified βTrp108 [13]. This precursor can be converted to active MADH containing mature TTQ by reaction with H_2O_2 mediated by MauG [108].

In the resting state, MauG binds tightly with its substrate protein, preMADH [111]. It is possible to isolate the MauG-preMADH complex in solution using size-exclusion chromatography [111]. This finding significantly fostered the crystallographic study of MauG; previous efforts in crystallizing MauG alone were unsuccessful until co-crystallization of MauG and preMADH was performed. The X-ray crystal structure of the MauG-preMADH complex was subsequently determined [112]. One molecule of preMADH interacts with two molecules of MauG, with each β subunit binding one MauG molecule [112] (Figure 1.4.1_A).

MauG possesses two *c*-type hemes in distinct spin states, *i.e.*, a hexacoordinated high-spin heme with an axial histidine coordination (denoted as $Heme_{5C}$) and a hexacoordinated low-spin heme with an unusual His-Tyr axial ligand set (denoted as $Heme_{6C}$) [12,112] (Figure 1.4.1_B). The two heme Fe ions in MauG are separated by 21.1 Å with the closest edge-to-edge distance between the porphyrin rings being 14.5 Å [112] (Figure 1.4.1_B). Despite a large physical separation, the two hemes are able to share electrons efficiently [113,114]. EPR studies showed that the two hemes are oxidized and reduced in unison rather than sequentially [113]. Thus, a mixed-valence state cannot be observed. This redox cooperativity suggests that a facile equilibration of electrons occurs between the hemes, allowing them to behave as a single di-heme unit rather than as independent redox centers. Notably, due to its axial coordination vacancy and solvent accessibility, only $Heme_{5C}$ is reactive towards exogenous small molecules [113,115]. The His-Tyr ligand set at the $Heme_{6C}$ site remains intact regardless of redox events and reactions of MauG [109,113].

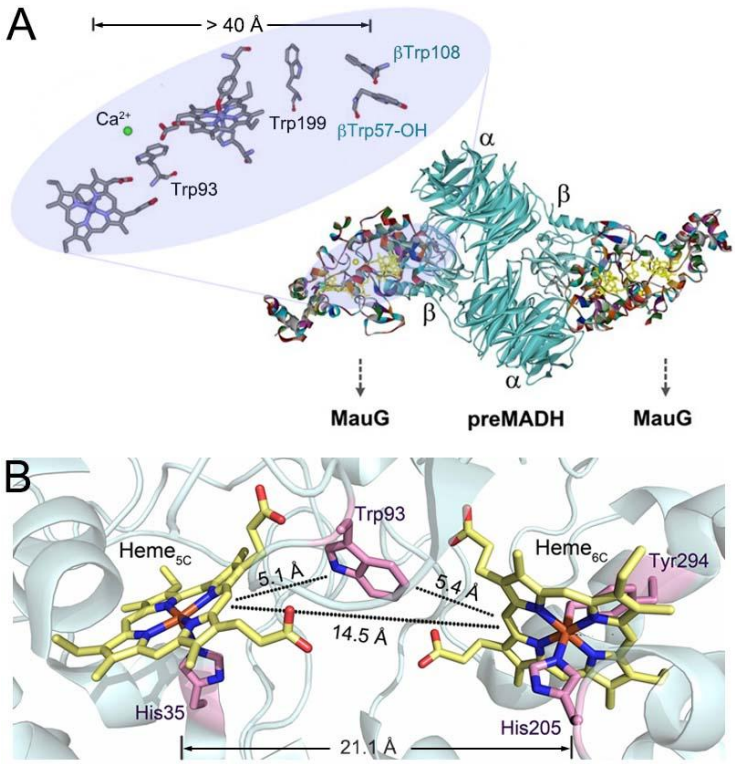

Figure 1.4.1 Crystal structure of MauG (PDB entry: 3L4M). (a) The overall structure of the MauG-preMADH complex. A zoom-in view of the key redox components along the catalytic pathway is shown in the left corner. The center of the two target residues of preMADH are over 40 Å away from Heme5C of MauG, the enzyme's "active site" for binding external oxidants. (b) Relative orientation of hemes and the intervening tryptophan residue. The edge-to-edge distances between the indole side chain of Trp93 and each heme porphyrin ring, and between the two heme porphyrin rings are illustrated.

1.4.2 Cytochrome c peroxidase-MauG superfamily

Structurally, MauG belongs to the cytochrome *c* peroxidases (CcP)-MauG superfamily. This superfamily contains the bacterial di-heme CcP (bCcP), MauG, and other di-heme peroxidases with unknown functions. Recently, another structurally characterized di-heme enzyme, rubber oxygenase (RoxA), has been proposed to be a member of this superfamily [116]. Despite similarities in the overall protein fold, a high degree of functional diversity is present in this superfamily. Different types of reactions are catalyzed by family members sharing a conserved structural core and the same redox cofactors. For instance, bCcP mediates peroxidase reactions in which it transfers the oxidizing equivalents from H_2O_2 to cytochrome *c* or other

small redox proteins, similar to the functional behavior of mono-heme cytochrome *c* peroxidases from other organisms [3]. RoxA, however, catalyzes dioxygenase reactions by incorporating both oxygen atoms of its co-substrate, dioxygen, into latex for rubber biodegradation [116,117]. Distinct from the former two, MauG orchestrates a complex, multi-step redox reaction during TTQ biosynthesis as described above.

A major determinant of the functional differences between these family members is believed to be the types of axial heme ligands [3]. In the catalytically active form of bCcP, MauG, and RoxA, the reactive heme that binds exogenous oxidant molecules is coordinated by one protein-based ligand, a histidine, while the other heme is hexacoordinated with varied axial ligand sets, *i.e.*, His-Met in bCcP [3], His-Tyr in MauG [112], and His-His in RoxA [116] (Figure 1.4.2). It is noteworthy that the axial ligands of the seemingly less important, hexacoordinated heme play an important role in defining the reaction type and enzymatic functionality by tuning the heme redox properties to control the nature of the reactive intermediates in the catalytic cycle. In bCcP, the thiol ligation to the hexacoordinated heme provided by the conserved methionine residue causes a significantly elevated heme redox potential compared to the other heme. Therefore, mixed-valence states of the di-heme cofactor can be generated and are essential to the enzymatic performance in most cases [118,119]. Despite notable exceptions [120,121], an Fe(III)/Fe(II) (His heme/His-Met heme) mixed-valence state is the common active form of bCcP [3,122,123] (Figure 1.4.2). Upon H_2O_2 binding to the ferric heme, an Fe(IV)/Fe(III) (His heme/His-Met heme) mixed-valence state is produced as a result of transferring the two oxidizing equivalents from H_2O_2 to the di-heme cofactor [3,122,123]. This mixed-valence intermediate is catalytically competent. During this process, the original ferrous His-Met heme functions as a redox reservoir to safely store one oxidizing equivalent, avoiding the formation of semi-stable radical species, *i.e.*, compound I and

compound ES. In contrast, MauG cannot stabilize a mixed-valence state. The replacement of the methionine ligand with a tyrosine at the hexacoordinated heme site lowers the heme redox potential and facilitates redox cooperativity within the di-heme system. As a result, an unprecedented *bis*-Fe(IV) intermediate, in which both hemes are oxidized to Fe(IV) by H_2O_2, is generated as a key reactive intermediate [109]. The aromatic moiety of the tyrosine ligand also plays an active role in stabilizing the Fe(IV) state via spin delocalization, which counters excess charge built up on the iron center [124].

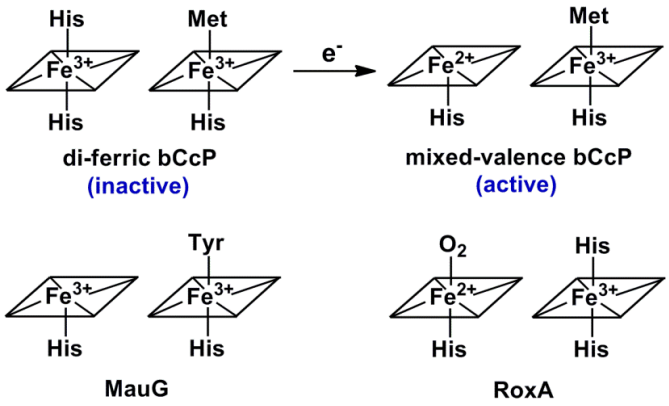

Figure 1.4.2 Axial heme ligand sets in bCcP, MauG, and RoxA. The "reductive activation" process in bCcP is illustrated on the top; the resting states of MauG and RoxA are presented at the bottom. RoxA is isolated with a dioxygen ligand bound to the His-coordinated heme (reference [116]).

Although the types of axial heme ligands determine the basic redox chemistry, it is the structural variations outside the conserved folding core that "shape" the substrate specificity of the family members. As shown in Figure 1.4.3, MauG and bCcP share remarkable structural homology [112,119]. The orientations of several key redox and structural components, including the two *c*-type hemes as well as a conserved tryptophan residue and a Ca^{2+} ion located in between the hemes, are nearly identical. However, notable structural differences are present in four color-coded regions at the protein surface shown in Figure 1.4.3.

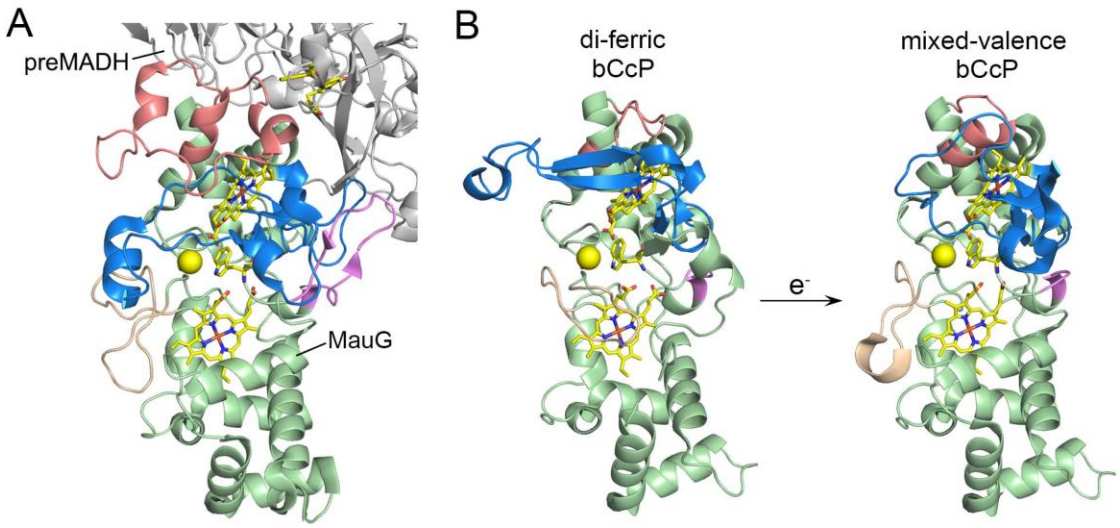

Figure 1.4.3 Structural comparisons between (a) MauG (PDB entry: 3L4M) and (b) bCcP from *Paracoccus pantotrophus* (PDB entries: 2C1V and 2C1U). The four regions that show significant structural differences between MauG and bCcP are color coded. Their corresponding positions are as follows: red, 292-334 in MauG vs. 287-298 in bCcP; blue, 202-265 in MauG vs. 212-260 in bCcP; violet, 75-90 in MauG vs. 102-105 in bCcP; wheat, 43-63 in MauG vs. 77-90 in bCcP. In each structure, the two *c*-type hemes as well as a conserved tryptophan residue and a Ca^{2+} ion located in between the hemes are highlighted in yellow. The MauG structure also includes a portion of its binding partner, preMADH, which is shown in gray with the two target tryptophan residues displayed in yellow.

In MauG, the length of these regions is generally longer than that in bCcP, and three regions are involved in protein-protein interactions with preMADH (Figure 1.4.3_A). The majority of bCcPs are isolated in an inactive di-ferric state in which one heme has an axial *bis*-His ligand set, and the other has a His-Met ligand set [118,119,125] (Figure 1.4.2). A "reductive activation" process usually occurs when a one-electron reduction of the high potential His-Met heme triggers conformational changes both locally and remotely [3,122,123]. The conformational changes are localized in 25% of the molecule [119], and almost overlap with the regions that display structural differences with MauG (Figure 1.4.3_B). The remote conformational changes affect the low potential *bis*-His heme site and cause displacement of one of the histidine ligands, allowing H_2O_2 access to that site [118,119]. The local conformational

changes surrounding the His-Met heme may facilitate the binding of small redox proteins to complete the electron transfer process [123]. Therefore, the structural variations on the exterior of protein are evolutionarily derived to accomplish the substrate specificity of the CcP-MauG superfamily members. This notion is verified by the recent structural characterization of RoxA, which reveals successive accumulation of extensions of peripheral loops [116]. These extended loops may function as "hydrophobic brushes" that can accommodate the entry of the substrate polymer by flexible movements [116].

1.4.3 Bis-Fe(IV) MauG, a lynchpin species in TTQ biogenesis

A striking feature revealed by the crystal structure of the MauG-preMADH complex is that the binding interface between the two proteins is distant from the di-heme cofactor [112]. Moreover, the heme that binds H_2O_2, $Heme_{5C}$, is further away from the preTTQ site than $Heme_{6C}$, with a physical distance of over 40 Å [112] (Figure 1.4.2). Given that the MauG-preMADH co-crystals are catalytically active, a long-range catalytic strategy must be utilized [126]. Consequently, it has become a legitimate concern as to how the oxidizing power of H_2O_2 is properly delivered to the preTTQ site through the protein matrix of MauG.

The most interesting redox property of MauG is the high-valence state that it stabilizes and utilizes to catalyze TTQ biosynthesis. Upon reaction with H_2O_2, a high-valence *bis*-Fe(IV) species of MauG is generated which spontaneously returns to the resting di-ferric state on the minute time-scale in the absence of preMADH [109] (Figure 1.4.4_A). The EPR spectrum of this intermediate showed that both high- and low-spin ferric heme signals are not present, suggesting that both hemes are in an EPR-silent Fe(IV) state [109]. Parallel Mössbauer characterization of this intermediate revealed two quadrupole doublets with the following parameters: Species 1 with an isomer shift (δ) value of 0.06 mm/s and a quadrupole splitting (ΔE_Q) value of 1.70 mm/s, Species 2 with a δ value of 0.17 mm/s and a ΔE_Q value of 2.56 mm/s [109]. Both isomer shift

values are characteristic of Fe(IV) species. Species 1 displays a quadrupole splitting value within the typical range for ferryl and protonated ferryl species [11,84,96,127,128], and is assigned as an Fe(IV)=O species at the $Heme_{5C}$ site (Figure 1.4.4_A). Species 2 shows an unusually large quadrupole splitting value which is attributed to an Fe(IV) moiety at the $Heme_{6C}$ site with the original His-Tyr axial ligand set retained (Figure 1.4.4_A). The Fe(IV) moiety in *bis*-Fe(IV) MauG is unique in biology because it lacks an exogenous oxo group which has been observed in all other protein systems and is considered to be crucial for stabilization of the ferryl ion. It is noteworthy that analogous Fe(IV) porphyrin species with two non-oxo axial ligands have been generated in inorganic model complexes and exhibit an uncommonly large quadrupole splitting value as well [129-131]. Together with these observations, the discovery of the *bis*-Fe(IV) state of MauG suggests that the term "ferryl' should be reserved for Fe(IV) just as "ferrous" and "ferric" for Fe(II) and Fe(III), respectively, and "oxo-ferryl" for Fe(IV)=O.

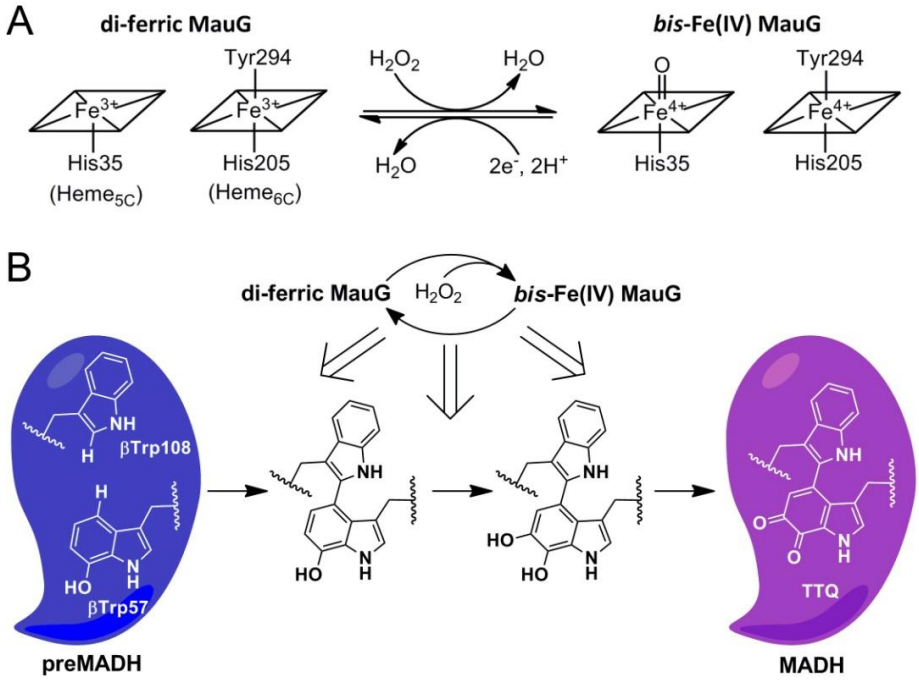

Figure 1.4.4 The *bis*-Fe(IV) intermediate of MauG. (a) Chemical conversion between di-ferric and *bis*-Fe(IV) MauG. (b) Involvement of the *bis*-Fe(IV) intermediate in TTQ biosynthesis.

Subsequent kinetic characterizations on the *bis*-Fe(IV) species demonstrated that it is catalytically competent in TTQ biosynthesis [107,109]. Upon reacting the *bis*-Fe(IV) species with a stoichiometric amount of preMADH, a cationic radical pair of $[\beta Trp57\text{-}OH]^{\bullet+}$ and $[\beta Trp108]^{\bullet+}$ is generated on preMADH as the *bis*-Fe(IV) species returns to the di-ferric state [107]. The first step of the MauG-mediated TTQ biosynthesis is then achieved via collision of the radical pair to form a new σ bond between the two tryptophan π moieties. Therefore, the apparent role of the high-valence Fe(IV) ions is to remotely extract electrons from the preTTQ site and generate radical species on it, activating the substrate for reactions. Based on this discovery, as well as a crystallographic study which visualized the time-resolved changes at the preTTQ site during catalysis, a mechanistic model for TTQ biosynthesis has been proposed [107]. Specifically, the *bis*-Fe(IV) species is expected to be involved in each of the two-electron oxidation step to initiate radical formation on preMADH. Radical chemistry occurs at the preTTQ site to accomplish the chemical modifications through sequential reactions of cross-linking, hydroxylation, and oxidation of quinol to quinone (Figure 1.4.4_B).

Quite a few protein components spanning the framework of MauG communicate with the di-heme cofactor to facilitate the formation and function of the *bis*-Fe(IV) species. For instance, the Tyr294 ligand of $Heme_{6C}$ plays a crucial role in stabilizing the Fe(IV) moiety of $Heme_{6C}$. In its absence, the Fe(IV) state of $Heme_{6C}$ cannot be observed upon reaction with H_2O_2 [132,133]. Consequently, the two oxidizing equivalents derived from H_2O_2 are trapped at the $Heme_{5C}$ site in the form of a compound I-like species [132,133]. In addition, the Pro107 residue located at the distal pocket of $Heme_{5C}$ is shown to be involved in binding exogenous ligands [134]. It also limits the unproductive oxidation of distal methionine residues by *bis*-Fe(IV) [134,135]. Trp199 is a surface residue that resides at the protein interface of the MauG-preMADH complex [112] (Figure 1.4.1_A). It has been demonstrated that the productive electron-flow from the preTTQ

site to the *bis*-Fe(IV) site is achieved through electron/hole hopping with Trp199 as a hopping relay [101]. Upon mutation of Trp199, the oxidizing power stored at the di-heme cofactor can no longer be channeled to the substrate [101]. Moreover, the structural studies of MauG revealed the presence of a Ca^{2+} ion in between the two hemes [112] (Figure 1.4.1_A). The positioning of the Ca^{2+} ion and the two hemes is essentially identical to that in bCcP (Figure 1.4.3) [118,119,125]. In bCcP, the Ca^{2+} ion plays critical structural roles for the enzymatic function. It is required to induce conformational changes around the *bis*-His heme during the "reductive activation" process [136]. The presence of the Ca^{2+} ion also governs the dimerization of bCcP, which is active in the dimeric state [137]. The activity of MauG also depends on the presence of the Ca^{2+} ion. Ca^{2+}-depleted MauG is unable to generate the *bis*-Fe(IV) state [138,139]. Addition of Ca^{2+} to Ca^{2+}-depleted MauG can restore its reactivity toward H_2O_2 and TTQ biosynthesis activity [138,139]. EPR and Mössbauer spectroscopic studies have shown that the presence of the Ca^{2+} ion exerts a significant influence on the magnetic properties of the two hemes and the relative orientations of the heme axial ligands: in the Ca^{2+}-depleted MauG, $Heme_{6C}$ exhibits a change in the relative orientations of its two axial ligands, while $Heme_{5C}$ is converted to low-spin by incorporating another protein residue as its sixth ligand [138]. These changes prevent the enzyme from generating and stabilizing the *bis*-Fe(IV) state. Given the aforementioned examples, it is evident that an extended network of interactions within the protein matrix is required for MauG to specifically utilize the *bis*-Fe(IV) species in TTQ biosynthesis.

1.4.4 Natural strategies for storing two oxidizing equivalents

The discovery of the *bis*-Fe(IV) species offers a conceptual contribution to iron-oxygen chemistry and enzymology. Iron-containing enzymes that utilize oxygen for oxidation and oxygenation reactions usually employ high-valence iron intermediates to perform demanding chemical transformations. These intermediates transiently store oxidizing equivalents from

molecular oxygen or peroxide and precisely deliver them to the specific substrates to accomplish chemical reactions. During these processes, the iron cofactor plays irreplaceable roles over other transition metals in activating the oxidant molecules and adjusting the chemical reactivity of high-valence intermediates, due to its ability to access multiple oxidation states. An important topic related to this scientific area is how to store two oxidizing equivalents in iron centers from biological systems. This topic is broadly associated with reactions catalyzed by Rieske non-heme iron-dependent oxygenases, cytochrome P450 oxygenases, and heme-dependent peroxidases.

Notably, a ferric hydroperoxo species is a common intermediate of all three groups of enzymes listed above. Release of the two oxidizing equivalents from the hydroperoxo moiety via heterolytic O-O bond cleavage is generally considered as a critical step to initiate productive transformations. Several different strategies have been identified to transiently stabilize the two oxidizing equivalents and channel them to the substrate. Directly storing two oxidizing equivalents at the ferric iron center results in an Fe(V) species. Thus far, catalytically competent Fe(V) intermediates have only been proposed in Rieske non-heme oxygenases at the form of Fe(V)=O(OH) [140-144] (Figure 1.4.5), but have never been captured in any biological reactions. The severe electron-deficiency of the Fe(V) ion makes it extremely destructive to any protein environment as it might oxidize its own coordination ligands or other surrounding residues. Despite the long-standing controversy in their involvement in enzymatic reactions, Fe(V) species have been generated in synthetic model complexes and demonstrated to be capable of performing different reactions, including alkene di-hydroxylation reactions [145-147].

In hemoenzymes, it is not practical to have an overly reactive Fe(V) species as a catalytic intermediate, for the heme porphyrin is susceptible to oxidation. As a result, an Fe(V) species is generally considered to be a hypothetical intermediate state connecting the starting ferric hydroperoxo species and subsequent reactive high-valence intermediates. The most well-known

example of reactive high-valence intermediates in hemoenzymes is the compound I species in P450-type monooxygenases [4,50,51]. Compound I consists of an oxo-ferryl ion (Fe(IV)=O) coupled with a π-cation radical located on the heme porphyrin (Figure 1.4.5). It transiently stabilizes two oxidizing equivalents above the ferric state and is chemically equivalent to an Fe(V) species. Delocalization of one oxidizing equivalent over the entire heme moiety, as observed in the compound I species, causes greater chemical stability compared to Fe(V). This modification in reactivity brings great advantages for facilitating enzymatic reactions. During a catalytic cycle, the enzyme active site usually undergoes reorganizations and conformational changes to activate substrates or stabilize intermediates. The charge redistribution makes compound I reactive enough to perform the target reaction, yet not so reactive as to cause non-specific oxidation prior to proper substrate orientation and active site reorganization.

Another form of high-valence iron species in hemoproteins is compound ES, which is composed of an oxo-ferryl heme and a nearby aromatic residue-based radical [148] (Figure 1.4.5). Compound ES also contains two oxidizing equivalents above the ferric state. Compared to compound I, the two oxidizing equivalents in compound ES are further separated and the spin-coupling interaction between them is significantly weakened or lost. Therefore, compound ES-type intermediates are frequently utilized by peroxidases which are capable of performing one-electron oxidation reactions. Moreover, compound ES is reportedly more stable than compound I [149]. The formation of compound ES rather than compound I may be a requirement for enzymes with a substrate of a larger size. For example, in cytochrome *c* peroxidase, the reducing equivalents for the compound ES intermediate come from cytochrome *c,* and thus protein-protein interactions are also a part of the catalytic process.

The *bis*-Fe(IV) species of MauG is the first of its kind and is chemically equivalent to an Fe(V), compound I, or compound ES (Figure 1.4.5). This species has proved a novel natural

strategy of storing two oxidizing equivalents in protein-based ferric iron centers. The two oxidizing equivalents of *bis*-Fe(IV) are stored in two discrete hemes with an intervening tryptophan residue mediating Type III CR and exhibit extraordinary stability when the substrate is absent. Notably, the 21 Å separation of the heme irons in the *bis*-Fe(IV) intermediate distinguishes itself from the only other documented protein-based iron intermediate with two Fe(IV) ions, Intermediate Q from the non-heme iron-dependent enzyme methane monooxygenase [150] (Figure 1.4.5). Intermediate Q displays an $Fe(IV)_2(\mu\text{-}O)_2$ diamond core structure and is capable of converting methane to methanol [151]. Intermediate Q has a very short Fe-Fe distance (~2.5 Å) and the proximity of the Fe(IV) ions causes them to be strongly coupled [151]. In contrast, the Fe(IV) ions of *bis*-Fe(IV) MauG are not close enough for direct coupling interactions. In *bis*-Fe(IV), the delocalization of the oxidizing equivalents over a large area of the protein effectively shifts the chemical power towards the substrate binding site by over 20 Å, enabling the remote electron-abstraction process from the preTTQ site. As mentioned above, blocking the charge delocalization by mutating the Tyr294 ligand of $Heme_{6C}$ results in accumulation of a compound I-like species [132,133]. While *bis*-Fe(IV) and compound I may possess similar oxidizing capability, only the former is catalytic competent in TTQ biosynthesis. This comparison highlights the critical role of *bis*-Fe(IV) in expanding the oxidizing power and shortening the electron-abstraction distance from the substrate.

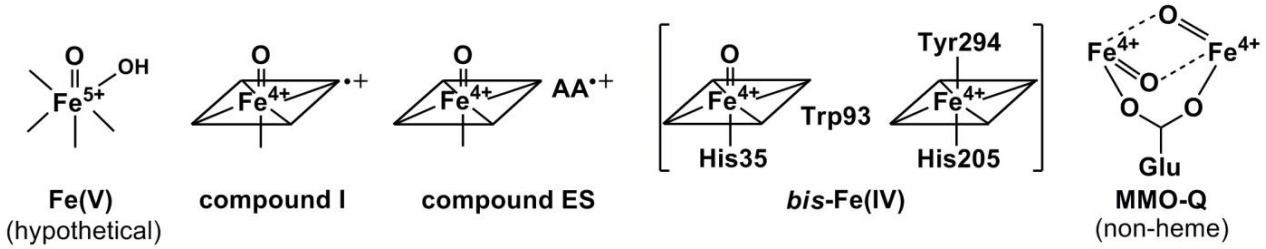

Figure 1.4.5 Electronically equivalent high-valence iron intermediates in biology.

1.4.5 Bis-Fe(IV) MauG delivers the oxidizing power at a distance through a radical mechanism

In TTQ biosynthesis, MauG generates a very powerful high-valence iron intermediate, *bis*-Fe(IV), at one end of the reaction pathway, and utilizes this potent oxidant to perform "remote enzyme microsurgery" [126] at the other end via protein radical chemistry. At the current stage, it is intriguing to have a "bird's-eye view" of how the oxidizing power initially derived from H_2O_2 is properly delivered to the preTTQ site over 40 Å away through the protein matrix of MauG. An overview of the reaction pathway of TTQ biosynthesis reveals that the key redox components of ET reactions consist of two types of aromatic moieties, heme and tryptophan (Figure 1.4.1). The closest distance between the target tryptophan residues at the preTTQ site and the iron center of $Heme_{6C}$ is 19 Å. This gap is bridged by the hopping process through the intervening Trp199 residue [101]. Similarly, the distance between the iron centers of $Heme_{6C}$ and $Heme_{5C}$ is 21 Å, and this gap is spanned by the hopping process through Trp93 [152]. The involvement of these redox components divides the overall ET pathway into small hopping segments, greatly enhancing the ET efficiency. It is noteworthy that the hopping relays (Trp93 and Trp199) are the same kind of residues as the oxidation targets on preMADH.

Although MauG structurally belongs to the CcP-MauG superfamily, from the perspective of the catalytic strategy, it shares more common features with several other enzymes that utilize radical chemistry to perform long-range chemical reactions, including ribonucleotide reductase (RNR) [100] and DNA photolyase [153]. In these two enzymes, it is also evident that the overall ET reaction is achieved via electron/hole hopping using the same kind of residues as hopping relays, *i.e.*, tyrosine in RNR and tryptophan in DNA photolyase. The use of hopping points that are nearly isopotential eliminates effects of $\Delta G°$on the ET rates of the hopping steps. It is noteworthy that compared to the other two systems, the overall ET pathway in the MauG-

preMADH system has two distinguishable segments: between $Heme_{5C}$ and $Heme_{6C}$, between $Heme_{6C}$ and preTTQ. In the absence of preMADH, the first segment is able to function independently to stabilize the *bis*-Fe(IV) species, and the ET process is reversible. This gives rise to a unique charge-resonance phenomenon, in which the Trp93 residue located between the hemes is reversibly oxidized and reduced to facilitate the dynamic charge equilibrium in the di-heme system, thereby stabilize the oxidizing equivalents in the *bis*-Fe(IV) species [152]. In the presence of preMADH, the two segments are connected, and the ET process becomes irreversible as preTTQ, which contains a hydroxylated tryptophan, is easier to be oxidized and thus serves as a sink for oxidizing equivalents. In general, the mechanistic study of MauG has supplemented and improved the current knowledge of this emerging group of protein radical-utilizing enzymes and generated a profound impact on the broad enzymology community.

1.4.6 Concluding remarks

The MauG-preMADH system is complex, and pursuing an understanding of its chemistry has been full of surprises. It has proved to be a model system to study high-valence iron species, charge-resonance phenomenon, protein radical chemistry, long-range electron transfer, and protein posttranslational modification. The discovery and characterization of *bis*-Fe(IV) MauG offers a conceptual contribution to heme chemistry and demonstrates a novel strategy of storing two oxidizing equivalents. This potent intermediate remotely initiates radical formation at the target site of the substrate protein via electron/hole hopping. The substrate itself then directs the sequential transformations of cross-link formation, incorporation of oxygen from the solvent, and quinol-to-quinone oxidation, during the multistep biosynthetic process.

2 ENZYME REACTIVATION BY HYDROGEN PEROXIDE IN TRYPTIOPHAN 2,3-DIOXYGENASE

(The main body of this chapter is selected and modified from a research article that JG coauthored: Fu R, Gupta R, Geng J, Dornevil K, Wang S, Zhang Y, Hendrich, MP, and Liu A (2011) Enzyme reactivation by hydrogen peroxide in heme-based tryptophan dioxygenase. ***J. Biol. Chem.*** 286(30), 26541-26554. Some contents in the "Introduction" and "Discussion" section are incorporated from the following review article that JG coauthored: Geng J, and Liu A (2014) Heme-dependent dioxygenases in tryptophan oxidation. ***Arch. Biochem. Biophys.***, 544, 18-26.)

2.1 Abstract

An intriguing mystery about TDO is its hydrogen peroxide-triggered enzyme reactivation from the resting ferric state to the catalytically active ferrous form. In this study, we found that such an odd Fe(III) reduction by an oxidant depends on the presence of L-Trp, which ultimately serves as the reductant for the enzyme. In the peroxide reaction of TDO, a previously unknown catalase-like activity was detected. A ferryl species (δ = 0.055 mm/s and ΔE_Q = 1.755 mm/s) and a protein-based free radical (g = 2.0028, 1.72 mT linewidth) were characterized by the Mössbauer and EPR spectroscopy, respectively. This is the first compound ES-type ferryl intermediate from a heme-based dioxygenase characterized by the EPR and Mössbauer spectroscopy. DFT calculations revealed the contribution of secondary ligand sphere to the spectroscopic properties of the ferryl species. In the presence of L-Trp, the reactivation was demonstrated by enzyme assays and various spectroscopic techniques. A Trp-Trp dimer and a monooxygenated L-Trp were both observed as the byproducts of the enzyme reactivation process. Together, these results lead to the unraveling of an over 60-year old mystery of the peroxide-driven reactivation mechanism. These results may shed light on how a metalloenzyme maintains its catalytic activity in an oxidizing environment.

2.2 Introduction

P450-type monooxygenases exhibit a "peroxide shunt" pathway in which the ferric form of enzymes can interact with single-oxygen donors such as peroxides, leading to direct formation of the compound I intermediate [4,50] (Figure 2.2.1_A). Compared to the native Fe(II)- and O_2-dependent reaction pathway, this alternative pathway allows the catalytic cycle to be completed without the participation of associated redox proteins and electron donors.

The ferrous heme of TDO is the catalytic center that binds and activates dioxygen. Like many other Fe(II)-dependent enzymes, TDO becomes autoxidized to the Fe(III) form in aerobic environments when the substrate L-Trp is absent. For quite a long time, the reactions involving hydrogen peroxide and the resting ferric state of TDO received little attention, despite several very interesting phenomena reported from discrete studies. In 1959, H_2O_2 was implicated as an activator of the ferric enzyme by the finding that ferric TDO becomes active towards L-Trp after treatment with H_2O_2 [20]. This observation was later confirmed by independent studies from different laboratories [16,154,155], and further proven by the observation that the activation effect is inhibited by catalase [16]. However, the mechanism by which ferric TDO is reduced to its ferrous form by reacting with H_2O_2 remains elusive after over 60 years.

Here, we provide unequivocal evidence in support of the formation of the ferrous form of the enzyme by reaction of ferric TDO with H_2O_2 and L-Trp. A previously unknown two-phase enzyme reactivation mechanism is proposed based on the identification and characterization of nearly all of the intermediates and products (Figure 2.2.1_B). In the first phase, the enzyme is oxidized by peroxide to generate a compound ES-type ferryl intermediate; in the second phase, the ferryl heme and the protein-based radical are each reduced by L-Trp (Figure 2.2.1_B). We further hypothesize that the physiological significance of the enzyme reactivation pathway is to allow for maintaining the catalytic activity of the enzyme in an oxidizing environment. This

study revealed the fundamental differences between TDO and P450-type monooxygenases in their peroxide reactions.

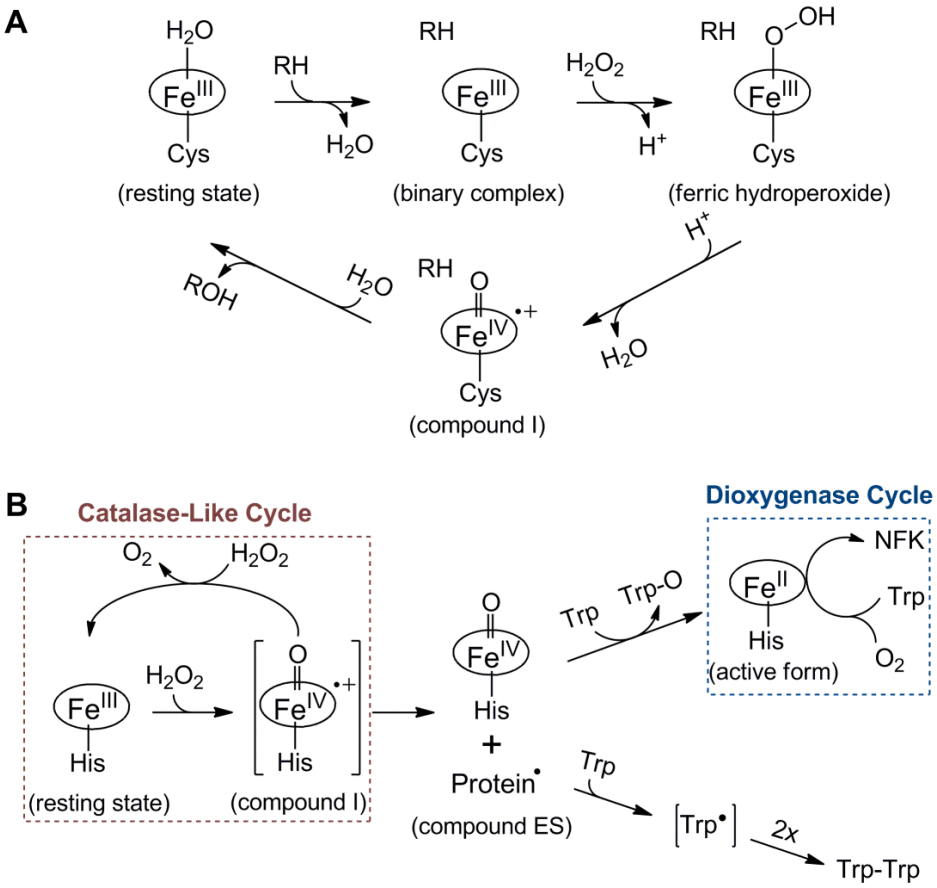

Figure 2.2.1 Peroxide-mediated alternative enzymatic pathways in heme-dependent oxygenases. (A) The "peroxide shunt" pathway in P450-type monooxygenases. "RH" represents the substrate and "ROH" represents the product. (B) The enzyme reactivation pathway in TDO. The enzyme reactivation occurs when the protein radical and the ferryl heme in the compound ES-type intermediate are each reduced by L-Trp. Intermediates shown in parentheses are predicted but not detected experimentally.

2.3 Experimental procedures

2.3.1 Reagents

L-Trp (99.5%) was purchased from Sigma-Aldrich. H_2O_2 (30%, v/v) was purchased from Fisher Scientific. The concentration of H_2O_2 was calculated based on the extinction coefficient of $\varepsilon_{240\ nm} = 43.6\ M^{-1}cm^{-1}$. $H_2{}^{18}O_2$ (2% v/v solution) and $H_2{}^{18}O$ were purchased from Icon Isotopes at

90.0 and 97.6% isotope enrichment, respectively. ^{57}Fe (95% enrichment) was purchased from Science Engineering and Education Co. (Edina, MN). All experiments were performed in the 50mM Tris-HCl buffer, pH 7.4, unless otherwise specified.

2.3.2 Expression and purification of cmTDO

The construction of the plasmid encoding full-length cmTDO has been described elsewhere [24]. The protein was purified using a 100-ml nickel-affinity column and a Superdex 200 size-exclusion column on an ÄKTA FPLC system as described in an earlier study of the enzyme [156]. The optical absorption spectrum of the as-isolated enzyme used in this work displays a 405:280 nm ratio of 1.4–1.5:1 (Figure 2.3.1), corresponding to 60–65% heme occupancy based on the determination of the protein concentration and the iron content using the inductively coupled plasma optical emission spectroscopy and the EPR spin quantitation technique. The purified enzyme demonstrated a specific activity of 25 μmol/min/mg. The ferrous enzyme used as control samples in the UV-vis and Mössbauer experiments was obtained by dithionite reduction of the ferric enzyme under anaerobic conditions.

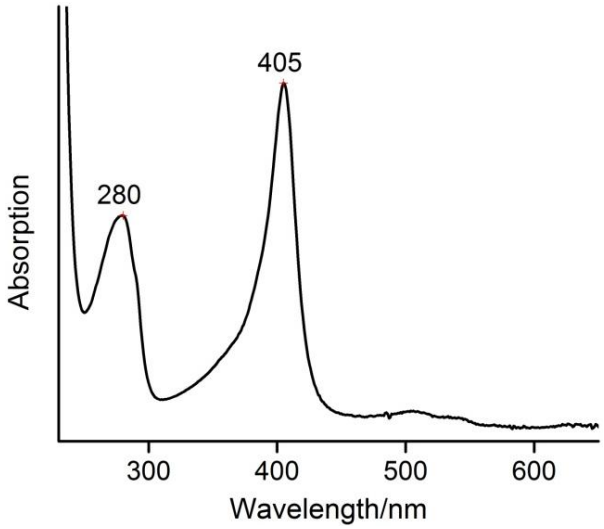

Figure 2.3.1 UV-vis spectrum of as-isolated TDO.

2.3.3 Catalase-like activity assays

Oxygen production was measured in a sealed reaction chamber (3 mL) with an integrated oxygen electrode unit (Oxygraph System, Hansatech Instruments) at room temperature. The oxygraph experiments were performed in the aerated buffer. The production of oxygen was monitored as a function of time. The kinetic data were fitted to Eq. 1, where υ is the steady state velocity, [E] is the concentration of the enzyme, [S] is the concentration of the substrate, k_{cat} is the catalytic turnover constant, and K_m is the Michaelis-Menten constant.

$$v/E = k_{cat}[S]/([S] + K_m) \qquad \text{Eq. 1}$$

2.3.4 Optical absorption spectroscopy

The absorption spectra were obtained using an Agilent 8453 UV-vis spectrophotometer at room temperature. The enzyme reactivation by peroxide was performed under anaerobic conditions using a homemade long-arm sealed cuvette (1 mL). All the reagents were degassed and purged with argon prior to the experiments. Both L-Trp and H_2O_2 were freshly prepared. Unless otherwise stated, the final concentration of TDO in the reaction system was 5 μM. The enzyme was made anaerobic in a glass vial by repeated evacuation and refilling with argon. A gastight microsyringe was used for addition of various amounts of argon-saturated oxygen-free H_2O_2 to the anaerobic enzyme-substrate complex. The NFK concentration was determined by the known extinction coefficient at 321 nm ($\varepsilon_{321\ nm}$ = 3152 $M^{-1}cm^{-1}$) [66]. The apparent rates of the dioxygenation reaction were determined from the initial velocity of the NFK formation. The aerobic reaction of H_2O_2 with TDO in the presence of L-Trp was performed similarly with exclusion of the steps associated with the oxygen removal.

To test whether the ferric form of TDO can react with H_2O_2 and directly produce NFK through a catalytic shunt pathway as observed in cytochrome P450s, we performed the enzyme reactivation assays in the presence of carbon monoxide (CO). In these experiments, CO was

introduced to the reaction system either prior to the reaction or in the middle of the reaction by directly bubbling CO into the reaction solution containing TDO, H_2O_2, and L-Trp.

2.3.5 MS characterization of the reaction products

All reagents for the MS experiments were prepared in the anaerobic 50 mM Tris-HCl buffer, pH 7.4. The reactions were performed on ice with stirring in septum-sealed reaction vials. Ferric TDO (100 μM) was allowed to react with H_2O_2 ($H_2{}^{16}O_2$ or $H_2{}^{18}O_2$) in the presence of L-Trp (5 mM). The peroxide was titrated to a final concentration of 4 mM. After 20 min of incubation, TDO was removed from the reaction system using Centriprep-10 at 3,000 × *g*, and the filtrate was collected for electrospray ionization mass spectrometry (ESI-MS) analysis.

ESI-MS analyses were conducted in a positive mode on a Waters ESI-Q-TOF micro mass spectrometer equipped with a Waters alliance 2695 HPLC system (Milford, MA). Samples were injected through either direct infusion or HPLC separation on a Waters 2695 alliance HPLC system before MS analysis. The TDO reaction samples were mixed with 50% acetonitrile in water containing 0.1% formic acid before analysis. HPLC separation was achieved on a Restek Allure C18 column (100 × 2-mm inner diameter). Mobile phase A was composed of water and 0.1% formic acid. Mobile phase B was composed of acetonitrile and 0.1% formic acid. The elution gradients were performed as follows: starting at 100% A for 5 min; falling to 0% A over 10 min; staying at 0% A for 15 min; and then rising to 100% A over 20 min at a constant flow rate of 200 μL/min. In MS/MS analysis, collision energy was set to 30 eV.

2.3.6 Oxygen exchange with solvent in NFK

^{16}O-NFK was prepared according to the enzyme-based procedures described above. A concentrated sample of ^{16}O-NFK was diluted in $H_2{}^{18}O$ with a final $H_2{}^{16}O/H_2{}^{18}O$ ratio of 1:4 (78.1% ^{18}O) and then incubated on ice for 20 min prior to the ESI-MS analysis. In a parallel

experiment, concentrated ^{16}O-NFK was first diluted in $H_2{}^{18}O$ in the same manner. After 20 min of incubation, the sample was concentrated by rapidly evaporating the solvent under vacuum and then re-diluted with $H_2{}^{16}O$. The final ratio of $H_2{}^{16}O$:$H_2{}^{18}O$ was 60:1. This experiment was designed to examine whether the oxygen exchange with the solvent would be fully reversible.

2.3.7 EPR spectroscopy

EPR samples were prepared in reaction vials with the 50 mM Tris-HCl buffer, pH 7.4 with 10% glycerol. The samples were then transferred to EPR tubes and quickly frozen in cold isopentane (-140 °C) or liquid nitrogen at the desired reaction time. Multiple sets of the EPR experiments were conducted to optimize the enzyme/peroxide ratio for the production of reactive intermediates while minimizing loss of the heme cofactor. X-band EPR spectra were recorded in the perpendicular mode on a Bruker EMX spectrometer at 100-kHz modulation frequency using a 4119HS resonator. The EPR measurement temperature was maintained with an ESR910 liquid helium cryostat and an ITC503 temperature controller. A calibrated frequency meter was used to aid the *g*-value determination. Spin concentration was determined by double integration of the EPR signals obtained under low microwave power conditions and comparing to a Cu-EDTA standard sample (0.5 mM $CuSO_4$, 5 mM EDTA) measured under identical conditions.

The EPR relaxation properties of the radical species at different temperatures were analyzed from EPR spectra obtained with varied microwave powers in the range of 0.002–200 mW. The values of half-saturation parameter ($P_{1/2}$) were obtained by fitting the data to Eq. 2, in which I is the EPR signal amplitude and P is microwave power.

$$I \propto 1/(1 + P/P_{1/2})^{1/2} \qquad \text{Eq. 2}$$

2.3.8 Mössbauer spectroscopy

The ^{57}Fe-enriched protein was obtained by expressing TDO in *Escherichia coli* using ^{57}Fe-enriched culture medium as previously described [156]. The Mössbauer samples were prepared from the as-isolated ^{57}Fe(III)-TDO and frozen in liquid nitrogen. For the detection of the formation of Fe(II)-TDO in the peroxide-driven reactivation reactions, a final concentration of 1.0 mM (heme concentration) ^{57}Fe-TDO was used. To generate the high-valence Fe(IV) intermediate, six eq. of H_2O_2 (9.6 mM) were added to ^{57}Fe(III)-TDO (1.6 mM heme concentration), and the samples were frozen in liquid nitrogen at 20 s and 50 s, respectively. Mössbauer spectra were recorded on a constant acceleration instrument with an available temperature range of 1.5 to 200 K. Isomer shifts are reported relative to the Fe metal at 298 K. Least-square fitting of the spectra was performed using the WMOSS software package (WEB Research, Edina, MN). The low-temperature Mössbauer spectra of ferric TDO were fit with the standard spin Hamiltonian (Eq. 3).

$$H = g\beta BS + D[S_z^2 - S(S+1)/3] + E(S_x^2 - S_y^2) + A_{iso}(SI) - g_n b_n BI + (eQV_{zz}/12)[3I_z^2 - I(I+1) + \eta(I_x^2 - I_y^2)] \quad \text{Eq. 3}$$

2.3.9 Computational modeling

The hybrid functional B3LYP [157] with a Wachter's basis (62111111/3311111/3111) for Fe [158], 6-311G* for all the other heavy atoms, and 6-31G* for hydrogen was used to predict the values of Mössbauer quadrupole splitting and isomer shift, as previously applied in other iron-containing proteins and models [159,160]. In all the investigated models, the heme group is represented by a porphyrin with original β substituent replaced by methyl groups, and the axial histidine group is truncated to be 5-methylimidazole. Geometries of all the structural models investigated in this work were optimized with the terminal atoms fixed at the X-ray

crystal structure positions to mimic the protein environment effect, using the DFT method BPW91 with the above basis set [161,162] which is the same approach used previously to investigate other oxy-ferryl species [159,160].

2.4 Results

2.4.1 Reaction of ferric TDO and H_2O_2 in the absence of L-Trp

The reaction of ferric TDO with H_2O_2 was examined with an oxygen electrode in a stirred cell at room temperature. Figure 2.4.1_A shows that the addition of 50 eq. of H_2O_2 to the ferric protein resulted in an immediate increase in the oxygen concentration of the reaction chamber. Another addition of H_2O_2 in the same amount led to a similar increase in the oxygen concentration, indicating that O_2 generation is reproducible (Figure 2.4.1_A). When ferric TDO was added to the buffer containing H_2O_2, similar O_2 production was observed (Figure 2.4.1_B), indicating no dependence on the order of additions. In contrast, addition of either the protein or peroxide alone, as shown in Figure 2.4.1, did not produce O_2. These results indicate that ferric TDO possesses a catalase-like activity in the absence of L-Trp. The k_{cat}, K_m, and k_{cat}/K_m values of the TDO catalase-like activity determined from steady-state analysis are 13 ± 2 s^{-1}, 16 ± 3 mM, and 850 ± 65 $M^{-1}s^{-1}$, respectively (Figure 2.4.1_C).

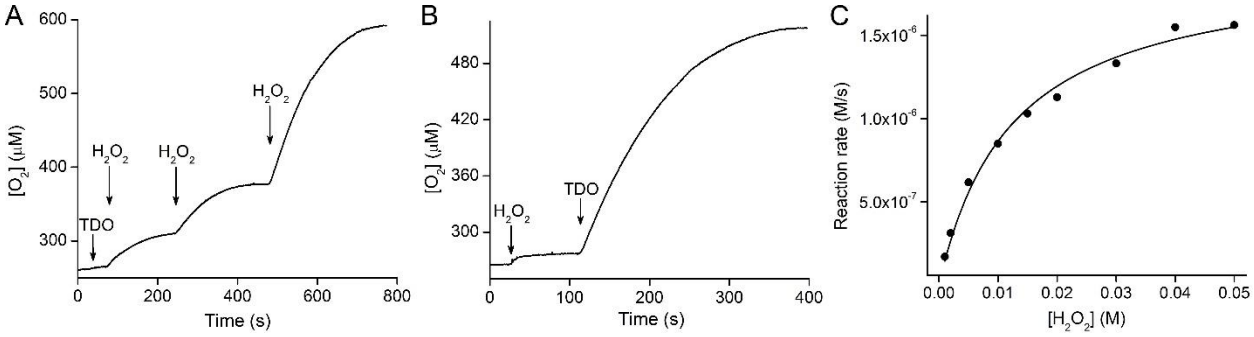

Figure 2.4.1 Catalase-like activity of cmTDO. (A) H_2O_2 decomposition and O_2 production mediated by ferric TDO in a stirred oxygen electrode cell in response to discrete additions of H_2O_2. (B) Reaction initiated by the addition of TDO. The arrows indicate the time points in which ferric TDO (5 μM) or H_2O_2

(250 μM or 1 mM in A and 1 mM in B) was added to the reaction cell. (C) Steady-state kinetic assay of the catalase-like activity of TDO. The solid line is the best fit of the experimental data to Eq. 1. Kinetic parameters were determined from the fitting results.

The reaction of ferric TDO with H_2O_2 was studied by Mössbauer spectroscopy (Figure 2.4.2). At 4.2 K, the as-isolated TDO protein shows a six-line magnetic pattern. The simulation overlaid on the experimental data (solid line) is calculated for an S = 5/2 iron site with δ = 0.42 mm/s, ΔE_Q = 1.53 mm/s, D = 13 cm^{-1}, E/D = 0.01, and A_{iso} = 195 kG (Figure 2.4.2_B). These values are indicative of a high-spin ferric heme [156]. A parallel sample was treated with six eq. of H_2O_2 and frozen after 30 s (Figure 2.4.2_A). The Mössbauer spectrum of this sample is composed of four species. One species is recognized as the high-spin ferric TDO which accounts for 25% of the iron in the sample. Figure 2.4.2_C shows the difference spectrum of A - 0.25B. This difference spectrum is composed of three overlapping doublets as indicated on the figure. The fits to the three doublets (the solid line in Figure 2.4.2_C) give the following Mössbauer parameters and relative amounts: (1) δ = 0.055 mm/s, ΔE_Q = 1.755 mm/s, 33%; (2) δ = 0.350 mm/s, ΔE_Q = 0.703 mm/s, 17%; (3) δ = 0.585 mm/s, ΔE_Q = 1.5 mm/s, 25%. Species 1 is assigned as an S = 1 Fe(IV) heme, tentatively in the Fe(IV)=O form. The parameter ranges of known S = 1 Fe(IV)-oxo heme species are 0–0.15 for δ and 1.0–1.6 mm/s for ΔE_Q. The other two species appear to be degradation products of the reaction. Species 2 has parameters characteristic of high-spin ferric hemes, but the diamagnetic doublet indicates that this heme species has formed μ-oxo bridges [163]. Species 3 is typical of nondescript ferric species [164], presumably due to a loss of the iron ion from heme. The difference spectrum is unchanged in character when recorded at 100 K. Thus, the addition of six eq. of H_2O_2, all at once, resulted in a 42% loss of heme from TDO, with 25% of heme unchanged and 33% of heme forming a ferryl species. The loss of heme is not surprising in this case since the *b*-type heme in TDO is not covalently bonded

to the protein and thus can be relatively easily detached from the protein during reaction or protein manipulation.

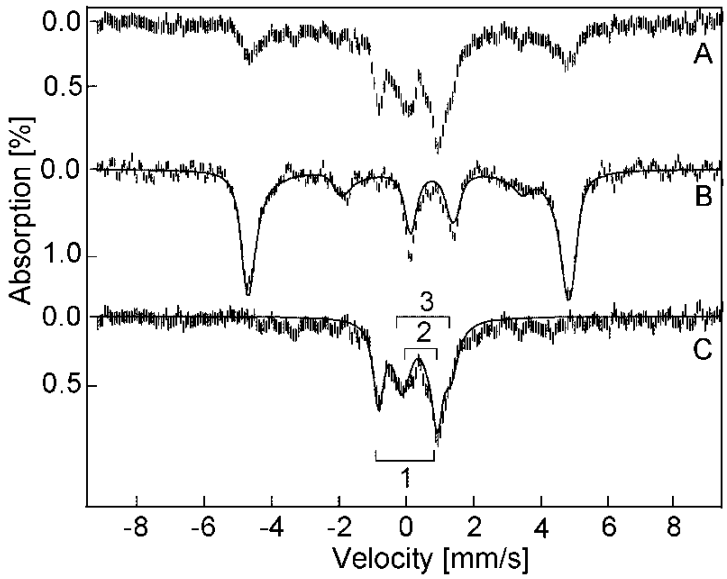

Figure 2.4.2 Mössbauer spectra of ^{57}Fe-cmTDO in the absence of L-Trp. (A) Ferric TDO (1.6 mM) + H_2O_2 (9.6 mM). The reaction time is *ca.* 30 s. (B) Ferric TDO (1.6 mM) prior to the reaction with H_2O_2. (C) The difference spectrum: A - 0.25B. All spectra were recorded at 4.2 K in an applied field of 45 mT parallel to the direction of the γ-ray beam. The solid lines are the least-squares fits.

The reaction of TDO with H_2O_2 was also studied by the EPR spectroscopy. The as-isolated ferric TDO displays a nearly axial EPR signal at g = 6 and a weak resonance at g = 2 (Figure 2.4.3), characteristic of a high-spin ferric heme. Upon the addition of H_2O_2, the ferric heme EPR signal decreased in intensity concomitantly with the formation of a g = 2.0028 radical signal (Figure 2.4.3_B). Thus, an EPR-active radical intermediate is present in addition to the postulated Fe(IV)-oxo species revealed by the Mössbauer spectroscopy. The amplitude of the EPR signal for the radical species is shown on a reduced scale for comparison with the ferric heme signal. A plot of the concentrations of the high-spin ferric heme and the radical species as a function of time is present in Figure 2.4.4. At 12 s, the radical species has a spin concentration of 40% of the initial iron concentration. A zoom-in view of the EPR signal of the radical species

from the 12-s sample is shown in the inset of Figure 2.4.5. This signal is omitted from Figure 2.4.3_B for clarity. At longer reaction times, the radical species decayed, and the high-spin ferric EPR signal gradually increased in intensity (Figure 2.4.3 and 2.4.4). At 10 min, the concentration of the high-spin ferric heme species is about 70% of its initial concentration. The detected loss (*ca.* 30%) of heme in the EPR samples is lower than the result obtained from the Mössbauer spectroscopy, presumably due to the relatively low concentration of H_2O_2 used in the EPR experiments. During the reaction time of Figure 2.4.3, the shape of the high-spin heme EPR signal subtly became more axial, which suggests that the electronic environment of the heme changes during the reaction with peroxide.

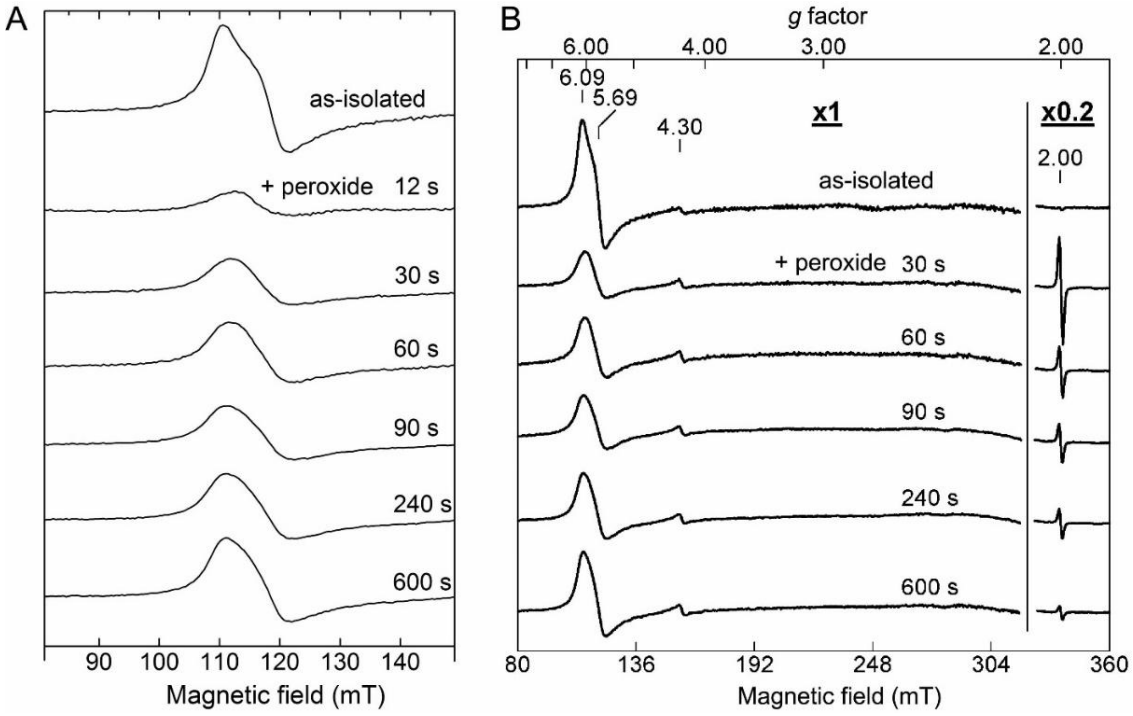

Figure 2.4.3 Changes in the EPR signals of cmTDO during the reaction of ferric TDO (150 μM) with H_2O_2 (900 μM). (A) EPR spectra of TDO before and after the reaction with H_2O_2. (B) Overall EPR spectra with a zoom-in view of the g = 2 region. The time points at which the EPR samples were frozen after the addition of H_2O_2 are listed in the figures. The spectra were collected at the following conditions: temperature, 10 K; microwave frenquency, 9.44 GHz; microwave power, 1 mW; and modulation amplitude, 0.8 mT.

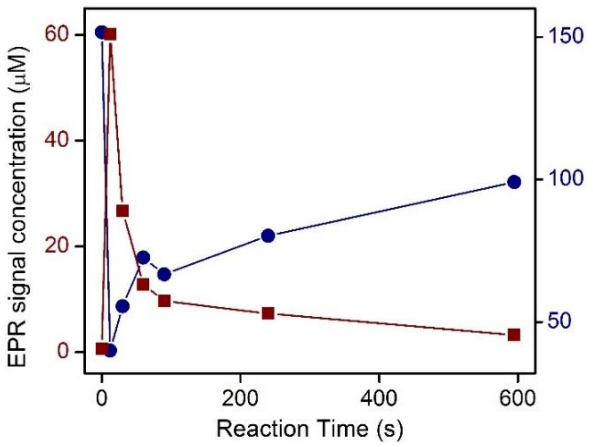

Figure 2.4.4 EPR signal intensity as a function of time for the radical species at g = 2.0028 (wine) and the high-spin ferric heme at g = 6 (navy). The plots were generated based on the experimental data from Figure 2.4.3.

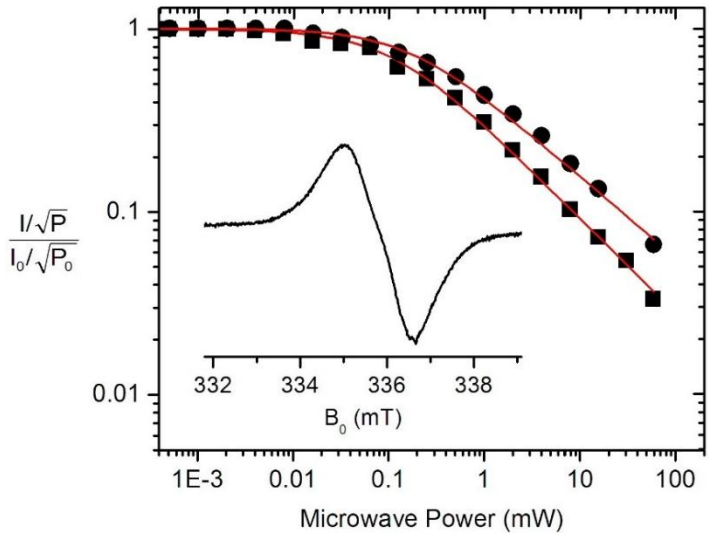

Figure 2.4.5 The g = 2.0028 radical species (inset) and its relaxation properties. The power saturation profiles at 10 K (■) and 100 K (●), and the fits to Eq. 2 are shown.

The peak-to-peak line width of the radical signal is 1.72 mT (Figure 2.4.5), which is too large for a peroxide-based free radical (< 1 mT) but typical for a protein-derived aromatic radical [165,166]. At approximately the same reaction time as the Mössbauer sample, the spin concentration of the protein radical is found to be comparable with the concentration of the Fe(IV)=O heme species. The microwave power saturation behavior of the radical signal at g =

2.0028 was measured at 10 and 100 K (Figure 2.4.5). The fits to the experimental data using Eq. 2 led to $P_{1/2}$ values of 0.11 and 1.16 mW for 10 and 100 K, respectively. These values suggest a weak interaction between the protein radical and the Fe(IV) ion. Together, these results suggest the formation of an intermediate composed of an Fe(IV)=O heme in close proximity to a protein-based radical, similar to the compound ES description based on the initial characterizations of cytochrome *c* peroxidases [148,167]. Compound ES of cytochrome *c* peroxidase is a semi-stable enzyme intermediate that contains an Fe(IV)=O heme and a tryptophan radical [168].

2.4.2 Reaction of ferric TDO and H_2O_2 in the presence L-Trp

The as-isolated TDO exhibits visible absorption characteristics of a histidine-ligated ferric heme protein with a Soret band at 405 nm (Figure 2.3.1). In the presence of L-Trp, the Soret band shifts to 406 nm (Figure 2.4.6). The intensity of this 406-nm band gradually decreases, and new features at 432 and 321 nm develop concomitantly during the titration of H_2O_2 to a reaction mixture containing ferric TDO and excess (1000 eq., 5 mM) L-Trp (Figure 2.4.6_C). The 321-nm spectral feature resembles the optical characteristic for the dioxygenase reaction of ferrous TDO with O_2 as the oxidant, and the absorbance in the range of 310–330 nm has previously been used to identify the formation of NFK [169,170]. Hence, the absorption peak at 321 nm is assigned to NFK production. When H_2O_2 was incubated with L-Trp in the absence of TDO, the development of the 321-nm chromophore did not occur, indicating that NFK formation is an enzymatic process. When the peroxide reaction was carried out in the presence of hydroxyurea, a known scavenger of protein-based free radicals, the NFK production in an anaerobic reaction with peroxide was significantly inhibited (Figure 2.4.7), suggesting the protein-based radical detected by the EPR spectroscopy is an essential intermediate in enzyme reactivation. In contrast, the NFK production in the normal catalytic reaction of Fe(II)-TDO and

O_2 is not affected by the presence of hydroxyurea (Figure 2.4.8). Notably, the inset of Figure 2.4.6 shows a slightly less than 1:2 ratio of [NFK]/[H_2O_2], suggesting that under anaerobic conditions the oxygen source for the dioxygenases reaction is solely derived from H_2O_2.

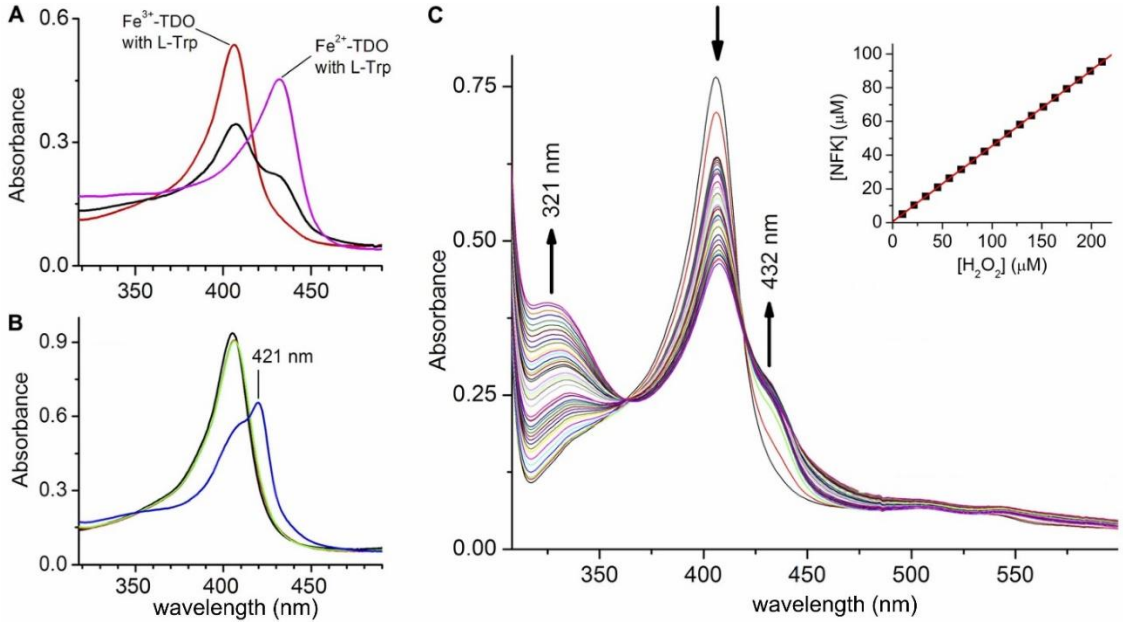

Figure 2.4.6 Optical spectra of cmTDO. (A) Soret bands of ferric and ferrous TDO (5 μM) in the presence of L-Trp (5 mM) are observed at 406 and 432 nm, respectively. The Soret band of the ferric sample split into two 30 s after the addition of H_2O_2 (30 μM). (B) Soret spectra of ferric TDO (black), after the sequential addition of L-Trp (red), CO (green), and H_2O_2 (blue). The red and green traces are nearly identical. (C) Spectral changes of ferric TDO and L-Trp upon the titration of H_2O_2. The inset is the calculated NFK concentration as a function of the added H_2O_2 concentration under anaerobic conditions.

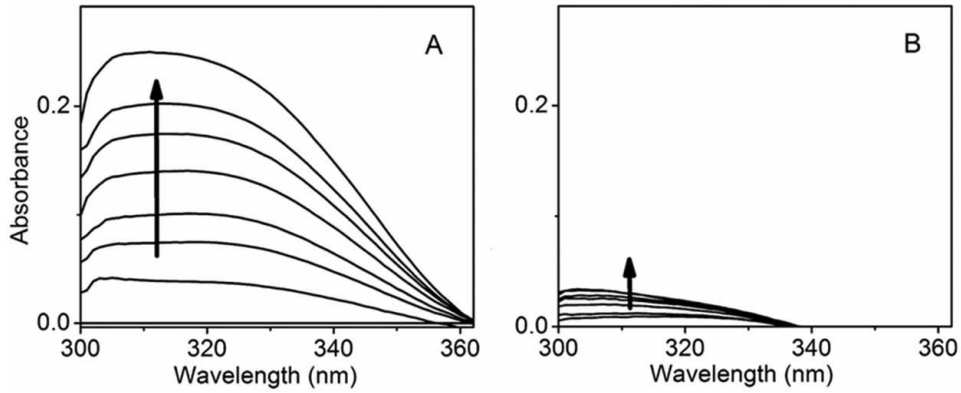

Figure 2.4.7 Effect of hydroxyurea on the production of NFK in an anaerobic reaction system containing ferric TDO (5 μM), L-Trp (5 mM), and titrated H_2O_2. H_2O_2 was titrated to a final concentration of 175

μM in the absence (A) and presence (B) of hydroxyurea (10 mM). Each trace was obtained after the reaction was complete and subtracted against a spectrum of ferric TDO at the same concentration.

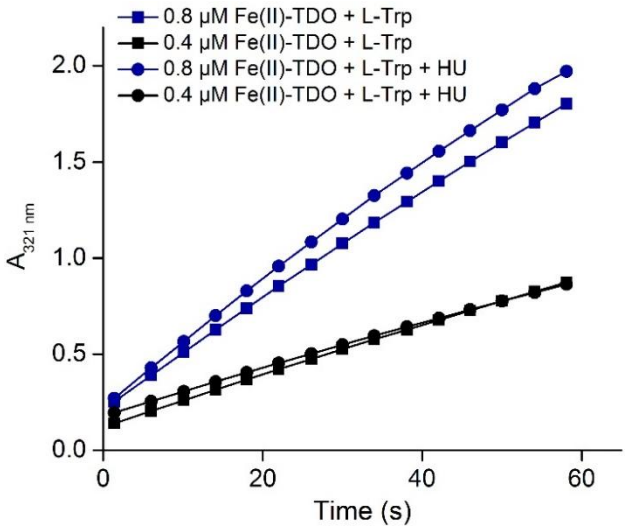

Figure 2.4.8 Effect of hydroxyurea on the enzymatic activity of ferrous TDO. The reactions were conducted in the O_2-saturated buffer containing 5 mM L-Trp in the absence and presence of hydroxyurea (5 mM).

Ferrous TDO presents a Soret band at 432 nm (Figure 2.4.6_A). During the course of the reaction of ferric TDO with H_2O_2 and L-Trp, the Soret band at 405 nm decreased, and an additional spectral feature emerged at 432 nm (Figure 2.4.6_A). The 432-nm chromophore matches the Soret band of ferrous TDO, suggesting the formation of the reduced form of TDO from a fraction of the ferric form. To confirm the formation of the Fe(II) heme, CO was introduced to stabilize the presumed ferrous species in a separate test. In our previous study of ferrous TDO, the CO adduct exhibits a Soret band at 421 nm in the presence of L-Trp, and it is stable in the presence of O_2 [96]. A similar 421-nm peak has also been reported for the ferrous-CO adduct of human TDO (hTDO) [171]. When CO was bubbled into a solution containing ferric TDO and L-Trp, the addition of CO did not cause an observable shift of the Soret band. However, upon further addition of H_2O_2, a 421-nm band corresponding to the Fe(II)-CO adduct of TDO was generated (Figure 2.4.6_B).

The formation of the active Fe(II) form of TDO from the ferric state by peroxide was further verified by the Mössbauer spectroscopy. Figure 2.4.9_A shows the Mössbauer spectrum of substrate-bound ferric TDO before the addition of CO and peroxide. The CO gas was bubbled into an anaerobic sample of ferric TDO with L-Trp for 5 min, after which two eq. of H_2O_2 were added, and the sample was immediately frozen in liquid nitrogen. The spectrum of the H_2O_2-treated sample is shown in Figure 2.4.9_B. The difference spectrum (Figure 2.4.9_C), generated by subtracting 50% of the unreacted enzyme-substrate complex, shows a doublet indicating a diamagnetic species. The Mössbauer parameters of this species are the same as those of the Fe-CO adduct of TDO characterized in our recent work [171].

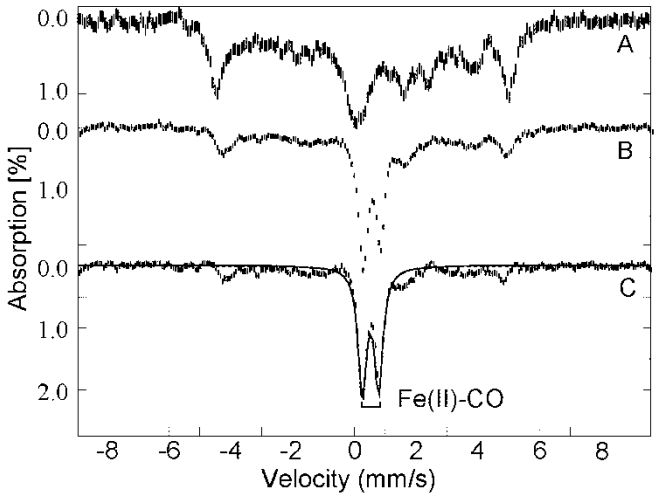

Figure 2.4.9 Mössbauer spectra of ^{57}Fe-cmTDO in the presence of L-Trp. (A) Ferric TDO (1 mM) with 50 eq. of L-Trp. (B) After treatment with CO and H_2O_2 (2mM). (C) The difference spectrum: A - 0.5B. All spectra were recorded at 4.2 K in an applied field of 45 mT parallel to the direction of the γ-ray beam. The solid line is the least-squares fit.

It is known that the Fe(II)-CO complex of TDO is catalytically inactive [171]. Like O_2, CO does not bind to ferric hemoproteins [172]. With this knowledge in mind, CO was again used as a probe to test whether the ferrous heme generated by the addition of H_2O_2 is the catalytically relavent species that gives rise to the observed dioxygense activity. Figure 2.4.10 shows that the

NFK production was inhibited by CO, indicating the dioxygenation product is generated by the ferrous enzyme. When the reaction was initiated by the addition of ferric TDO, the initial rate of the CO-treated reaction system dropped by *ca.* 6.5-fold compared with that of the untreated sample under the same conditions (Figure 2.4.10_A). In a separate set of experiments, CO was introduced into the system 15 s after the reaction was initiated. An inhibition of the NFK formation was observed (Figure 2.4.10_B), demonstrating that the depletion of the catalytically active ferrous enzyme was achieved by forming a stable but inactive Fe(II)-CO complex. Before CO was bubbled into the system, the formation of Fe(II) heme was visualized at 432 nm. After a small lag phase upon the addition of CO, a sharp decrease in the absorbance at 432 nm was observed (Figure 2.4.10_C). The absorbance at 421 nm was concomitantly increased due to the formation of the ferrous-CO adduct (Figure 2.4.10_C). These experiments support the notion that the formation of NFK is catalyzed by ferrous TDO, and an enzyme reactivation mechanism must exist during the reaction with peroxide.

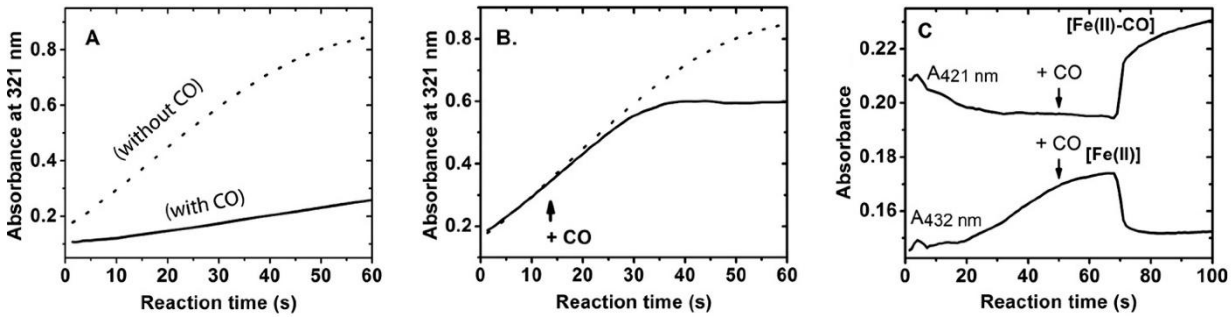

Figure 2.4.10 Effect of CO on the enzyme reactivation process. (A) The pre-injection of CO decreased the NFK production rate in a reaction system containing ferric TDO (1 μM), L-Trp (5 mM), and H_2O_2 (10 μM). The reaction was initiated by the addition of ferric TDO. (B) A parallel experiment of (A) with CO bubbled into the reaction system 15 s after the reaction was initiated (solid trace). The dotted trace shows a control experiment without the injection of CO. (C) Time-dependent changes of the Soret absorbance at 421 nm (corresponding to the Fe(II)-CO adduct) and 432 nm (the Fe(II) species). CO was bubbled into the reaction system containing ferric TDO (1 μM), L-Trp (5 mM), and H_2O_2 (10 μM) 50 s after the reaction started. All the experiments were carried out under aerobic conditions.

2.4.3 Source of oxygen in NFK

MS analysis of the reactions of ferric TDO and L-Trp with $H_2{}^{16}O_2$ and $H_2{}^{18}O_2$ were conducted. The enzyme was removed by filtration after a five-min reaction with peroxide and L-Trp prior to MS analysis. Figure 2.4.11_A shows that the substrate L-Trp presented an ion of mass-to-charge ratio (*m/z*) 205, corresponding to the anticipated $[M + H]^+$ form. The ion at *m/z* 243 in this control sample is assigned to the dimer of Tris ($M_r = 242$). A new ion at *m/z* 237 was present in the TDO reaction mixture with $H_2{}^{16}O_2$ as the oxidant (Figure 2.4.11_B). This ion corresponds to a 32-Da mass shift from L-Trp and is consistent with the production of NFK.

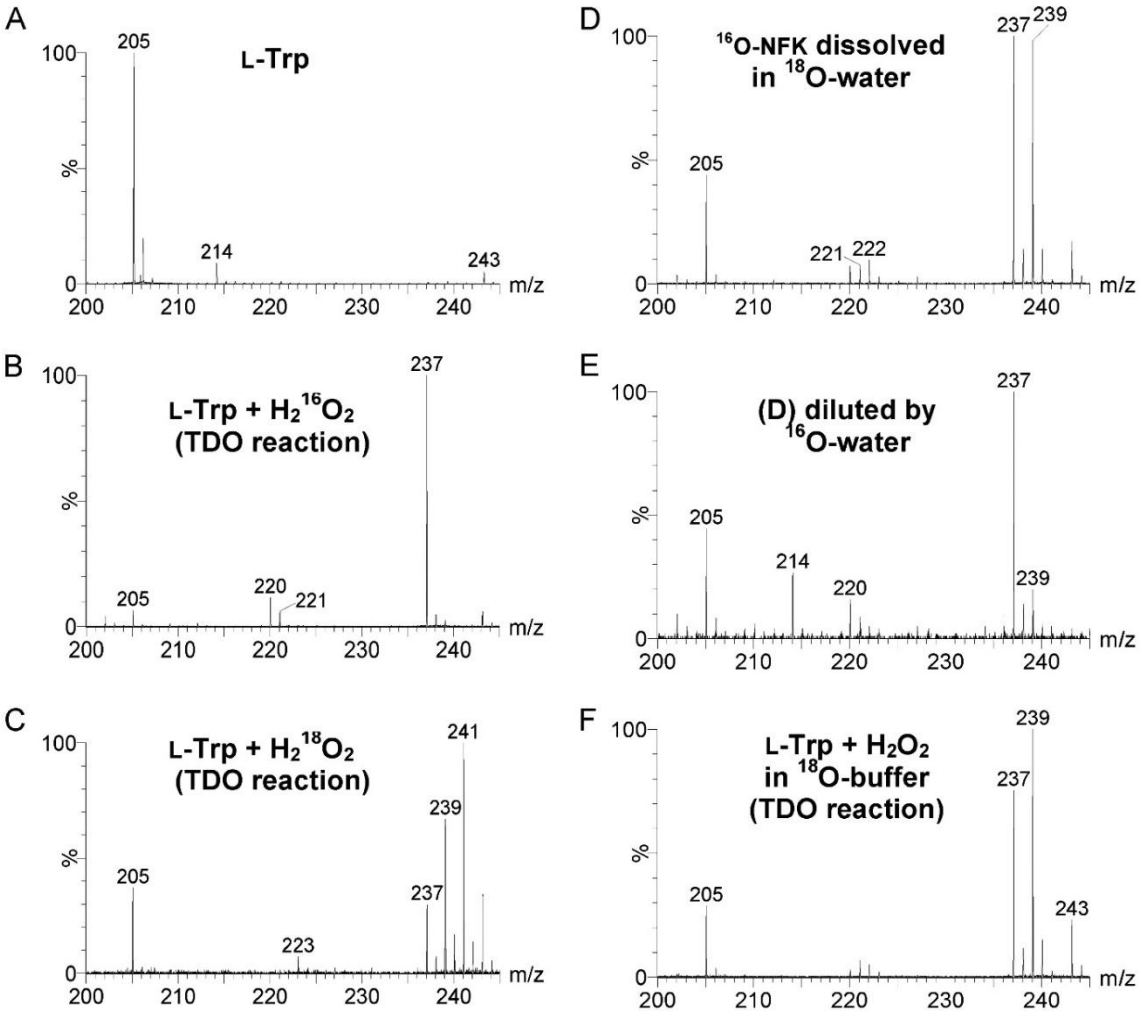

Figure 2.4.11 ESI-MS characterization of L-Trp (A), the reaction product of L-Trp, $H_2{}^{16}O_2$, and ferric TDO (B), and the reaction product of L-Trp, $H_2{}^{18}O_2$, and ferric TDO (C). (D) A ^{16}O-NFK sample,

generated from the TDO reactivation reaction, was diluted by the ^{18}O-enriched water after removal of the enzyme by filtration. The final $H_2{}^{16}O/H_2{}^{18}O$ ratio is 1:4 (78.1% ^{18}O) (E) A copy of the sample D was further diluted by $H_2{}^{16}O$ to reach a final $H_2{}^{16}O/H_2{}^{18}O$ ratio of 60:1 (1.6% ^{18}O). (F) A parallel sample of the sample B, yet carried out in the $H_2{}^{18}O$-based buffer. All the reactions were performed under an anaerobic condition prior to the MS analysis.

When $H_2{}^{18}O_2$ was used instead of $H_2{}^{16}O_2$, an ion at *m/z* 241 was detected (Figure 2.4.11_C). This ion is consistent with the incorporation of two atoms of ^{18}O into L-Trp from $H_2{}^{18}O_2$. An ion at *m/z* 237 was also observed due to the presence of the unlabeled ^{16}O fraction of the peroxide reagent (90% ^{18}O-enrichment). Although the experiment was carried out under O_2-free conditions, oxygen leak could occur during the process of filtering the enzyme out of the reaction system, thereby generating another small fraction of NFK containing unlabeled oxygen. The amplitude of the *m/z* 237 ion is estimated to be less than 20% of the sum of the total product ions.

In Figure 2.4.11_C, a product ion of *m/z* 239 is also present, which corresponds to the incorporation of one atom of ^{16}O and one atom of ^{18}O into L-Trp. To investigate the cause of the $^{16}O/^{18}O$ scrambling, a sample of ^{16}O-NFK was prepared in the same condition as that of Figure 2.4.11_B. The ^{16}O-NFK sample was concentrated and then diluted by the ^{18}O-enriched water to reach a final $H_2{}^{16}O/H_2{}^{18}O$ ratio of 1:4 (78.1% ^{18}O). Figure 2.4.11_D shows that a new ion at *m/z* 239 was generated from the non-labeled NFK in a post-enzymatic reaction process in the presence of the ^{18}O-enriched water. This observation suggests that one ^{18}O atom from the solvent was exchanged into ^{16}O-NFK. A copy of the sample containing both the *m/z* 237 and 239 ions was further diluted by the unlabeled water to reach a $H_2{}^{16}O/H_2{}^{18}O$ ratio of 60:1 (1.6% ^{18}O) and was analyzed again by ESI-MS. Figure 2.4.11_E shows that the *m/z* 239 ion was substantially reduced in intensity, whereas the original *m/z* 237 ion became the dominant species, which indicates a reversible oxygen exchange with the solvent for NFK. It should be noted that no *m/z*

241 peak was observed in either abovementioned samples, indicating that only one oxygen atom in NFK is solvent-exchangeable.

A parallel sample to Figure 2.4.11_B was prepared using unlabeled H_2O_2 as the oxidant in the $H_2{}^{18}O$-based solvent. As shown in Figure 2.4.11_F, the *m/z* 237 and 239 ions are present in this sample, consistent with a single oxygen-atom exchange with the solvent after the catalytic reaction to form the *m/z* 239 ion. Collectively, these results suggest that the two oxygen atoms incorporated into NFK are both derived from H_2O_2, and one of the oxygen atoms is readily exchangeable with the solvent.

In addition, a minor product peak at *m/z* 409 was observed after the reaction of ferric TDO and L-Trp with either $H_2{}^{16}O_2$ or $H_2{}^{18}O_2$ (Figure 2.4.12). This species is tentatively assigned to an L-Trp dimer. It was undetectable when either TDO or H_2O_2 was absent or in regular dioxygenase reactions of ferrous TDO.

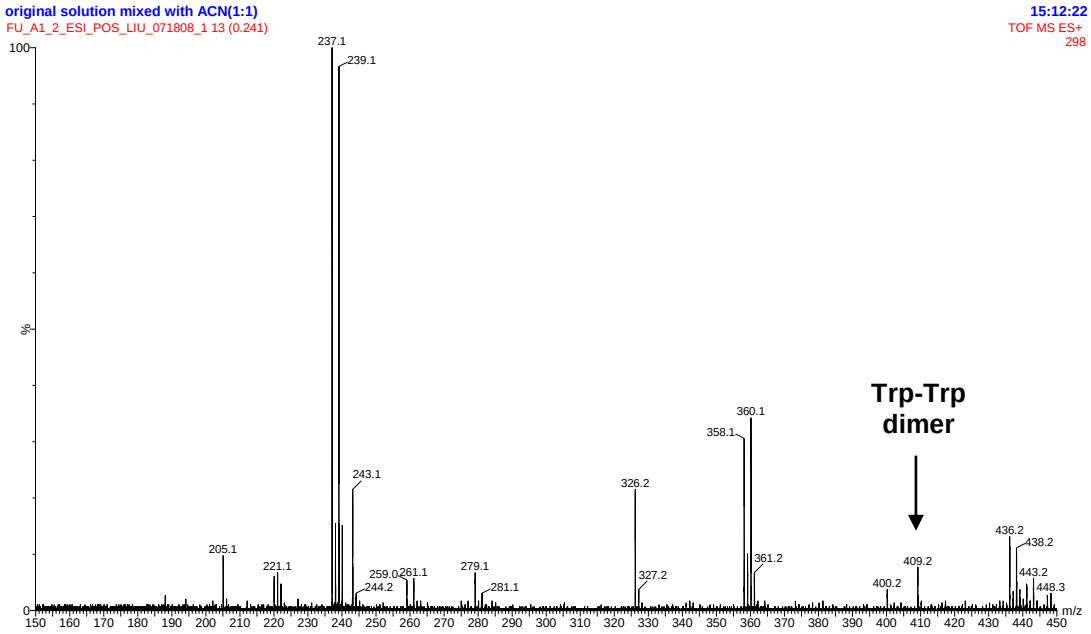

Figure 2.4.12 ESI-MS detection of the Trp-Trp dimer from the TDO reactivation reaction. The reaction system was composed of 5 mM L-Trp, 4 mM $H_2{}^{18}O_2$, and 100 μM ferric TDO under an anaerobic condition.

2.4.4 Identification of a minor monooxygenated product of L-Trp

In addition to the dioxygenation product NFK, two ions at *m/z* 220 and 221 are observed in the reaction of ferric TDO and L-Trp with unlabeled H_2O_2 (Figure 2.4.11_B). As described below, the *m/z* 220 ion was shown in the tandem MS experiments to be a fragment of NFK. The *m/z* 221 ion is, however, 16 Da greater than L-Trp, consistent with the insertion of one oxygen atom into L-Trp. In the isotope-labeling experiment using $H_2{}^{18}O_2$ as the oxidant, a corresponding ion at *m/z* 223, 18 Da greater than L-Trp, was observed (Figure 2.4.11_C). Thus, a putative monooxygenated product of L-Trp was generated in the peroxide-driven reactivation reactions of ferric TDO and the inserted oxygen atom was derived from the peroxide. No such product was detected in the regular dioxygenation reaction of ferrous TDO with O_2 as the oxidant.

Figure 2.4.13 presents the results of a liquid chromatography-mass spectrometry (LC-MS) experiment using $H_2{}^{16}O_2$ as the oxidant with the $H_2{}^{18}O$-based solvent to further characterize the monooxygenated product of L-Trp. The substrate (*m/z* 205) shows the greatest retention time of 16.6 min (Figure 2.4.13_A). The *m/z* 237 and 239 ions with a retention time of 6.1 min correspond to the dioxygenation product NFK (Figure 2.4.13_D). The former has two ^{16}O atoms inserted, and the latter has an ^{16}O atom and an ^{18}O atom inserted into the substrate. The *m/z* 239 ion was generated via the aforementioned single oxygen-atom exchange with the solvent. The *m/z* 243 ion with a 2.9-min retention time is attributed to the dimer form of Tris (Figure 2.4.13_B). The monooxygenated product at *m/z* 221 has a retention time of 5.3 min (Figure 2.4.13_C). The observation of an *m/z* 223 ion together with the *m/z* 221 ion indicates that the inserted oxygen atom is solvent-exchangeable.

Tandem MS experiments were subsequently conducted to further characterize the *m/z* 237 and 239 ions eluted at 6.1 min. Figure 2.4.14 shows that the *m/z* 220 and 222 ions are the

fragments of NFK (*m/z* 237 and 239, respectively), as a consequence of losing a $-^{16}OH$ or $-^{18}OH$ group during ionization. The absence of the *m/z* 221 or 223 ion in the tandem MS spectra is consistent with the LC-MS and isotope-labeling results, confirming that neither ion is a fragment of NFK.

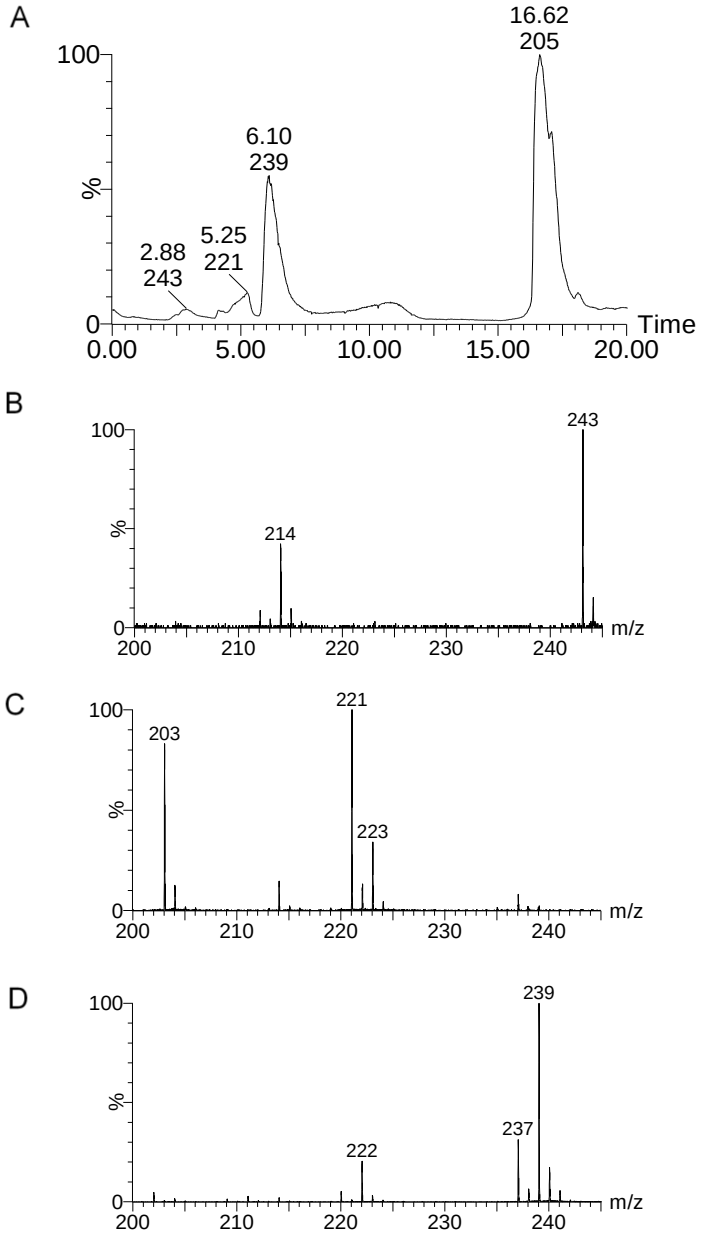

Figure 2.4.13 LC-MS characterization of the TDO reaction with $H_2{}^{16}O_2$ and L-Trp in the $H_2{}^{18}O$-based buffer. (A) LC-MS separation profile of the reaction products. Mass spectra at the retention time of 2.88, 5.25, and 6.10 min are shown in (B), (C), and (D), respectively.

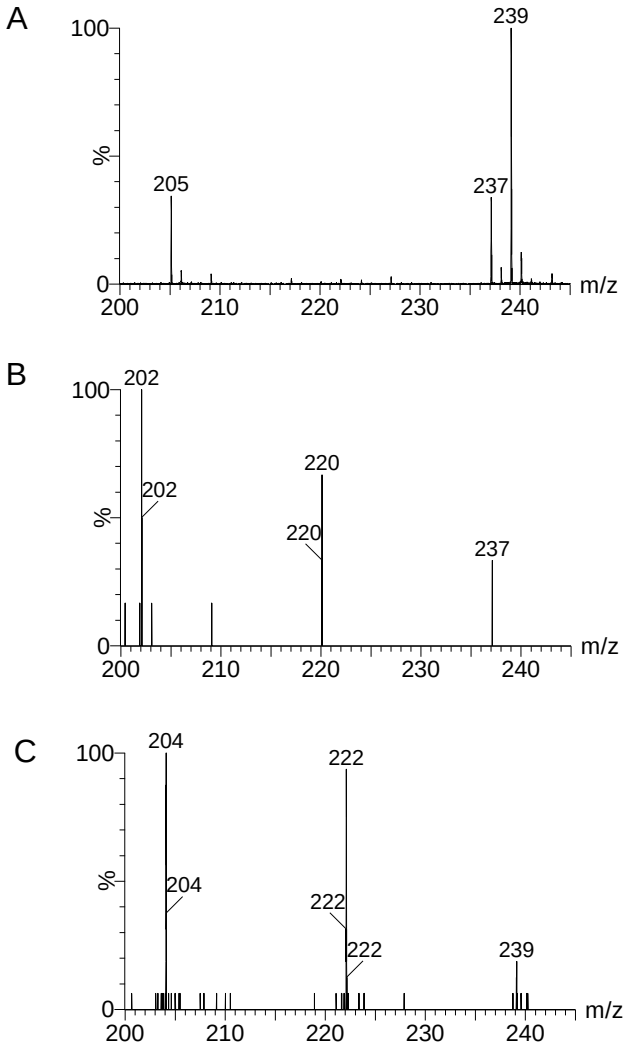

Figure 2.4.14 Tandem MS analysis of the NFK ion peaks at *m/z* 237 and 239, which were co-eluted at 6.10 min as shown in Figure 2.4.13. (A) The MS spectrum of the NFK ion peaks from the LC-MS analysis. The tandem MS results for the *m/z* 237 and 239 ions in (A) are shown in (B) and (C), respectively.

2.4.5 Computational study

The TDO ferryl species observed in our Mössbauer study exhibits an unusually large ΔE_Q parameter of 1.755 mm/s at pH 7.4. This value is greater than those of other Fe(IV)-oxo species of hemoproteins but is smaller than those of protonated Fe(IV)-oxo species (see the section 2.5.4 for details). DFT calculations on the TDO ferryl intermediate were performed to evaluate the

possible structural influences on the Mössbauer parameters, including the protonation state of the oxo group, H-bonding interactions to the oxo group from a distal histidine and a conserved Ser-Gly pair, and conformational changes of the proximal histidine ligand (Table 2.4.1). The data presented suggest that the relatively large positive value of the ΔE_Q parameter is a result of an H-bonding interaction to the ferryl oxo group.

Table 2.4.1 Computational results of various models for the cmTDO ferryl species

	Model	R_{FeO} (Å)	ΔE_Q (mm/s)	δ (mm/s)
TDO	Experimental		1.755	0.055
1A	$Fe^{IV}(Por)^{2-}(His)^{0}(O)^{2-}$	1.654	1.54	0.14
1B	+ twisted His	1.648	1.97	0.13
2A	$Fe^{IV}(Por)^{2-}(His)^{0}(OH)^{1-}$	1.799	3.02	0.08
2B	+ twisted His	1.795	3.19	0.11
3A	$Fe^{IV}(Por)^{2-}(His)^{0}(O\cdots HB)^{2-}$	1.663	1.78	0.12
3B	+ twisted His	1.657	2.20	0.11
4A	$Fe^{IV}(Por)^{2-}(His\cdots H_2O)^{0}(O)^{2-}$	1.656	1.44	0.14
4B	+ twisted His	1.646	2.14	0.12
5A	$Fe^{IV}(Por)^{2-}(His\cdots H_2O)^{0}(O\cdots HB)^{2-}$	1.665	1.66	0.11
5B	+ twisted His	1.660	2.11	0.11
6A	$Fe^{IV}(Por)^{2-}(His)^{0}(OH\cdots HB)^{1-}$	1.792	3.07	0.10
7A	$Fe^{IV}(Por)^{2-}(His)^{0}(O\cdots HB)^{2-}$(distalHis)-1	1.664	1.82	0.12
8A	$Fe^{IV}(Por)^{2-}(His)^{0}(O\cdots HB)^{2-}$(distalHis)-2	1.672	1.97	0.09
9A	$Fe^{IV}(Por)^{2-}(His)^{0}(O\cdots HB)^{2-}$(distalHis)-3	1.670	2.01	0.10

HB represents the Ser124-Gly125 pair H-bonded to the oxo group. In 7A, the terminal atoms in the distal histidine are fixed at X-ray determined positions, while in 8A, those atoms are allowed to be optimized. In 9A, all atoms of the HB group (Ser124-Gly125) are also allowed to be optimized.

2.5 Discussion

2.5.1 Reactivation of ferric TDO

This work describes an extensive effort to uncover the long standing mystery of the reactivation mechanism of ferric TDO by an oxidant, H_2O_2. Although the activation of ferric TDO by H_2O_2 in the presence of L-Trp was discovered in 1950 [20], the mechanism of this

phenomenon was not resolved. The optical and Mössbauer spectroscopic data shown in this work confirm that the addition of H_2O_2 to the ferric form of TDO in the presence of L-Trp results in reduction of the enzyme to produce ferrous heme. The enzymatic assays demonstrate that the ferrous enzyme generated by peroxide is catalytically active and is inhibited by CO. A plausible mechanistic model is presented in Figure 2.2.1_B that brings together the EPR, Mössbauer, optical, and MS data. The biochemical and spectroscopic identification and characterization of the proposed intermediates and products, including the ferryl intermediate, the protein-based radical, molecular oxygen, Trp-Trp dimer, monooxygenated L-Trp, and the dioxygenation product NFK, provide unequivocal support for this model.

In the proposed reactivation model, the first step of the reaction involves a peroxide-dependent oxidation of ferric TDO to generate high-valence heme intermediates (Figure 2.2.1_B). The second step involves the following two branching pathways that deplete the high-valence intermediates: (*a*) a catalase-like reaction leading to O_2 production, and (*b*) reduction of the protein radical and the Fe(IV)=O heme of the compound ES-type intermediate by L-Trp in two separate events, resulting in the formation of Trp-O and ferrous TDO. The later pathway consumes the oxidizing equivalents stored in the compound ES-type intermediate and leads to enzyme reactivation and L-Trp dimerization. The reduction of the protein radical by L-Trp is a necessary step for the Fe(IV)=O heme to oxidize another molecule of L-Trp and become reduced to the ferrous state in branch B, because the high-valence Fe(IV) ion alone can no longer perform the catalase-like reaction.

The presence of CO inhibits the production of NFK, indicating that the formation of NFK is originated from the normal dioxygenase cycle catalyzed by ferrous TDO rather than a short circuit or peroxide shunt described for cytochrome P450 enzymes. Under anaerobic conditions,

the source of oxygen for the Fe(II)-dependent dioxygenation reaction arises solely from the catalase-like catalytic cycle. Under aerobic conditions the oxygen is not limited to that produced by the catalase-like activity.

Although the presence of both H_2O_2 and L-Trp can cause TDO reactivation, there are two prerequisites for spectral detection of the Fe(II) heme: 1) L-Trp must be present in large excess compared to the enzyme, and 2) the L-Trp/H_2O_2 ratio must be greater than 2. The branched pathways shown in Figure 2.2.1_B are competing reactions. Branch A is dependent on [H_2O_2] but independent on [L-Trp]. In constrast, branch B is [L-Trp]-dependent. H_2O_2 is also required for branch B to take place, so it is not independent on [H_2O_2]. A large excess of L-Trp must be present for branch B to effectively compete with branch A. The two branching pathways are also internally connected. When the concentration of H_2O_2 is elevated, the rate of O_2 formation increases. In the meanwhile, the NFK formation is anticipated to decrease as branch A competes with branch B. However, the O_2 generated from branch A is a substrate of the dioxygenation reaction in branch B, hence masking the inhibitory effect on the NFK production. Notably, a full conversion from Fe(III) to Fe(II) in the TDO reactivation reaction was never observed in this work. This is due to the presence of competing reactions and the re-oxidation of the newly generated ferrous TDO by H_2O_2. Therefore, the amount of ferrous heme generated by the reactivation mechanism is dependent on the concentrations of H_2O_2 and L-Trp.

The O_2 production was also detected in the reaction of TDO and H_2O_2 in the presence of L-Trp, but at a much slower and variable rate depending on the relative ratio of [H_2O_2] and [L-Trp]. Because ferrous TDO consumes O_2, the change of the O_2 concentration is a net effect of the catalase-like activity of ferric TDO and the dioxygenase activity of ferrous TDO. Thus, the classic kinetic measurements would not be very informative unless the exact concentration of the

ferrous enzyme is constantly monitored by spectroscopic methods. Nevertheless, the observation of the O_2 production in the presence of L-Trp suggests that the catalase-like reaction is not affected by the presence of the substrate. Hence, the catalase-like activity is an intrinsic property of TDO.

The experimental results presented here do not include evidence for a ferryl intermediate in the presence of L-Trp, but the observation of a compound ES-type ferryl intermediate in the absence of L-Trp suggests that the protein active site is capable of forming a ferryl intermediate. Previously, a high-valence ferryl intermediate has never been trapped in TDO. Hence, it is likely that the decay rate of the high-valence Fe(IV) intermediate is greater than the formation rate when the primary substrate L-Trp is available, making it impossible for the ferryl intermediate to accumulate.

2.5.2 By-products of the enzyme reactivation

Two minor by-products, a Trp-Trp dimer and a monooxygenated L-Trp species, Trp-O, were detected after the enzyme reactivation reaction of TDO. An ion peak at *m/z* 409 corresponding to the L-Trp dimer was observed in our MS study. The dimerization of L-Trp is tentatively attributed to the coupling reaction between the L-Trp radicals generated from the reduction of the protein-based radical in the compound ES-type intermediate by L-Trp. The Fe(IV)-oxo moiety of the compound ES-type intermediate can oxidize an enzyme-bound L-Trp molecule to generate a monooxygenated product via a two-electron oxidation reaction. This monooxygenated product survived through the enzyme reactivation process and was experimentally detected by MS. An ^{18}O-enriched form (*m/z* 223) was also observed in the reaction with $H_2{}^{18}O_2$. LC-MS and tandem MS experiments provided further evidence for the identity of the monooxygenated product. However, its precise chemical structure is presently

unknown. The most likely candidate is an epoxide, derived from oxygen-insertion into the indole moiety of L-Trp. An alternative candidate is 6-hydroxytryptophan, which is observed in the reaction of L-Trp, H_2O_2, and a triple mutant of myoglobin [173]. A similar Trp-O product was not observed in the dioxygenase cycle of ferrous TDO with O_2 as the oxidant. The structure of the Trp-O species is probably insignificant in this work because this minor product is not generated from the Fe(II)-heme-dependent catalytic cycle. Nonetheless, the finding of the Trp-O by-product has helped us understand how the reactivation proceeds through the involvement of L-Trp.

2.5.3 Catalase-like activity of TDO

We identified a previously unknown catalase-like activity of TDO by two sets of experiments. The first set was a direct observation of the O_2 production from H_2O_2 using oxygen electrode, and the second set was the spectroscopic study of a compound ES-like species necessary for the catalase-like catalytic mechanism. The reaction with H_2O_2 in the absence of L-Trp is detrimental to the enzyme. The addition of H_2O_2 without L-Trp resulted in radical formation and an irreversible and partial loss of the heme iron as shown by the EPR and Mössbauer experiments.

It has been shown that the heme-based catalases and the enzymes with a promiscuous catalase-like catalytic activity have a wide range of catalytic efficiencies (Table 2.5.1). The turnover number of the catalase-like activity observed in TDO is significantly smaller those found in native catalases or the bi-functional catalase-peroxidase KatG. However, it is appreciable in comparison with the catalase activities of other hemoproteins whose primary biological activities are not catalase (Table 2.5.1). Whether the catalase-like activity of TDO has

a physiological role *in vivo* is speculative. However, the reactivity of TDO with H_2O_2 is important for enzyme reactivation when the primary substrate is present.

Table 2.5.1 Kinetic parameters of the catalase activity in selected hemoproteins

Protein	k_{cat} (s^{-1})	K_m (mM)	k_{cat}/K_m ($M^{-1} s^{-1}$)
Horse liver catalase [174]	3.8×10^7	1100	3.5×10^7
E. coli catalase-peroxidase[175]	1.6×10^4	3.9	4.1×10^6
M. tuberculosis KatG [176]	1.0×10^4	5.2	1.9×10^6
Periplasmic catalase–peroxidase (KatP) [177]	1.8×10^4	27	6.4×10^5
*N*α-Acetylated microperoxidase-8 [178]	4.1	40.9	100.2
Bovin hemoglobin [179]	1.92	24	80
C. metallidurans TDO (this work)	13	16	850

In the mechanism of catalase, the ferric heme reacts with the first peroxide molecule to produce a reactive compound I intermediate, which is composed of an oxy-ferryl moiety and a cationic porphyrin radical. This intermediate subsequently reacts with a second peroxide molecule to produce an O_2 molecule and water [180,181]. Our observation of an approximate ratio of 1:2 of [NFK]/[H_2O_2] stoichiometry under anaerobic conditions (Figure 2.4.6_C) is consistent with the catalase mechanism. The observed NFK/H_2O_2 ratio is slightly under 1:2. This deviation may be explained by the non-productive consumption of H_2O_2 in the following processes: 1) a small amount of H_2O_2 used to generate the ferrous heme; 2) H_2O_2-induced heme degradation; and 3) oxidation of the newly generated ferrous heme.

2.5.4 Ferryl intermediate of TDO

We presented clear spectroscopic evidence for the first experimental identification and characterization of a high-valence Fe(IV) species in TDO. The addition of H_2O_2 to ferric TDO, in the absence of L-Trp, generates an oxy-ferryl species and a protein-based radical with a concomitant decrease in the ferric TDO concentration. At the same reaction time, the

concentrations of the oxy-ferryl species and the radical species are comparable. The generation of these two species in nearly equal amounts is consistent with the formation of a compound ES-type intermediate, rather than a compound I-type intermediate as observed in catalases. The formation of the compound ES species, which may be derived from a compound I-type intermediate in this case, is critical for the enzyme reactivation to occur, because the oxy-ferryl moiety and the radical are not spin-coupled and can be reduced by L-Trp through separate reactions. The detection of a monooxygenated product is consistent with the oxygen insertion reaction performed the oxy-ferryl moiety of this high-valence species. Notably, a compound II-type oxy-ferryl intermediate was proposed to be involved in the dioxygenase mechanism of TDO based on computational studies [57]. A similar oxy-ferryl intermediate was identified in the dioxygenase reaction of IDO by RR spectroscopy [59]. Although the compound ES species identified in the reactivation reaction of TDO is different from the proposed ferryl intermediate in the dioxygenase reaction, its structural and chemical information is still useful since the overall heme binding pocket does not change much.

In the compound ES intermediate of TDO, the radical species has properties in common with those of protein-based aromatic radicals. The $P_{1/2}$ value of the radical species in TDO (1.2 mW at 100 K) is significantly higher than those of isolated free radicals [166], for example 0.07 mW at 90 K [182], indicating the presence of a relaxation mechanism. The $P_{1/2}$ value for the protein-based tryptophan radical of the compound ES species of cytochrome *c* peroxidase is 1.5 mW at 100 K [183], and the Tyr radical of P450 compound ES is 1 mW at 70 K [184]. These higher $P_{1/2}$ values have all been attributed to the relaxation of the radical by the adjacent heme iron. The $P_{1/2}$ value of the TDO radical is indicative of its close proximity to the metal center. The site of the radical in TDO is to be determined by future studies. There are at least four

tyrosine and tryptophan residues in the immediate vicinity of the enzyme active site. The identification of the radical site is challenging because a mutation of the target tyrosine/tryptophan residue that is fated to be a free radical can result in the radical migration to a nearby tyrosine/tryptophan residue, as demonstrated in other heme-based enzymes such as prostaglandin H synthase [185].

Recent experimental studies and DFT calculations suggest that the ΔE_Q value of oxy-ferryl species might correlate with the protonation state of the oxo group [127,128]. The parameter range for protonated Fe(IV)-OH species is 2.00–2.5 mm/s [186], whereas the range for unprotonated Fe(IV)=O is 1.0–1.6 mm/s [127,128,186-188]. The ΔE_Q value of the TDO oxy-ferryl intermediate (1.755 mm/s determined at pH 7.4) lies in between these two groups (Table 2.5.2). The nearest value, 1.70 mm/s, is found in the oxy-ferryl heme in the *bis*-Fe(IV) intermediate of MauG, another enzyme that oxidizes tryptophan residues in a protein substrate [109].

Table 2.5.2 Comparison of the Mössbauer parameters of the cmTDO oxy-ferryl intermediate with other known heme-based ferryl species

Intermediate	Iron species	Axial ligand	Spin	δ (mm/s)	ΔE_Q (mm/s)	Refs
CcP-ES	$[Fe^{4+}=O^{2-}]^{\bullet+}$	histidine	$S = 1$	0.05	1.55	[148]
HRP-I	$[Fe^{4+}=O^{2-}]^{\bullet+}$	histidine	$S = 1$	0.08	1.25	[189]
HRP-II	$Fe^{4+}=O^{2-}$	histidine	$S = 1$	0.03	1.61	[189]
Mb-II	$Fe^{4+}=O^{2-}$	histidine	$S = 1$	0.09	1.43	[190]
JRP-I	$[Fe^{4+}=O^{2-}]^{\bullet+}$	histidine	$S = 1$	0.10	1.33	[191]
JRP-II	$Fe^{4+}=O^{2-}$	histidine	$S = 1$	0.03	1.59	[190]
Mb (annealed)	$Fe^{4+}=O^{2-}$	histidine	$S = 1$	0.10	1.49	[192]
CPO-I	$[Fe^{4+}=O^{2-}]^{\bullet+}$	cysteine	$S = 1$	0.15	1.02	[193]
CPO-II	$Fe^{4+}=O^{2-}$	cysteine	$S = 1$	0.11(3)	1.59	[128]

P450-I	$[Fe^{4+}=O^{2-}]^{\bullet+}$	cysteine	$S = 1$	0.11	0.90	[51]
TDO-ES	$Fe^{4+}=O^{2-}$	histidine	$S = 1$	0.055	1.755	this work
MauG-*bis*-Fe(IV)	$Fe^{4+}=O^{2-}$ ($Heme_{5C}$)	histidine	$S = 1$	0.06	1.70	[109]
Basic CPO-II	$[Fe^{4+}=O^{2-}]H^{+}$	cysteine	$S = 1$	0.10(3)	2.06(3)	[128]
Basic $P450_{BM3}$	$[Fe^{4+}=O^{2-}]H^{+}$	cysteine	$S = 1$	0.13	2.16	[127]
Basic $P450_{cam}$	$[Fe^{4+}=O^{2-}]H^{+}$	cysteine	$S = 1$	0.14	2.06	[127]

Abbreviations used in this table: CcP, cytochrome *c* peroxidases; HRP, horseradish peroxidases; Mb, myoglobin; JRP, Japanese radish peroxidases; CPO, chloroperoxidase.

Protein environments can conceivably provide H-bonding interactions with the oxy-ferryl heme. A possible interpretation of the atypical ΔE_Q value of the compound ES species of TDO was examined in this work by DFT calculations performed on 14 structural models (Table 2.4.1). These models were used to evaluate the structural contributions that can directly affect the coordination structure of the heme iron, including 1) the protonation state of the oxo group; 2) H-bonding interactions to the oxo group; 3) H-bonding interactions to the proximal histidine ligand; and 4) the conformation of the proximal histidine ligand. All the models were generated on the basis of the X-ray crystal structure of substrate-free TDO (PDB entry: 2NW7). Geometries of the models were optimized using the method developed previously for defining other oxy-ferryl species [159] with the terminal atoms fixed at the X-ray crystal structure positions to mimic the protein environment effect. Both the Mössbauer ΔE_Q and δ parameters for these models were calculated using the DFT method, which enabled accurate predictions of these two parameters in various iron proteins and models covering all iron spin states and coordination states [159,160].

As shown in Table 2.4.1, the predicted δ values of these models are all close to the experimental value with no significant variations, indicating its insensitivity to the secondary structural changes around the axial positions. In contrast, the predicted ΔE_Q values display a

large range from 1.44 to 3.19 mm/s, suggesting that it is sensitive to structural changes in the active site. The best agreement with the experimental value was found by the incorporation of an H-bonding interaction with a nearby Ser124-Gly125 residue pair (these two residues are fixed at their X-ray positions except for the peptide bond atoms CONH, which were allowed to be optimized) (Figure 2.5.1). The predicted ΔE_Q value of 1.78 mm/s for model 3A (*i.e.*, $Fe^{IV}(Por)^{2-}(His)^{0}(O^{\cdots}HB)^{2-}$) is in excellent agreement with the experimental measurement of 1.755mm/s. These calculations suggest that the unusual ΔE_Q value of the TDO ferryl species originates from an H-bonding interaction provided by the protein matrix, similar to the computational results obtained for the *bis*-Fe(IV) species of MauG [160].

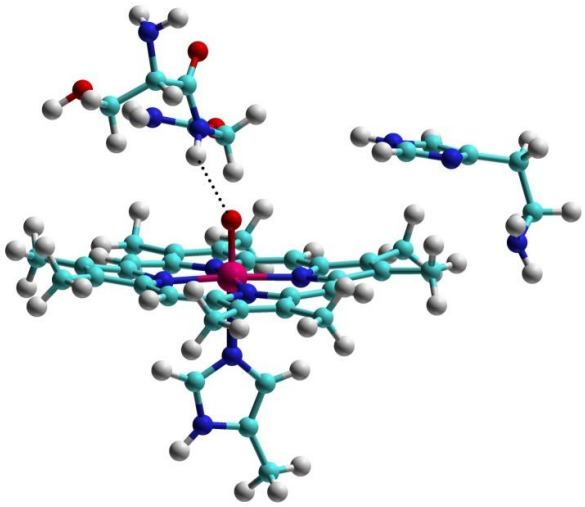

Figure 2.5.1 Representative structural model of 3A from Table 2.4.1 in a scaled ball-and-stick representation. The Mössbauer parameters calculated from this model provide the closed match to the experimental data. Color schemes are as follows: Fe, pink; O, red; N, blue; C, cyan; and H, grey. The green dashed lines represents the H-bonding interaction between the Fe(IV)-oxo group to the backbone NH group of Gly125 (cmTDO amino acid numbering).

An examination of the crystal structures of TDO from both *Cupriavidus metallidurans* and *Xanthomonas campestris* (PDB entries: 2NOX, 2NW7, and 2NW8) suggests that the conserved active site residues at the distal pocket, His72 and Gly125 (cmTDO numbering

system), are ideal candidates for H-bonding interactions with the Fe(IV)-oxo group. These residues are also conserved in the human enzyme. The role of these two residues has already been investigated in recent experimental and computational studies ([59,61,73,78]) by several laboratories. The consensus is that the heme site in the dioxygenase can indeed generate a high-valence Fe(IV)-oxo species under appropriate conditions and that the protein microenvironment is critical for dictating the chemical and physical property of the intermediate.

2.5.5 Oxygen exchange with solvent in NFK

An unexpected finding of this study is that one of the oxygen atoms in the reaction product NFK is exchangeable with the solvent in the time frame of minutes. Based on the well-known ketonic oxygen exchange with the solvent, and the fact that the carboxylate oxygen exchanges with a buffered solvent slower than a ketone [194,195], we propose that the ketone carbonyl group in NFK exchanges its oxygen with the solvent via a mechanism involving a diol intermediate. Figure 2.5.2 depicts a plausible mechanism for the oxygen exchange. The nucleophilic attack at the ketone carbon by water generates a diol intermediate. This step is facilitated by a transient state with a six-member ring structure. The finding of the oxygen exchange in NFK may become important in the mechanistic studies of the enzyme with ^{18}O-isotope labeling. A previous ^{18}O-isotope labeling study was carried out by Hayaishi *et al.* in the absence of the knowledge of the oxygen exchange described in this work [15]. The less than theoretical ^{18}O content was found in kynurenine, the hydrolysis product of NFK, and the exact content varied in different sets of experiments [15]. Furthermore, the results of different experimental sets with $^{18}O_2$ and $H_2{}^{18}O$ are not mutually consistent. These observations were thought to be caused by either an exchange reaction during the isolation procedure or by

preferential utilization of ^{16}O over ^{18}O by TDO [15]. Our findings suggest that the previous observations are caused by the oxygen exchange phenomenon that occurred during reaction.

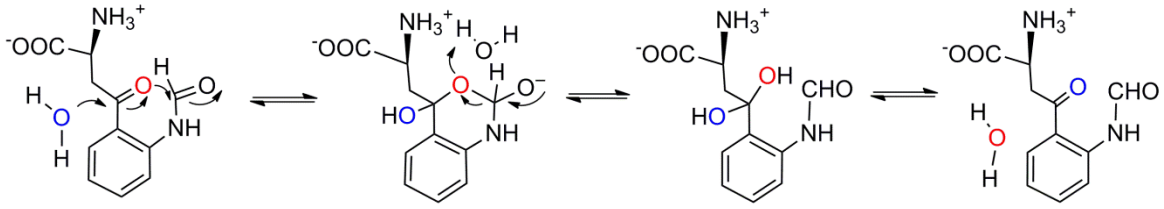

Figure 2.5.2 Proposed oxygen exchange mechanism on the carbonyl group of NFK

2.5.6 Reactions involving ferric IDO and H_2O_2

Unlike TDO, IDO does not possess a H_2O_2-mediated enzyme reactivation pathway. Thus, the catalytic activity of IDO is inhibited by H_2O_2 [196]. Recently, Freewan *et al.* reported that H_2O_2 inhibits cellular IDO dioxygenase activity and that the inactivation is achieved via compound I-initiated oxidative damage to the heme as well as the protein structure [95]. The inhibition effect can be significantly suppressed by L-Trp. The presence of L-Trp leads to either two-electron or one electron reduction on the IDO compound I species produced by peroxide oxidation of the ferric enzyme, consequently regenerate ferric IDO or yield an IDO compound II species, respectively [95]. Moreover, excess L-Trp can form a lethargic complex with the newly generated IDO compound II species [70,95], thereby further protecting the protein from oxidative damage.

Despite lacking a catalase-like activity [31], IDO displays other types of activities towards H_2O_2. In addition to common peroxidase substrates, including 2,2'-azino-bis(3-ethylbenzothiazoline-6-sulphonic acid (ABTS) and guaiacol [31,70], IDO can catalyze peroxidase reactions with physiological peroxidase substrates, such as ascorbate, tyrosine, and NADH [94,95]. The metabolisms of nitric oxide (NO) and its oxidation product, nitrite (NO_2^-), are recognized as key reactions catalyzed by heme-dependent peroxidases in inflammatory tissues. High-valence ferryl species of heme-dependent peroxidases can consume NO and

convert NO_2^- into a nitrating species, nitrogen dioxide radical, $NO_2^{\bullet}$, which is capable of performing nitration reactions on tyrosine residues in proteins [197-200]. In the presence of H_2O_2, IDO was demonstrated to catalytically consume NO and utilize NO_2^- to promote formation of 3-nitrotyrosine as a self-modification [95]. In another report, it was found that IDO can catalyze oxidation reactions of indole, but not L-Trp, by H_2O_2 with 2- and 3-oxoindole as the major products [201]. The reactions were proposed to proceed via a peroxygenase mechanism in which the reactive compound I species of IDO generated by peroxide oxidation of the ferric enzyme transfers its ferryl oxygen to indole to yield monooxygenated products, a process resembling the "peroxide shunt" in P450 enzymes [201]. Therefore, the IDO compound I intermediate is a catalytically competent species responsible for both the peroxidase and peroxygenase activities of the enzyme, and it is also the primary source of oxidative damage to the protein in the absence of any small-molecule substrates.

2.5.7 Potential physiological relevance

The different behaviors between TDO and IDO in their peroxide reactions are most likely rooted in the different reactivities of their high-valence ferryl species generated upon peroxide oxidation. The slightly different designs of the heme environment between these two enzymes may account for the observed differences. Specifically, a highly conserved distal histidine residue (His72 in cmTDO amino acid numbering, Figure 1.3.1_C), which is present in TDO but absent in IDO, is likely the major factor that differentiates the reactivities of the ferryl species via providing a H-bonding interaction to the ferryl oxo group in TDO [84].

The differences in peroxide reactions between these two enzymes might be physiologically important. TDO is a hepatic enzyme, and hepatocytes are known to be in an oxidizing environment that may cause inactivation of TDO by oxidation of the heme iron. While IDO is proposed to be maintained in the reduced state *in vivo* by the action of cytochrome b_5 and

cytochrome b_5 reductase [202,203], no biological reagents have been identified to perform the same function for TDO. Under normal physiological conditions, H_2O_2 is present at low levels in cells. However, a small amount of H_2O_2 is sufficient to cause enzyme reactivation in TDO under aerobic conditions when the substrate L-Trp is present. Amino acids are neither stored in the human body nor excreted. Rather, they are utilized for protein synthesis or degraded with the highest priority relative to glucose and other energy sources. As a key enzyme responsible for L-Trp degradation, TDO may adopt the reactivation pathway to ensure sustainable catalytic efficiency. In general, the discovery of the enzyme reactivation mechanism is important for understanding how a ferrous enzyme maintains its catalytic activity in an oxidizing environment. Unlike TDO, IDO primarily utilizes its dioxygenase activity to ubiquitously regulate local cellular levels of L-Trp and L-Trp catabolites for immune regulatory functions. It should be noted that L-Trp can efficiently retard all of the aforementioned peroxidase/peroxygenase-type reactions of IDO by occupying the active site [70,95,201]. This observation suggests that the H_2O_2-mediated reactions of IDO are inhibited in normal tissues where L-Trp is present at a certain level. However, in inflammatory tissues where the levels of H_2O_2 and NO are elevated, but the level of L-Trp is diminished, the biological actions of IDO might be modulated by its peroxidases/peroxygenase activities. This may cause dioxygenase inactivation, NO consumption, and protein nitration.

3 CHEMICAL RESCUE OF THE DISTAL HISTIDINE MUTANTS OF TRYPTOPHAN 2,3-DIOXYGENASE

(This chapter is modified from a research article that JG coauthored: Geng J, Dornevil K, and Liu A (2012) Chemical rescue of the distal histidine mutants of tryptophan 2,3-dioxygenase. ***J. Am. Chem. Soc.*** 134(29), 12209-12218.)

3.1 Abstract

A highly conserved histidine residue (His72 in cmTDO amino acid numbering) in the distal heme pocket of TDO has attracted great attention in the mechanistic studies of this enzyme. However, a consensus was not reached regarding whether and how this distal histidine plays a catalytic role after substrate binding. In this study, three mutant proteins, H72S, H72N, and Q73F were generated to investigate the function of the His72 residue in cmTDO. Spectroscopic characterizations, kinetic studies, and chemical rescue assays were employed to investigate the biochemical properties of the wild-type (WT) enzyme and the mutant proteins. Rapid kinetic methods were utilized to explore the molecular basis for the observed stimulation of the catalytic activity by 2-methylimidazole in the His72 variants. The results indicate that the distal histidine plays multiple roles in TDO. Firstly, His72 contributes to but is not essential for substrate binding. In addition, it shields the heme center from non-productive binding of exogenous small molecule ligands (*i.e.*, imidazole and its analogs) via steric hindrance. Most importantly, His72 participates in the subsequent chemical catalytic steps after substrate binding possibly by providing an H-bonding interaction to the heme-bound oxygen species.

3.2 Introduction

Histidine participates in various important functions in a wide range of proteins and enzymes. Particularly, distal histidines have been shown to play crucial roles in many hemoproteins, and in some cases, they are versatile enough to perform multiple functions. For

instance, in hemoglobin the oxy-ferrous complex is stabilized via an H-bonding interaction between the distal histidine and O_2. Moreover, the distal histidine in hemoglobin also effectively prevents undesired heme iron oxidation and inhibits interactions between the heme center and competing small molecules such as CO and NO without compromising the binding of O_2 [204]. In the present study, we probed the role of a conserved distal histidine in TDO.

It was initially believed that TDO begins its catalytic cycle with deprotonation of the indole NH group of the substrate by an active-site base, and the distal histidine of TDO is the apparent candidate for playing such a role [4,37,52,53,77]. This histidine is a highly conserved residue and replaced by threonine in only three putative TDO sequences [37]. In the crystal structure of the binary complex of xcTDO and L-Trp, the corresponding distal histidine (His55 in xcTDO amino acid numbering) is H-bonded to the indole group of the substrate, suggesting its involvement in substrate binding [36]. The crystal structures of the H55A and H55S variants from xcTDO in binary complexes with L-Trp were reported in a subsequent paper, which showed that the aforementioned H-bonding interaction is abolished in the mutant proteins [73]. Since both His55 mutants exhibited detectable activity, the distal histidine was proposed to function as a transition-state stabilizer, rather than an essential base [73]. A detailed model for such a stabilization role remains to be explored. It has also been shown that the distal histidine is able to prevent the formation of the non-productive ferric enzyme-substrate complex, as revealed by the sharp increase in the affinity of L-Trp to the ferric enzyme upon the replacement of the distal histidine [73]. Based on the RR study of the ternary complex of L-Trp-O_2-TDO from hTDO, it has been suggested that the distal histidine (His76 in hTDO amino acid numbering) plays a critical role in catalysis by regulating substrate-protein interactions and deprotonating the indole NH group of the substrate to initiate the reaction [61]. Fukumura *et al.* reported that His76 is involved in regulating the spin state of the heme iron in hTDO and they were also in favor of

the acid-base catalyst role of His76 [78]. However, 1-Me-L-Trp was demonstrated to be a slow substrate for IDO, the His55 variants of xcTDO, and the His76 variants of hTDO, thereby throwing into question the necessity for deprotonation of the indole NH group of the substrate during catalysis [85]. Davydov *et al*. showed that mutation of His55 in xcTDO or methylation of the indole nitrogen of the substrate had no observable effect on the spectroscopic properties of the cryoreduced oxy heme moiety or its annealing behavior, arguing against proton abstraction of the indole group as the initial catalytic step [62].

Recent computational studies further cast doubt on the catalytic role of the distal histidine as an active-site base by demonstrating that the proton abstraction process is not energetically favorable [56,57,59,60]. A recent ONIOM study on xcTDO suggested that the distal histidine, through the H-bonding interaction with the indole moiety, potentially serves as an electrostatic catalyst [57]. It is worth noting that in IDO, a serine residue, Ser167, which is incapable of proton abstraction, occupies the position of the distal histidine [35]. The S167A mutant of IDO exhibits a similar catalytic activity to that of the WT enzyme, indicating that the distal serine residue is not essential for catalysis in IDO [35,74].

To investigate the function of the distal histidine, especially in the catalytic steps after substrate binding, we performed site-directed mutagenesis, spectroscopic characterizations as well as enzymatic kinetic studies on cmTDO. Our results strengthen the notion that the distal histidine, *i.e.*, His72 in cmTDO amino acid numbering, is involved in substrate binding while excluding the possibility that His72 acts as an active-site base during catalysis. The chemical-rescue assays demonstrate that the catalytic activity of the His72 variants can be restored to a significant degree by an exogenous histidine analogue. Additional stopped-flow UV-vis experiments provide a molecular basis for the observed results from the chemical-rescue studies.

3.3 Materials and methods

3.3.1 Reagents

L-Trp (99%), 1-Me-L-Trp (95%), imidazole (IM) (99%), 2-methylimidazole (2MI) (99%), and 4-methylimidazole (4MI) (≥ 96%) were purchased from Sigma-Aldrich. H_2O_2 (30%, v/v) was obtained from Fisher Scientific. The concentration of H_2O_2 was determined based on the extinction coefficient of 43.6 $M^{-1}cm^{-1}$ at 240 nm. All the experiments were performed in 50 mM Tris-HCl buffer, pH 7.4, unless otherwise specified.

3.3.2 Mutant construction, expression, and purification of cmTDO

The construction of the plasmid encoding His-tagged full-length cmTDO has been reported elsewhere [24]. This plasmid was used as a template for mutant construction. H72S, H72N, and Q73F were created using the QuikChange II kit (Stratagene). The sequences of the three mutant genes were verified by DNA sequencing. The procedures used for expression and purification of the TDO variants were the same as those for WT TDO [96,156]. Briefly, the proteins were purified using a Ni-NTA affinity column on an ÄKTA FPLC system, followed by a Superdex 200 gel-filtration column for salt removal and further purification. The levels of protein expression and the yields of purified protein for the mutants were similar to WT TDO. The heme concentrations of the as-isolated ferric proteins were calculated based on their extinction coefficients of Soret band absorption maxima (WT: $\varepsilon_{405\ nm}$ = 130 $mM^{-1}cm^{-1}$; Q73F: $\varepsilon_{405\ nm}$ = 120 $mM^{-1}cm^{-1}$; H72S: $\varepsilon_{404\ nm}$ = 120 $mM^{-1}cm^{-1}$; H72N: $\varepsilon_{404\ nm}$ = 120 $mM^{-1}cm^{-1}$), which were determined by the inductively coupled plasma optical emission spectroscopy and EPR spin quantitation technique as reported previously [96,156].

3.3.3 Spectroscopic characterizations

The optical spectra of cmTDO and its mutants were recorded on an Agilent 8453 UV-vis spectrophotometer at room temperature. The ferrous enzymes were prepared by reducing the

ferric proteins with sodium dithionite under anaerobic conditions and the corresponding optical spectra were measured with a custom anaerobic cuvette.

X-band EPR spectra were measured on a Bruker ER200D spectrometer at 100 kHz modulation frequency coupled with a 4116DM resonator. The measurement temperature was maintained at 10 K using an ESR910 liquid helium cryostat and an ITC503 temperature controller from Oxford Instruments (Concord, MA). The final heme concentration of each EPR sample was 200 μM.

3.3.4 Enzymatic assays

Steady-state kinetic assays were performed at room temperature using an Agilent 8453 UV-vis spectrophotometer. The enzyme activities of cmTDO and its variants were measured by monitoring formation of the dioxygenation product NFK at 321 nm ($\varepsilon_{321\ nm}$ = 3152 $M^{-1}cm^{-1}$) [66]. The reaction rates were calculated from the initial velocities of the NFK formation. L-Trp stock solution was prepared freshly in the reaction buffer (*i.e.*, 50 mM Tris-HCl, pH 7.4) in a warm water bath. Reactions were performed in the presence of an excess amount (*i.e.*, 1 mM) of L-ascorbate, as typically used by many others [37,53,61,66]. TDO was added at the end to initiate the reaction. Each reaction was repeated in triplicate to determine the initial velocity. The kinetic parameters were obtained by varying the concentration of the substrate and fitting the reaction rates at different substrate concentrations to the Michaelis-Menten equation (Eq. 1), where υ is the steady-state velocity, [E] is the concentration of enzyme, [S] is the concentration of substrate, k_{cat} is the catalytic turnover constant, and K_m is the Michaelis-Menten constant. At least two different preps of protein were measured using the same method for each mutant and there was no observable difference in the kinetic parameters between preps.

$$v/E = k_{cat}[S]/([S] + K_m) \qquad \text{Eq. 1}$$

In the chemical-rescue assays, the rescuing reagent (IM, 2MI or 4MI) was added to the reaction system prior to the addition of the enzyme. The $K_{activation}$ values of 2MI from the His72 mutants were determined by varying the concentration of 2MI while the concentration of L-Trp was kept constant (*i.e.*, 1 mM) and calculating the corresponding rescued dioxygenase activities, which were the differences between the reaction rates determined in the presence and absence of 2MI. The rescued reaction rate was plotted as a function of the concentration of 2MI, and the data were fit to Eq. 1 with the Michaelis-Menten constants of the fitting results assigned as the $K_{activation}$ values. The kinetic parameters of the His72 mutants under saturating 2MI concentration (*i.e.*, 50 mM) conditions were measured by varying the concentration of the substrate and analyzing the reaction rates at different substrate concentrations by Michealis-Menten fitting.

3.3.5 Rapid kinetic studies

Transient kinetic measurements were performed at 4 °C using an Applied Photophysics (Leatherhead, UK) SX20 stopped-flow spectrometer equipped with a photodiode array detector. The sample handling unit of the SX20 spectrometer was housed in an anaerobic chamber from COY Laboratory Products (MI, USA). All reagents, including enzymes, L-Trp, and imidazoles were prepared in the 50 mM Tris-HCl buffer, pH 7.4. The experimental data were analyzed using the ProK software package from Applied Photophysics.

3.4 Results

To probe the catalytic role of His72, two variants, H72S and H72N, were constructed. The mutation of His72 to serine mimics the scenario in IDO. The asparagine in H72N is incapable of functioning as an acid-base catalyst but potentially capable of maintaining H-bonding interactions in which His72 participates. A third mutant, Q73F, was also created. Gln73 is a conserved residue adjacent to His72 with the apparent role of maintaining the proper

orientation of His72. The substitution of Gln73 by a bulky and hydrophobic amino acid such as phenylalanine could not directly affect His72, but would be likely to change its physical position.

3.4.1 Spectroscopic characterizations of TDO

Ferric cmTDO showed an axial EPR signal at g = 6.18, 5.73 and 2.00 (Figure 3.4.1_A), representing a high-spin ferric heme center with approximate axial symmetry [156]. Similar axial signals with slight rhombicity were observed in H72S and H72N (Figure 3.4.1_C and D), suggesting that the replacement of His72 had little effect on the overall protein conformation and heme symmetry. However, a minor low-spin ferric species with very broad absorption feature at g = 2.98, 2.31 and 1.58 was identified in both His72 variants (Figure 3.4.1_C and D). This species is assigned as an imidazole-ligated hexacoordinated heme based on the similarity of its g-factors to those of other histidine-coordinated hemoproteins with imidazole in the sixth coordination position [205-207]. The EPR parameters of this low-spin species also exhibit a very large g_{max} value (2.98) and g-anisotropy value ($|g_x - g_z|$ = 1.40), thereby suggesting the presence of a so-called highly anisotropic low-spin (HALS)-like heme species [138,208-210]. The coordinating imidazole was most likely introduced into the active site of the His72 mutants during the initial protein purification step via the affinity chromatography, in which buffer solutions containing a high concentration of imidazole (*i.e.*, 500 mM) were used during the gradient elution process. Even though the gel-filtration chromatography was utilized to remove imidazole in a subsequent purification step, a small portion of heme (< 10%, calculated based on spin quantitation of the high-spin ferric heme) from the His72 variants remained to be coordinated by imidazole, giving rise to the HALS-like species. Proteins of the His72 variants obtained from different preps showed similar percentage of this minor species. Q73F, on the other hand, presented a more axial high-spin signal at g = 5.83 and 2.00 with no additional low-spin signal (Figure 3.4.1_B). All the EPR parameters for cmTDO are summarized in Table 3.4.1.

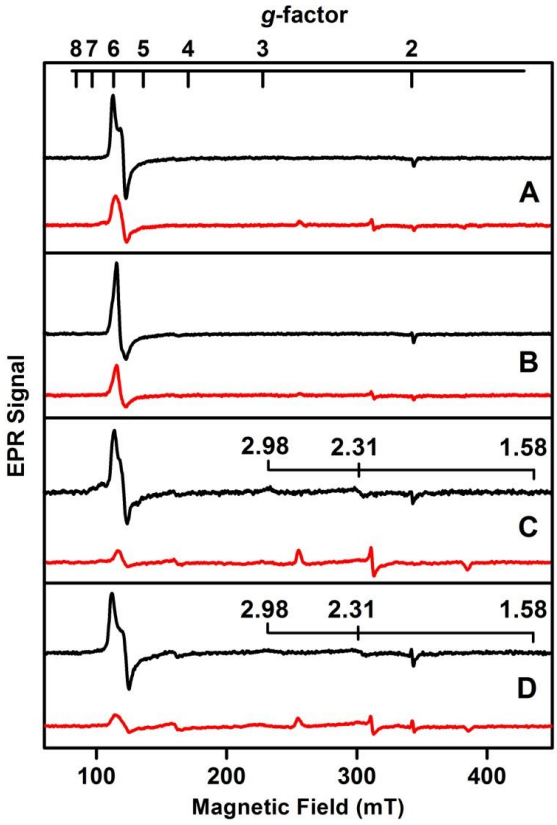

Figure 3.4.1 EPR spectra of cmTDO (200 μM heme concentration) in the absence (black) and presence (red) of L-Trp (10 mM). (A) WT TDO, (B) Q73F, (C) H72S, (D) H72N. The minor low-spin species in the His72 mutants were labeled for clarification. Experimental conditions: temperature, 10 K; microwave frequency, 9.65 GHz; microwave power, 3 mW; modulation amplitude, 0.5 mT.

Table 3.4.1 EPR parameters of cmTDO

Sample	*g*-values		
	High-spin	Low-spin 1	Low-spin 2
WT TDO	6.18, 5.73, 2.00	N/A	N/A
WT TDO + L-Trp	5.72, 2.00	N/A	2.69, 2.19, 1.80
Q73F	5.83, 2.00	N/A	N/A
Q73F + L-Trp	5.80, 2.00	N/A	2.69, 2.20, 1.80
H72S	6.04, 5.69, 2.00	2.98, 2.31, 1.58	N/A
H72S + L-Trp	5.67, 2.00	N/D[a]	2.70, 2.21, 1.79
H72N	6.16, 5.65, 2.00	2.98, 2.31, 1.58	N/A
H72N + L-Trp	6.03, 2.00	N/D[a]	2.70, 2.21, 1.79

[a] N/D: undetermined.

Upon the addition of L-Trp to WT TDO, there was a substantial decrease in the high-spin ferric signal concomitant with the appearance of a new low-spin ferric species at g = 2.69, 2.19 and 1.80 (Figure 3.4.1_A). This substrate-driven spin-transition process was characterized in TDOs from different sources using different spectroscopic methods [61,63,171,211]. A similar phenomenon was observed in IDO as well [74,81,212,213]. All of the cmTDO mutants showed the same trend of change in spin transition upon substrate binding (Figure 3.4.1_B-D). By comparing its g-values with those of the hydroxide-bound ferric low-spin species identified in other hemoproteins [171,214], this newly produced low-spin species can be assigned as such. It has been proposed that the hydroxide ligand is derived from an active-site water [61,63,156], which has been shown to be H-bonded to the amine group of the substrate in the ligand-bound crystal structure of xcTDO [36,73]. In the His72 variants, the spin-transition process was more pronounced than those observed in WT TDO and Q73F TDO, suggesting that mutation of His72 alters the binding conformation of the substrate and thus affects the pK_a of the active-site water. Moreover, the original imidazole-induced HALS-like species significantly decreased in intensity upon substrate binding (Figure 3.4.1_C and D), indicating that the active-site water competes with imidazole to ligate to the heme center in the presence of L-Trp.

Figure 3.4.2 shows the optical absorption spectra of ferric and ferrous cmTDO and its mutants in the absence and presence of L-Trp. Q73F TDO shares similar optical spectra with WT TDO in almost every aspect. Despite some moderate alterations, there are no substantial spectral changes upon replacement of His72. After the addition of excess substrate to cmTDO and its mutants, the Soret band decreased in intensity in both ferric and ferrous states and red-shifted approximately 1 nm in the ferric state. The visible bands were not observably sensitive to substrate binding. Table 3.4.2 summarizes the optical absorption maxima of cmTDO and its

mutants. It should be noted that the spectral features of cmTDO change as the buffer pH varies. The mutant proteins follow the same pattern as that observed in the WT enzyme (Figure 3.4.3).

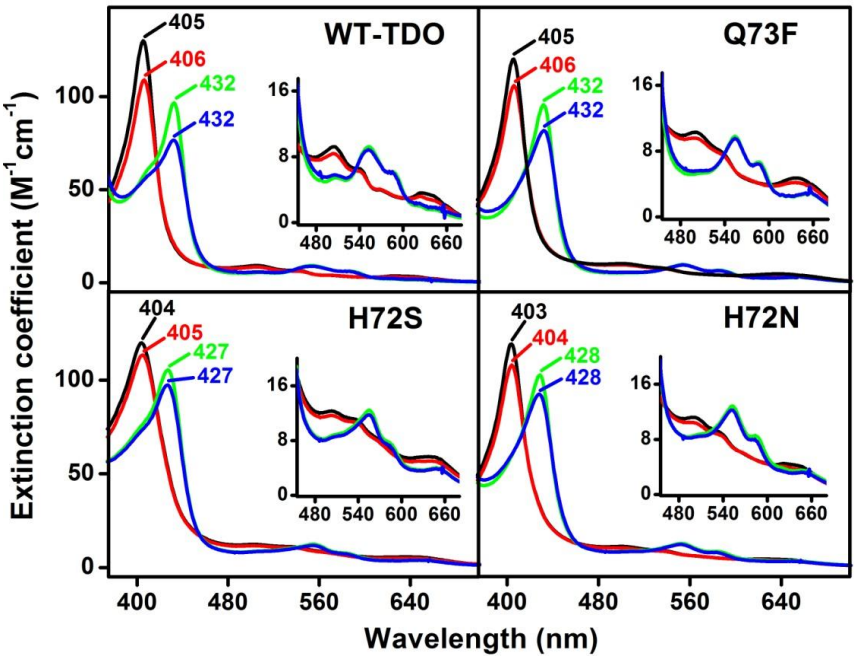

Figure 3.4.2 Optical absorption spectra of cmTDO (10 μM) in the absence and presence of L-Trp (10 mM). Black: ferric TDO; Red: ferric TDO + L-Trp; Green: ferrous TDO; Blue: ferrous TDO + L-Trp. The insets are the expanded views of the visible bands.

Table 3.4.2 Optical absorption maxima of cmTDO

Sample	Ferric form (nm)	Ferrous form (nm)
WT TDO	405, 504, 539	432, 553, 585
WT TDO + L-Trp	406, 504, 539	432, 552, 585
Q73F	405, 503, 539	432, 554, 586
Q73F + L-Trp	406, 502, 539	432, 554, 586
H72S	404, 503, 537	428, 555, 583
H72S+ L-Trp	405, 503, 537	428, 555, 583
H72N	403, 501, 537	428, 553, 584
H72N + L-Trp	404, 501, 537	428, 553, 583

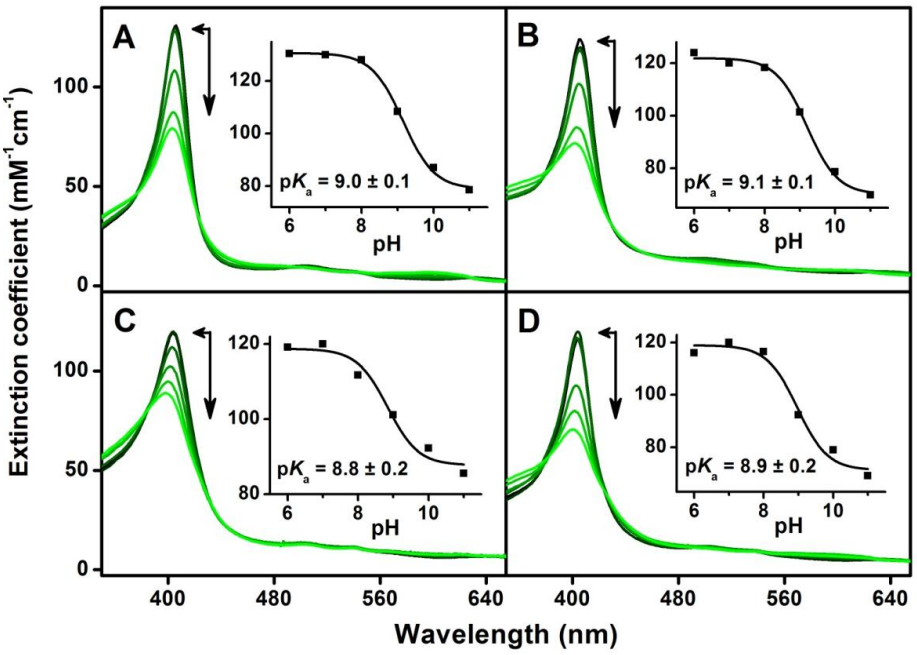

Figure 3.4.3 Effect of pH on the optical absorption spectra of cmTDO and its mutants (8 μM). (A) WT TDO, (B) Q73F, (C) H72S, (D) H72N. This experiment was performed over the pH range from 6 (black) to 11 (green) in multi-component buffer solutions containing 50 mM Tris, 50 mM MOPS, and 50 mM glycine. The pH difference between each two adjacent data set is 1 unit. The arrows indicate the trends of changes in the spectra. The insets present the changes in the Soret band absorption intensity as a function of pH. The solid lines are the best fits of the experimental data to one-proton titration curves.

3.4.2 Steady-state kinetic study of TDO

The steady-state kinetic assays of cmTDO and its derivatives were performed at room temperature. The kinetic parameters are listed in Table 3.4.3. For WT TDO, the k_{cat} and K_m values were determined to be 12.0 ± 0.4 s^{-1} and 0.22 ± 0.01 mM, respectively. Collectively, they lead to a k_{cat}/K_m value of 55 $mM^{-1}s^{-1}$. The mutation of Gln73 to Phe caused the least decrease among the cmTDO mutants in the turnover number to ~30% of the value in WT TDO. It did, however, introduce the most distinct influence on the K_m value – a *ca.* 5-fold increase. The replacement of His72 to Ser/Asn resulted in a dramatic decrease in the catalytic activity, with the k_{cat} value being reduced to *ca.* 5% and 0.5% of that of the WT enzyme, respectively. In contrast, the K_m value was relatively less affected, as shown by the *ca.* 2-fold and 3-fold increase from H72S and H72N,

respectively. Concerns regarding reliability of the enzymatic kinetic results of the His72 mutants may arise due to the heterogeneity of protein caused by the presence of the aforementioned HALS-like species. Such concerns can be eliminated by the following two facts: a) the HALS-like species is a minor species (< 10%), the relative amount of which barely varies between preps; b) the ligation of imidazole at the sixth heme coordination is not strong and has shown to be vulnerable to substitution by an active-site water in the presence of the substrate. The steady-state kinetic parameters of WT TDO and the distal histidine variants from other sources are also summarized in Table 3.4.3 for comparison.

Table 3.4.3 Steady-state kinetic properties of TDO

Source	Protein	k_{cat} (s^{-1})	K_m (mM)	k_{cat}/K_m ($mM^{-1}s^{-1}$)	% of activity (k_{cat}/K_m)	Reference
cmTDO[a] (pH 7.4)	WT	12.0 ± 0.4	0.22 ± 0.01	55	100	This work
	Q73F	3.6 ± 0.2	1.1 ± 0.1	3.3	6.0	
	H72S	0.55 ± 0.01	0.42 ± 0.02	1.3	2.4	
	H72S + 2MI[b]	3.1 ± 0.2	0.43 ± 0.06	7.2	13	
	H72N	0.060 ± 0.003	0.62 ± 0.08	0.097	0.17	
	H72N + 2MI[b]	0.23 ± 0.01	0.43 ± 0.04	0.53	0.96	
hTDO (pH 8.0)	WT	6.12 ± 0.02	0.0825 ± 0.0038	74.2	100	[78]
	H76A	0.04 ± 0.00	0.488 ± 0.051	0.09	0.12	
hTDO (pH 7.0)	WT	2.1	0.19	11.05	100	[61,63]
	H76A	0.2	0.5	0.4	3.6	
	H76S	0.03	1.2	0.025	0.23	
xcTDO (pH 7.5)	WT	19.5 ± 1.2	0.114 ± 0.001	171.1	100	[73]
	H55A	2.86 ± 0.10	0.133 ± 0.007	21.5	13	
	H55S	2.6 ± 0.01	0.197 ± 0.002	13.2	7.7	

[a] The steady-state kinetic assays were performed in the 50 mM Tris-HCl buffer, pH 7.4, in the presence of 1 mM L-ascorbate at room temperature. See more details in the "Materials and methods" section.
[b] The kinetic parameters were determined in the presence of 50 mM 2MI.

3.4.3 1-Me-L-Trp as an alternative substrate

Steady-state kinetic assays were performed to investigate the reactivity of 1-Me-L-Trp to cmTDO. Interestingly, 1-Me-L-Trp was a fairly active substrate for WT cmTDO with a k_{cat} value of 8.4 ± 0.4 s^{-1} (Figure 3.4.4), comparable to that of cmTDO with L-Trp as the substrate. The K_m value, however, was elevated by *ca.* 7-fold to 1.5 ± 0.2 mM. 1-Me-L-Trp was a very poor substrate for the His72 variants of cmTDO. There were no measurable kinetic parameters for these two mutants with 1-Me-L-Trp as the substrate.

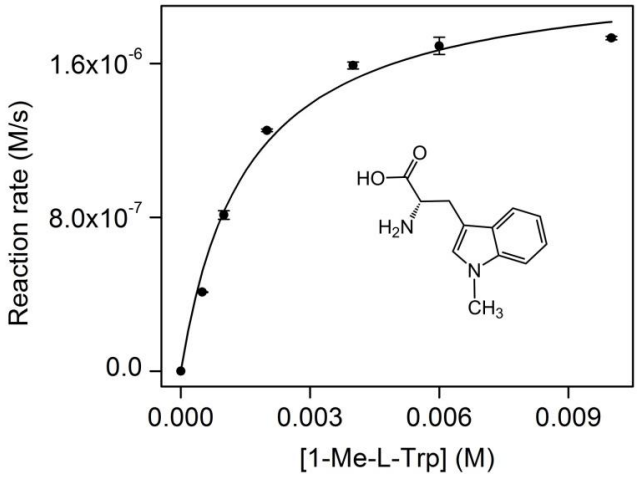

Figure 3.4.4 Steady-state kinetic assay of cmTDO with 1-Me-L-Trp as the substrate. The reaction rates were measured at room temperature in the presence of 1 mM L-ascorbate. The final concentration of TDO in the reaction system was 0.25 μM. The solid line is the best fit of experimental data to Eq. 1.

3.4.4 Interactions between exogenous imidazoles and the heme center

Imidazole and its analogues have been widely used as histidine surrogates in chemical rescue experiments on histidine mutants to investigate the functions of active-site histidine in many enzyme systems [215-219]. However, they are also potential ligand molecules and have been extensively used in coordination chemistry studies of model heme complexes and hemoproteins.[5,220-222] Therefore, caution should be exercised when introducing imidazole and its analogues to the reaction systems of heme-dependent enzymes as rescuing reagent.

CmTDO and its variants in the ferric state were incubated with an excess amount (*i.e.*, 50 mM) of different imidazoles (IM, 2MI, and 4MI) in separate experiments, and characterized by the UV-vis and EPR spectroscopy. In WT TDO, there were no changes in the absorption maximum of the Soret band upon the addition of imidazoles (Figure 3.4.5_A). In Q73F, a subtle red shift of ~1 nm in the Soret band was observed in the presence of IM and 4MI but not 2MI (Figure 3.4.5_B). In the His72 variants, the red shift became more observable (4-5 nm) upon the addition of IM and 4MI, accompanied by a pronounced decrease in the absorption intensity (Figure 3.4.5_C and D). In contrast, 2MI did not cause the same phenomenon in either of the His72 mutants with the corresponding UV-vis spectra resembled those of the as-isolated proteins yet with slightly decreased Soret band (Figure 3.4.5_C and D). Previous studies have demonstrated that the direct ligation of imidazole and its analogs to the heme iron causes a red shift in the Soret band [5,219,222]. 2MI, however, is not able to effectively ligate to the heme center of TDO, possibly due to the steric hindrance caused by the methyl group seated in between the two nitrogen atoms.

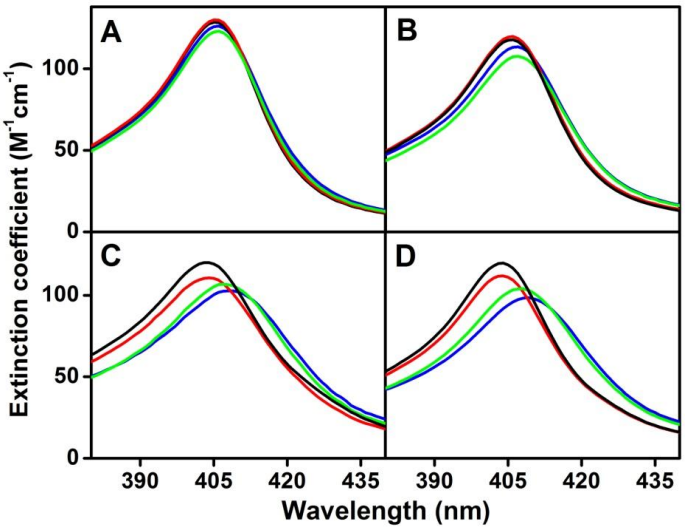

Figure 3.4.5 Optical absorption spectra of the Soret band in ferric cmTDO (8 μM) in the absence and presence of exogenous imidazoles (50 mM). (A) WT TDO, (B) Q73F, (C) H72S, (D) H72N. Black: as-isolated; Red: with 2MI; Green: with IM; Blue: with 4MI.

Addition of 2MI to cmTDO and the three mutants did not lead to observable changes in the EPR spectra (Figure 3.4.6), confirming that 2MI is not an effective heme ligand. However, in the presence of IM or 4MI, the high-spin ferric signal in the His72 mutants vanished, with a concurrent increase in the signal of the imidazole-induced HALS-like species described earlier (Figure 3.4.6_C and D). In contrast, addition of IM or 4MI had relatively less effect on the EPR spectrum of Q73F and almost no influence on the EPR spectrum of WT TDO (Figure 3.4.6_A and B).

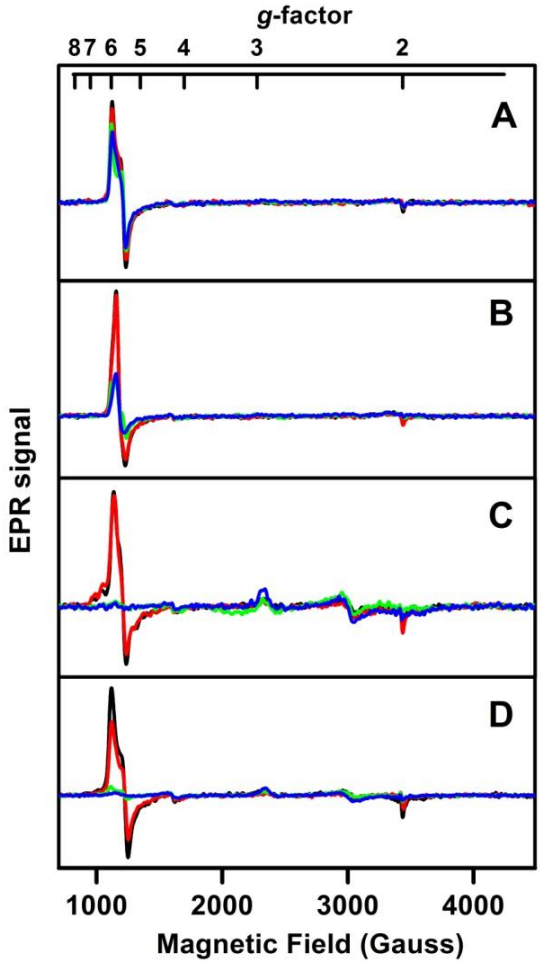

Figure 3.4.6 EPR spectra of cmTDO (200 μM heme concentration) in the absence and presence of exogenous imidazole and its analogs (50 mM). (A) WT TDO, (B) Q73F, (C) H72S, (D) H72N. Black: as-isolated; Red: with 2MI; Green: with IM; Blue: with 4MI. Experimental conditions: temperature, 10K; microwave frequency, 9.65 GHz; microwave power, 3 mW.

3.4.5 Chemical rescue for the dioxygenase activity of the His72 mutants

Kinetic assays were performed on cmTDO and its mutants in the absence and presence of different imidazoles. In WT TDO and Q73F, exogenous imidazoles had little effect on the catalytic activity (Figure 3.4.7_A and B). In contrast, the presence of 2MI in the reaction system enhanced the reaction rates of both His72 variants, whereas the addition of IM or 4MI was not able to contribute as much (Figure 3.4.7_C and D). Therefore, 2MI was selected as the rescuing reagent for the catalytic activities of the His72 variants.

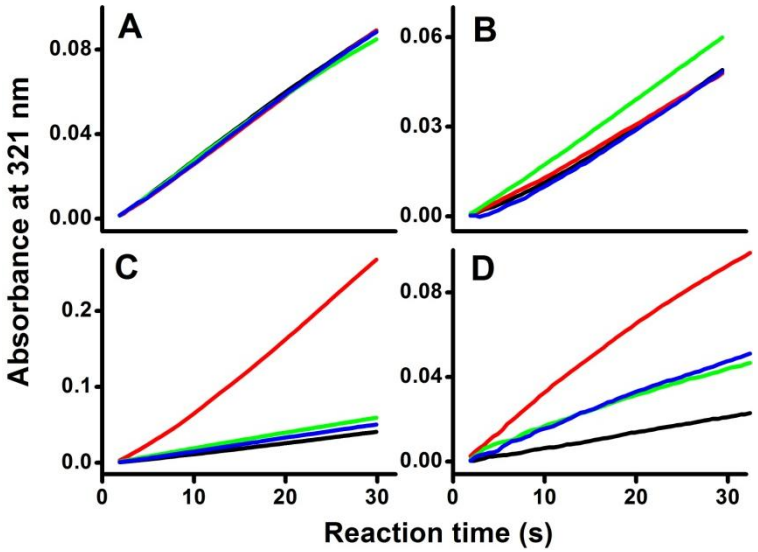

Figure 3.4.7 Comparison of enzymatic activities of cmTDO in the absence and presence of exogenous imidazoles. (A) WT TDO, (B) Q73F, (C) H72S, (D) H72N. Formation of NFK was monitored by the increase of absorbance at 321 nm. The kinetic traces were obtained in the presence of 1 mM L-Trp and 1 mM L-ascorbate, with no exogenous imidazoles (black), 50 mM 2MI (red), 50 mM IM (green), or 50 mM 4MI (blue). The final enzyme concentration was 0.15 μM for WT TDO, 0.2 μM for Q73F, 1.5 μM for H72S, and 5 μM for H72N. For each trace, the absorbance at the starting point was subtracted over the whole time course to correct for background.

The His72 mutants adhered to saturation kinetics with 2MI (Figure 3.4.8). By fitting the experimental data to Eq. 1, the Michaelis-Menten constants for 2MI, which were redefined here as $K_{activation}$, were determined to be 18 ± 3 and 16 ± 2 mM for H72S and H72N, respectively.

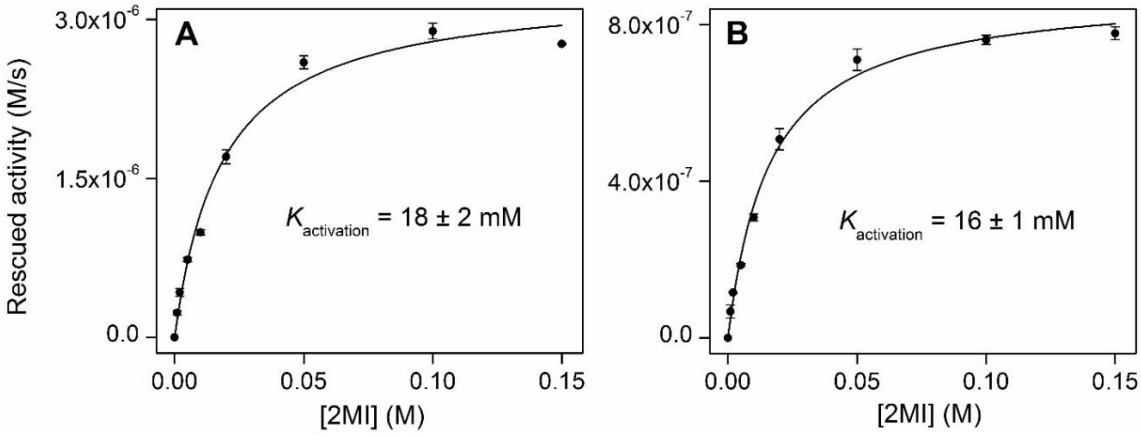

Figure 3.4.8 Rescued catalytic activities of H72S (A) and H72N (B) as a function of 2MI concentration. The reaction rates were measured at room temperature in the presence and absence different concentrations of 2MI, with 1 mM L-ascorbate and 1mM L-Trp in the reaction systems. The final concentration of enzyme was 1.5 μM for H72S and 5 μM for H72N. The rescued catalytic activity is the difference between the reaction rates determined in the presence and absence of 2MI. The solid lines are the best fits of experimental data to Eq. 1. The $K_{activation}$ values were determined from the fitting results.

The turnover numbers of H72S and H72N at saturating 2MI conditions (*i.e.*, 50 mM) were determined as 3.1 ± 0.2 and 0.23 ± 0.01 s^{-1}, respectively, which are *ca.* 6- and 4-fold higher than the k_{cat} values determined in the absence of 2MI (Figure 3.4.9 and Table 3.4.3). The K_m values for L-Trp were determined as 0.43 ± 0.06 and 0.43 ± 0.04 mM for H72S and H72N in the presence of 2MI, respectively, which were similar to the values obtained in the absence of 2MI.

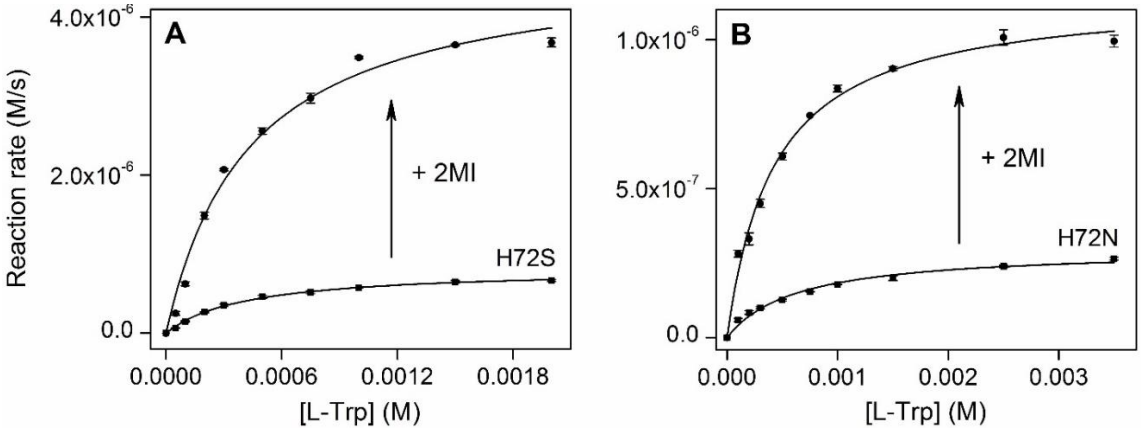

Figure 3.4.9 Steady-state kinetic assays of H72S (A) and H72N (B) in the absence (■) and presence (●) of 2MI (50 mM). The reaction rates were measured at room temperature in the presence of 1 mM L-

ascorbate. The final concentration of enzyme was 1.5 μM for H72S and 5 μM for H72N. The solid lines are the best fits of experimental data to Eq. 1.

3.4.6 Stopped-flow UV-vis characterization of a ferryl species in TDO

Previously, we reported a peroxide-mediated enzyme reactivation pathway of TDO [96]. A compound ES-type ferryl species was identified in the reactivation process and characterized by the EPR and Mössbauer spectroscopy [96]. Here, we took advantage of the previous findings to examine the effects of mutation and chemical rescue on this ferryl species. Upon rapid mixing of ferric WT TDO (UV-vis spectrum: 405, 504, and 539 nm) with H_2O_2 (5 mM), a new heme species with a red-shifted Soret band (414 nm) as well as altered visible bands (526 and 548 nm) was generated in the millisecond time window as measured by stopped-flow UV-vis spectroscopy (Figure 3.4.10_A) and was assigned as the aforementioned compound ES species. Concurrent with the formation of the ferryl species, the charge transfer band around 630 nm was reduced in intensity. The observation of isosbestic points at 461, 514, and 618 nm (Table 3.4.4) suggests that this is a single transition process (*i.e.*, from ferric to ferryl TDO). The formation rate of this ferryl species was determined to be 27.2 ± 0.2 s^{-1} by following the decay of the ferric enzyme at its Soret band absorption intensity. Parallel experiments performed in the presence of highly concentrated H_2O_2 (*i.e.*, above 100 mM) revealed the formation of the same type of ferryl species (data not shown). In the reaction between Q73F and H_2O_2 (5 mM), a similar ferryl species with nearly identical optical absorption features (413, 526, and 548 nm) was observed (Figure 3.4.11_A). The formation rate of this ferryl species was calculated to be 16.7 ± 0.4 s^{-1} based on the decay of the ferric heme.

In sharp contrast, no transient intermediates were detected during the reactions between the His72 mutants and peroxide (Figure 3.4.10_B and Figure 3.4.11_B), suggesting the functional importance of His72 in generating or stabilizing the ferryl species in cmTDO. However, in the presence of highly concentrated H_2O_2 (*i.e.*, above 100 mM), the formation of a

new species, possibly a ferryl heme species as judged by the spectral features, could be observed in the millisecond time window (Figure 3.4.10_C and Figure 3.4.11_C). The formation rates of this new species generated by 375 mM H_2O_2 were determined to be 53 ± 6 and 15.5 ± 0.3 s^{-1} in H72S and H72N, respectively. At longer time scales, the heme became severely bleached by the presence of such high concentrations of H_2O_2.

Inspired by our chemical rescue results, we introduced 2MI to the stopped-flow experiments with the aim of rescuing the ferryl species from the His72 variants in the presence of less concentrated H_2O_2 (*i.e.*, 5 mM). While no significant changes in the time-resolved spectra were observed during the reaction of H72S and 5 mM H_2O_2, the accumulation of a new species with a red-shifted Soret band (411 nm), altered visible bands, and a reduced charge transfer band, was observed in the same reaction system supplemented with 50 mM 2MI (Figure 3.4.10_D). Again, this species was assigned as a ferryl species based on the similarity of its spectral features to those of the compound ES species from WT TDO. Similar chemical rescue results were obtained from H72N (Figure 3.4.11_D). The formation rates of this rescued ferryl species were calculated to be 7.3 ± 0.1 and 1.4 ± 0.1 s^{-1} for H72S/2MI and H72N/2MI, respectively.

We were able to generate two forms of ferryl species in the His72 mutants via two different strategies. Direct comparison of the time-resolved stopped-flow spectra between these two groups of ferryl species only revealed slight differences, due to the similarity of their redox states and the incomplete accumulation caused by either too much H_2O_2 in the reaction system or relatively low formation rates. Therefore, time-resolved difference spectra were constructed for better comparison and differentiation of the transition processes from ferric to ferryl in different reaction systems. Table 3.4.4 summarized the key features of these difference spectra. In the difference spectra of WT TDO, two negative peaks developed at 493 and 638 nm, and a positive peak at 555 nm with two shoulders at 528 nm and 598 nm (Figure 3.4.12_A). In addition, three

isosbestic points (461, 514, and 518 nm) were identified for the transition process. Q73F showed almost the same difference spectra (Figure 3.4.13_A). The putative ferryl species rescued by 2MI from the His72 variants presented very similar difference spectra with nearly identical isosbestic points (Figure 3.4.12_C and Figure 3.4.13_C). On the other hand, the putative ferryl species accumulating in the presence of highly concentrated H_2O_2 showed quite different difference spectra (Figure 3.4.12_B and Figure 3.4.13_B) as compared to the ferryl species from WT TDO and Q73F. The differences were outlined by significant alterations in the absorption maxima of both the positive and negative peaks on the spectra as well as the positions of the isosbestic points (Table 3.4.4).

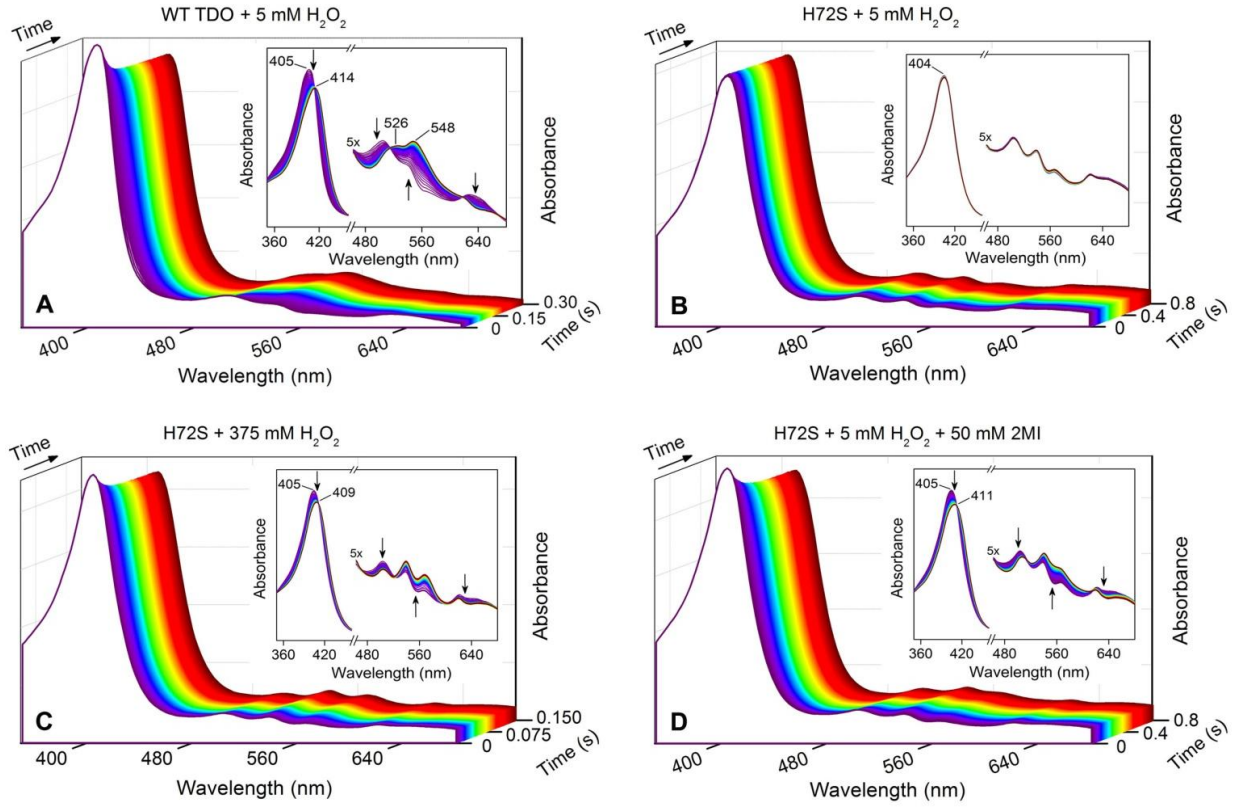

Figure 3.4.10 Time-resolved stopped-flow UV-vis spectra of the reactions between cmTDO (15 μM) and H_2O_2 at 4 °C. (A) WT TDO + 5 mM H_2O_2 (0–0.3 s); (B) H72S + 5 mM H_2O_2 (0–0.8 s); (C) H72S + 375 mM H_2O_2 (0–0.15 s); (D) H72S + 5 mM H_2O_2 with 50 mM 2MI in the reaction system (0–0.8 s). The insets are expanded views of the visible bands. The arrows indicate the trends of changes in the spectra.

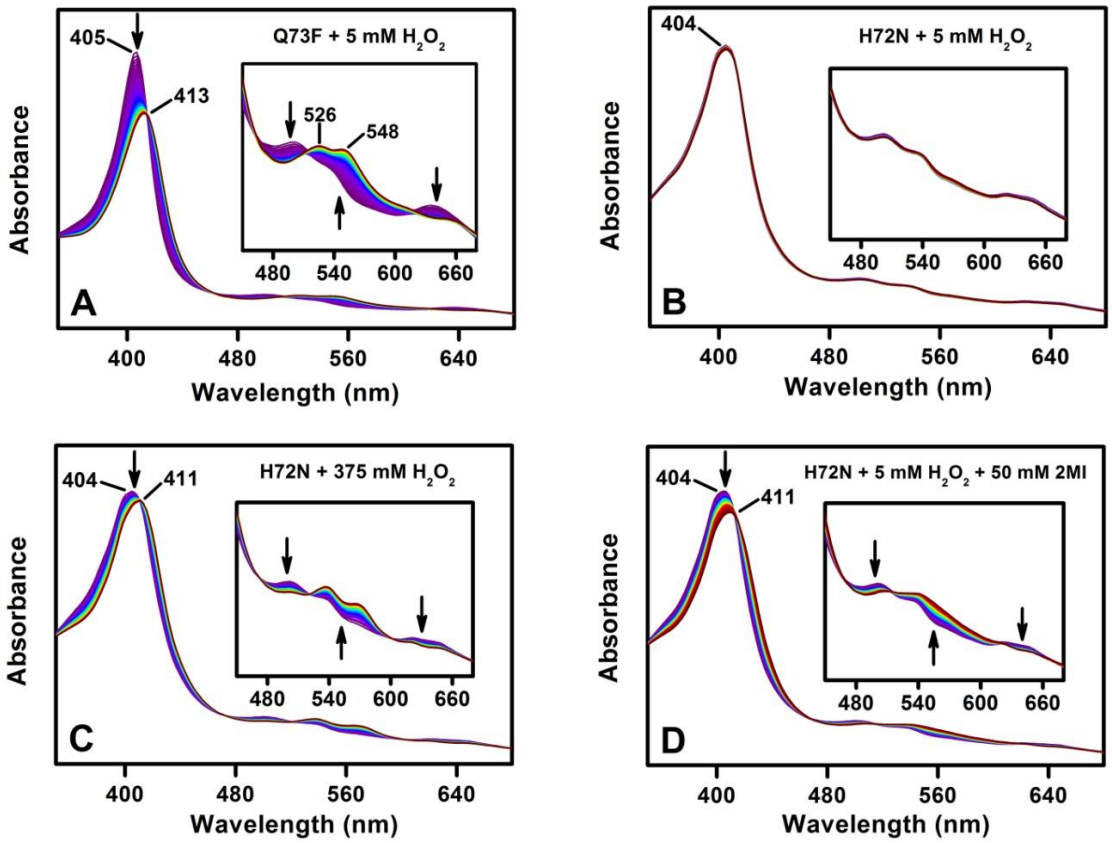

Figure 3.4.11 Time-resolved stopped-flow UV-vis spectra of the reactions between cmTDO (15 μM) and H_2O_2 at 4 °C. (A) Q73F + 5 mM H_2O_2 (0–0.5 s); (B) H72N + 5 mM H_2O_2 (0–2.5 s); (C) H72N + 375 mM H_2O_2 (0–0.2 s); (D) H72N + 5 mM H_2O_2 with 50 mM 2MI in the reaction system (0–2.5 s). The insets are expanded views of the visible bands. The arrows indicate the trends of changes.

Table 3.4.4 Optical absorption features identified in the time-resolved difference spectra during the peroxide-induced transition processes from ferric to ferryl TDO

Protein	Positive peak (nm)			Negative peak (nm)		Isosbestic point (nm)		
	#1	#2	#3	#1	#2	#1	#2	#3
WT TDO	528	555	598	493	638	461	514	618
Q73F	528	555	598	494	638	461	514	618
H72S[a]	546	570	-	500	636	471	522	602
H72N[a]	546	570	-	501	636	472	521	602
H72S + 2MI[b]	528	555	598	492	638	461	514	618
H72N + 2MI[b]	528	555	598	494	638	464	514	618

[a] Highly concentrated H_2O_2 (*i.e.*, 375 mM) was used to generated the putative ferryl species in this set of

experiments.
[b] The experiments were performed in the presence of 50 mM 2MI.

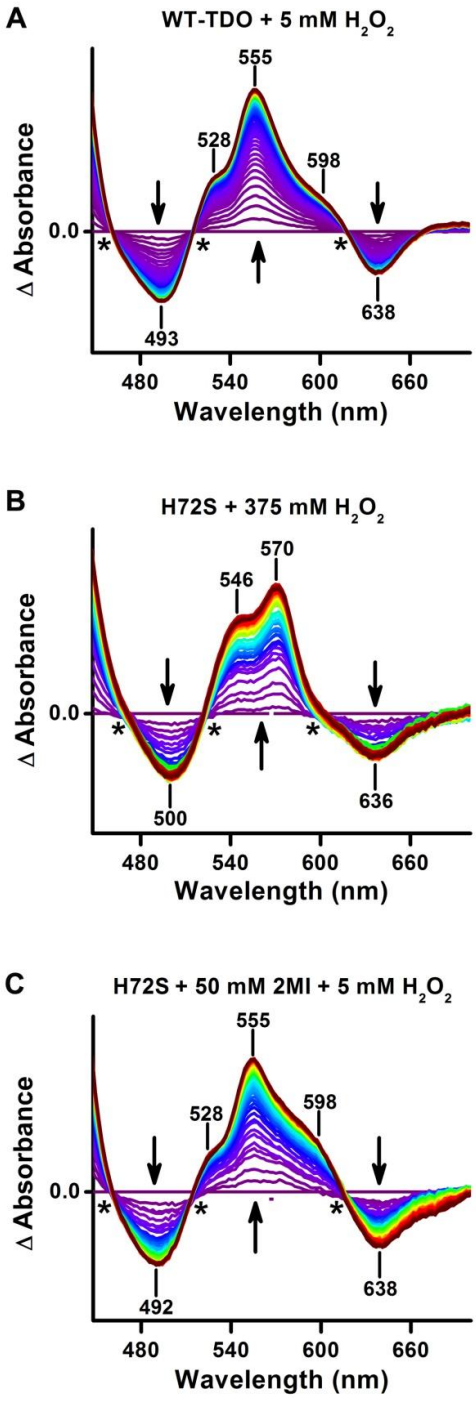

Figure 3.4.12 Time-resolved stopped-flow UV-vis difference spectra of the reactions between cmTDO (15 μM) and H_2O_2 at 4 °C. (A) WT TDO + 5 mM H_2O_2 (0–0.3 s); (B) H72S + 375 mM H_2O_2 (0–0.15 s);

(C) H72S + 5 mM H_2O_2 with 50 mM 2MI in the reaction system (0–0.8 s). The arrows indicate the trends of changes in the spectra. The "*" symbol indicates the isosbestic points identified in the visible region.

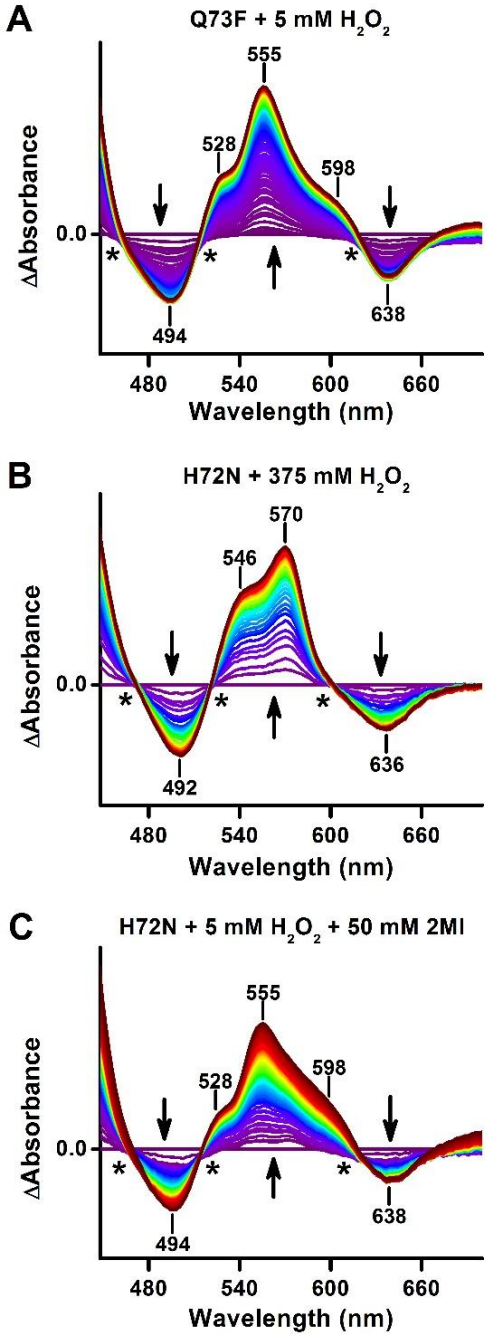

Figure 3.4.13 Time-resolved stopped-flow UV-vis difference spectra of the reactions between cmTDO (15 μM) and H_2O_2 at 4 °C. (A) Q73F + 5 mM H_2O_2 (0–0.5 s); (B) H72N + 375 mM H_2O_2 (0–0.2 s); (C) H72N + 5 mM H_2O_2 with 50 mM 2MI in the reaction system (0–2.5 s). The arrows indicate the trends of changes in the spectra. The "*" symbols indicate the three isosbestic points identified in the visible regions.

3.5 Discussion

3.5.1 The role of the distal histidine

We propose a dual function for the distal His72 in cmTDO: a) facilitating substrate binding through H-bonding interaction while protecting the heme center from non-productive binding of exogenous small ligand molecules (*i.e.*, imidazole and its analogs) via steric effect, and b) contributing to the chemical catalysis process by providing H-bonding interaction to the oxygen-bound heme intermediates including the putative ferryl intermediate that was proposed in the dioxygenase catalytic cycle [55,57,59].

The first function is supported by the kinetic assays with 1-Me-L-Trp as the substrate and the spectroscopic characterizations of the binding events with exogenous imidazoles. Additional support is provided by the biochemical studies on the Q73F mutant. The second function is proposed based on our chemical rescue experiments on the distal histidine variants of the enzymatic activity in both the dioxygenase catalytic reaction and the formation of a peroxide-induced ferryl species with 2MI as the rescuing reagent. The proposed H-bonding interaction provided by the distal histidine would contribute to stabilization of the putative ferryl intermediate and thus help boost the catalytic efficiency. Detailed discussions on the proposed functions of the distal histidine are presented below.

3.5.2 The effects of site-directed mutagenesis

Upon replacement of His72 with Ser/Asn, a significant decrease in the catalytic activity was observed, with a more pronounced effect on k_{cat} than K_m. Distal histidine variants from other sources also presented declines in the enzymatic activity at different degrees (Table 3.4.3). The notable decrease in the catalytic activity of the His72 mutants appears to result from the absence

of the imidazole side chain of His72 rather than structural changes in the active site, since spectroscopic characterizations of the mutant proteins revealed no substantial changes.

Exogenous imidazole was not able to coordinate to the heme iron of WT cmTDO. In contrast, the same molecule was allowed to directly ligate to the heme center after the substitution of His72 to Ser/Asn and generate an HALS-like species at the expense of the resting high-spin ferric species. Interestingly, it was demonstrated by Sono and colleagues that imidazole can coordinate to the heme center of IDO, which has a serine residue occupying the analogous distal position of His72, and cause a distinctive red shift of the Soret band [213]. They also observed a HALS-like species with similar EPR parameters (g = 2.86, 2.28, and 1.60) from as-isolated IDO, which became the major species in the EPR spectrum upon the addition of exogenous imidazole [213]. A similar HALS-like species (g = 2.94, 2.25 and 1.50) was reported in as-isolated IDO [212]. Upon the addition of the L-Trp, the amount of this species decreased to generate the substrate-induced hydroxide-bound low-spin heme species [212], resembling the phenomenon observed in the His72 mutants in this study. Taken together, it can be concluded that possibly via steric hindrance, the distal His72 can efficiently shield the heme center of cmTDO from non-productive binding of exogenous small ligand molecules, such as imidazole and its analogs. Moreover, Basran e*t al.* reported the existence of the same type of HALS-like species (g = 2.8, 2.3 and 1.6) in as-isolated hTDO [171], suggesting that imidazole is capable of coordinating to the heme center of hTDO in the presence of the distal histidine. Therefore, TDO proteins from different sources might possess slightly different active-site architectures.

In contrast to the His72 mutants, Q73F inherited the majority of the key features from WT TDO, including the spectroscopic properties and enzymatic reactivity, without distinctive alterations. Therefore, with the distal histidine present, most of the biochemical properties of the enzyme are well-conserved. However, this variant differed from the native enzyme in certain

aspects: the replacement of Gln73 introduced the most distinct influence on the K_m value (a *ca.* 5-fold increase); the mutation also moderately increased the heme accessibility to allow the coordination of exogenous small molecules. Thus, the physical position of His72 is very important in maintaining the biological functions of TDO.

3.5.3 1-Me-L-Trp as an alternative substrate

It has been previously reported by Raven and colleagues that 1-Me-L-Trp is a slow substrate for IDO as well as the distal histidine variants of hTDO (H76A) and xcTDO (H55A and H55S) but is inactive to the WT TDO enzymes [85]. This finding has important mechanistic implications. Under the assumption that 1-Me-L-Trp and L-Trp react by the same mechanism, it is suggested that the deprotonation of the indole NH group of the substrate is not an essential step for catalysis [85]. In the present study, 1-Me-L-Trp is demonstrated for the first time to be an active substrate to a WT TDO enzyme with comparable reactivity to that of L-Trp. This finding adds one more piece of direct and strong experimental evidence to the above-mentioned notion, *i.e.*, the catalytic cycle of TDO is not initiated by the deprotonation of the substrate indole group, which has also been supported by some recent computational studies [56,57,59,60].

With a methyl group attached to the indole nitrogen, 1-Me-L-Trp is shown to present a significantly altered K_m value. The nearly 7-fold increase in K_m reflects a lower affinity of this substrate analogue to the enzyme, which can be attributed to the loss of the H-bonding interaction between the imidazole group of His72 and the indole NH group of the substrate.

3.5.4 Chemical rescue for the dioxygenase activity of the His72 mutants

The distal histidine was mutated to alanine and serine by several laboratories in the past [61,73,78]. This is the first time that the diminished catalytic activity, due to site-directed mutation, has been shown to be recoverable to an appreciable degree by a histidine analogue (*i.e.*, 2MI). In contrast, both IM and 4MI failed to show a comparable ability to stimulate the

enzymatic activity of the His72 mutants, presumably due to the fact that their chemical rescue effect was nullified by the inhibition effect caused by the direct coordination to the heme iron. Spectroscopic studies demonstrated that IM and 4MI are able to coordinate to the heme center of the His72 variants to produce hexacoordinated heme species, whereas 2MI cannot directly ligate to the heme iron. It should be noted that while 2MI is able to cause an appreciable increase in the k_{cat} values, this compound only minutely altered the K_m values. Thus, the chemical rescue effect was mainly focused on the chemical catalytic steps rather than the substrate binding step. This suggests that the enzyme-bound 2MI molecules are less likely to play a role in assisting substrate binding; rather, they are able to participate in the chemical catalytic steps in a way that mimics the role of His72.

3.5.5 Chemical rescue for the ferryl species of the His72 mutants: Implications on the proposed role of His72 in catalysis

TDO and IDO are generally thought to share similar catalytic strategies. An Fe(IV)=O intermediate (compound II-type) has been observed from IDO and characterized by RR spectroscopy [59]. Such a ferryl intermediate has not yet been captured in TDO, presumably because the catalytic reaction rate is much faster. However, it has been proposed as one of the key intermediates in the dioxygenase catalytic cycle of TDO in recent computational studies [57,59]. Previously, we have identified and characterized a peroxide-mediated ferryl species (compound ES-type) in TDO via the EPR and Mössbauer spectroscopy during the enzyme reactivation cycle, demonstrating an alternative way to generate the ferryl species in TDO [96].

While the ferryl species was observed from WT TDO via the stopped-flow UV-vis spectroscopy in the reaction with H_2O_2, no such intermediate could be identified during the reaction between His72 variants and H_2O_2 under the same conditions. By significantly increasing the H_2O_2 concentration, we were able to generate a different ferryl species from the His72

variants with disparate spectral features as revealed by the difference spectra. It has been shown that the visible bands of ferryl heme are sensitive to the changes in the electronic structure of the Fe(IV)=O moiety. For example, the visible bands of ferryl heme in myoglobin and hemoglobin have been demonstrated to be susceptible to the protonation state of the Fe(IV)=O moiety [223]. Herein, we propose that the differences in the spectral features between the ferryl species from WT TDO and the His72 mutants resulted from the loss of the H-bonding interaction between the distal histidine and the Fe(IV)-oxo group. The proposed H-bonding interaction plays an important structural role in stabilizing the Fe(IV)=O moiety of the ferryl species in cmTDO, as suggested by the requirement of such high concentrations of H_2O_2 for the occurrence of the accumulation of the ferryl species in the His72 mutants. Our previous Mössbauer spectroscopic characterization revealed a unique ΔEQ value (1.755 mm/s at pH 7.4) for the peroxide-mediated ferryl species from WT TDO [96], which lies in between the ranges for protonated Fe(IV)-OH species (2.0–2.5 mm/s) [186] and unprotonated Fe(IV)=O species (1.0–1.6 mm/s) [127,128,186-188]. Subsequent DFT calculations indicated that the unusual ΔE_Q value originates from H-bonding interaction provided by the protein matrix [96], and His72 is an ideal candidate for the proposed H-bonding interaction with the Fe(IV)-oxo group.

The spectral similarities between the ferryl species from WT TDO and those rescued by 2MI from the His72 variants suggest that these two groups of ferryl species structurally resemble each other. Therefore, by substituting for His72, 2MI is able to rescue the accumulation of the same compound ES-type ferryl species as that from WT TDO in both His72 mutants at a relatively low H_2O_2 concentration (Figure 3.5.1). However, due to its exogenous nature, the binding occupancy and the effective binding ratio of 2MI are expected to be limited, hampering its rescuing effect, as suggested by the relatively low formation rate of the rescued ferryl species.

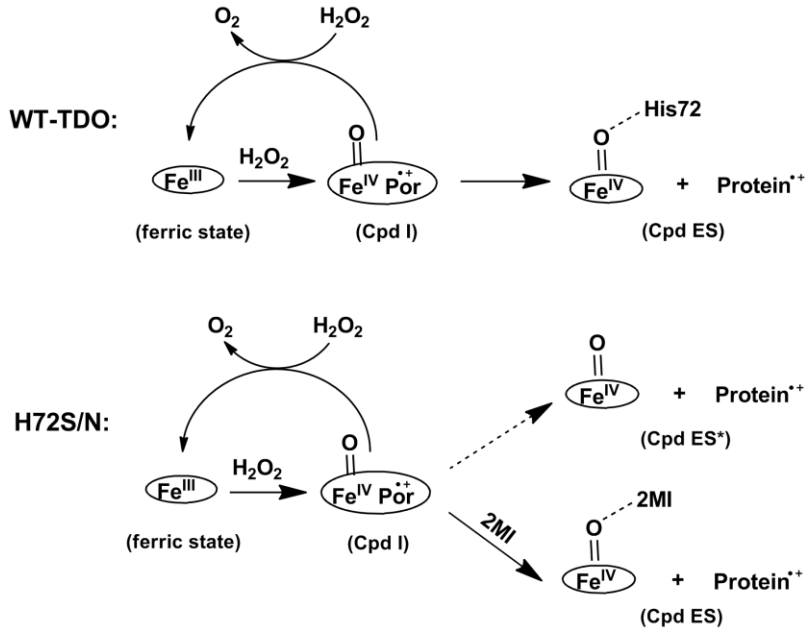

Figure 3.5.1 Proposed role of His72 in stabilizing the ferryl species in cmTDO in the reaction with H_2O_2. The catalase-like cycle of TDO has been reported previously [96]. "Cpd ES" differ from "Cpd ES*" by an additional H-bonding interaction to either the His72 residue or 2MI. The accumulation of "Cpd ES*" can be observed only in the presence of highly concentrated H_2O_2 (*i.e.*, over 100 mM).

Figure 3.5.2 illustrates the proposed role of His72 during the dioxygenase reaction of cmTDO. Other than participating in the initial L-Trp binding process and properly positioning it at the active site, His72 is proposed to stabilize the oxygen-bound heme intermediates during the subsequent catalytic steps. The key catalytic intermediate is a compound II-type ferryl species, which is similar, but not the same as the compound ES species observed in the peroxide-mediated enzyme reactivation pathway, which possess an additional oxidizing equivalent stored as a protein-based radical. However, oxidation of L-Trp by the Fe(IV)=O moiety and by the protein-based radical are separated reactions in the enzyme reactivation mechanism [96]. Therefore, the proposed compound II species has been implicated in the later stage of the enzyme reactivation pathway. The data presented in this work showed that the properties and reactivity of the ferryl species in cmTDO are dependent on the presence of the distal His72. In its absence, 2MI can effectively play the part played by His72, thus rescuing the enzymatic activity.

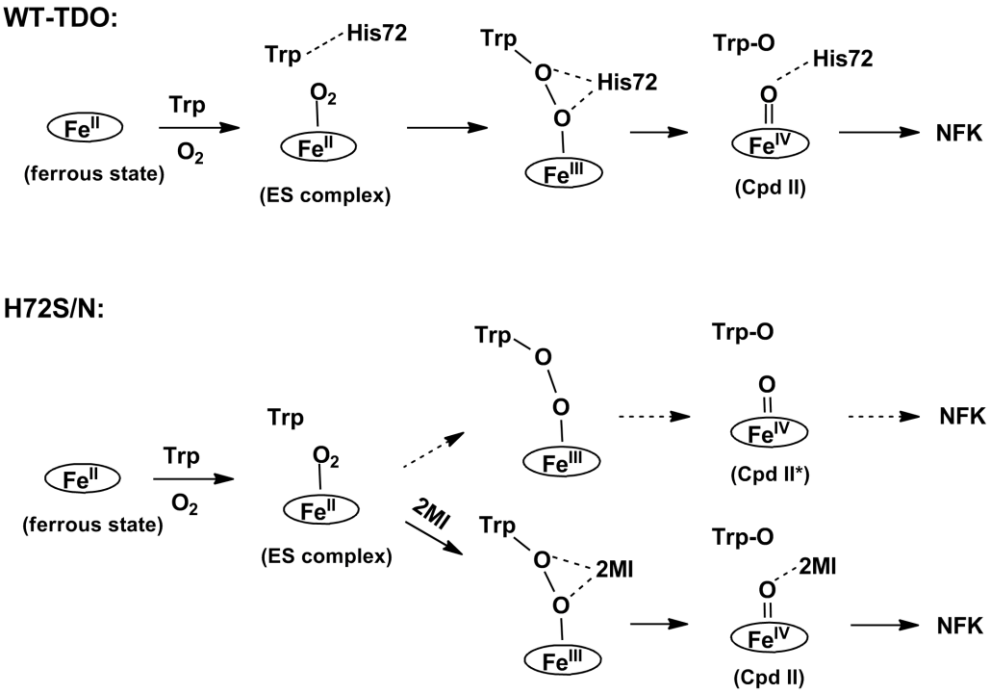

Figure 3.5.2 Proposed role of His72 in catalysis during the dioxygenase reaction cycle of cmTDO. "Cpd II" differ from "Cpd II*" by an additional H-bonding interaction to either the His72 residue or 2MI.

4 EFFECTS OF THE LOSS OF THE AXAIL TYROSINE LIGAND OF HEME$_{5C}$ ON THE PHYSICAL PROPERTIES AND REACTIVITY OF MAUG

(This chapter is modified from a research article that JG coauthored: Abu Tarboush N, Shin S, Geng J, Liu A, and Davidson, VL (2012) Effects of the loss of the axial tyrosine ligand of the low-spin heme of MauG on its physical properties and reactivity. ***FEBS Lett.***, 586(24), 4339-4343.)

4.1 Abstract

MauG catalyzes posttranslational modifications of MADH to complete the biosynthesis of its protein-derived TTQ cofactor. MauG possesses a pentacoordinated high-spin and a hexacoordinated low-spin ferric heme, the latter with His-Tyr ligation. Replacement of this tyrosine with lysine generates a MauG variant with only high-spin ferric heme and altered spectroscopic and redox properties. Y294K MauG cannot stabilize the *bis*-Fe(IV) redox state required for TTQ biosynthesis but instead forms a compound I-like high-valence species upon reaction with peroxide. The results clarify the role of tyrosine ligation in determining the physical properties and reactivity of MauG.

4.2 Introduction

MauG from *Paracoccus denitrificans* [12] is a di-heme enzyme which catalyzes the biosynthesis of the protein-derived TTQ cofactor [104] of MADH [224]. The substrate for MauG is an MADH precursor protein, preMADH, in which residue βTrp57 has been monohydroxylated [13]. MauG catalyzes the six-electron oxidation of preMADH which results in cross-linking of βTrp57 and βTrp108, a second hydroxylation of βTrp57, and oxidation of the quinol species to the quinone [108,225] (Figure 1.2.2). Di-ferric MauG contains two *c*-type hemes. One is high-spin with His35 providing an axial ligand and the other is low-spin with axial ligands provided by His205 and Tyr294 [12,112]. Natural Tyr-His heme *c* ligation has not previously been

described, and MauG is the first known example of a *c*-type heme with axial ligation by tyrosine. Despite a 21 Å separation of the heme iron centers [112], the di-heme system of MauG exhibits redox cooperativity with the two hemes behaving as a single di-heme unit rather than as independent hemes [114]. As such, the two oxidation/reduction midpoint potential (E_m) values for the inter-conversion between di-ferric and di-ferrous states correspond to the sequential addition or removal of the first and second electrons from the di-heme system, rather than being attributable to one or the other heme. A novel feature of MauG is that on reaction with H_2O_2 it generates a *bis*-Fe(IV) state with the pentacoordinated heme as Fe(IV)=O and the other heme as Fe(IV) with the two axial ligands from the protein retained [109]. This *bis*-Fe(IV) state is required for each of the three sequential two-electron oxidations of preMADH. However, the catalytic mechanism requires long-range electron/hole transfer as the substrate is *ca.* 40 Å away from the H_2O_2-binding heme iron [101,112,226]. This mechanism also requires that solvent rather than the ferryl heme is the source of the oxygen that is added to βTrp57 during biosynthesis (Figure 1.2.2).

Previously, Try294, the distal axial ligand of the low-spin heme, was mutated to His and the crystal structure of Y294H MauG revealed that the hexacoordinated heme had His-His axial ligation [132]. Y294H MauG was able to interact with preMADH and participate in interprotein ET, but it was unable to catalyze the TTQ biosynthesis reactions that require the *bis*-Fe(IV) state. Furthermore, this mutation affected the redox properties of both hemes. Spectroscopic data revealed that Y294H MauG could not stabilize the *bis*-Fe(IV) state, but instead formed a compound I-like species which could not catalyze TTQ biosynthesis [132].

In this study, Tyr294 was converted to Lys, which resulted in loss rather than replacement of the axial heme ligand provided by Tyr294. This provides an opportunity to

characterize a form of MauG with two pentacoordinated hemes. The results of this study and previous work allow us to clarify the role of Tyr ligation in determining the physical properties and reactivity of MauG.

4.3 Materials and methods

4.3.1 Protein expression and purification

Methods for the expression and purification of MADH [227], preMADH [13], and MauG [12] were described previously. Site-directed mutagenesis to create Y294K MauG was performed on double-stranded pMEG391 [12], which contains *mauG*, with the Quick-Change site-directed mutagenesis kit (Strategene). The entire *mauG*-containing fragment was sequenced to ensure that no additional mutations were present. Y294K MauG was expressed in *P. denitrificans* cells and isolated from the periplasmic fraction as described for recombinant WT MauG [12]. The yield was approximately 1 mg/L of culture, which is comparable to the yield of WT MauG.

4.3.2 EPR spectroscopy

EPR samples were prepared in 50 mM potassium phosphate buffer, pH 7.4, with 150 µM WT or Y294K MauG. Continous-wave X-band EPR spectra were taken on a Bruker ER200D spectrometer at 100-kHz modulation frequency coupled with a dual mode resonator. The measurement temperature was maintained at 10 K with an ESR910 liquid helium cryostat and an ITC503 temperature controller from Oxford Instrument (Concord, MA).

4.3.3 Redox titrations

E_m values were determined by anaerobic spectrochemical titration as described previously for WT MauG [114] using FMN as a mediator. Sodium dithionite was used in

reductive titrations and potassium ferricyanide was used in oxidative titrations. The titrations were fully reversible. The fraction reduced was determined by comparison with the spectra of the completely oxidized and reduced forms of MauG and quantitated from the absorbance at 550 nm. E_m values were obtained by fitting the experimental data to Eq. 1, where a and $(1 - a)$ are the fraction of the total absorbance change attributable to each of the two one-electron redox couples. E_m values are reported versus NHE.

$$\text{Fraction reduced} = a/[1 + 10^{((E-Em1)/0.059V)}] + (1 - a)/[1 + 10^{((E-Em2)/0.059V)}] \qquad \text{Eq. 1}$$

4.3.4 Assays for MauG-dependent TTQ biosynthesis

Steady-state kinetic studies of MauG-dependent TTQ biosynthesis from preMADH were performed using a previously described spectrophotometric assay [111,134]. Y294K MauG was mixed with preMADH in 10 mM potassium phosphate buffer, pH 7.5 at 25 °C. Reactions were initiated by the addition of 100 μM H_2O_2 and the rate of appearance of quinone MADH was monitored at 440 nm.

4.3.5 Assays for ET from di-ferrous Y294K MauG to quinone MADH

The single-turnover kinetics of the reaction of di-ferrous Y294K MauG with quinone MADH were studied as described previously for WT MauG [228]. The reaction was monitored by the decrease in absorbance at 550 nm which corresponds to the conversion of di-ferrous to di-ferric MauG [12]. Data were analyzed using Eq. 2 and 3 where S is quinone MADH, E is di-ferrous MauG, E' is di-ferric MauG, and P is quinol MADH.

$$\mathrm{E + S} \underset{}{\overset{K_d}{\rightleftharpoons}} \mathrm{ES} \underset{k_4}{\overset{k_3}{\rightleftharpoons}} \mathrm{E'P} \qquad \text{Eq. 2}$$

$$k_{obs} = k_3[S]/([S] + K_d) + k_4 \qquad \text{Eq. 3}$$

4.4 Results

4.4.1 Effects of the Y294K mutation on the optical absorption spectra

It should be noted that since MauG is a di-heme protein, its spectral features represent a combination of contributions from each heme. It was confirmed that Y294K MauG possessed two covalently bound hemes and the extinction coefficients of peaks in the absorption spectrum were determined by the pyridine hemochrome method [229]. Anaerobic titrations of Y249K MauG with sodium dithionite confirmed that two electron equivalents are required for conversion of the di-ferric state to di-ferrous. The spectra of the di-ferrous and di-ferric forms reveal that the Y294K mutation caused subtle changes in the absorption maxima of the Soret and β peaks of MauG, as well as increases in the extinction coefficients for all peaks in the di-ferrous spectrum (Table 4.4.1). These changes are very similar to spectral changes which were caused by the Y294H mutation of MauG [132].

Table 4.4.1 Effects of the Y294K mutation on absorption maxima and extinction coefficients of MauG

Redox state	λ_{max} (ε) nm ($mM^{-1}cm^{-1}$)		
	MauG	Y294K MauG	Y294H MauG[a]
Di-ferric	406 (309)	403 (348)	404 (347)
Di-ferrous	418 (327)	415 (411)	416 (434)
	524 (34)	522 (41)	522 (39)
	552 (50)	550 (61)	550 (66)
High-valence	407 (271)	403 (280)	406 (286)
	-	655 (9.0)	655 (8.5)

[a] The values for Y294H MauG were taken from reference [132].

4.4.2 Effects of the Y294K mutation on the EPR spectrum

Figure 4.4.1 presents the EPR spectra of WT and Y294K MauG. The Y294K spectrum is dominated by high-spin heme signals (g = 5.57, 1.99), which indicates that the majority of heme

are in the pentacoordinated state with axial His ligation. A minor low-spin ferric component with *g* values of 2.89, 2.32 and 1.52 is also apparent in the Y294K spectrum. This signal was previously seen in the spectrum of WT MauG and was assigned as a hexacoordinated artifact derived from the original pentacoordinated heme after binding another ligand from solvent on freezing [134,138]. Our previous Mössbauer characterization of WT di-ferric MauG revealed that about half of the pentacoordinated heme is converted to this hexacoordinated artifact [138]. The conversion of high-spin to low-spin heme on freezing has been documented in other di-heme enzymes [121,230,231]. Further evidence supporting this interpretation is that a P107S mutation of MauG introduced a sixth ligand from protein to the pentacoordinated heme, and the artifact was absent in this mutant [134]. Thus, this spectral feature does not describe the true low-spin heme. The major low-spin ferric species (g = 2.54, 2.19, 1.87) in the EPR spectrum of WT MauG, which corresponds to the hexacoordinated, His-Tyr ligated heme disappears in the spectrum of Y294K MauG, consistent with the loss of the Tyr heme ligand.

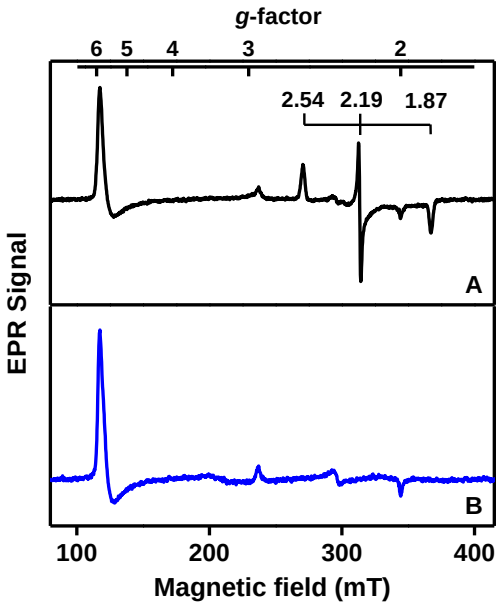

Figure 4.4.1 EPR spectra of WT (A) and Y294K (B) MauG. The low-spin ferric species in the spectrum of WT MauG, which corresponds to the His-Tyr ligated heme, is labeled for clarification. Experimental

condition: temperature, 10 K; microwave frequency, 9.65 GHz; microwave power: 1 mW; and modulation magnitude, 0.5 mT.

4.4.3 Effects of the Y294K mutation on the E_m values

MauG exhibits two E_m values which correspond to the sequential addition or removal of the first and second electron from the di-heme system [114]. Y294K MauG exhibited E_m values of -75 and -268 mV, whereas the E_m values for WT MauG are -158 and -246 mV (Figure 4.4.2, Table 4.4.2). The spectrochemical titration was reversible and yielded the same E_m values in each direction. The effect of this mutation is qualitatively similar to what was observed in Y294H MauG [132], except that in the latter case the increase in separation of the E_m values was much greater with E_m values of -17 and -377 mV.

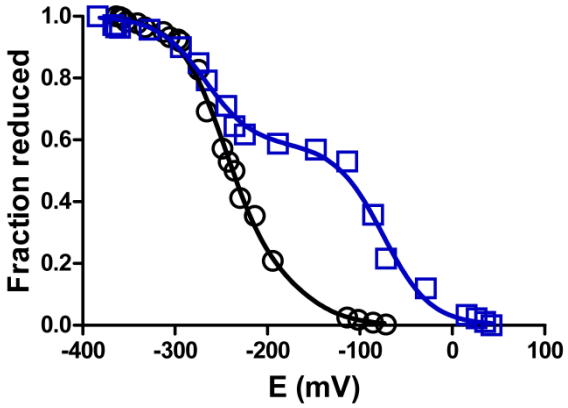

Figure 4.4.2 Redox titrations of WT MauG (circles, black) and Y294K MauG (squares, blue). Titrations were performed anaerobically in 50 mM potassium phosphate, pH 7.5. Solid lines are fits of the data by Eq. 1.

Table 4.4.2 Effects of the Y294K mutation on redox properties and reactivity of MauG

Properties	WT MauG	Y294K MauG	Y294H MauG[a]
E_m values (mV)	-158 ± 9 -246 ± 3	-75 ± 4 -268 ± 5	-17 ± 13 -377 ± 2
k_{cat} for TTQ biosynthesis from preMADH (s^{-1})	0.2[b]	0	0

k_{cat} for TTQ biosynthesis from quinol MADH (s^{-1})	4.2[c]	0	0
Electron transfer reaction from di-ferrous MauG to quinone MADH (s^{-1})	k = 0.07 ± 0.01 s^{-1}[c] K_d = 10.1 ± 1.6 μM[c]	k = 0.16 ± 0.02 s^{-1} K_d = 14.4 ± 3.4 μM	k = 0.21 ± 0.01 s^{-1} K_d = 9.4 ± 1.1 μM

[a] The values for Y294H MauG were taken from reference [132].

[b] Taken from reference [111].

[c] Taken from reference [228].

4.4.4 Effects of the Y294K mutation on the reaction of MauG with H_2O_2

Reaction of di-ferric MauG with H_2O_2 results in the formation of a *bis*-Fe(IV) species which is reactive towards preMADH [109]. The formation and decay of this high-valence species is accompanied by changes in the optical absorption spectrum of MauG [232]. Reaction of Y294K MauG with H_2O_2 caused changes in the visible absorption spectrum which were different from those observed for WT MauG (Figure 4.4.3). Upon reaction of WT MauG with H_2O_2, the Soret band displays a red shift of both sides of the absorption envelope, a slight shift in λ_{max}, and a decrease in intensity at λ_{max} (Figure 4.4.3_A). Reaction of Y294K MauG with H_2O_2 results in a red shift for only the lower wavelength side of the Soret band to produce a sharper peak, with a similar decrease in intensity to that observed for reaction of WT MauG with H_2O_2 (Figure 4.4.3_B). This result is similar to what was observed for Y294H MauG [132]. For that variant it was shown that addition of H_2O_2 also resulted in the appearance of broad absorption in the 600-700 nm range with a major peak centered at 655 nm. The appearance of such absorption peaks in the 600-700 nm region with an accompanying decrease in absorption intensity of the Soret band is characteristic of compound I (*i.e.*, Fe(IV)=$O^{\bullet+}$) species [121,233-236]. The same absorption feature was observed after the addition of H_2O_2 to Y294K MauG (Figure 4.4.3_C), suggesting that it also forms a compound I-like high-valence species rather than *bis*-Fe(IV). This high-valence species of Y294K MauG formed within the dead-time of mixing in stopped-flow

experiments (*i.e.*, > 300 s^{-1}) and it spontaneously decayed to the di-ferric state with a half-life of about 3 min (Figure 4.4.3_D). This is similar to what was observed with WT MauG where the *bis*-Fe(IV) state also forms within the dead-time of mixing and exhibits a similar rate of spontaneous decay [232].

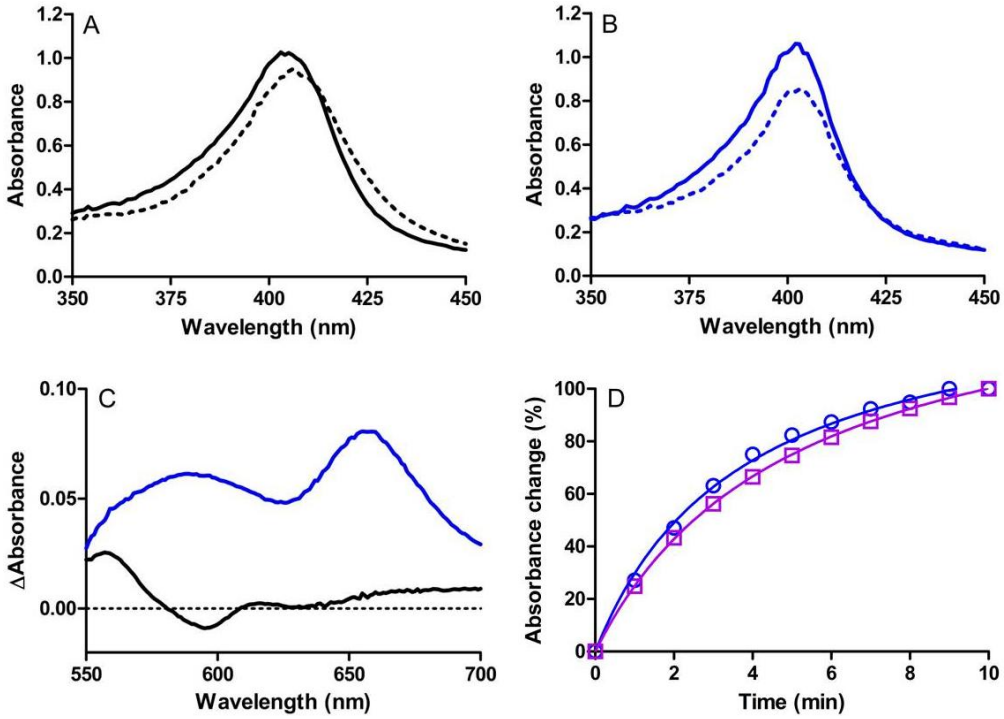

Figure 4.4.3 Changes in the absorption spectra of WT and Y294K MauG upon the addition of H_2O_2. (A) Soret region of 3 μM WT MauG before (solid line) and immediately after (dashed line) the addition of H_2O_2. (B) Soret region of 3 μM Y294K MauG before (solid line) and immediately after (dashed line) the addition of H_2O_2. (C) Difference spectra (immediately after H_2O_2 addition minus di-ferric spectra) of the higher wavelength region of the spectra for WT MauG (black) and Y294K MauG (blue). The concentration of protein was 15 μM for these spectra. (D) Time course for the return to the di-ferric state after the addition of H_2O_2 to generate the high-valence species in Y294K MauG. The changes in absorbance were monitored at 404 nm (blue circles) and 655 nm (purple squares). All spectra were recorded in 50 mM potassium phosphate, pH 7.5, at 25 ºC.

4.4.5 Effects of the Y294K mutation on the TTQ biosynthesis

Whereas the *bis*-Fe(IV) intermediate of WT MauG spontaneously decays to the di-ferric state slowly over several minutes, the addition of preMADH to *bis*-Fe(IV) WT MauG causes an

accelerated return to the di-ferric state with a rate constant of 0.8 s^{-1} [232]. In contrast, the addition of preMADH to the high-valence compound I-like Y294K MauG species did not cause any increase over the slow rate of spontaneous return to the di-ferric state. Furthermore, when tested in steady-state kinetic assay of TTQ biosynthesis from preMADH, Y294K MauG showed no enzymatic activity (Table 4.4.2). These results are similar to those previously reported for Y294H MauG [132].

4.4.6 Effects of the Y294K mutation on the ET reaction from di-ferrous MauG to quinone MADH

In addition to the biosynthetic oxidation reactions described above which require formation of the *bis*-Fe(IV) intermediate, a thermodynamically favorable ET reaction from di-ferrous MauG to quinone MADH may be monitored [228]. This reaction does not require formation of the *bis*-Fe(IV) state and has been used to distinguish whether mutations of MauG affect stabilization of the *bis*-Fe(IV) state, the capacity for long-range ET between the redox centers of the proteins, or neither, or both [101,132]. Y294K MauG was active in this reaction and exhibited a rate constant and K_d value of 0.16 s^{-1} and 14.4 μM, respectively, compared to 0.07 s^{-1} and 10.1 μM for WT MauG (Figure 4.4.4, Table 4.4.2).

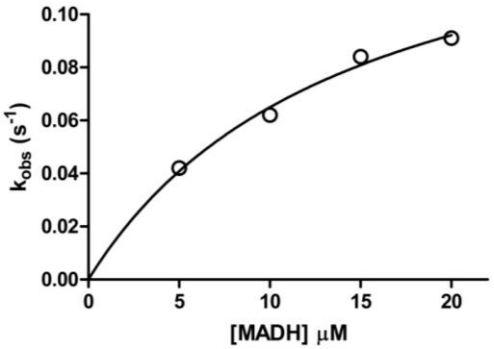

Figure 4.4.4 Single-turnover kinetics of the reaction of di-ferrous Y294K MauG. Each reaction was performed in 10 mM potassium phosphate buffer, pH 7.5, at 25 ºC. The reaction mixture contained 1.5 μM of the limiting reactant, di-ferrous Y294K MauG. The line represents the fit of the data by Eq. 3.

4.5 Discussion

MauG is distinct from other heme proteins in its function and physical properties. It catalyzes three successive, different oxidation reactions on amino acid residues of a substrate protein via long-range electron/hole transfer [101,112,226]. These oxidation reactions proceed via a *bis*-Fe(IV) intermediate in which the hexacoordinated heme stabilizes the Fe(IV) state without an exogenous ligand [109]. An unprecedented structural feature of MauG is that the hexacoordinated *c*-type heme has His-Tyr axial ligation [112]. Previous studies indicated that replacement of this tyrosine residue with histidine to generate a His-His ligated heme abolished TTQ biosynthesis and the ability to stabilize the *bis*-Fe(IV) state. To further probe the role of the distal axial ligand of the hexacoordinated heme of MauG, a Y294K variant was created. The EPR spectrum of di-ferric Y294K MauG shows only the presence of high-spin heme, consistent with the loss of the distal heme ligand of the native hexacoordinated low-spin heme, which results in an enzyme with two pentacoordinated hemes.

The properties of Y294K MauG are more similar to those of Y294H MauG than to those of WT MauG. The changes in the two E_m values caused by the Y294K mutation are similar to those caused by the Y294H mutation in that one E_m value increased and the other decreased. The redox cooperativity of the hemes remains intact as the mutation of the ligand of one heme affects both E_m values. However, the magnitude of the changes was much less in Y294K MauG (Table 4.4.2). The fact that the His-Tyr ligated heme in WT MauG is in a low-spin state rather than high-spin suggests that Tyr294 coordinates to the heme iron as a tyrosinate [237]. X-ray absorption and computational studies also indicate that the Tyr294 ligand in WT MauG is deprotonated in all redox states [124]. Thus, it seems reasonable the loss of that ligand or replacement of the ligand with His increases the E_m value for the first electron reduction by +83

mV for Y294K MauG and +141 mV for Y294H MauG (Table 4.4.2). It is not obvious why the E_m value for the second electron reduction instead is decreased relative to WT MauG. The basis for this phenomenon requires further study.

The most significant similarity to Y294H MauG is that Y294K MauG also forms a high-valence compound I-like species rather than the *bis*-Fe(IV) species upon reaction with peroxide. This renders both variants incapable of TTQ biosynthesis, in contrast to WT MauG which forms the *bis*-Fe(IV) species. Like Y294H MauG, Y294K MauG is competent in the ET reaction from di-ferrous MauG to quinone MADH, which does not require formation of the *bis*-Fe(IV) species. This confirms that the mutation has not affected binding between the proteins or the ET pathway that connects the redox centers, but rather the ability of the second heme to stabilize Fe(IV). The similar effects of either replacing the Tyr294 distal heme ligand with His, or the total loss of that ligand as in Y294K MauG, indicate that the changes in spectroscopic properties and inability to stabilize the *bis*-Fe(IV) state are attributable primarily to the absence of tyrosine as a heme ligand and that its replacement with an alternative ligand cannot compensate for the loss of tyrosine. Furthermore, even though this heme in Y294K MauG lacks a distal ligand, the heme iron is apparently not accessible to H_2O_2. This highlights the functional role of this heme in electron transport rather than in binding exogenous ligands.

5 ELECTRON HOPPING VIA TRP199 IS REQUIRED FOR MAUG-DEPENDENT TRYPTOPHAN TRYPTOPHYLQUINONE BIOSYNTHESIS

(This chapter is modified from a research article that JG coauthored: Abu Tarboush N, Jensen LMR, Yukl ET, Geng J, Liu A, Wilmot CM, and Davidson, VL (2011) Mutagenesis of tryptophan199 suggests that electron hopping is required for MauG-dependent tryptophan tryptophylquinone biosynthesis. ***Proc. Natl. Acad. Sci. U.S.A.***, 108(41), 16956-16961.)

5.1 Abstract

The di-heme enzyme MauG catalyzes posttranslational modifications of the precursor protein of MADH, preMADH, to complete the biosynthesis of its protein-derived TTQ cofactor. Catalysis proceeds through a high-valence *bis*-Fe(IV) redox state and requires long-range ET, as the distance between the modified residues of preMADH and the nearest heme iron of MauG is 19.4 Å. Trp199 of MauG resides at the MauG-preMADH interface, positioned midway between the residues which are modified and the nearest heme, *i.e.*, the hexacoordinated heme. W199F and W199K mutations did not affect the spectroscopic and redox properties of MauG, or its ability to stabilize the *bis*-Fe(IV) state. Crystal structures of complexes of W199F/K MauG with preMADH showed no significant perturbation of the MauG-preMADH structure or protein interface. However, neither MauG variant was able to synthesize TTQ from preMADH. In contrast, an ET reaction from di-ferrous MauG to quinone MADH, which does not require the *bis*-Fe(IV) intermediate, was minimally affected by the W199F/K mutations. W199F/K MauGs were able to oxidize quinol MADH to form TTQ, the putative final two-electron oxidation of the biosynthetic process, but with k_{cat}/K_m values approximately 10% that of WT MauG. The differential effects of the W199F/K mutations on these three different reactions reveal a critical role for Trp199 in mediating multistep hopping from preMADH to *bis*-Fe(IV) MauG during the long-range ET that is required for TTQ biosynthesis.

5.2 Introduction

Long-range ET through proteins is required for biological processes including respiration, photosynthesis, and metabolism. Mechanisms by which ET occurs over large distances to specific sites within a protein have been extensively studied [238-241]. For interprotein ET, kinetic mechanisms are more complex, as the overall redox reaction requires additional steps such as protein-protein association and reorientation of the protein complex to optimize the system for ET [242,243]. "Long-range catalysis" is a related process in which the redox center that provides the oxidizing or reducing power is physically distinct from the site of chemical reaction of the substrate, so that long-range ET is required for catalysis. Thus far two enzymes have been postulated to employ long-range catalysis. RNR catalyzes the formation of deoxyribonucleotides from ribonucleotides by long-range ET via multiple tyrosyl residues [100,244]. DNA photolyase is a flavoprotein that catalyzes DNA repair of pyrimidine-pyrimidine dimers via multiple tryptophan residues [245]. In these enzymes it is believed that the long-range ET proceeds by hopping through residues that can stabilize a radical state [246], rather than via a single long-range electron tunneling event.

The crystal structure of the MauG-preMADH complex [112] revealed that βTrp57 and βTrp108 do not make direct contact with either heme of MauG (Figure. 1.4.1). The distance between the side chain of βTrp108 of preMADH and the iron of the H_2O_2-binding pentacoordinated heme is 40.1 Å, and the closest distance to the iron of the hexacoordinated heme is 19.4 Å. Nonetheless, the addition of H_2O_2 to MauG-preMADH crystals causes synthesis of the TTQ cofactor, demonstrating that the crystallized complex is catalytically active. Trp199 of MauG resides on the protein surface at the site of interaction with preMADH and is positioned midway between βTrp108 and the nearest heme of MauG (8.0 Å to the hexacoordinated heme

and 6.5 Å to the preTTQ site). Tryptophan side chains have been implicated in electron/radical transfer in DNA photolyase [245] and in heme proteins [247-252]. However, the role of tryptophan in mediating hopping during long-range ET requires further elucidation.

In this study, Trp199 of MauG was converted to Phe and Lys by site-directed mutagenesis to determine its role in the MauG-dependent catalysis. The structures of the W199F/K-preMADH complexes were determined and the effect of each mutation was assessed on three different ET reactions (Figure. 5.2.1): preMADH to *bis*-Fe(IV) MauG, quinol MADH to *bis*-Fe(IV) MauG, and di-ferrous MauG to quinone MADH. The results are explained by a critical role for Trp199 in mediating hopping during ET from preMADH to *bis*-Fe(IV) MauG which is required for TTQ biosynthesis.

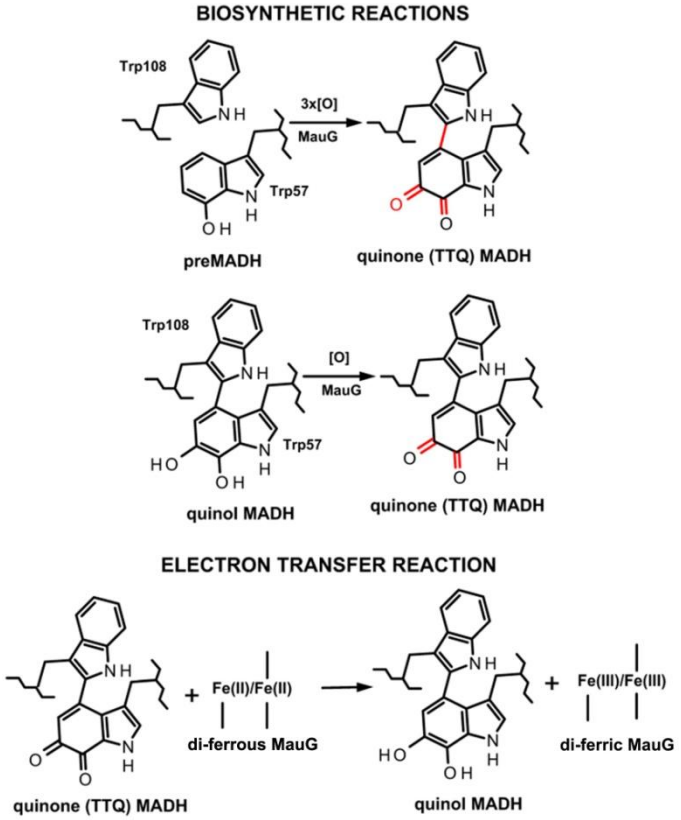

Figure 5.2.1 Reactions of MauG with different forms of MADH and preMADH. The six-electron oxidation of preMADH to form TTQ (top), the two-electron oxidation of quinol MADH to form TTQ

(middle), the non-biosynthetic thermodynamically favorable ET reaction from TTQ to di-ferrous MauG (bottom).

5.3 Materials and methods

5.3.1 Protein expression and purification

Recombinant MauG [12] and MADH [227] were purified from *P. denitrificans* as described previously. PreMADH [13] was expressed in *R. sphaeroides* and purified as described previously [253]. Trp199 of MauG was converted to Lys and Phe by site-directed mutagenesis of double-stranded pMEG391 [12], which contains *mau*G, using the QuikChange kit (Strategene). W199F/K MauGs were expressed in *P. denitrificans* and isolated from the periplasmic fraction as described for recombinant WT MauG.

5.3.2 MS analysis

WT and W199F/K MauGs, and samples from reaction mixtures of these proteins with preMADH and H_2O_2, were subjected to MS analysis. The latter reactions were performed in 10 mM potassium phosphate containing 100 μM preMADH, 10 μM WT or W199F/K MauG, initiated by the addition of 1 mM H_2O_2 and incubated for 10 min. Samples were diluted in 0.1% formic acid and desalted using C4 resin ZipTip® pipet tips (Millipore). Data were acquired on a QSTAR XL (AB Sciex) quadrupole time-of-flight (TOF) mass spectrometer with the IonSpray electrospray source. Samples were manually injected into a 10 μl sample loop plumbed into the divert/inject valve of the instrument. Samples were infused at a flow rate of 10 μl/minute with 50:50, acetonitrile:water, 0.1% formic acid. The IonSpray voltage was 4700 volts. The TOF region acceleration voltage was 4 kV and the injection pulse repetition rate was 4.9 kHz. The monoisotopic peaks of human renin substrate tetra-decapeptide from Sigma-Alrdich (St. Louis, MO) were used for external calibration ($[M + 3H]^{3+}$ at 586.9830 and $[M + 2H]^{2+}$ at 879.9705). TOF MS spectra were acquired from 700–2200 *m/z* for approximately five min with a one-sec

accumulation time. The acquisition software was Analyst™ QS v1.0 (AB Sciex). The Bayesian protein reconstruct tool in BioAnalyst™ extensions v1.1 (AB Sciex) was used for multiple charge state data deconvolution of the intact proteins.

5.3.3 Redox titrations

E_m values of W199F/K MauGs were determined by anaerobic spectrochemical titrations, as described previously for WT MauG [114]. Data were fit using Eq. 1, which describes the redox behavior of a system with two redox-active centers, where *a* is the fraction of the total absorbance change attributable to one center and (1 – *a*) is the fraction of the total absorbance change attributable to the other.

$$\text{Fraction reduced} = a/[1 + 10^{((E\text{-}E\text{m}1)/0.059\text{V})}] + (1 - a)/[1 + 10^{((E\text{-}E\text{m}2)/0.059\text{V})}] \quad \text{Eq. 1}$$

5.3.4 Steady-state spectrophotometric kinetic assays

W199F/K MauGs were tested in previously described steady-state assays of TTQ biosynthesis from preMADH [111] and from quinol MADH [108]. Each assay was performed in 0.01 M potassium phosphate buffer, pH 7.5 at 25 °C. The rate of appearance of TTQ (quinone) MADH was monitored by the increase in ΔA_{440} and the data were fit by Eq. 2.

$$v/E = k_{cat}[S]/([S] + K_m) \quad \text{Eq. 2}$$

5.3.5 Single-turnover kinetic studies

Two different reactions were studied. The dependence of the observed rate constant (k_{obs}) on the concentration of the varied reactant was analyzed using a two-step kinetic model (Eq. 3) fit to either Eq. 4 for a hyperbolic concentration dependence or Eq. 5 for a linear concentration dependence. Each reaction was performed in the 10 mM potassium phosphate buffer, pH 7.5 at 25 °C. In one reaction, varied concentrations of quinol MADH were mixed with 2 µM *bis*-Fe(IV) MauG that had been generated by the stoichiometric addition of H_2O_2 [228]. Reactions were

monitored from 366–446 nm to observe the conversion of *bis*-Fe(IV) MauG (E) to di-ferric MauG (E'). In the other reaction, varied concentrations of quinone MADH were mixed with 1.25 μM di-ferrous MauG under anaerobic conditions. The reaction was monitored by the decrease in A_{550} which corresponds to the conversion of di-ferrous MauG (E) to di-ferric MauG (E').

$$E + S \underset{k_2}{\overset{k_1}{\rightleftharpoons}} ES \underset{k_4}{\overset{k_3}{\rightleftharpoons}} E'P \qquad \text{Eq. 3}$$

$$k_{obs} = k_3[S]/([S] + K_d) + k_4 \qquad \text{Eq. 4}$$

$$k_{obs} = k_1[S] + [k_2k_4/(k_3 + k_4)] \qquad \text{Eq. 5}$$

5.3.6 EPR spectroscopy

EPR samples were prepared in 50 mM potassium phosphate buffer, pH 7.4, with 150 μM WT or W199F/K MauG. For the H_2O_2-treated samples, stoichiometric H_2O_2 was added to the enzyme in a stirred reaction vial at room temperature and the reaction mixtures were immediately transferred to quartz EPR tubes and frozen in liquid nitrogen. The total reaction time was 30–40 s. Continuous wave X-band EPR spectra were taken by a Bruker E200 spectrometer at 100-kHz modulation frequency using a dual mode resonator. Temperature was maintained at 10 K with an ESR910 liquid helium cryostat and an ITC503 temperature controller.

5.3.7 Crystallization and X-ray structure determinations of the W199F/K MauG-preMADH complexes

W199F/K MauGs were each co-crystallized with preMADH from a solution containing 100 μM W199F/K MauG and 50 μM preMADH. A 2:1 ratio of W199X MauG/preMADH was used as this corresponds to the observed ratio in the molecular complex of WT MauG-preMADH. The W199X MauG-preMADH complexes crystallized through optimization of the conditions previously established for WT MauG-preMADH by hanging drop vapor diffusion in

VDX plates (Hampton Research). Single crystals suitable for X-ray data collection were obtained from drops assembled with 1 μL protein solution layered with 3 μL (W199F) or 2.5 μL (W199K) reservoir solution over a 22% w/v PEG 8000, 100 mM sodium acetate, 100 mM MES, pH 6.4 reservoir. Crystals were cryoprotected as described previously through the inclusion of 10% PEG 400 [112]. X-ray diffraction data were collected at GM/CA-CAT beamline 23-ID-D of the Advanced Photon Source, Argonne National Laboratory, Argonne, IL. Data were collected for 360º at 100 K using either the full beam (~140 × 40 μm) for crystals of W199K or else matching the beam size to the dimensions of the largest crystal face (90 × 60 μm) for W199K. The diffraction data were essentially isomorphous with the data obtained from WT MauG-preMADH crystals, and are in the space group *P*1 with one complex (two W199X MauG bound to one preMADH) in one asymmetric unit. The data were processed with HKL2000.

The structure solutions were obtained by difference Fourier. Refinement was carried out using REFMAC in the CCP4 program suite and model-building was carried out in COOT. The initial model used the coordinates of WT MauG-preMADH (PDB entry 3L4M) retaining only the protein and solvent components and with residue 199 of MauG truncated to Ala. Restrained refinement with TLS was carried out using no distance restraints between the heme iron centers and their ligands. Residue 199 of each MauG mutant was well-ordered, and added to the model based on the $2F_o$-F_c and F_o-F_c electron density maps. Refinement was assessed as complete when the F_o-F_c electron density contained only noise.

5.3.8 ET rate prediction

The HARLEM program [254] was used to calculate relative values of H_{AB} from the crystal structures of WT and W199F/K MauG-preMADH complexes using the direct distance approach of Dutton and coworkers [238].

5.4 Results

5.4.1 Expression of MauG mutant proteins

W199F/K MauGs were expressed with a yield of protein of 0.8–1.2 mg/L of culture. MS analysis confirmed the expected mass differences relative to WT MauG.

5.4.2 Spectroscopic and redox properties of W199F/K mutants

The absorption spectra of each mutant were essentially identical to those of WT MauG (Figure 5.4.1). The di-ferric forms exhibited a Soret peak at 406 nm. In the di-ferrous forms, the Soret peak shifts to 418 nm and α and β bands appear at 552 and 524 nm, respectively. A shoulder in the Soret peak of each di-ferrous W199F/K MauG is present at 427 nm, which was previously noted for WT MauG [114]. EPR spectra of di-ferric W199F/K MauGs exhibit high-spin and low-spin heme signals that are very similar to those of WT MauG [12] (Figure 5.4.2). MauG exhibits two E_m values for the interconversion between di-ferric and di-ferrous states, which correspond to the sequential addition or removal of one electron from the di-heme system. The E_m values of W199F/K MauGs are the same as those for WT MauG (Table 5.4.1).

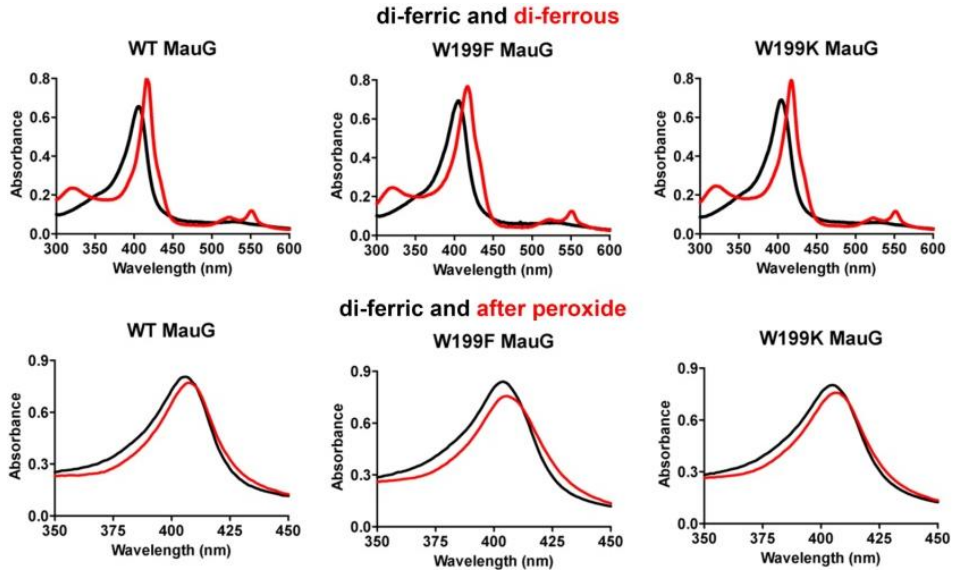

Figure 5.4.1 Absorption spectra of different redox states of WT and W199F/K MauGs. The top panels compare the spectra of di-ferric (black) and di-ferrous (red) forms of the proteins. The di-ferrous forms

were prepared by anaerobic titration with sodium dithionite. The bottom panels compare the spectra of the di-ferric proteins before (black) and after (red) addition of H_2O_2 which forms the *bis*-Fe(IV) redox state.

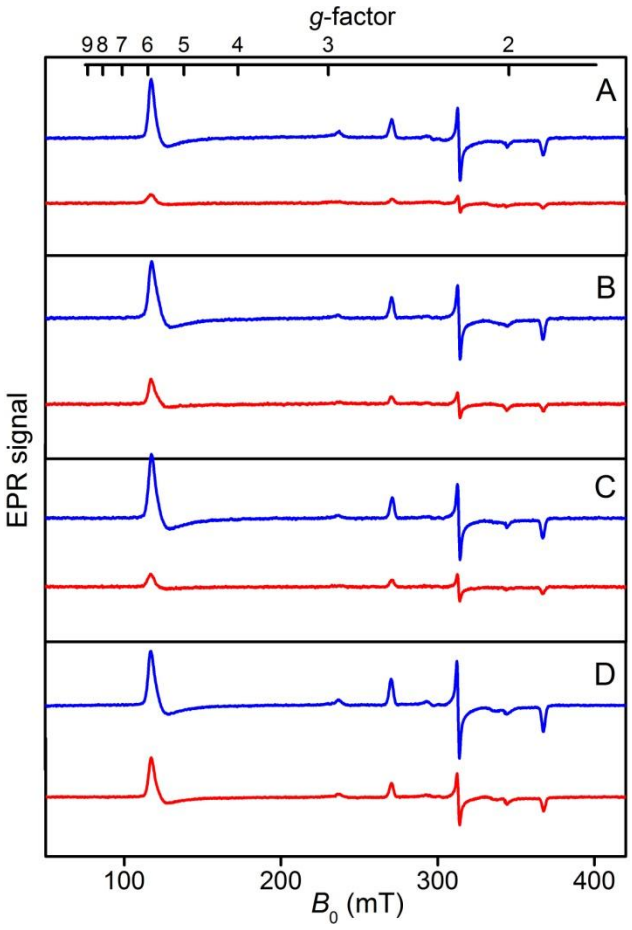

Figure 5.4.2 EPR spectra of WT MauG (A), W199F MauG (B), and W199K MauG. Spectra of each were recorded before (blue) and after (red) the addition of one eq. of H_2O_2. EPR parameters for obtaining the spectra are as follows: temperature, 10 K; microwave, 1 mW at 9.44 GHz; modulation amplitude, 0.5 mT.

Table 5.4.1 Effects of W199F/K mutations on the reactivity of MauG

	WT MauG[a]	W199F MauG	W199K MauG
Redox potentials			
E_{m1} (mV) E_{m2} (mV)	-158 ± 9 -246 ± 3	-145 ± 3 -237 ± 5	-144 ± 5 -253 ± 5
Steady-state TTQ formation from preMADH			
k_{cat} (s^{-1})	0.2	NR[b]	NR
K_m (μM)	6.6	NR	NR

Oxidation of preMADH by *bis*-Fe(IV) MauG			
k (s^{-1})	0.8 ± 0.1	NR	NR
K_d (μM)	< 1.5	NR	NR
Steady-state TTQ formation from quinol MADH			
k_{cat} (s^{-1})	4.1 ± 0.2	0.55 ± 0.04	0.37 ± 0.02
K_m (μM)	11.1 ± 1.3	25.6 ± 3.1	12.5 ± 1.3
$k_{cat}/K_m \times 10^5$ ($M^{-1}s^{-1}$)	3.7 ± 0.5	0.22 ± 0.03	0.29 ± 0.03
Oxidation of quinol MADH by *bis*-Fe(IV) MauG[c]			
k (s^{-1})	20 ± 1.3	-	-
K_d (μM)	11.2 ± 2.3	-	-
$K_1 \times 10^5$ ($M^{-1}s^{-1}$)	-	0.17 ± 0.01	0.23 ± 0.01
Oxidation of di-ferrous MauG by quinone MADH			
k (s^{-1})	0.07 ± 0.01	0.03 ± 0.01	0.03 ±0.01
K_d (μM)	10.6 ± 1.6	6.4 ± 2.4	6.0 ± 2.6

[a] The results for WT MauG were taken from reference [111,228,232].

[b] NR indicates no detectable reaction.

[c] The data for WT MauG were fit to Eq. 4 and for W199F/K MauG to Eq. 5.

5.4.3 X-ray crystal structures of W199F/K MauG-preMADH complexes

W199F/K MauGs were each co-crystallized with preMADH and the structures solved to resolutions of 1.74 and 2.08 Å, respectively. For the W199K MauG-preMADH complex, the data to 1.93 Å was used in refinement, but due to the lower completeness in the higher resolution shell (46.6%), the structure is reported to 2.08 Å resolution (completeness in 2.12 Å to 2.08 Å, 84.4%). Data collection and refinement statistics are given in Table 5.4.2. Each W199F/K MauG-preMADH complex has the same overall structure as that of WT MauG-preMADH (PDB entry 3L4M), with two crystallographically independent copies of W199F/K MauG in an asymmetric unit. Each structure is superimposable with WT MauG-preMADH within coordinate error (RMSD values on C_α positions in the range of 0.20–0.32 Å). The

positions of the nascent TTQ site, the Ca^{2+} ion, both hemes, and the intervening Trp93 residue are preserved in the W199F/K MauGs relative to the WT MauG structure.

Table 5.4.2 X-ray crystallography data collection and refinement statistics for the W199F/K mutants[a]

	W199F MauG-preMADH	**W199K MauG-preMADH**
Data collection		
Detector type	MAR*mosaic* 4×4 tiled CCD	MAR*mosaic* 4×4 tiled CCD
Source	APS, Sector 23	APS, Sector 23
Space group	*P*1	*P*1
Unit cell lengths (Å)[b]	55.53 × 83.52 × 107.78	55.53 × 83.52 × 107.78
Unit cell angles (°)[b]	109.94, 91.54, 105.78	109.94, 91.54, 105.78
Wavelength (Å)	1.03315	1.03315
Resolution (Å)	50.00–1.74 (1.77–1.74)	50.00–1.93 (2.12–2.08) [1.96–1.93][c]
Measured reflections	658,736	413,823
Unique reflections	173,890	116,940
Completeness (%)	96.4 (82.7)	88.8 (84.4) [46.6][c]
R_{merge} (%)[d]	6.4 (35.5)	8.5 (30.9) [42.0][c]
$I/\sigma I$	18.3 (2.8)	12.2 (3.2) [2.0][c]
Multiplicity	3.8 (2.8)	3.5 (3.0) [2.5][c]
Refinement		
Resolution (Å)	39.58–1.72 (1.77–1.72)	39.58–1.91 (1.96–1.91)
No. reflections; working/test	156,301/8,789	105,184/5,868
R_{work} (%)[e]	13.8	17.3
R_{free} (%)[f]	18.1	23.0
Protein atoms	13,458	13,255
Ligand atoms	241	222
Solvent sites	1,876	1,180
Ramachandran statistics[g]		
Allowed (%)	99.22	99.05

Outliers (%)	0.78	0.95
Root mean square deviation		
Bond lengths (Å)	0.027	0.024
Bond angles (°)	2.308	2.178
Average *B* factor (Å^2)	20.26	33.99
ESU (Å)[h]; R_{work}/R_{free}	0.096/0.099	0.186/0.170
PDB code	3RMZ	3RN0

[a] Values in parentheses are for the highest resolution shell.

[b] The cell constants for the native W199X MauG-preMADH structures were isomorphous with WT MauG-preMADH, and therefore set to those of PDB entry 3L4M.

[c] Values for the highest resolution shell with > 80% completeness are given in parentheses, and followed by values in square brackets for the highest resolution shell included in refinement.

[d] $R_{merge} = \Sigma_i |I_{hkl,i} - \langle I_{hkl} \rangle| / \Sigma_{hkl} \Sigma_i I_{hkl,i}$, where I is the observed intensity and $\langle I_{hkl} \rangle$ is the average intensity of multiple measurements.

[e] $R_{work} = \Sigma||F_o|-|F_c|| / \Sigma|F_o|$, where $|F_o|$ is the observed structure factor amplitude, and $|F_c|$ is the calculated structure factor amplitude.

[f] R_{free} is the R factor based on 5% of the data excluded from refinement.

[g] Based on values attained from refinement validation options in COOT

[h] Estimated standard uncertainties generated for R_{work} and R_{free} in Refmac5.5 in the CCP4i suite.

The positions of Phe199 and Lys199 in the MauG mutants at the interface with preMADH are essentially the same as that of the native Trp199 (Figure 5.4.3). βGlu101 of preMADH is the only residue that shows a change in the two mutant structures (Figure 5.4.4). In the WT structures, the βGlu101 side chain is directed toward the MauG residue 199 and forms a long H-bond with the indole nitrogen of Trp199 in the WT MauG-preMADH structure (Figure 5.4.4_A). In the W199K MauG-preMADH structure, the terminal N of Lys199 is H-bonded with a water molecule that has the same position in the WT MauG-preMADH structure (Figure 5.4.4_C). In the W199F MauG-preMADH structure the βGlu101 side chain is rotated so that the carboxylate head group points away from

Phe199 and H-bonds to the preMADH side chains of αArg197 and βArg99 (Figure 5.4.4_B). This appears due to steric reasons, as one of the Phe199 aromatic carbons is almost coincident with the H-bonding indole N of Trp199 in WT MauG. The rotation of βGlu101 places the closest preMADH β-subunit atom over 6 Å from any atom of Phe199. The protein interface has an unusually large number of solvent molecules that mediate interactions between MauG and preMADH, including around the Trp199 side chain which only directly contacts preMADH is through the side chain of βGlu101. This explains the minimal perturbations to the MauG-preMADH interface, as it is the water structure that primarily changes to accommodate the different side residue 199 chains.

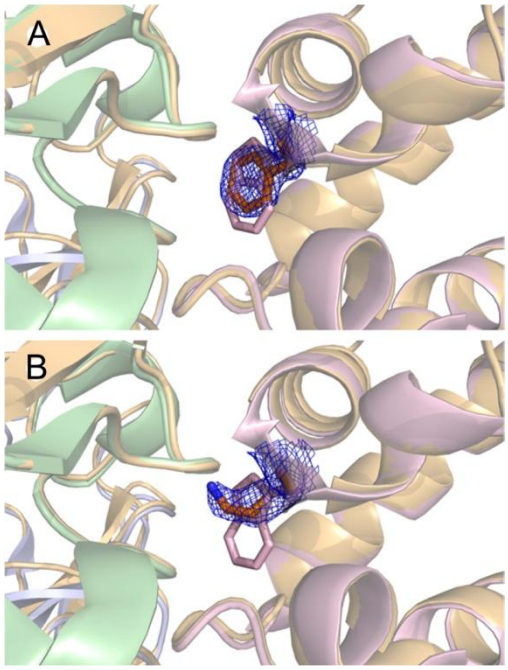

Figure 5.4.3 Overlay of the interface regions of complexes of W199F MauG-preMADH (A) and W199K MauG-preMADH (B) with WT MauG-preMADH. Coordinates of the Trp/Phe/Lys199 side chains are shown as sticks, with the $2F_o–F_c$ electron density for the Phe/Lys199 side chains in blue mesh (contour levels 1.5 σ (W199F) and 1.0 σ (W199K)). The surrounding protein is shown as gold cartoon and the WT MauG-preMADH coordinates are overlaid as cartoon (MauG: pink; β-preMADH: green; and α-preMADH: blue).

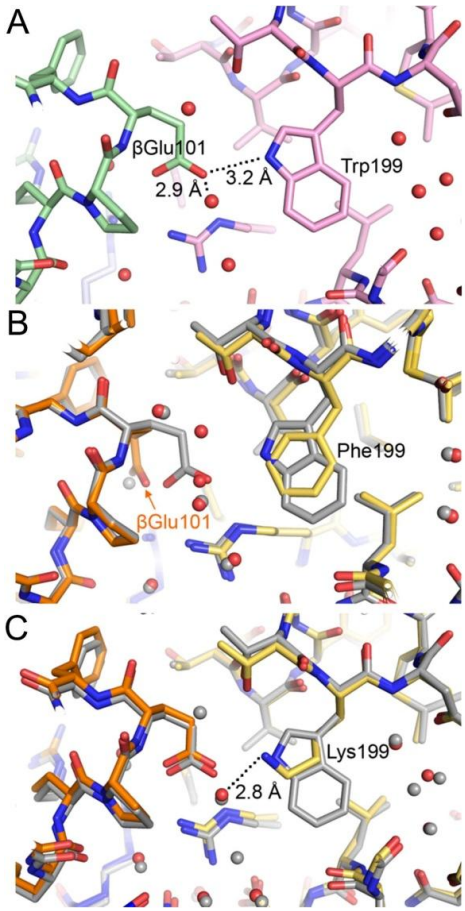

Figure 5.4.4 Interface structure of the MauG-preMADH complex near residue 199. (A) H-bonding network in the WT MauG-preMADH structure (PDB entry 3L4M) involving Trp199 and βGlu101 of preMADH (WT MauG, pink; β-preMADH, green; α-preMADH, blue). Overlays of 3L4M with the W199F MauG-preMADH coordinates (B) and the W199K MauG-preMADH coordinates (C) are also shown (W199F/K MauG, yellow; β-preMADH, orange; α-preMADH, blue; WT MauG-preMADH, gray).

5.4.4 Effects of Trp199 mutations on the formation of the bis-Fe(IV) intermediate and its reactivity towards preMADH

EPR and Mössbauer spectroscopy studies previously showed that reaction of di-ferric MauG with H_2O_2 resulted in formation of a *bis*-Fe(IV) redox state [109]. The formation of the *bis*-Fe(IV) species is accompanied by a decrease in intensity and shift of the Soret peak from 406 nm to 408 nm in the absorption spectrum of MauG, and a decrease in the intensity of the di-ferric heme signals in the EPR spectrum [109,232]. These spectral changes were also observed upon

reaction of each di-ferric W199F/K MauG with H_2O_2 (Figure 5.4.1 and 5.4.2). WT and W199F/K *bis*-Fe(IV) MauGs spontaneously decay to the di-ferric state over minutes as gauged by the return to the resting-state spectra. Whereas the addition of preMADH to WT *bis*-Fe(IV) MauG increased the rate of return to the di-ferric state to 0.8 s^{-1} with a K_d value < 1.5 μM [232], the addition of up to 20 μM preMADH to W199F/K MauGs did not increase the rate of return to the di-ferric state indicating that *bis*-Fe(IV) W199F/K MauGs were unable to oxidize preMADH.

The reactivity of W199F/K MauGs was also examined using a steady-state assay for TTQ biosynthesis using preMADH as the substrate [232]. Whereas WT MauG exhibited a k_{cat} value of 0.2 s^{-1} and K_m value of 6.6 μM for preMADH, no detectable TTQ biosynthesis was observed in this assay with W199F/K MauGs, using up to 20 μM preMADH as the substrate (Table 5.4.1). The MS analysis of the reaction mixture confirmed that no chemical alterations of preMADH had occurred (data not shown). The reactivity of W199F MauG was also examined *in crystallo*. Whereas incubation of WT MauG-preMADH crystals with 2.0 mM H_2O_2 for 2 min leads to generation of TTQ [112], similar treatment of a W199F MauG-preMADH crystal caused no changes at the preTTQ site. These results demonstrate that, while W199F/K MauGs can attain and stabilize the *bis*-Fe(IV) state, they cannot catalyze the initial two-electron oxidation of preMADH either in solution or in complex with preMADH *in crystallo*.

6-Hydroxyindole reacts with *bis*-Fe(IV) MauG [255] with a rate of 5 s^{-1} and a K_d value of 2.5 mM. As this rate is faster than that with preMADH (0.8 s^{-1}) and the K_d much greater than that for preMADH (< 1.5 μM), it was concluded that 6-hydoxyindole react directly with the ferryl heme rather than bind to the same site as preMADH. While W199F/K *bis*-Fe(IV) MauGs did not react with preMADH, the addition of 3 mM 6-hydroxyindole did cause rapid return to the di-ferric state. These results establish that the lack of reactivity of W199F/K MauGs with

preMADH is not due to a change in heme reactivity but to a specific disruption of the long-range catalysis.

5.4.5 Effects of Trp199 mutations on the reactivity of the bis-Fe(IV) intermediate towards quinol MADH

It was postulated that the final step of the MauG-dependent TTQ biosynthesis is the oxidation of quinol MADH to the TTQ quinone. Transient formation of the quinol was observed in the steady-state reactions, and *bis*-Fe(IV) WT MauG can oxidize quinol MADH [108]. The steady-state kinetic parameters using WT MauG are K_m of 11.1 μM and k_{cat} of 4.2 s^{-1} [228]. W199F/K MauGs were able to catalyze this reaction (Figure 5.4.5_A, Table 5.4.1), but much less efficiently than WT MauG. The k_{cat}/K_m values for W199F/K MauGs decreased by *ca.* 90%. These data indicate that, whereas Trp199 is essential for the initial two-electron oxidation of preMADH, it is important, but not essential, for the two-electron oxidation of quinol to quinone.

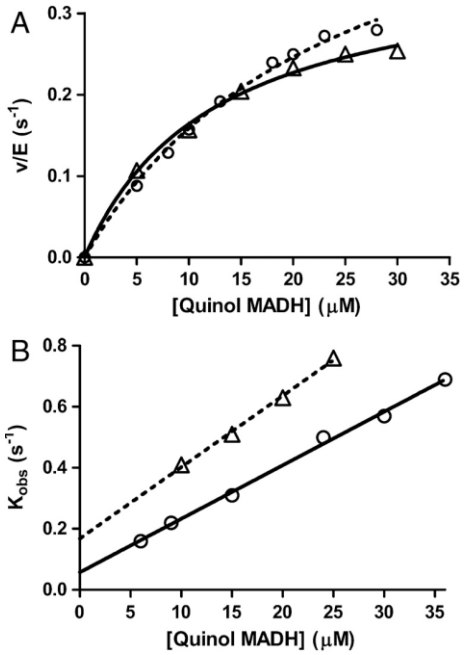

Figure 5.4.5 Reactions between W199F/K MauGs with quinol MADH. (A) Steady-state kinetic analysis of the oxidation of quinol MADH by W199F (○) and W199K (Δ) MauG. The lines are fits of the data to

Eq. 2. (B) Single-turnover kinetics of the reaction of quinol MADH with *bis*-Fe(IV) W199F (○) and W199K (Δ) MauG. The lines are fits of the data to Eq. 5.

Under single-turnover conditions the reaction of *bis*-Fe(IV) WT MauG with quinol MADH exhibits a hyperbolic dependence of k_{obs} on [quinol MADH] with a limiting first order rate constant of 20 s^{-1} and a K_d value of 11.2 μM [228]. In contrast, the reactions of the *bis*-Fe(IV) W199F/K MauGs exhibited a linear dependence of k_{obs} on [quinol MADH] (Figure 5.4.5_B). Thus, these mutations have caused the binding to quinol MADH rather than the catalytic step to be rate-limiting for the overall reaction (*i.e.*, $(k_1[S] + k_2) < k_3$). As such it was possible to determine only the bimolecular rate constant (k_1) for these reactions; 0.17 ± 0.01 ($M^{-1}s^{-1}$) × 10^5 for W199F MauG and 0.23 ± 0.01 ($M^{-1}s^{-1}$) × 10^5 for W199K MauG.

5.4.6 Analysis of the ET reaction from di-ferrous MauG to quinone MADH

While not involved in TTQ biosynthesis, a thermodynamically favorable ET reaction from di-ferrous MauG to quinone MADH, which does not require formation of the *bis*-Fe(IV) state, has been characterized [228]. In this reaction WT MauG exhibited a limiting first-order rate constant of 0.07 s^{-1} and K_d value of 10.1 μM. The results obtained for W199F/K MauGs (Figure 5.4.6 and Table 5.4.1) in this reaction were similar to those for WT MauG.

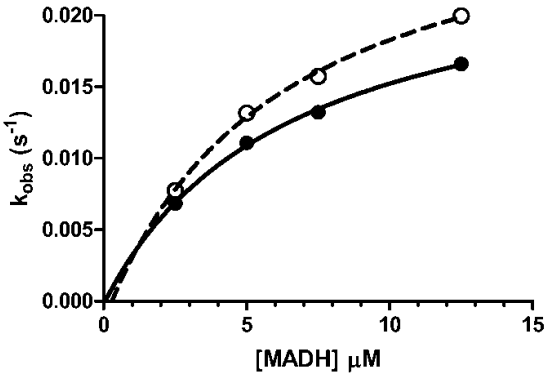

Figure 5.4.5 Single-turnover kinetics of the reaction quinone MADH with di-ferrous W199F (●) and W199K (○) MauG. The lines are fits of the data to Eq. 4.

5.4.7 ET rate prediction

When ET is rate-determining for an observed reaction, the rate will depend upon the activation energy for the reaction ($\Delta G° + \lambda$) and the electronic coupling (H_{AB}) according to Eq. 6 [256] where λ is the reorganization energy and $\Delta G°$ is determined from the ΔE_m for the redox reaction. H_{AB} is related to the ET distance and nature of the intervening medium between ET donor and acceptor. The structures of WT and W199F/K MauG-preMADH complexes were analyzed with HARLEM [254] to calculate relative values of H_{AB} for electron tunneling segments between residues β57 and β108 of preMADH, and residue 199, and the hemes of MauG (Table 5.4.3). The effects of the W199F/K mutations on H_{AB} for direct tunneling between the residues of preMADH and the nearest heme of MauG were minimal and cannot explain the lack of reactivity of W199F/K MauG towards preMADH. However, if Trp199 mediates hopping during ET, then the observed rate will be that of the slowest hopping segment (*i.e.*, the segment with the smallest H_{AB}). In WT MauG this is the segment from preMADH β57/β108 to Trp199, and hopping versus single-step tunneling leads to a 62-fold increase in the effective H_{AB}. As $k_{ET} \propto H_{AB}^2$, in the absence of any other changes, the observed k_{ET} will be *ca.* 3800-fold greater if the reaction occurs via hopping rather than direct long-range electron tunneling. If hopping could occur via Phe199 or Lys199, then a similar enhancement would be observed (Table 5.4.3) and the rate of reaction with preMADH would be similar to that of WT MauG. The undetectable reaction of W199K/F with preMADH is explained by the fact that only Trp can mediate hopping.

$$k_{ET} = [4\pi^2 H_{AB}^2/h(4\pi\lambda RT)^{0.5}] \exp[-(\Delta G° + \lambda)^2/4\lambda RT] \qquad \text{Eq. 6}$$

Table 5.4.3 Effects of W199F/K mutations on the ET reactions in the MauG-preMADH complex

Tunneling segment		Relative H_{AB}[a]		
Donor	Acceptor	WT MauG	W199F MauG	W199K MauG
Direct single-step tunneling				

preMADH β57/β108	MauG hexacoordinated heme	1.0	0.92	0.98
Steps in residue 199-mediated hopping				
preMADH β57/β108	MauG residue 199	62	49	100
MauG residue 199	MauG pentacoordinated heme	470	509	647

[a] Values of H_{AB} were determined with HARLEM using the direct distance approach. For ease of comparison all values were normalized to that for the H_{AB} value for the ET reaction from shortest distance between an atom of residues β57 or β108 of preMADH and the hexacoordinated heme of MauG.

5.5 Discussion

The differential effects of the W199F/K MauG mutations on the three different reactions are best explained by a hopping mechanism in which Trp199 is reversibly oxidized and reduced during the long-range ET that is required for TTQ biosynthesis. Two alternative mechanisms of hopping may be considered. If preMADH reduces Trp199 which in turn reduces *bis*-Fe(IV) MauG, then this would be electron hopping. If *bis*-Fe(IV) MauG oxidizes Trp199 which in turn oxidizes preMADH, then this would be hole hopping. As discussed below, the latter is the mechanism which is used for MauG-dependent TTQ biosynthesis.

The initial oxidation reaction of *bis*-Fe(IV) WT MauG with preMADH yields a preMADH-based radical intermediate which has yet to be characterized [109]. The E_m value associated with the conversion of preMADH to this radical species is not known. However, the residues of preMADH which are modified are tryptophans and E_m values for $Trp^{\bullet+}$/Trp redox couples have been determined to be in the range of 640–1080 mV [257-260]. The E_m value for the *bis*-Fe(IV)/di-ferric MauG redox couple is also unknown, but E_m values for Fe(IV)/Fe(III) couples in many heme-dependent peroxidases have been determined. These values range from 724 to 1160 mV [248] and are similar to the values for $Trp^{\bullet+}$/Trp couples. This suggests that the ΔE_m for the reaction may be close to zero. Given the low driving force and long distance for this

reaction, the loss of activity of W199F/K MauGs is likely due to disruption of Trp199-mediated electron hopping. The *bis*-Fe(IV) species is a sufficiently strong oxidant to oxidize Trp199 which in turn oxidizes preMADH. Conversely, Phe199 and Lys199 cannot be oxidized by the *bis*-Fe(IV) species. Thus, hole hopping via residue 199 cannot occur in the W199K and W199F variants, and no reaction with preMADH is observed.

In contrast to the biosynthetic reaction with preMADH, the ET reactions of di-ferrous W199F/K MauGs with quinone MADH are relatively unaffected by the mutations. This is consistent with a common mechanism for WT and W199F/K MauG in this reaction. As Phe and Lys cannot mediate hopping, this common mechanism is likely one of electron tunneling via sigma bonds, which is consistent with the crystal structures that show minimal structural impact. The E_m value of +102 mV for the quinone/quinol redox couple is not enough for quinone MADH to oxidize Trp199, as does the more potent *bis*-Fe(IV) oxidant. However, as the di-ferric/di-ferrous MauG couple is -201 mV, the overall reaction is thermodynamically favorable with a ΔE_m of 303 mV [114,139], and this supports the long-range electron tunneling. This difference in mechanism is also consistent with the previous observation that, for WT MauG [228], this favorable reaction is slower (0.07 s^{-1}) than the reaction of preMADH with *bis*-Fe(IV) MauG (0.8 s^{-1}), for which we have estimated a ΔE_m value of about zero, but which can occur via hopping.

Quinol MADH does react with W199F/K MauGs. Again, the ΔE_m value for this reaction is not known but can be estimated using the range of E_m values for the Fe(IV)/Fe(III) couple of 724–1160 mV and the known value of +102 mV for quinone/quinol MADH. This yields a ΔE_m value for the reaction of *bis*-Fe(IV) MauG with quinol MADH in the range of 622–1058 mV. This driving force is much greater than that for the reaction with preMADH and allows the reaction of quinol MADH with W199F/K MauGs to proceed via long-range electron tunneling in

the absence of Trp199-mediated hopping, albeit much less efficiently. Unfortunately it was not possible to obtain first-order rate constants for the reaction of *bis*-Fe(IV) W199F/K MauG with quinol MADH because binding was rate-limiting for the observed reaction (Figure 5.4.5). Therefore, it is not possible to directly compare the rate constant for this reaction with the rate constants for the other two.

It is noteworthy that a tryptophan residue is used by MauG as a hopping relay, as the residues on preMADH that are being oxidized are also tryptophans. Another tryptophan (Trp93 in Figure 1.4.1) is believed to mediate ET between the two hemes of MauG [112]. Using the same amino acid for different points in a multistep hopping mechanism may facilitate the reaction. The reported range of E_m values for the heme Fe(IV)/Fe(III) and $Trp^{\bullet+}$/Trp redox couples are similar and suggest that the driving force for the reaction of *bis*-Fe(IV) MauG with preMADH is very low. Thus, a hopping mechanism is required to reduce the effective ET distance. It should be noted that the rate of the slowest hopping step in the overall reaction will depend not only on distance, but also on the ΔG^o value for that hop. By using the same amino acid as staging points, the ΔG^o value for each hop will be nearly zero. If a different amino acid residue that is more difficult to oxidize is present then this would lessen the rate of hopping from that residue. Alternatively, if a residue that is more difficult to reduce is present then this would lessen the rate of hopping into that residue. The use of hopping points that are nearly iso-potential eliminates effects of ΔG^o on the rates of the hopping steps. This notion is consistent with the observations that electron hopping through RNR proceeds primarily via a sequence of tyrosine residues, and that electron hopping through DNA photolyase proceeds primarily via a sequence of tryptophan residues. The results here demonstrate that by employing a mechanism of

hopping with appropriately spaced radical sites, distance can be removed as a limiting factor in enzyme-mediated long-range catalysis, as well as long-range interprotein ET reactions.

6 TRYPTOPHAN-MEDIATED CHARGE-RESONANCE STABILIZATION IN THE *BIS*-FE(IV) REDOX STATE OF MAUG

(This chapter is modified from a research article that JG coauthored: Geng J, Dornevil K, and Liu A (2013) Tryptophan-mediated charge-resonance stabilization in the *bis*-Fe(IV) redox state of MauG. ***Proc. Natl. Acad. Sci. U.S.A.***, 110(24), 9639-9644.)

6.1 Abstract

The di-heme enzyme MauG catalyzes posttranslational modifications of a precursor protein to generate a TTQ cofactor. The MauG-catalyzed reaction proceeds via a *bis*-Fe(IV) intermediate in which one heme is present as Fe(IV)=O and the other as Fe(IV) with axial histidine and tyrosine ligation. Herein, a unique near-infrared absorption feature exhibited specifically in *bis*-Fe(IV) MauG is described, and evidence is presented that it results from a charge-resonance-transition phenomenon. As the two hemes are physically separated by 14.5 Å, a hole-hopping mechanism is proposed in which a tryptophan residue located between the hemes is reversibly oxidized and reduced to increase the effective electronic coupling element and enhance the rate of reversible ET between the hemes in *bis*-Fe(IV) MauG. Analysis of the MauG structure reveals that ET via this mechanism is rapid enough to enable a charge-resonance stabilization of the *bis*-Fe(IV) state without direct contact between the hemes. The discovery of the charge-resonance-transition phenomenon explains why the *bis*-Fe(IV) intermediate is stabilized in MauG and does not permanently oxidize its own aromatic residues.

6.2 Introduction

It has long been known that under certain conditions aromatic hydrocarbon cation radicals can interact with their parent neutral molecules in a face-to-face manner to generate non-covalent cation radical dimers, which present a unique electronic absorption band in the near-

infrared (NIR) region [261]. The NIR spectral feature is a characteristic property of resonance stabilization of the spin and charge within the dimeric complexes and therefore termed as a charge-resonance (CR) band. The CR-transition phenomenon has been studied in various organic model systems with conjugated structures [262-266]. However, it is rarely observed in biological systems. A literature review revealed only one example, *i.e.*, the radical cation of the primary electron donor P (known as the "special pair") in bacterial photosynthetic reaction centers [267,268]. Here we present evidence for a CR-transition phenomenon arising from a system consisting of two protein-bound hemes and a tryptophan residue in a di-heme enzyme, MauG.

Although the two hemes in MauG are physically separated, they share electrons efficiently [113]. Redox titrations revealed that the di-heme system exhibits redox cooperativity with the two hemes behaving as a single di-heme unit rather than as independent hemes [114]. A tryptophan residue, Trp93, is positioned midway between the hemes without direct covalent or H-bonding interactions with either heme (Figure 1.4.1). Previously, we reported the presence of a radical species detectable by the EPR spectroscopy within the same time-window as the one in which the *bis*-Fe(IV) species was observed [109]. This radical species, representing only a few percent of the oxidized protein, was proposed to be located on Trp93 [109].

Despite being a highly potent oxidant, the *bis*-Fe(IV) species displays extraordinary stability in the absence of preMADH with a half-life of several minutes [109,232], rather than permanently oxidizing its own aromatic residues, such as Trp93, Trp199, or the heme ligand Tyr294. In this study, a NIR electronic absorption feature was observed in the *bis*-Fe(IV) state of MauG. This spectral feature is characteristic of a CR-transition phenomenon. Evidence is presented that this phenomenon occurs in the absence of direct heme-heme contact by ultrafast and reversible ET between the two hemes, via hole hopping through the intervening Trp93 residue. This discovery reveals the chemical basis for the stability of the *bis*-Fe(IV) species.

6.3 Methods

6.3.1 Protein expression and purification

WT, W199F, P107V, and Y294H MauG were expressed in *Paracoccus denitrificans*. PreMADH was expressed in *Rhodobacter sphaeroides*. These proteins were purified as described previously [12,13,101,132,134].

6.3.2 Vis-NIR absorption spectroscopy

The optical spectra of MauG were recorded aerobically on a Cary 5000 UV-vis-NIR spectrophotometer at room temperature in 50 mM potassium phosphate buffer, pH 7.5. The concentration of H_2O_2 was determined from the molar absorptivity of 43.6 $M^{-1}cm^{-1}$ at 240 nm.

6.3.3 ET pathway prediction

The HARLEM program developed by Kurnikov (http://harlem.chem.cmu.edu/index.php) was used to analyze the ET pathway between the two hemes of MauG based on the crystal structure [112]. The ET parameters, including the decay constants (β) and the relative values of electronic coupling element (H_{AB}), for the single-step tunneling mechanism and the two-step Trp93-mediated hopping mechanism were calculated using the direct distance approach of Dutton and coworkers [238]. When defining redox centers, the iron-porphyrin complexes without the propionate groups of the hemes, and the indole moiety without the amino acid backbone of Trp93 were selected.

6.3.4 Hopping map construction

The MATLAB program for hopping map construction was obtained at http://www.bilrc.caltech.edu [103]. The parameters used to construct the hopping maps consist of the temperature (T), the reorganization energy (λ), the distances (r) and the decay constants (β) for the single-step tunneling pathway as well as each hopping segment. The temperature was set

as 298 K. λ was varied from 0.6 to 1.0 eV to examine its effect on the ET process. The values of *r* and β were adopted from the results of the HARLEM calculation.

6.4 Results and discussion

6.4.1 Spectroscopic signature of bis-Fe(IV) MauG in the NIR region

The NIR region of the electronic absorption spectrum of the *bis*-Fe(IV) species was not explored in previous studies [101,109,132,232]. Inspection of this region revealed that a broad band centered at 950 nm developed upon the addition of H_2O_2 to di-ferric MauG concomitant with the previously observed changes in the visible region of the spectrum (Figure 6.4.1_A). No such absorption feature in the NIR region was observed in the spectra of either di-ferric or di-ferrous MauG. Parallel experiments were performed in a D_2O-based buffer to avoid interference from H_2O, which has intense NIR absorption over 1300 nm. The peak at 950 nm was unchanged in the D_2O buffer, and no additional features were observed at longer wavelengths (Figure 6.4.1_B). The intensity of the NIR band was maximized by adding ten eq. of H_2O_2 to MauG. This ratio is consistent with the result of a recent X-ray absorption study, which reported a near complete conversion from di-ferric to *bis*-Fe(IV) MauG after the addition of ten eq. of H_2O_2 [124]. At the 10:1 ratio of [H_2O_2] to [MauG], a plot of the intensity of the NIR band against [MauG] was linear with a slope of $7.0 \pm 0.1 \times 10^3$ $M^{-1}cm^{-1}$ (Figure 6.4.1_B), equal to the molar absorptivity of the *bis*-Fe(IV) species at 950 nm, assuming complete conversion from the di-ferric state. Notably, in some synthetic Fe(IV)=O complexes, broad NIR electronic absorption bands in the range of 700–1000 nm have been observed [269]. A subsequent study revealed that these bands originate from *d-d* transitions of the high-valence iron ions [270]. Such spectral features are rarely reported in biological ferryl systems because the molar absorptivities of absorption bands caused by *d-d* transitions are very low (5–500 $M^{-1}cm^{-1}$) [271]. As the molar

absorptivity of the NIR band observed in *bis*-Fe(IV) MauG is much larger, it must have a different molecular origin.

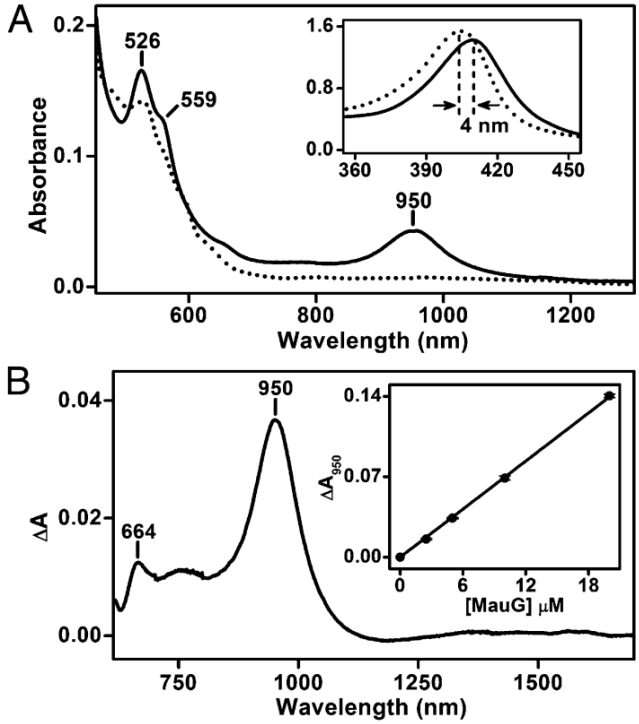

Figure 6.4.1 The *bis*-Fe(IV) state of MauG exhibits a spectral feature in the NIR region. (A) Vis-NIR spectra of MauG (5 μM) before (dotted trace) and after (solid trace) addition of ten eq. of H_2O_2. The inset shows an expanded view of the Soret region. (B) Vis-NIR difference spectrum of MauG (5 μM) obtained in D_2O-based buffer by subtracting the initial spectrum of di-ferric MauG from the one after the addition of ten eq. of H_2O_2. The inset presents the absorption change at 950 nm (ΔA950) as a function of [MauG] with the ratio of [H_2O_2] to [MauG] kept at 10:1. The solid line is the linear fit of the experimental data.

In the visible region of the spectrum, formation of *bis*-Fe(IV) MauG altered both the Soret peak and the Q-bands. The Soret peak exhibited a 4-nm red shift and decreased intensity, while the Q-bands presented two new peaks at 526 and 559 nm (Figure 6.4.1_A). These spectral changes were more pronounced with the optimized 10:1 ratio of H_2O_2 than with the stoichiometric ratio employed in prior studies [132,232], consistent with a more complete formation of the *bis*-Fe(IV) species. The absorption maxima for the newly developed Q-bands are similar to those observed in ferryl species from non-globin peroxidases, such as cytochrome

c peroxidase [272] and horseradish peroxidases [273], but are different from those reported for ferryl species from globins (540–545 and 580–590 nm) [274]. Addition of H_2O_2 also resulted in the emergence of a very minor spectral feature in the 600–700 nm region with the absorption maximum at 664 nm (Figure 6.4.1_B). An absorption peak in this region is characteristic of a compound I species [233], suggesting that a small portion of the high-valence MauG is in a compound I-like state.

It was shown previously that, although *bis*-Fe(IV) MauG is relatively stable, it can be rapidly converted to di-ferric MauG by the addition of the substrate protein, preMADH [109]. In Figure 6.4.2_A, the *bis*-Fe(IV) species was first generated by mixing di-ferric MauG with one eq. of H_2O_2, followed by mixing with one eq. of preMADH. After the second mix, the *bis*-Fe(IV) species immediately decayed to the di-ferric state as evidenced by the return of the heme Soret and Q-bands to the resting state. The simultaneous disappearance of the NIR band confirms that this signal is a spectral feature of *bis*-Fe(IV) MauG (Figure 6.4.2_A). Furthermore, in the absence of preMADH, the rate of decay of the NIR band is very similar to the rate of change in the Soret peak that correlates with the decay of the *bis*-Fe(IV) species (Figure 6.4.2_B and C).

Three structurally characterized MauG variants were also examined. Upon reaction with H_2O_2, the same NIR band was observed in W199F (Figure 6.4.2_D) and P107V MauG (Figure 6.4.2_E). Both variants were previously shown to be capable of stabilizing the *bis*-Fe(IV) species [101,134]. In contrast, the NIR spectral feature was not observed in Y294H MauG upon the addition of H_2O_2 (Figure 6.4.2_F). Tyr294 is one of the axial ligands of $Heme_{6C}$. In Y294H MauG, $Heme_{6C}$ has an axial *bis*-histidine coordination, and the *bis*-Fe(IV) intermediate is not generated [132]. Instead, this mutant stabilizes a compound I-like species with a characteristic

absorption band at 655 nm after the H_2O_2 treatment [132]. These results validate the association of the NIR spectral feature with the *bis*-Fe(IV) state rather than just any ferryl species.

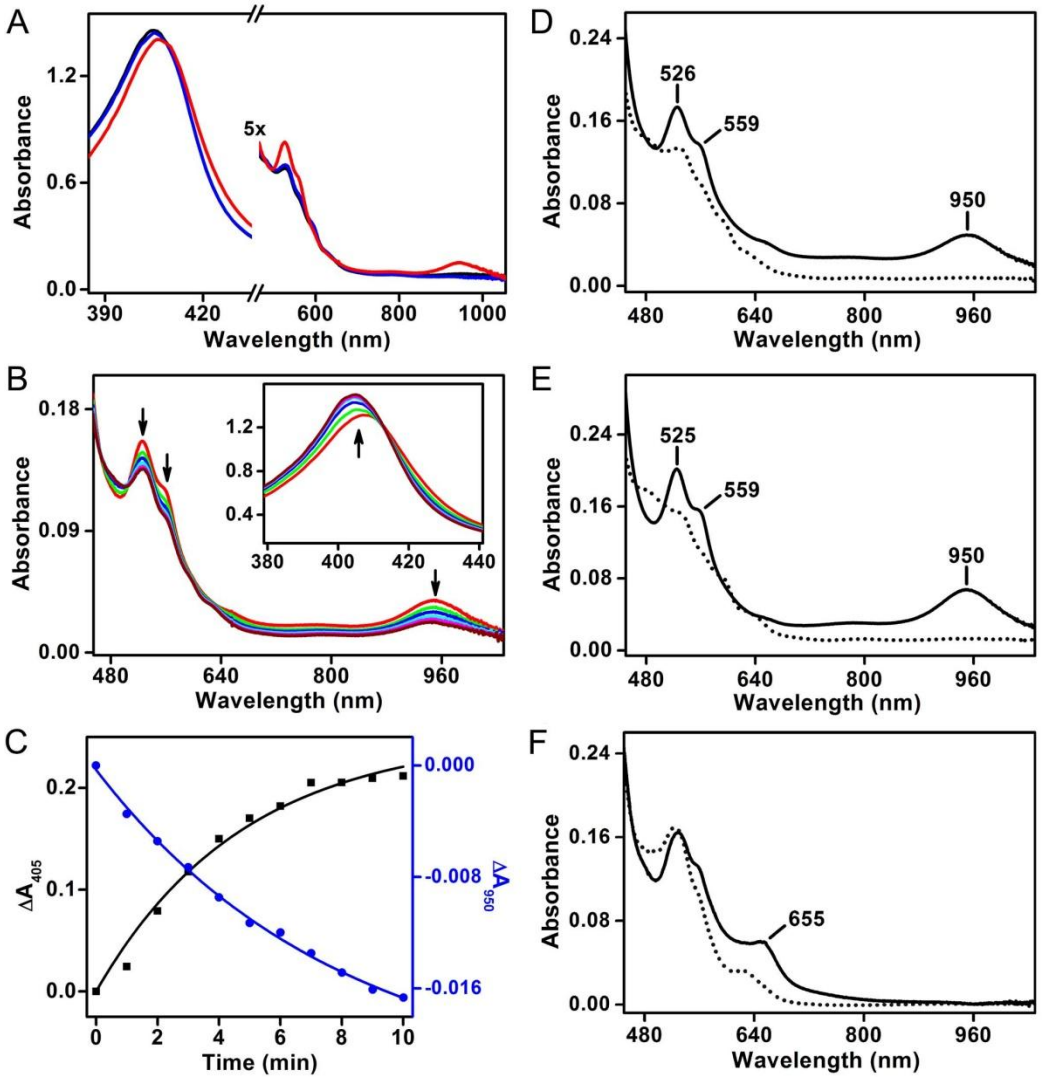

Figure 6.4.2 The NIR spectral feature is specific for the *bis*-Fe(IV) state of MauG. (A) Absorption spectra of di-ferric MauG (5 μM, black trace), after sequential mixing with one eq. of H_2O_2 (red trace) and one eq. of preMADH (blue trace). The black and blue traces are nearly identical. (B) Time-resolved spectra for the spontaneous decay of *bis*-Fe(IV) MauG in the absence of preMADH. The spectra were recorded every 2 min for 10 min after addition of ten eq. of H_2O_2 to di-ferric MauG. The inset shows an expanded view of the Soret region. The arrows indicate trends of changes in the spectra. (C) Time courses for the changes in absorbance at 405 nm (black squares) and 950 nm (blue circles) within the same time window as in (B). The solid lines represent fits of the experimental data to a single exponential rise/decay. (D) Absorption spectra of W199F before (dotted trace) and after (solid trace) addition of ten eq. of H_2O_2. (E)

Absorption spectra of P107V before (dotted trace) and after (solid trace) addition of ten eq. of H_2O_2. (F) Absorption spectra of Y294H before (dotted trace) and after (solid trace) addition of ten eq. of H_2O_2.

6.4.2 Origin of the NIR spectral feature: A model for CR stabilization of the bis-Fe(IV) redox state of MauG

A molecular orbital (MO) diagram for the CR complex of a mixed-valence cation radical $(\Pi)_2^{\bullet+}$ is shown in Figure 6.4.3_A. The CR stabilization energy (ΔE_{CR}) originates from exchange interactions between the molecular orbitals of each monomer and subsequent delocalization of the spin and charge over a greater number of atoms. The CR band ($h\upsilon_{CR}$) is typically observed in the NIR region and it is a characteristic signature of resonance stabilization of spins and charge within the CR complex. Kochi and coworkers investigated the ET process between the two monomer units in the CR systems and demonstrated that a CR transition can proceed via through-space or through-bond ET [263-265]. The former requires parallel alignment and close proximity of the monomers to allow direct interaction between their π-orbitals; the latter requires covalent linkage of the monomers by suitable bridging structures serving as an "electric wire" to efficiently shuttle the spin and charge between them. In both cases, ultrafast and reversible ET with rate constants in the range of 10^7–10^{11} s^{-1} is frequently observed and suggested to be essential for delocalization of the spin and charge within the CR complexes [263-265,275].

Resonance stabilization of the spins and charges has also been observed in the binuclear di-cation di-radical complex of $(\Pi^{\bullet+})_2$ (Figure 6.4.3_B) [264,276-281]. We term the former case with an odd number of spin/charge as Type I CR and the latter case with an even number as Type II CR. Notably, both types of CR-transition phenomena can be observed from the same system and further distinguished by the relative positions of their CR bands [264,279-281]. Despite the inherent energy penalty caused by electrostatic repulsion in the doubly charged

complex, the ΔE_{CR} value of Type II CR is usually larger than that of Type I CR from the same system, which causes a blue shift of the CR band of the $(\Pi^{\bullet+})_2$ complex compared to the $(\Pi)_2^{\bullet+}$ complex [264,279-281]. In principle, both types of CR complexes bear a close relationship to the conventional charge-transfer complexes derived from closed-shell diamagnetic precursors consisting of electron-rich donors and electron-poor acceptors. The assembly of Type II CR complexes can be considered from an alternative perspective that starts from a pair of closed-shell species such as a di-cation and its parent neutral molecule [280,282].

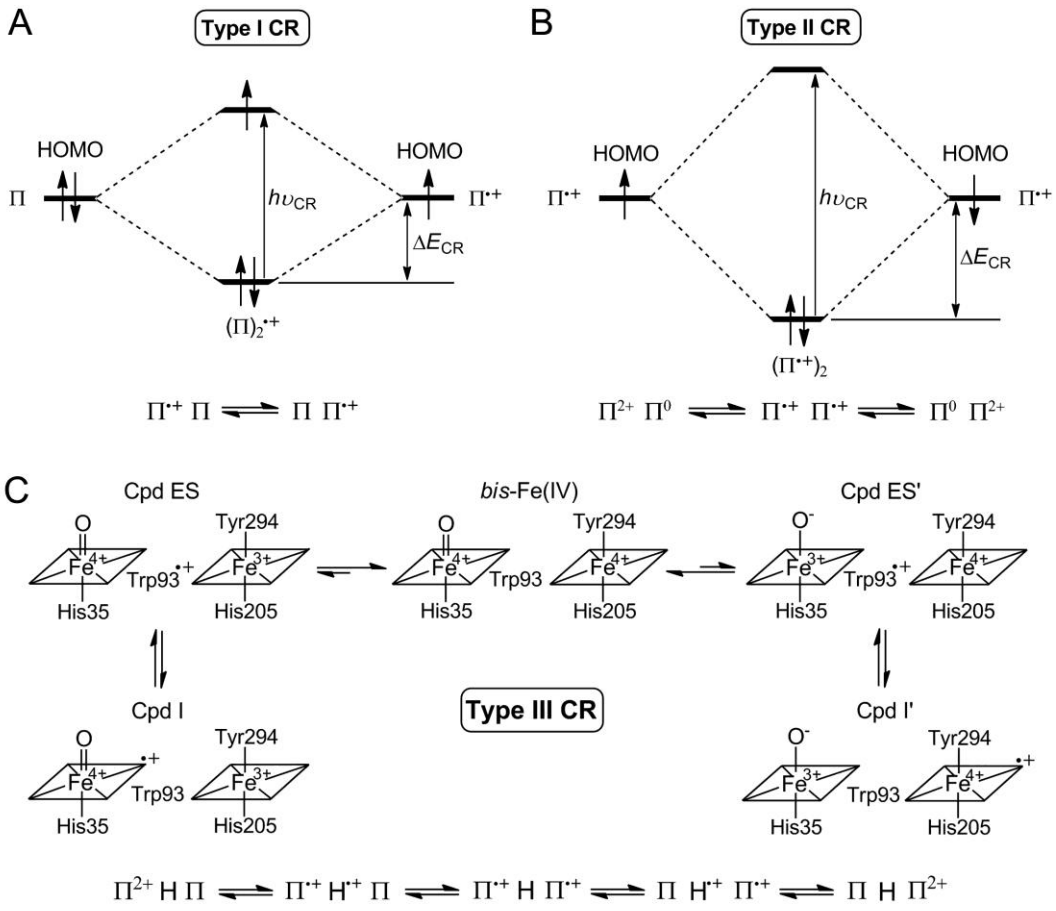

Figure 6.4.3 CR stabilization of *bis*-Fe(IV) MauG. Qualitative MO diagrams and resonance structures are described for non-covalent dimeric complexes of (A) Type I CR in the mixed-valence cation radical $(\Pi)_2^{\bullet+}$ and (B) Type II CR in the di-cation di-radical $(\Pi^{\bullet+})_2$. The origins of the CR stabilization energy (ΔE_{CR}) and CR bands ($h\upsilon_{CR}$) are illustrated. (C) Proposed resonance structures for Type III CR in the *bis*-Fe(IV) redox state of MauG. The spins and charges are delocalized throughout the di-heme system and

stabilized via a series of CR structures with "*bis*-Fe(IV)" as the dominant one. "H" represents the hopping site; "Cpd ES" represents compound ES; and "Cpd I" represents compound I.

Through one electron oxidation of zinc octaethylporphyrin, Fuhrhop and colleagues were able to generate cation porphyrin radical derivatives which self-assembled to produce dimeric complexes displaying a broad NIR absorption band centered around 950 nm [278]. Similar phenomena were reported for the radical derivatives of some other metalloporphyrins [277,279]. Subsequent crystallization studies demonstrated that the cation porphyrin radicals formed tight dimeric complexes in a face-to-face manner with an interplanar separation distance smaller than 3.5 Å [283]. The spectral characteristics and molar absorptivity of the NIR band observed in *bis*-Fe(IV) MauG are highly reminiscent of the CR bands from these metalloporphyrin complexes. In MauG, the two oxidizing equivalents derived from H_2O_2 are distributed within the di-heme system as two positive charges, giving rise to the *bis*-Fe(IV) redox state. This is electronically equivalent to two ferric hemes each coupled with a porphyrin cation radical, a scenario that resembles the binuclear di-cation di-radical complex of $(\Pi^{\bullet+})_2$ in Type II CR. The observed NIR spectral feature in MauG is unlikely due to Type I-like CR in a one-electron reduced system of *bis*-Fe(IV), *i.e.*, [Fe(IV)•••Fe(III)] ↔ [Fe(III)•••Fe(IV)], in which case one would expect the CR band to be located at a wavelength much longer than 950 nm [268,279-281]. For the di-heme system of MauG, the critical question is how the CR-transition phenomenon originates when the two hemes are separated by 14.5 Å and have no covalent bridging structures between them.

Trp93, which resides midway between the hemes, is proposed to be critical for the occurrence of this seemingly inexplicable CR-transition phenomenon in *bis*-Fe(IV) MauG. Each Fe(IV) heme is a sufficiently strong oxidant to oxidize Trp93 as evidenced by the observation that a minor radical species is always observed along with *bis*-Fe(IV) MauG [109]. Although Trp93 is capable of donating an electron to either of them, it cannot fill two holes simultaneously.

Thus, it is proposed that hole hopping via Trp93 is involved in the reversible ET process between the hemes to enable CR stabilization of *bis*-Fe(IV) MauG. This residue would need to be reversibly oxidized and reduced, at a sufficiently fast speed, to facilitate CR transition by increasing the effective electron coupling element while decreasing the effective ET distance.

Because neither of the previously discussed mechanisms of CR satisfactorily applies to the phenomenon in MauG, we propose a new class, Type III, whereby ET between the two interacting moieties in the CR complex is facilitated by electron/hole hopping through a third π system (*i.e.*, Trp93 in this biological case). The proposed resonance structures which give rise to the CR stabilization of *bis*-Fe(IV) MauG are shown in Figure 6.4.3_C and represent the first Type III CR model. Among the resonance structures of two-electron oxidized MauG, the *bis*-Fe(IV) resonance structure is the most stable one and was confirmed as the dominant species by our previous spectroscopic studies [109]. The Type III CR model is consistent with the observation that a minor radical species was detected by the EPR spectroscopy concomitant with the observation of the *bis*-Fe(IV) species [109]. This radical species is now attributed to the existence of the Cpd ES and Cpd ES' resonance structures in the CR system with the radical located at Trp93. Moreover, the appearance of the additional minor absorption peak at 664 nm upon the addition of H_2O_2 to di-ferric MauG (Figure 6.4.1_B) suggests that a small amount of compound I-like species exists in the CR system. Our previous Mössbauer characterization of the reaction mixture of MauG and H_2O_2 revealed that other than the *bis*-Fe(IV) and Fe(III) species, a minor portion of other heme species was present [109]. The spin-coupled compound I-like species, such as Cpd I and Cpd I' in the CR model, are reasonable candidates.

In the proposed Type III CR model, the spins and charges are delocalized within a ternary system composed of two hemes and one tryptophan residue spanning over 20 Å. Notably, both

Cpd ES and Cpd ES' in the model contain a cation radical form of Trp93, the residue that is proposed to be the hopping site. Such radical intermediates in a hopping mechanism are expected to be transient and have rarely been detected. One example is the observation of a $Trp^{\bullet+}$ hopping intermediate formed during the activation of the R2 subunit of *Escherichia coli* class I RNR [244], and another example is from a mutant protein of DNA photolyase [153]. In the Type III CR system of *bis*-Fe(IV) MauG, the hopping intermediates are long-lived because of the reversibility of ET that allows resonance stabilization of the spins and charges.

6.4.3 Mechanism of ET between the hemes in bis-Fe(IV) MauG

Ultrafast and reversible ET between the two interacting moieties is essential for a CR-transition phenomenon. Unfortunately, it is not possible to directly monitor the ET rate between the hemes in *bis*-Fe(IV) MauG. The formation of the *bis*-Fe(IV) species upon the addition of H_2O_2 is complete within the dead-time of the stopped-flow mixing (*ca*. 2–3 ms) [232]. Furthermore, the spectral changes in the two hemes are complementary and there is no net change in the absorbance spectrum that can be monitored. It is possible, however, to estimate the ET rate and determine the likely ET mechanism from analysis of the MauG structure in the context of ET theory [256].

ET between redox centers can proceed via two different mechanisms, single-step electron tunneling or multi-step hopping [103,256]. In the former case, there is no change in the redox state of the conductive medium. In contrast, if hopping is involved in ET, certain elements of the medium will be reversibly oxidized and reduced. In a hopping mechanism, the electron which leaves the electron donor is not the same as the one which enters the electron acceptor. Rather it is an electron which is displaced from the hopping site. The observed ET rate is determined by the rate of the slowest "hop", which is typically much faster than that of the corresponding direct

single-step tunneling reaction. For a single-step tunneling pathway or an individual segment of a multi-step hopping pathway, the ET rate (k_{ET}) is described by Eq. 1 [256]. At a given temperature, k_{ET} varies predictably with the driving force ($\Delta G°$) determined from ΔE_m of the ET reaction, the reorganization energy (λ) comprising the inner-sphere and outer-sphere nuclear rearrangement, and the electronic coupling element (H_{AB}). H_{AB} depends on the ET distance and the nature of the intervening medium between the donor and acceptor as shown in Eq. 2 [103], where β is the decay constant, a parameter that quantifies the efficiency of the medium in mediating ET, r is the distance between the donor and acceptor, r_0 is the close contact distance (the sum of van der Waals radii) and $H_{AB}(r_0)$ is the electronic coupling element at $r = r_0$.

$$k_{ET} = [4\pi^2 H_{AB}^2/h(4\pi\lambda RT)^{0.5}] \exp[-(\Delta G° + \lambda)^2/4\lambda RT] \qquad \text{Eq. 1}$$

$$H_{AB} = H_{AB}(r_0) \exp[-0.5\beta(r - r_0)] \qquad \text{Eq. 2}$$

The HARLEM program was used to calculate H_{AB} and β values for ET reactions in MauG using its crystal structure. These values were calculated for the single-step electron tunneling pathway between the hemes and the electron tunneling segments between Trp93 and each heme, the latter of which are parts of the proposed hopping mechanism for CR stabilization of *bis*-Fe(IV) MauG. Table 6.4.1 shows that each of the two hopping segments exhibits an H_{AB} value that is 10^3-fold greater than that of the single-step tunneling reaction. As $k_{ET} \propto H_{AB}^2$, in the absence of other changes k_{ET} of the hopping-mediated ET is expected to be six orders of magnitude larger than that of the single-step direct tunneling mechanism.

Table 6.4.1 Theoretical calculations of ET properties in MauG

HARLEM analysis of ET reactions in MauG[a]			
ET route	r (Å)[b]	β (Å^{-1})	H_{AB}[c]
Single-step tunneling			
between $Heme_{6C}$ and $Heme_{5C}$	14.5	1.40	3.8×10^{-5}

Segments of Trp93-mediated hopping			
between $Heme_{6C}$ and Trp93	5.4	1.24	3.7×10^{-2}
between Trp93 and $Heme_{5C}$	5.1	1.29	3.8×10^{-2}
Predicted ET rates from the hopping maps[d]			
λ (eV)	$k_{hopping}$ (s^{-1})[e]		$k_{tunneling}$ (s^{-1})[e,f]
$Heme_{6C}$ as the electron donor			
0.6	5.2×10^7–4.0×10^9		7.3×10^3–4.9×10^4
0.8	7.2×10^6–5.0×10^8		8.5×10^2–6.5×10^3
1.0	1.0×10^6–6.1×10^7		1.1×10^2–9.0×10^2
$Heme_{5C}$ as the electron donor			
0.6	5.7×10^7–3.9×10^9		7.3×10^3–4.9×10^4
0.8	8.0×10^6–4.9×10^8		8.5×10^2–6.5×10^3
1.0	1.0×10^6–6.3×10^7		1.1×10^2–9.0×10^2

[a] The calculation was performed using the structure of the MauG-preMADH complex (PDB entry 3L4M).

[b] r is the direct (edge-to-edge) distance between the redox cofactors.

[c] H_{AB} is in dimensionless units for relative comparison.

[d] The ranges for the predicted rates of ET reactions between the hemes of MauG were estimated under the assumption that both $\Delta G°_{DA}$ and $\Delta G°_{DI}$ are in the range from -0.15 to 0.15 eV.

[e] $k_{hopping} = 1/\tau_{hopping}$; $k_{tunneling} = 1/\tau_{tunneling}$. The range for $\tau_{hopping}$ is determined from the triangle region outlined by the dotted lines on each of the hopping map. The range for $\tau_{tunneling}$ is determined based upon the corresponding $\tau_{hopping}$ values on the upper right boarder line of each of the hopping map where $\tau_{hopping}$ is equal to $\tau_{tunneling}$.

[f] It should be noted that the two ranges for $k_{tunneling}$ with $Heme_{6C}$ and $Heme_{5C}$ as the electron donor, respectively, are essentially identical.

The HARLEM analysis did not take into account the effects of $\Delta G°$ and λ on the rate of ET. Using the method developed by Gray and coworkers [103], hopping maps were constructed for the ET reactions between the two hemes with Trp93 as the hopping site to examine the effects of these parameters as well as H_{AB} (Figure 6.4.4). The hopping map is a contour plot of $-\log_{10}(\tau_{hopping})$ against $\Delta G°_{DA}$ and $\Delta G°_{DH}$, where τ is the average ET time, $\Delta G°_{DA}$ is the driving force for the overall ET process from the donor to the acceptor, and $\Delta G°_{DH}$ is the driving force

for the first hopping step from the donor (*i.e.*, one of the hemes) to the hopping site (*i.e.*, Trp93). There are two blank regions on the map representing scenarios where hopping cannot occur. The upper right corner is the region in which single-step tunneling is calculated to be faster than hopping ($\tau_{hopping} > \tau_{tunneling}$), and the bottom left corner is the region in which $\Delta G°_{DA}$ is larger than $\Delta G°_{DH}$ (the hopping site is an electron/hole sink).

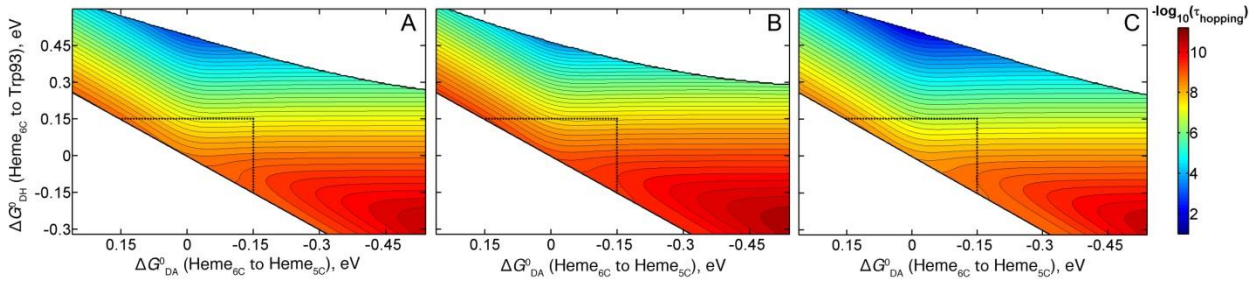

Figure 6.4.4 Hopping maps for the ET reactions between the hemes. The hopping maps were constructed with Trp93 as the hopping site, $Heme_{6C}$ as the electron donor, and $Heme_{5C}$ as the electron acceptor at 298 K with (A) λ = 0.8 eV, (B) λ = 0.6 eV, and (C) λ = 1.0 eV. The ET parameters used to construct the hopping maps, *i.e.*, the distance (r) and the decay constant (β), were adopted from the results of the HARLEM calculation in Table 6.4.1. The dashed lines indicate $\Delta G°$ at ± 0.15 eV.

In *bis*-Fe(IV) MauG, the precise $\Delta G°$ value of the ET reactions between the hemes is unknown as the two consecutive E_m values for the *bis*-Fe(IV)/di-ferric MauG redox couple are not known. However, the E_m values for Fe(IV)/Fe(III) redox couples in many heme-dependent peroxidases have been determined to be in the range from 724 to 1040 mV [248], and are similar to the values for compound I/II redox couples (802–1156 mV) [248] as well as the values for $Trp^{+\bullet}$/Trp redox couples (890–1080 mV) [260]. These values suggest that $\Delta G°$ of ET reactions between the hemes in *bis*-Fe(IV) MauG is near zero. If hopping via Trp93 is involved, $\Delta G°$ of each hopping segment is also near zero. This is consistent with the observation that both Fe(IV) hemes and the Trp93 radical are in redox equilibrium. Thus, in interpreting these hopping maps it was assumed that both $\Delta G°_{DA}$ and $\Delta G°_{DH}$ are in the range from -0.15 to 0.15 eV (see the

triangle region outlined by the dashed lines on each map). The λ value used to construct the hopping maps is also unknown in the ET system of *bis*-Fe(IV) MauG. Instead of a specific value (0.7 or 0.8 eV as conventionally used in intra-protein ET predictions [103,238]), a range of values from 0.6 to 1.0 eV was tested. During the inter-conversion between the resonance structures of Cpd I and Cpd I' shown in Figure 6.4.3_C, there are two consecutive one-electron ET reactions between the hemes: from Cpd I (Cpd I') to *bis*-Fe(IV) and from *bis*-Fe(IV) to Cpd I'(Cpd I). The hopping map study cannot distinguish these two ET reactions because they share the same ET path and the same redox centers, including the electron donor, the electron acceptor, and the hopping site. Even though the electron donor and acceptor are at different redox states in these two cases, the hopping map study is unbiased because it is the ΔE_m values of ET reactions rather than the absolute E_m values of each individual redox center that determine the results.

Figure 6.4.4_A shows a hopping map constructed with $Heme_{6C}$ as the electron donor and $Heme_{5C}$ as the electron acceptor at λ = 0.8 eV. This map can be used to examine both the ET reaction converting Cpd I to *bis*-Fe(IV) and the ET reaction converting *bis*-Fe(IV) to Cpd I'. The ET rate between the hemes is estimated to be 7.2×10^6–5.0×10^8 s^{-1} when Trp93-mediated hopping is involved in the ET reactions (Table 6.4.1). In contrast, single-step tunneling with $\Delta G°_{DA}$ in the same range is much slower, with the rate constant estimated to be 8.5×10^2–6.5×10^3 s^{-1}. With λ varying from 0.6 to 1.0 eV, the ET rate for both the Trp93-mediated hopping pathway and the single-step tunneling pathway increases as λ decreases, and decreases as λ increases (Figure 6.4.4 and Table 6.4.1). In each case, the hopping mechanism leads to a 4–5 orders of magnitude of increase in the ET rate versus direct tunneling (Table 6.4.1). This is in reasonable agreement with the HARLEM analysis that predicted a difference of approximately six orders of magnitude in the ET rate. The same conclusions were obtained from the hopping

maps constructed with $Heme_{5C}$ as the electron donor and $Heme_{6C}$ as the electron acceptor. Despite no advantage in the driving force, hopping via Trp93 can considerably enhance the ET rate by substantially decreasing the effective ET distance and increasing the effective electronic coupling element compared to single-step direct tunneling. A point of critical significance is that the hopping maps predict ET rates greater than 10^7 s^{-1} for the hopping mechanism. As was stated earlier, model studies suggest that rate constants in the range of 10^7–10^{11} s^{-1} are essential for delocalization of the spin and charge within CR complexes [263-265]. Thus, a hole-hopping mechanism of ET between the hemes mediated by Trp93 is capable of explaining the observed CR-transition phenomenon in *bis*-Fe(IV) MauG in the absence of direct contact between the hemes. It is interesting to note that ET via hole hopping is also suggested to occur between *bis*-Fe(IV) MauG and the tryptophan residues being oxidized in preMADH via a tryptophan residue located at the interface of the MauG-preMADH complex [101].

6.5 Conclusions

This work describes a CR-transition phenomenon involving two hemes in an enzyme-based high-valence catalytic iron intermediate. CR-transition phenomena reported in model systems usually require irradiation or electrochemical oxidation to produce the CR complexes and low temperatures for stabilization [261-263,277-279], whereas the CR complex of MauG is relatively stable under physiologically relevant conditions. The CR complex of MauG is a ternary system composed of two physically separated hemes and a tryptophan residue, unlike those in model systems. A novel hopping-mediated CR model is proposed, in which very rapid and reversible ET between the hemes with an intervening tryptophan as the hopping site mimics the distribution of the spins and charges that one would observe in an extended conjugated

system. The identification of the spectroscopic signature of this CR phenomenon will be useful to identify similar CR interactions in other biological systems.

8 DISRUPTION OF *BIS*-FE(IV) MAUG BY SMALL LIGAND MOLECULES — EVIDENCE FOR THE TYPE III CHARGE-RESONANCE MODEL

(This chapter is modified from a manuscript that JG coauthored: Geng J, and Liu A, Disruption of *bis*-Fe(IV) MauG by small molecule ligands – Evidence for the Type III charge-resonance model.)

8.1 Abstract

The oxidative biosynthesis of TTQ involves a 40-Å, long-range reaction catalyzed by MauG. A high-valence intermediate of MauG, known as *bis*-Fe(IV), acts as a potent oxidant during turnover. Recently, a unique CR phenomenon was discovered in this intermediate, and further revealed a new CR model, namely Type III, which suggests that the chemical nature of the *bis*-Fe(IV) species may not be as simple as it appears but rather composed of a collection of resonance structures in a dynamic equilibrium. In this study, we experimentally evaluated the proposed Type III CR model by introducing small molecule ligands to disrupt *bis*-Fe(IV) MauG. The results support this new model of CR and bring a fresh concept to classical CR theory.

8.2 Introduction

Since the first documentation by Brocklehurst and Badgers in 1968 [261], the investigation of CR phenomena has been actively researched by organic chemists [275]. In a typical CR event, one-electron oxidation of a certain aromatic compound generates a cation radical, which spontaneously associates with its parent neutral molecule, or another molecule of the cation radical, to form non-covalent "sandwich-like" dimeric complexes. The former scenario stabilizes an odd number of spin/charge in a mixed-valence cation radical, $(\Pi)_2^{\bullet+}$, and is classified as Type I CR; the latter one stabilizes an even number of spin/charge in a di-cation di-radical, $(\Pi^{\bullet+})_2$, and is classified as Type II CR [152]. Unique electronic absorption bands in the NIR region are characteristic of the resonance stabilization of spin/charge in the CR complexes

and termed as CR bands [266,279,281,284]. CR complexes represent the simplest intermolecular units that carry delocalized spin/charge and the investigation of these phenomena may provide the chemical basis for ET, conductivity, and ferromagnetism in many organic materials.

Like many other classic chemical models which are adopted by nature, the utilization of CR in biological systems to transiently stabilize spin/charge was first suggested in a pair of chlorophyll molecules, known as the "special pair", in bacterial photosynthetic reaction centers [267,268]. Recently, a second example was revealed from a di-heme enzyme, MauG.[152] MauG performs three cycles of H_2O_2-dependent oxidation on two tryptophan residues of preMADH to produce TTQ (Figure 1.2.2) [107]. Each two-electron oxidation cycle is proposed to be mediated by a unique *bis*-Fe(IV) intermediate of MauG (Figure 1.4.4) [109].

It is in this *bis*-Fe(IV) intermediate that the CR phenomenon was identified [6,152]. As shown in Figure 6.4.1, a broad electronic absorption band centered at 950 nm is observed specifically in the *bis*-Fe(IV) state of MauG [152]. It is noteworthy that the spectral properties of the NIR band are highly reminiscent of the reported CR bands from metalloporphyrin complexes [278,279]. In *bis*-Fe(IV) MauG, the two oxidizing equivalents derived from H_2O_2 are distributed in the di-heme system as two positive charges. This is electronically equivalent to two ferric hemes each coupled with a porphyrin cation radical, a scenario resembling the di-cation di-radical complexes in Type II CR. However, this case cannot be simply illustrated by the classic CR models as the two hemes in MauG are 14.5 Å apart, much wider separated than the interacting moieties in model CR complexes [265,283]. Thus, a new class of CR, Type III, is proposed, whereby the resonance stabilization of spin/charge in *bis*-Fe(IV) MauG is facilitated by an additional π moiety, the Trp93 residue located in between the hemes (Figure 7.2.1_A) [152]. Electron/hole hopping through Trp93 is postulated to occur in the ET process between the hemes to enable CR stabilization of *bis*-Fe(IV) MauG. Ultrafast and reversible ET with Trp93 as

the hopping site mimics the distribution of spin/charge as if this was in an extended conjugated system. The Type III CR in *bis*-Fe(IV) MauG represents a dynamic equilibrium of different electronically equivalent resonance structures when one electron from Trp93 cannot simultaneously fill two holes. This CR model is supported by theoretical calculations, which predict that in *bis*-Fe(IV) MauG electron/hole hopping through Trp93 makes possible a rate of inter-heme ET greater than 10^7 s^{-1}, comparable to the ET rates from other CR systems [152].

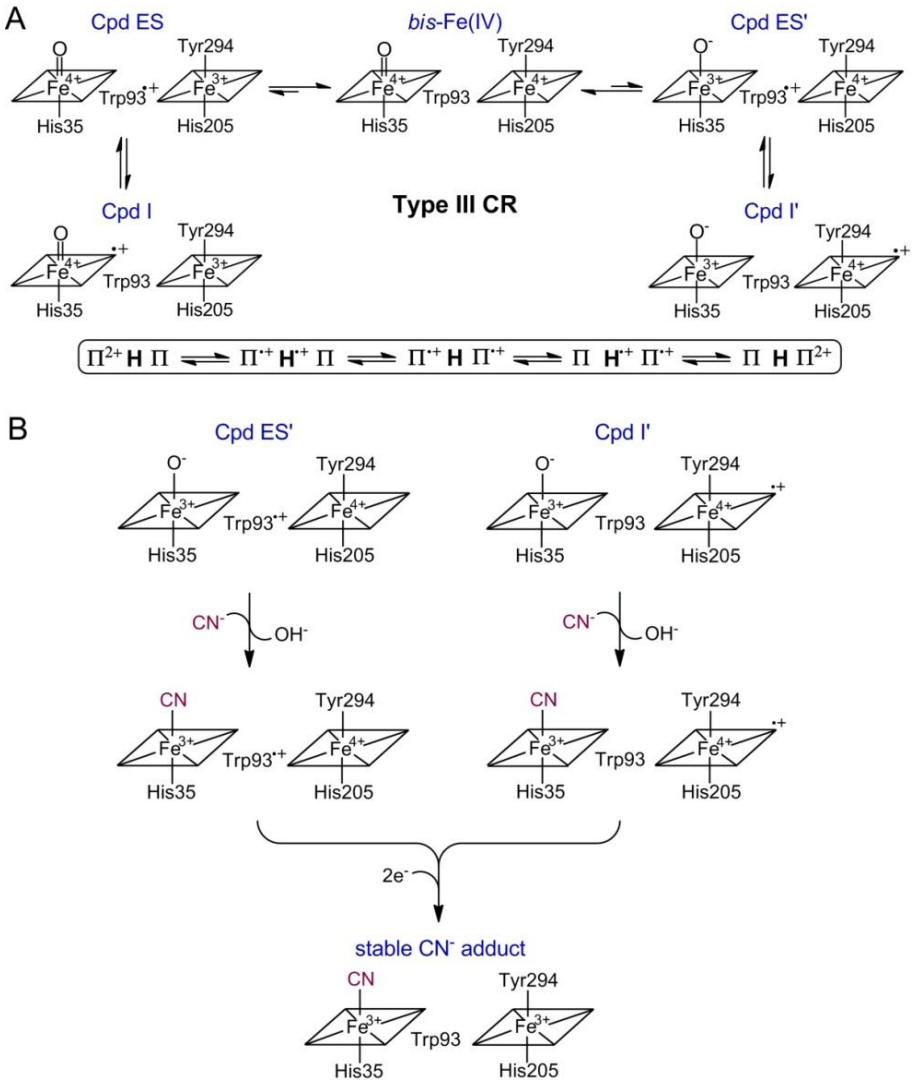

Figure 8.2.1 Type III CR phenomenon in *bis*-Fe(IV) MauG. (A) Proposed resonance structures for Type III CR. "H" represents a third aromatic moiety, which is a hopping relay facilitating ET between the two primary aromatic moieties; "Cpd ES" represents compound ES; and "Cpd I" represents compound I. (B) Specific targeting of two resonance structures (Cpd ES' and Cpd I') by CN^- to disrupt the Type III CR.

8.3 Materials and methods

8.3.1 Reagents

Sodium cyanide (97%), imidazole (>99%) and sodium fluoride (≥99%) were purchased from Sigma-Aldrich. H_2O_2 (30% v/v) was obtained from Fisher Scientific. The concentration of H_2O_2 was determined based on the molar absorptivity of 43.6 $M^{-1}cm^{-1}$ at 240 nm.

8.3.2 Protein expression and purification

WT and Y294H MauG were expressed in *Paracoccus denitrificans* and purified as described previously [12,132].

8.3.3 Spectroscopic characterizations

The spectroscopic experiments were performed in 50 mM potassium phosphate buffer, pH 7.5. The Vis-NIR spectra of MauG were recorded on an Agilent 8453 spectrometer, which has a photodiode-assay detector with a detection range of 190–1100 nm. For WT MauG, the *bis*-Fe(IV) species was generated by rapidly adding one eq. of H_2O_2 to di-ferric MauG (15 μM). The selected small molecule ligands were then introduced to the reaction system immediately after the addition of H_2O_2. The time-dependent change of the NIR band at 950 nm was monitored to evaluate the effect of these small molecule ligands on the decay rate of *bis*-Fe(IV). For Y294H MauG, a similar procedure was followed. The compound I-like species of Y294H MauG was generated by rapidly adding one eq. of H_2O_2 to di-ferric Y294H (4.4 μM). The selected small molecule ligands were then introduced to the reaction system immediately after the addition of H_2O_2. The time-dependent change of the absorption band at 655 nm was monitored. EPR spectra were recorded on a Bruker ER200D spectrometer coupled with a 4116DM resonator at 100 kHz modulation frequency. The measurement temperature was maintained at 10 K using an ESR910 liquid helium cryostat and an ITC503 temperature controller from Oxford Instruments (Concord, MA). The heme concentration of each EPR sample was 200 μM.

8.4 Results and discussion

In this work, to experimentally evaluate the Type III CR model and determine the chemical nature of the *bis*-Fe(IV) species, *i.e.*, whether it is a single redox species or composed of multiple resonance structures, we introduced small molecule ligands to disrupt this high-valence species. The selected ligand molecules include cyanide (CN^-), imidazole (IM), and fluoride (F^-). They are all capable of binding to the heme iron when there is a coordinate vacancy, yet with different binding affinities. If *bis*-Fe(IV) MauG is a single redox species, exogenous small molecule ligands (CN^-, for instance) would not cause a notable effect on its chemical properties because both hemes are coordinate-saturated and the axial ligands are either irreplaceable ($Heme_{5C}$) or inaccessible ($Heme_{6C}$) [112,113]. However, if *bis*-Fe(IV) MauG represents an equilibrium of resonance structures as proposed in Figure 7.2.1_A, exogenous CN^- might be able to specifically target species like Cpd ES' and Cpd I' by outcompeting the relatively weakly associated axial ligand of $Heme_{5C}$ to generate the [Fe(III)CN^- ····Trp93$^{\bullet+}$····Fe(IV)] and [Fe(III)CN^-····Trp93····Fe(IV)$^{\bullet+}$] complexes, respectively (Figure 7.2.1_B). Neither CN^- adduct is capable of maintaining the CR stabilization due to changes in the heme redox properties, and thus it is highly possible that they will quickly return to a reduced state by releasing two oxidizing equivalents (Figure 7.2.1_B). Despite the fact that Cpd ES' and Cpd I' are present as minor species in the proposed CR model [152], the dynamic exchange with other resonance structures would allow the CN^- disruption to gradually shift the equilibrium and break the electronic communication between the hemes. This will eventually destroy the Type III CR stabilization, leading to an accelerated decay of *bis*-Fe(IV).

It was previously demonstrated that though chemically equivalent to reactive high-valence iron intermediates such as the Fe(V), Cpd I, and Cpd ES species, *bis*-Fe(IV) MauG displays extraordinary stability in the absence of preMADH with a half-life of several minutes

[109,232]. Figure 7.4.1_A shows that the introduction of CN^- to the reaction system containing *bis*-Fe(IV) MauG leads to an increase in the decay rate of the NIR band at 950 nm. In the presence of 25 mM CN^-, the NIR band becomes completely diminished *ca.* 75 s after the addition of CN^- with a decay rate nearly one order of magnitude greater than that without CN^-. When different small molecule ligands were examined, they exhibited different degrees of disruptive effects on the decay rate of the NIR band with CN^- presenting the most pronounced influence, followed by IM and further by F^- (Figure 7.4.1_B). This trend correlates well with the binding affinities of these small molecule ligands to ferric heme centers. It is known that in many hemoproteins di-atomic molecules like CN^- are the most tightly associated ligands, whereas small heterocyclic compounds and halide anions are usually weaker ligands [285,286].

EPR spectroscopy was also used to characterize the aforementioned chemical events. As shown in the black trace of Figure 7.4.1_C, there are three types of heme species revealed from the EPR spectrumof di-ferric MauG, a high-spin species ($Heme_{5C}$), a major low-spin species ($Heme_{6C}$), and a minor low-spin species attributed as a freezing-induced artifact derived from the high-spin species [138]. CN^- can only coordinate to $Heme_{5C}$ and cause a spin-transition to produce a new low-spin species with a very broad signal around g = 3.37 at the expense of the high-spin species (Figure 7.4.1_C, the red trace). The freezing-induced artifact is also removed in the presence of CN^-. Upon adding H_2O_2 to di-ferric MauG, most of the high-spin and low-spin ferric signals disappear owing to the formation of *bis*-Fe(IV) MauG (Figure 7.4.1_C, the blue trace) [109]. The introduction of CN^- to this system accelerates the decay of the newly generated *bis*-Fe(IV) species as indicated by a more rapid return of the low-spin signal of $Heme_{6C}$ compared to a control sample without CN^- (Figure 7.4.1_C, the green and purple traces). It should be noted that $Heme_{6C}$ is buried in the protein matrix and inaccessible to exogenous CN^-. Thus, the accelerated decay of the ferryl species at the $Heme_{6C}$ site is most likely due to

disruptive events that remotely occur at the $Heme_{5C}$ site and cause a loss of the electronic communication between the two hemes. The EPR sample freeze-quenched 75 s after the addition of CN^- to *bis*-Fe(IV) MauG displays a spectrum that is almost identical to that of the sample containing the CN^- adduct of MauG (Figure 7.4.1_C, the green and red traces). This observation suggests that almost all the newly generated *bis*-Fe(IV) species has been eliminated after the CN^- treatment for 75 s, consistent with the result from monitoring the decay of the NIR absorption band. It also indicates that the dead end of this chemical processing is a di-ferric CN^- adduct of MauG, in accordance with our proposed scheme in Figure 7.2.1_B.

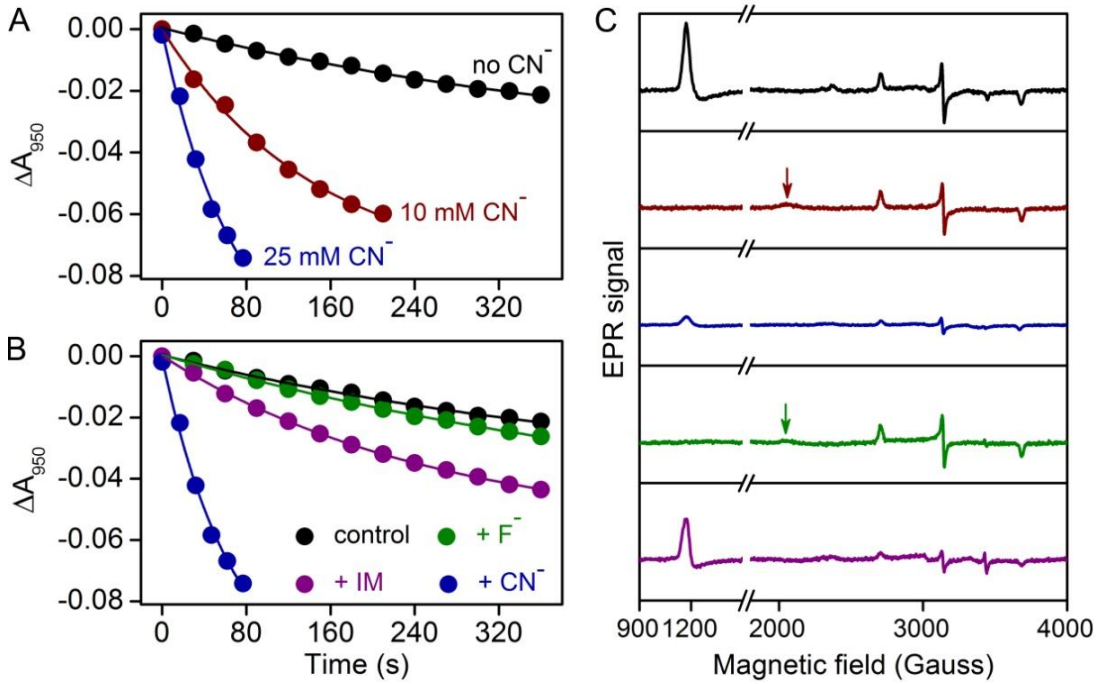

Figure 8.4.1 Disruption of *bis*-Fe(IV) MauG by small molecule ligands. (A) The addition of CN^- accelerates the decay of the NIR band of *bis*-Fe(IV) MauG. CN^- was added immediately after *bis*-Fe(IV) formation. The solid lines are fits of the data to single-exponential decay. (B) Effect of different small molecule ligands on the decay rate of the NIR band. Each small molecule ligand (25 mM) was added immediately after *bis*-Fe(IV) formation. (C) 10 K EPR spectra of as-isolated MauG (black trace), MauG + 25 mM CN^- (red trace), MauG + 1 × H_2O_2 (blue trace), MauG + 1 × H_2O_2 + 25 mM CN^- (green trace, CN^- was added immediately after the H_2O_2 addition and the sample was freeze-quenched 75 s after the CN^- addition), MauG + 1 × H_2O_2 (purple trace, frozen 75 s after reaction). The arrows indicate the CN^- adduct.

Given the relatively high concentration of small molecule ligands added to the system, could it be possible that direct reduction by these molecules or exchange of the ferryl oxo group with exogenous ligands occur at the $Heme_{5C}$ site, thereby causing a more rapid decay of *bis*-Fe(IV)? Our further investigation on a Y294H MauG mutant rules out this possibility. Tyr294 is an axial ligand of $Heme_{6C}$ (Figure 1.4.1). In Y294H, $Heme_{6C}$ possesses a *bis*-histidine ligand set and a ferryl state cannot be generated [132]. Upon reaction with H_2O_2, the two oxidizing equivalents from H_2O_2 are trapped at the $Heme_{5C}$ site in the form of a compound I-like species (Figure 7.4.2_A), which displays a characteristic absorption band at 655 nm (Figure 7.4.2_B) [132,133]. The introduction of small molecule ligands such as CN^- and IM to Y294H compound I only causes a minimal effect on its decay rate as revealed from the time-dependent spectral change at 655 nm (Figure 7.4.2_C). Therefore, the observed accelerated decay of the *bis*-Fe(IV) species in the WT protein in the presence of small molecule ligands is unlikely due to direct reduction or ligand exchange on the oxy-ferryl species at the $Heme_{5C}$ site.

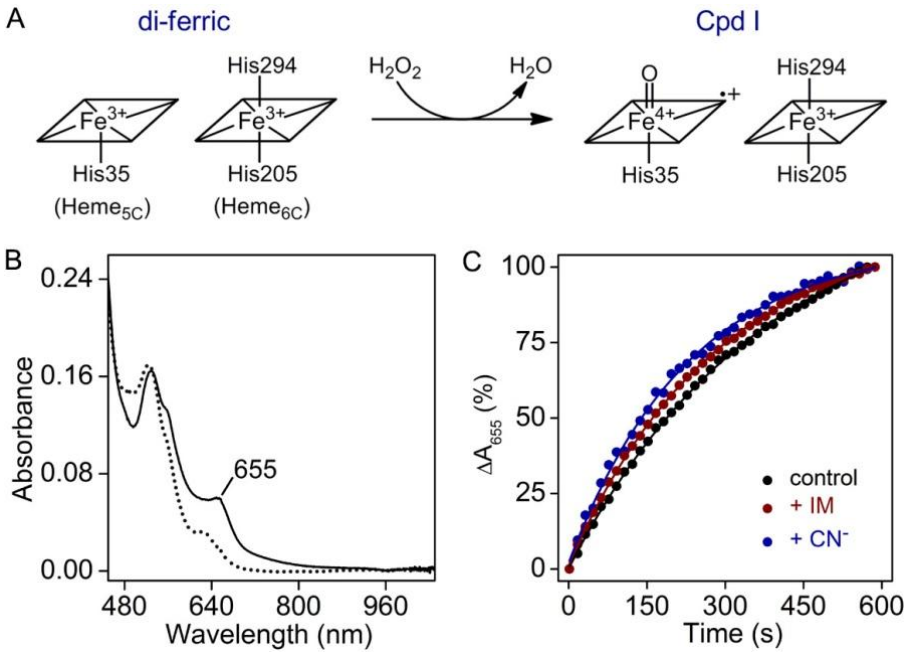

Figure 8.4.2 Compound I-like species in Y294H MauG. (A) Chemical conversion from di-ferric to compound I Y294H MauG. (B) Optical absorption spectra of Y294H before (dotted trace) and after (solid

trace) the addition of H_2O_2. (C) Effect of small molecule ligands on the decay rate of Y294H compound I. Each small molecule ligand (25 mM) was added immediately after the formation of Y294H compound I. The solid lines are fits of the data to a single-exponential equation.

Taken together, it is evident that *bis*-Fe(IV) MauG is not a single redox species as it appears but rather an equilibrium of resonance structures. This finding provides a piece of strong evidence supporting our proposed Type III CR model, which brings a new concept to the well-documented CR phenomenon.

SUMMARY

This dissertation study focused on the mechanistic aspects of two heme-dependent enzymes that catalyze a unique type of reactions, *i.e.*, tryptophan-oxidation reactions. The first enzyme, TDO, catalyzes a dioxygenation reaction on free L-Trp with molecular oxygen as the oxidant to yield a ring-cleaved product, NFK. The second enzyme, MauG, catalyzes oxidative modifications on two tryptophan residues of preMADH with peroxide as the oxidant to complete the biosynthesis of TTQ. In the former case, molecular oxygen serves as both the oxidant and the oxygen donor, whereas in the latter case, peroxide only provides the oxidizing equivalents without donating its oxygen atoms.

In this study, we first explored the mechanism of the peroxide-driven enzyme-reactivation pathway of ferric TDO in the presence of L-Trp, and demonstrated that the enzyme reactivation process proceeds through a compound ES-type ferryl species generated from oxidation of ferric TDO by peroxide. Ferrous TDO is produced from the reaction system via two-electron reduction of the oxy-ferryl moiety of the compound ES-type ferryl species by L-Trp. The newly generated ferrous enzyme is the catalytic competent species and is responsible for the observed catalytic activity. Moreover, to probe the dioxygenase mechanism of TDO, we tested whether 1-Me-L-Trp is an active substrate for TDO. The steady-state kinetic assay showed that this substrate analog is very active, with a k_{cat} value comparable to that of the reaction with L-Trp as the substrate. This result provides a piece of direct and strong evidence against the notion that the catalytic reaction of TDO is initiated by deprotonation of the indole NH group of the substrate. In addition, the catalytic functions of a distal histidine, His72, was investigated by chemical-rescue approaches. An imidazole derivative, 2MI, showed two chemical-rescue activities with the His72 variants, *i.e.*, accelerating the dioxygenase reaction rate and facilitating

the formation of the compound ES-type ferryl species in the reaction between ferric TDO and peroxide in the absence of L-Trp. Notably, ferryl intermediates of TDO are believed to be involved in both reactions. These results, together with further biochemical, spectroscopic, and kinetic studies on the His72 variants, suggest a dual function of this conserved residue. Prior to and during substrate binding, His72 contributes to the proper binding of L-Trp via an H-bonding interaction with the indole NH group of the substrate and shields the heme center from non-productive binding of other small molecule ligands. During chemical catalysis, His72 regulates the reactivity of high-valence reactive intermediates through an H-bonding interaction to the heme-bound oxygen.

For MauG-catalyzed TTQ biosynthesis, we examined the chemical and structural basis for the reactivity of the *bis*-Fe(IV) intermediate, a lynchpin species in TTQ biosynthesis. In the *bis*-Fe(IV) intermediate, $Heme_{5C}$ is in an Fe(IV)=O state, and $Heme_{6C}$ is in an Fe(IV) state with its original His-Tyr axial ligand set retained. Mutagenesis on Tyr294, one of the axial ligand of $Heme_{6C}$, generated mutant proteins that cannot stabilize the *bis*-Fe(IV) redox state required for TTQ biosynthesis, but instead forms a compound-I like species upon reaction with peroxide. These results highlight the importance of Tyr294 in stabilizing the Fe(IV) state of $Heme_{6C}$. Mutagenesis on Trp199, a surface residue of MauG located at the protein-protein interface of the MauG-preMADH complex, generated mutant proteins that display essentially the same physical properties as the WT enzyme yet with no catalytic activity. It was proposed that electron/hole hopping via Trp199 is critical for channeling the oxidizing equivalents from the di-heme cofactor of MauG to the preTTQ site of preMADH over a long range. A CR phenomenon was observed in the *bis*-Fe(IV) redox state of MauG with a characteristic CR band at 950 nm. A novel Type III CR model was proposed in which a tryptophan residue located midway in between the two

hemes, Trp93, mediates ultrafast and reversible ET between the two hemes via hopping. Computational studies on the ET process between the hemes in MauG supported the proposed Type III CR model by demonstrating that the ET rate of the Trp93-mediated hopping pathway is much faster than that of the single-step tunneling pathway, and is comparable to the reported ET rates in other CR complexes. Additional experiments using small molecule ligands to disrupt the *bis*-Fe(IV) species also confirmed the proposed CR model and revealed the chemical nature of the *bis*-Fe(IV) redox state, which is not a single redox species but rather composed of a collection of electronically equivalent resonance structures in a dynamic equilibrium. Overall, the MauG-catalyzed TTQ biosynthesis proceeds via ordered, consecutive one-electron steps. The *bis*-Fe(IV) intermediate remotely extracts electrons from the preTTQ site. The associated long-range ET is mediated by hopping through two tryptophan residues of MauG: Trp199 in between the preTTQ site and $Heme_{6C}$, and Trp93 in between $Heme_{6C}$ and $Heme_{5C}$. The Type III CR phenomenon in *bis*-Fe(IV) MauG prevents non-productive oxidation of the nearby aromatic residues of MauG, contributing to the potency of this high-valence intermediate.

Though using distinctive catalytic strategies to perform different types of tryptophan-oxidation reactions, the two heme-dependent enzymes of interest in this study both employ high-valence ferryl intermediates in their reactions. TDO utilizes a compound II-type oxy-ferryl species to perform oxygen insertion into a substrate-based epoxide intermediate. Such a chemical transformation can occur because the epoxide intermediate is already activated and reactive. MauG uses a *bis*-Fe(IV) intermediate to generate a high redox potential at one end of the reaction pathway and remotely extract electrons from the substrate at the other end of the reaction pathway. Notably, the ferryl heme without an oxo group at the $Heme_{6C}$ site is closer to the preTTQ site. It is the frontier heme that directly accepts electrons from the substrate. The

absence of the oxo group in this ferryl heme avoids non-productive oxygen insertion reactions, thereby improving the catalytic efficiency.

REFERENCES

1. Gonzales, D. H., and Neupert, W. (1990) Biogenesis of mitochondrial *c*-type cytochromes, *J. Bioenerg. Biomembr. 22*, 753-768.

2. Hansson, M., and Vonwachenfeldt, C. (1993) Heme *b* (protoheme IX) is a precursor of heme *a* and heme *d* in *Bacillus subtilis*, *FEMS Microbiol. Lett. 107*, 121-126.

3. Poulos, T. L. (2014) Heme enzyme structure and function, *Chem. Rev. 114*, 3919-3962.

4. Sono, M., Roach, M. P., Coulter, E. D., and Dawson, J. H. (1996) Heme-containing oxygenases, *Chem. Rev. 96*, 2841-2888.

5. Dawson, J. H., and Sono, M. (1987) Cytochrome P-450 and chloroperoxidase: Thiolate-ligated heme enzymes. Spectroscopic determination of their active site structures and mechanistic implications of thiolate ligation, *Chem. Rev. 87*, 1255-1276.

6. Geng, J., Davis, I., Liu, F., and Liu, A. (2014) Bis-Fe(IV): Nature's sniper for long-range oxidation, *J. Biol. Inorg. Chem.* in press (DOI 10.1007/s00775-014-1123-8)

7. Kadish, K. M. (2007) The electrochemistry of metalloporphyrins in nonaqueous media, In *Progress in Inorganic Chemistry*, 435-605, John Wiley & Sons, Inc.

8. Nesset, M. J. M., Shokhirev, N. V., Enemark, P. D., Jacobson, S. E., and Walker, F. A. (1996) Models of the cytochromes. Redox properties and thermodynamic stabilities of complexes of "hindered" iron(III) and iron(II) tetraphenylporphyrinates with substituted pyridines and imidazoles, *Inorg. Chem. 35*, 5188-5200.

9. Zhuang, J. Y., Amoroso, J. H., Kinloch, R., Dawson, J. H., Baldwin, M. J., and Gibney, B. R. (2006) Evaluation of electron-withdrawing group effects on heme binding in designed proteins: Implications for heme *a* in cytochrome *c* oxidase, *Inorg. Chem. 45*, 4685-4694.

10. Fufezan, C., Zhang, J., and Gunner, M. R. (2008) Ligand preference and orientation in *b*- and *c*-type heme-binding proteins, *Proteins: Struct., Funct., Bioinf. 73*, 690-704.

11. Geng, J., and Liu, A. (2014) Heme-dependent dioxygenases in tryptophan oxidation, *Arch. Biochem. Biophys. 544*, 18-26.

12. Wang, Y., Graichen, M. E., Liu, A., Pearson, A. R., Wilmot, C. M., and Davidson, V. L. (2003) MauG, a novel diheme protein required for tryptophan tryptophylquinone biogenesis, *Biochemistry 42*, 7318-7325.

13. Pearson, A. R., De la Mora-Rey, T., Graichen, M. E., Wang, Y., Jones, L. H., Marimanikkupam, S., Agger, S. A., Grimsrud, P. A., Davidson, V. L., and Wilmot, C. M. (2004) Further insights into quinone cofactor biogenesis: Probing the role of mauG in methylamine dehydrogenase tryptophan tryptophylquinone formation, *Biochemistry 43*, 5494-5502.

14. Kotake, Y., and Masayama, I. (1936) The intermediary metabolism of tryptophan. XVIII. The mechanism of formation of kynurenine from tryptophan, *Z. Physiol. Chem. 243*, 237-244.

15. Hayaishi, O., Rothberg, S., Mehler, A. H., and Saito, Y. (1957) Studies on oxygenases: Enzymatic formation of kynurenine from tryptophan, *J. Biol. Chem. 229*, 889-896.

16. Tanaka, T., and Knox, W. E. (1959) The nature and mechanism of the tryptophan pyrrolase (peroxidase-oxidase) reaction of Pseudomonas and rat liver, *J. Biol. Chem. 234*, 1162-1170.

17. Stone, T. W., and Darlington, L. G. (2002) Endogenous kynurenines as targets for drug discovery and development, *Nat. Rev. Drug Discov. 1*, 609-620.

18. Schwarcz, R. (2004) The kynurenine pathway of tryptophan degradation as a drug target, *Curr. Opin. Pharmacol. 4*, 12-17.

19. Guillemin, G. J., and Brew, B. J. (2002) Implications of the kynurenine pathway and quinolinic acid in Alzheimer's disease, *Redox Rep. 7*, 199-206.

20. Knox, W. E., and Mehler, A. H. (1950) The conversion of tryptophan to kynurenine in liver. I. The coupled tryptophan peroxidase-oxidase system forming formylkynurenine, *J. Biol. Chem. 187*, 419-430.

21. Knox, W. E., Yip, A., and Reshef, L. (1970) L-Tryptophan 2,3-dioxygenase (tryptophan pyrrolase), *Methods Enzymol. 17*, 415-421.

22. Guillemin, G. J., Meininger, V., and Brew, B. J. (2005) Implications for the kynurenine pathway and quinolinic acid in amyotrophic lateral sclerosis, *Neurodegener. Dis. 2*, 166-176.

23. Magni, G., Amici, A., Emanuelli, M., Raffaelli, N., and Ruggieri, S. (1999) Enzymology of NAD^+ synthesis, *Adv. Enzymol. Relat. Areas Mol. Biol. 73*, 135-182.

24. Kurnasov, O., Goral, V., Colabroy, K., Gerdes, S., Anantha, S., Osterman, A., and Begley, T. P. (2003) NAD biosynthesis: Identification of the tryptophan to quinolinate pathway in bacteria, *Chem. Biol. 10*, 1195-1204.

25. Paglino, A., Lombardo, F., Arca, B., Rizzi, M., and Rossi, F. (2008) Purification and biochemical characterization of a recombinant *Anopheles gambiae* tryptophan 2,3-dioxygenase expressed in *Escherichia coli*, *Insect Biochem. Mol. Biol. 38*, 871-876.

26. Colabroy, K. L., and Begley, T. P. (2005) Tryptophan catabolism: Identification and characterization of a new degradative pathway, *J. Bacteriol. 187*, 7866-7869.

27. Huang, W., Gong, Z., Li, J., and Ding, J. P. (2013) Crystal structure of *Drosophila melanogaster* tryptophan 2,3-dioxygenase reveals insights into substrate recognition and catalytic mechanism, *J. Struct. Biol. 181*, 291-299.

28. Yamamoto, S., and Hayaishi, O. (1967) Tryptophan pyrrolase of rabbit intestine. D- and L-tryptophan-cleaving enzyme or enzymes, *J. Biol. Chem. 242*, 5260-5266.

29. Higuchi, K., and Hayaishi, O. (1967) Enzymic formation of D-kynurenine from D-tryptophan, *Arch. Biochem. Biophys. 120*, 397-403.

30. Hirata, F., and Hayaishi, O. (1972) New degradative routes of 5-hydroxytryptophan and serotonin by intestinal tryptophan 2,3-dioxygenase, *Biochem. Biophys. Res. Commun. 47*, 1112-1119.

31. Shimizu, T., Nomiyama, S., Hirata, F., and Hayaishi, O. (1978) Indoleamine 2,3-dioxygenase. Purification and some properties, *J. Biol. Chem. 253*, 4700-4706.

32. Hayaishi, O. (1976) Properties and function of indoleamine 2,3-dioxygenase, *J. Biochem. 79*, 13-21.

33. Takikawa, O. (2005) Biochemical and medical aspects of the indoleamine 2,3-dioxygenase-initiated L-tryptophan metabolism, *Biochem. Biophys. Res. Commun. 338*, 12-19.

34. Hayaishi, O. (1993) My life with tryptophan – Never a dull moment, *Protein Sci. 2*, 472-475.

35. Sugimoto, H., Oda, S., Otsuki, T., Hino, T., Yoshida, T., and Shiro, Y. (2006) Crystal structure of human indoleamine 2,3-dioxygenase: Catalytic mechanism of O_2 incorporation by a heme-containing dioxygenase, *Proc. Natl. Acad. Sci. U.S.A. 103*, 2611-2616.

36. Forouhar, F., Anderson, J. L., Mowat, C. G., Vorobiev, S. M., Hussain, A., Abashidze, M., Bruckmann, C., Thackray, S. J., Seetharaman, J., Tucker, T., Xiao, R., Ma, L. C., Zhao, L., Acton, T. B., Montelione, G. T., Chapman, S. K., and Tong, L. (2007) Molecular insights into substrate recognition and catalysis by tryptophan 2,3-dioxygenase, *Proc. Natl. Acad. Sci. U.S.A. 104*, 473-478.

37. Zhang, Y., Kang, S. A., Mukherjee, T., Bale, S., Crane, B. R., Begley, T. P., and Ealick, S. E. (2007) Crystal structure and mechanism of tryptophan 2,3-dioxygenase, a heme enzyme involved in tryptophan catabolism and in quinolinate biosynthesis, *Biochemistry 46*, 145-155.

38. Zhu, X., van Pée, K. H., and Naismith, J. H. (2010) The ternary complex of PrnB (the second enzyme in the pyrrolnitrin biosynthesis pathway), tryptophan, and cyanide yields new mechanistic insights into the indolamine dioxygenase superfamily, *J. Biol. Chem. 285*, 21126-21133.

39. Katz, J. B., Muller, A. J., and Prendergast, G. C. (2008) Indoleamine 2,3-dioxygenase in T-cell tolerance and tumoral immune escape, *Immunol. Rev. 222*, 206-221.

40. Taylor, M. W., and Feng, G. S. (1991) Relationship between interferon-γ, indoleamine 2,3-dioxygenase, and tryptophan catabolism, *FASEB J. 5*, 2516-2522.

41. King, N. J. C., and Thomas, S. R. (2007) Molecules in focus: Indoleamine 2,3-dioxygenase, *Int. J. Biochem. Cell Biol. 39*, 2167-2172.

42. Mellor, A. L., and Munn, D. H. (2004) IDO expression by dendritic cells: Tolerance and tryptophan catabolism, *Nat. Rev. Immunol. 4*, 762-774.

43. Mellor, A. L., and Munn, D. H. (2001) Extinguishing maternal immune responses during pregnancy: implications for immunosuppression, *Semin. Immunol. 13*, 213-218.

44. Muller, A. J., and Prendergast, G. C. (2007) Indoleamine 2,3-dioxygenase in immune suppression and cancer, *Curr. Cancer Drug Targets 7*, 31-40.

45. Munn, D. H., and Mellor, A. L. (2007) Indoleamine 2,3-dioxygenase and tumor-induced tolerance, *J. Clin. Invest. 117*, 1147-1154.

46. Grohmann, U., Fallarino, F., and Puccetti, P. (2003) Tolerance, DCs and tryptophan: Much ado about IDO, *Trends Immunol. 24*, 242-248.

47. Lob, S., Konigsrainer, A., Rammensee, H. G., Opelz, G., and Terness, P. (2009) Inhibitors of indoleamine-2,3-dioxygenase for cancer therapy: Can we see the wood for the trees?, *Nat. Rev. Cancer 9*, 445-452.

48. Platten, M., Wick, W., and Van den Eynde, B. (2012) Tryptophan catabolism in cancer: Beyond IDO and tryptophan depletion, *Cancer Res. 72*, 5435-5440.

49. Dolusic, E., Larrieu, P., Moineaux, L., Stroobant, V., Pilotte, L., Colau, D., Pochet, L., Van den Eynde, B., Masereel, B., Wouters, J., and Frederick, R. (2011) Tryptophan 2,3-dioxygenase (TDO) inhibitors. 3-(2-(pyridyl)ethenyl)indoles as potential anticancer immunomodulators, *J. Med. Chem. 54*, 5320-5334.

50. Denisov, I. G., Makris, T. M., Sligar, S. G., and Schlichting, I. (2005) Structure and chemistry of cytochrome P450, *Chem. Rev. 105*, 2253-2277.

51. Rittle, J., and Green, M. T. (2010) Cytochrome P450 compound I: Capture, characterization, and C-H bond activation kinetics, *Science 330*, 933-937.

52. Hamilton, G. A. (1969) Mechanisms of two- and four-electron oxidations catalyzed by some metalloenzymes, *Adv. Enzymol. Relat. Areas Mol. Biol. 32*, 55-96.

53. Leeds, J. M., Brown, P. J., Mcgeehan, G. M., Brown, F. K., and Wiseman, J. S. (1993) Isotope effects and alternative substrate reactivities for tryptophan 2,3-dioxygenase, *J. Biol. Chem. 268*, 17781-17786.

54. Millett, E. S., Efimov, I., Basran, J., Handa, S., Mowat, C. G., and Raven, E. L. (2012) Heme-containing dioxygenases involved in tryptophan oxidation, *Curr. Opin. Chem. Biol. 16*, 60-66.

55. Efimov, I., Basran, J., Thackray, S. J., Handa, S., Mowat, C. G., and Raven, E. L. (2011) Structure and reaction mechanism in the heme dioxygenases, *Biochemistry 50*, 2717-2724.

56. Chung, L. W., Li, X., Sugimoto, H., Shiro, Y., and Morokuma, K. (2008) Density functional theory study on a missing piece in understanding of heme chemistry: The reaction mechanism for indoleamine 2,3-dioxygenase and tryptophan 2,3-dioxygenase, *J. Am. Chem. Soc. 130*, 12299-12309.

57. Chung, L. W., Li, X., Sugimoto, H., Shiro, Y., and Morokuma, K. (2010) ONIOM study on a missing piece in our understanding of heme chemistry: Bacterial tryptophan 2,3-dioxygenase with dual oxidants, *J. Am. Chem. Soc. 132*, 11993-12005.

58. Capece, L., Lewis-Ballester, A., Yeh, S. R., Estrin, D. A., and Marti, M. A. (2012) Complete reaction mechanism of indoleamine 2,3-dioxygenase as revealed by QM/MM simulations, *J. Phys. Chem. B 116*, 1401-1413.

59. Lewis-Ballester, A., Batabyal, D., Egawa, T., Lu, C., Lin, Y., Marti, M. A., Capece, L., Estrin, D. A., and Yeh, S. R. (2009) Evidence for a ferryl intermediate in a heme-based dioxygenase, *Proc. Natl. Acad. Sci. U.S.A. 106*, 17371-17376.

60. Capece, L., Lewis-Ballester, A., Batabyal, D., Di Russo, N., Yeh, S. R., Estrin, D. A., and Marti, M. A. (2010) The first step of the dioxygenation reaction carried out by tryptophan

dioxygenase and indoleamine 2,3-dioxygenase as revealed by quantum mechanical/molecular mechanical studies, *J. Biol. Inorg. Chem. 15*, 811-823.

61. Batabyal, D., and Yeh, S. R. (2009) Substrate-protein interaction in human tryptophan dioxygenase: The critical role of H76, *J. Am. Chem. Soc. 131*, 3260-3270.

62. Davydov, R. M., Chauhan, N., Thackray, S. J., Anderson, J. L. R., Papadopoulou, N. D., Mowat, C. G., Chapman, S. K., Raven, E. L., and Hoffman, B. M. (2010) Probing the ternary complexes of indoleamine and tryptophan 2,3-dioxygenases by cryoreduction EPR and ENDOR spectroscopy, *J. Am. Chem. Soc. 132*, 5494-5500.

63. Batabyal, D., and Yeh, S. R. (2007) Human tryptophan dioxygenase: A comparison to indoleamine 2,3-dioxygenase, *J. Am. Chem. Soc. 129*, 15690-15701.

64. Capece, L., Lewis-Ballester, A., Marti, M. A., Estrin, D. A., and Yeh, S. R. (2011) Molecular basis for the substrate stereoselectivity in tryptophan dioxygenase, *Biochemistry 50*, 10910-10918.

65. Capece, L., Arrar, M., Roitberg, A. E., Yeh, S. R., Marti, M. A., and Estrin, D. A. (2010) Substrate stereo-specificity in tryptophan dioxygenase and indoleamine 2,3-dioxygenase, *Proteins: Struct., Funct., Bioinf. 78*, 2961-2972.

66. Ishimura, Y., Nozaki, M., Hayaishi, O., Nakamura, T., Tamura, M., and Yamazaki, I. (1970) The oxygenated form of L-tryptophan 2,3-dioxygenase as reaction intermediate, *J. Biol. Chem. 245*, 3593-3602.

67. Lu, C. Y., Lin, Y., and Yeh, S. R. (2010) Spectroscopic studies of ligand and substrate binding to human indoleamine 2,3-dioxygenase, *Biochemistry 49*, 5028-5034.

68. Efimov, I., Basran, J., Sun, X., Chauhan, N., Chapman, S. K., Mowat, C. G., and Raven, E. L. (2012) The mechanism of substrate inhibition in human indoleamine 2,3-dioxygenase, *J. Am. Chem. Soc. 134*, 3034-3041.

69. Taniguchi, T., Sono, M., Hirata, F., Hayaishi, O., Tamura, M., Hayashi, K., Iizuka, T., and Ishimura, Y. (1979) Indoleamine 2,3-dioxygenase. Kinetic studies on the binding of superoxide anion and molecular oxygen to enzyme, *J. Biol. Chem. 254*, 3288-3294.

70. Lu, C. Y., and Yeh, S. R. (2011) Ferryl derivatives of human indoleamine 2,3-dioxygenase, *J. Biol. Chem. 286*, 21220-21230.

71. Lu, C. Y., Lin, Y., and Yeh, S. R. (2009) Inhibitory substrate binding site of human indoleamine 2,3-dioxygenase, *J. Am. Chem. Soc. 131*, 12866-12867.

72. Sono, M., Taniguchi, T., Watanabe, Y., and Hayaishi, O. (1980) Indoleamine 2,3-dioxygenase. Equilibrium studies of the tryptophan binding to the ferric, ferrous, and CO-bound enzymes, *J. Biol. Chem. 255*, 1339-1345.

73. Thackray, S. J., Bruckmann, C., Anderson, J. L. R., Campbell, L. P., Xiao, R., Zhao, L., Mowat, C. G., Forouhar, F., Tong, L., and Chapman, S. K. (2008) Histidine 55 of tryptophan 2,3-dioxygenase is not an active site base but regulates catalysis by controlling substrate binding, *Biochemistry 47*, 10677-10684.

74. Chauhan, N., Basran, J., Efimov, I., Svistunenko, D. A., Seward, H. E., Moody, P. C., and Raven, E. L. (2008) The role of serine 167 in human indoleamine 2,3-dioxygenase: A comparison with tryptophan 2,3-dioxygenase, *Biochemistry 47*, 4761-4769.

75. Abu-Omar, M. M., Loaiza, A., and Hontzeas, N. (2005) Reaction mechanisms of mononuclear non-heme iron oxygenases, *Chem. Rev. 105*, 2227-2252.

76. Denisov, I. G., Grinkova, Y. V., McLean, M. A., and Sligar, S. G. (2007) The one-electron autoxidation of human cytochrome P450 3A4, *J. Biol. Chem. 282*, 26865-26873.

77. Thackray, S. J., Mowat, C. G., and Chapman, S. K. (2008) Exploring the mechanism of tryptophan 2,3-dioxygenase, *Biochem. Soc. Trans. 36*, 1120-1123.

78. Fukumura, E., Sugimoto, H., Misumi, Y., Ogura, T., and Shiro, Y. (2009) Cooperative binding of L-Trp to human tryptophan 2,3-dioxygenase: Resonance Raman spectroscopic analysis, *J. Biochem. 145*, 505-515.

79. Ronsein, G. E., Oliveira, M. C. B., Miyamoto, S., Medeiros, M. H. G., and Di Mascio, P. (2008) Tryptophan oxidation by singlet molecular oxygen [O_2 ($^1\Delta_g$)]: Mechanistic studies using ^{18}O-labeled hydroperoxides, mass spectrometry, and light emission measurements, *Chem. Res. Toxicol. 21*, 1271-1283.

80. Ronsein, G. E., Oliveira, M. C. B., Miyamoto, S., Medeiros, M. H. G., and Di Mascio, P. (2009) Characterization of O_2 ($^1\Delta_g$)-derived oxidation products of tryptophan: A combination of tandem mass spectrometry analyses and isotopic labeling studies, *J. Am. Soc. Mass. Spectrom. 20*, 188-197.

81. Terentis, A. C., Thomas, S. R., Takikawa, O., Littlejohn, T. K., Truscott, R. J., Armstrong, R. S., Yeh, S. R., and Stocker, R. (2002) The heme environment of recombinant human indoleamine 2,3-dioxygenase. Structural properties and substrate-ligand interactions, *J. Biol. Chem. 277*, 15788-15794.

82. Yagil, G. (1967) The proton dissociation constant of pyrrole, indole and related compounds, *Tetrahedron 23*, 2855-2861.

83. Chauhan, N., Basran, J., Rafice, S. A., Efimov, I., Millett, E. S., Mowat, C. G., Moody, P. C. E., Handa, S., and Raven, E. L. (2012) How is the distal pocket of a heme protein optimized for binding of tryptophan?, *FEBS J. 279*, 4501-4509.

84. Geng, J., Dornevil, K., and Liu, A. (2012) Chemical rescue of the distal histidine mutants of tryptophan 2,3-dioxygenase, *J. Am. Chem. Soc. 134*, 12209-12218.

85. Chauhan, N., Thackray, S. J., Rafice, S. A., Eaton, G., Lee, M., Efimov, I., Basran, J., Jenkins, P. R., Mowat, C. G., Chapman, S. K., and Raven, E. L. (2009) Reassessment of the reaction mechanism in the heme dioxygenases, *J. Am. Chem. Soc. 131*, 4186-4187.

86. Yanagisawa, S., Horitani, M., Sugimoto, H., Shiro, Y., Okada, N., and Ogura, T. (2011) Resonance Raman study on the oxygenated and the ferryl-oxo species of indoleamine 2,3-dioxygenase during catalytic turnover, *Faraday Discuss. 148*, 239-247.

87. Basran, J., Efimov, I., Chauhan, N., Thackray, S. J., Krupa, J. L., Eaton, G., Griffith, G. A., Mowat, C. G., Handa, S., and Raven, E. L. (2011) The mechanism of formation of *N*-formylkynurenine by heme dioxygenases, *J. Am. Chem. Soc. 133*, 16251-16257.

88. Yanagisawa, S., Yotsuya, K., Hashiwaki, Y., Horitani, M., Sugimoto, H., Shiro, Y., Appelman, E. H., and Ogura, T. (2010) Identification of the Fe-O_2 and the Fe=O heme species for indoleamine 2,3-dioxygenase during catalytic turnover, *Chem. Lett. 39*, 36-37.

89. Hirata, F., Ohnishi, T., and Hayaishi, O. (1977) Indoleamine 2,3-dioxygenase. Characterization and properties of enzyme•O_2^- complex, *J. Biol. Chem. 252*, 4637-4642.

90. Daley-Yates, P. T., Powell, A. P., and Smith, L. L. (1988) Pulmonary indoleamine 2,3-dioxygenase activity and its significance in the response of rats, mice, and rabbits to oxidative stress, *Toxicol. Appl. Pharmacol. 96*, 222-232.

91. Taniguchi, T., Hirata, F., and Hayaishi, O. (1977) Intracellular utilization of superoxide anion by indoleamine 2,3-dioxygenase of rabbit enterocytes, *J. Biol. Chem. 252*, 2774-2776.

92. Ozaki, Y., Nichol, C. A., and Duch, D. S. (1987) Utilization of dihydroflavin mononucleotide and superoxide anion for the decyclization of L-tryptophan by murine epididymal indoleamine 2,3-dioxygenase, *Arch. Biochem. Biophys. 257*, 207-216.

93. Kobayashi, K., Hayashi, K., and Sono, M. (1989) Effects of tryptophan and pH on the kinetics of superoxide radical binding to indoleamine 2,3-dioxygenase studied by pulse radiolysis, *J. Biol. Chem. 264*, 15280-15283.

94. Rosell, F. I., Kuo, H. H., and Mauk, A. G. (2011) NADH oxidase activity of indoleamine 2,3-dioxygenase, *J. Biol. Chem. 286*, 29273-29283.

95. Freewan, M., Rees, M. D., Plaza, T. S. S., Glaros, E., Lim, Y. J., Wang, X. S., Yeung, A. W. S., Witting, P. K., Terentis, A. C., and Thomas, S. R. (2013) Human indoleamine 2,3-dioxygenase is a catalyst of physiological heme peroxidase reactions. Implications for the inhibition of dioxygenase activity by hydrogen peroxide, *J. Biol. Chem. 288*, 1548-1567.

96. Fu, R., Gupta, R., Geng, J., Dornevil, K., Wang, S., Zhang, Y., Hendrich, M. P., and Liu, A. (2011) Enzyme reactivation by hydrogen peroxide in heme-based tryptophan dioxygenase, *J. Biol. Chem. 286*, 26541-26554.

97. Ferry, G., Ubeaud, C., Lambert, P. H., Bertin, S., Coge, F., Chomarat, P., Delagrange, P., Serkiz, B., Bouchet, J. P., Truscottj, R. J. W., and Boutin, J. A. (2005) Molecular evidence that melatonin is enzymatically oxidized in a different manner than tryptophan: investigations with both indoleamine 2,3-dioxygenase and myeloperoxidase, *Biochem. J. 388*, 205-215.

98. van der Donk, W. A., Krebs, C., and Bollinger, J. M., Jr. (2010) Substrate activation by iron superoxo intermediates, *Curr. Opin. Struc. Biol. 20*, 673-683.

99. Lai, W. Z., and Shaik, S. (2011) Can ferric-superoxide act as a potential oxidant in $P450_{cam}$? QM/MM investigation of hydroxylation, epoxidation, and sulfoxidation, *J. Am. Chem. Soc. 133*, 5444-5452.

100. Minnihan, E. C., Nocera, D. G., and Stubbe, J. (2013) Reversible, long-range radical transfer in *E. coli* class Ia ribonucleotide reductase, *Acc. Chem. Res. 46*, 2524-2535.

101. Abu Tarboush, N., Jensen, L. M. R., Yukl, E. T., Geng, J., Liu, A., Wilmot, C. M., and Davidson, V. L. (2011) Mutagenesis of tryptophan199 suggests that hopping is required

for MauG-dependent tryptophan tryptophylquinone biosynthesis, *Proc. Natl. Acad. Sci. U.S.A. 108*, 16956-16961.

102. Gray, H. B., and Winkler, J. R. (2010) Electron flow through metalloproteins, *Biochim. Biophys. Acta. 1797*, 1563-1572.

103. Warren, J. J., Ener, M. E., Vlček, A. J., Winkler, J. R., and Gray, H. B. (2012) Electron hopping through proteins, *Coord. Chem. Rev. 256*, 2478-2487.

104. McIntire, W. S., Wemmer, D. E., Chistoserdov, A., and Lidstrom, M. E. (1991) A new cofactor in a prokaryotic enzyme: Tryptophan tryptophylquinone as the redox prosthetic group in methylamine dehydrogenase, *Science 252*, 817-824.

105. Eady, R. R., and Large, P. J. (1968) Purification and properties of an amine dehydrogenase from *Pseudomonas* AM1 and its role in growth on methylamine, *Biochem. J. 106*, 245-255.

106. Chen, L., Doi, M., Durley, R. C., Chistoserdov, A. Y., Lidstrom, M. E., Davidson, V. L., and Mathews, F. S. (1998) Refined crystal structure of methylamine dehydrogenase from *Paracoccus denitrificans* at 1.75 Å resolution, *J. Mol. Biol. 276*, 131-149.

107. Yukl, E. T., Liu, F., Krzystek, J., Shin, S., Jensen, L. M. R., Davidson, V. L., Wilmot, C. M., and Liu, A. (2013) Diradical intermediate within the context of tryptophan tryptophylquinone biosynthesis, *Proc. Natl. Acad. Sci. U.S.A. 110*, 4569-4573.

108. Li, X. H., Jones, L. H., Pearson, A. R., Wilmot, C. M., and Davidson, V. L. (2006) Mechanistic possibilities in MauG-dependent tryptophan tryptophylquinone biosynthesis, *Biochemistry 45*, 13276-13283.

109. Li, X., Fu, R., Lee, S. Y., Krebs, C., Davidson, V. L., and Liu, A. (2008) A catalytic di-heme *bis*-Fe(IV) intermediate, alternative to an Fe(IV)=O porphyrin radical, *Proc. Natl. Acad. Sci. U.S.A. 105*, 8597-8600.

110. Chistoserdov, A. Y., Boyd, J., Mathews, F. S., and Lidstrom, M. E. (1992) The genetic organization of the *mau* gene cluster of the facultative autotroph *Paracoccus denitrificans*, *Biochem. Biophys. Res. Commun. 184*, 1181-1189.

111. Li, X., Fu, R., Liu, A., and Davidson, V. L. (2008) Kinetic and physical evidence that the diheme enzyme MauG tightly binds to a biosynthetic precursor of methylamine dehydrogenase with incompletely formed tryptophan tryptophylquinone, *Biochemistry 47*, 2908-2912.

112. Jensen, L. M. R., Sanishvili, R., Davidson, V. L., and Wilmot, C. M. (2010) *In crystallo* posttranslational modification within a MauG/pre-methylamine dehydrogenase complex, *Science 327*, 1392-1394.

113. Fu, R., Liu, F., Davidson, V. L., and Liu, A. (2009) Heme iron nitrosyl complex of MauG reveals an efficient redox equilibrium between hemes with only one heme exclusively binding exogenous ligands, *Biochemistry 48*, 11603-11605.

114. Li, X. H., Feng, M. L., Wang, Y. T., Tachikawa, H., and Davidson, V. L. (2006) Evidence for redox cooperativity between c-type hemes of MauG which is likely coupled

to oxygen activation during tryptophan tryptophylquinone biosynthesis, *Biochemistry 45*, 821-828.

115. Yukl, E. T., Goblirsch, B. R., Davidson, V. L., and Wilmot, C. M. (2011) Crystal structures of CO and NO adducts of MauG in complex with pre-methylamine dehydrogenase: Implications for the mechanism of dioxygen activation, *Biochemistry 50*, 2931-2938.

116. Seidel, J., Schmitt, G., Hoffmann, M., Jendrossek, D., and Einsle, O. (2013) Structure of the processive rubber oxygenase RoxA from *Xanthomonas* sp, *Proc. Natl. Acad. Sci. U.S.A. 110*, 13833-13838.

117. Braaz, R., Fischer, P., and Jendrossek, D. (2004) Novel type of heme-dependent oxygenase catalyzes oxidative cleavage of rubber (poly-cis-1,4-isoprene), *Appl .Environ. Microbiol. 70*, 7388-7395.

118. Hoffmann, M., Seidel, J., and Einsle, O. (2009) CcpA from *Geobacter sulfurreducens* is a basic di-heme cytochrome *c* peroxidase, *J. Mol. Biol. 393*, 951-965.

119. Echalier, A., Goodhew, C. F., Pettigrew, G. W., and Fulop, V. (2006) Activation and catalysis of the di-heme cytochrome *c* peroxidase from *Paracoccus pantotrophus*, *Structure 14*, 107-117.

120. Zahn, J. A., Arciero, D. M., Hooper, A. B., Coats, J. R., and DiSpirito, A. A. (1997) Cytochrome *c* peroxidase from *Methylococcus capsulatus* Bath, *Arch. Microbiol. 168*, 362-372.

121. Arciero, D. M., and Hooper, A. B. (1994) A di-heme cytochrome *c* peroxidase from *Nitrosomonas europaea* catalytically active in both the oxidized and half-reduced states, *J. Biol. Chem. 269*, 11878-11886.

122. Bewley, K. D., Ellis, K. E., Firer-Sherwood, M. A., and Elliott, S. J. (2013) Multi-heme proteins: Nature's electronic multi-purpose tool, *Biochim. Biophys. Acta. 1827*, 938-948.

123. Pettigrew, G. W., Echalier, A., and Pauleta, S. R. (2006) Structure and mechanism in the bacterial dihaem cytochrome *c* peroxidases, *J. Inorg. Biochem. 100*, 551-567.

124. Jensen, L. M. R., Meharenna, Y. T., Davidson, V. L., Poulos, T. L., Hedman, B., Wilmot, C. M., and Sarangi, R. (2012) Geometric and electronic structures of the His-Fe(IV)=O and His-Fe(IV)-Tyr hemes of MauG, *J. Biol. Inorg. Chem. 17*, 1241-1255.

125. Fülöp, V., Ridout, C. J., Greenwood, C., and Hajdu, J. (1995) Crystal structure of the di-haem cytochrome *c* peroxidase from *Pseudomonas aeruginosa*, *Structure 3*, 1225-1233.

126. Bollinger, J. M., Jr., and Matthews, M. L. (2010) Remote enzyme microsurgery, *Science 327*, 1337-1338.

127. Behan, R. K., Hoffart, L. M., Stone, K. L., Krebs, C., and Green, M. T. (2006) Evidence for basic ferryls in cytochromes P450, *J. Am. Chem. Soc. 128*, 11471-11474.

128. Stone, K. L., Hoffart, L. M., Behan, R. K., Krebs, C., and Green, M. T. (2006) Evidence for two ferryl species in chloroperoxidase compound II, *J. Am. Chem. Soc. 128*, 6147-6153.

129. Groves, J. T., Quinn, R., McMurry, T. J., Nakamura, M., Lang, G., and Boso, B. (1985) Preparation and characterization of a dialkoxyiron(IV) porphyrin, *J. Am. Chem. Soc. 107,* 354-360.

130. Bill, E., Schünemann, V., Trautwein, A. X., Weiss, R., Fischer, J., Tabard, A., and Guilard, R. (2002) Mössbauer investigations of the hexachlorantimonate salt of the phenyliron 2,3,7,8,l2,13,17,18-octaethyl-5,10,15,20-tetraphenylporphyrinate, [Fe(oetpp)Ph]$SbCl_6$ and X-ray structure of the phenyliron(III) precursor Fe(III)(oetpp)Ph, *Inorganica. Chimica. Acta. 339,* 420-426.

131. Ikezaki, A., Takahashi, M., and Nakamura, M. (2013) Equilibrium between Fe(IV) porphyrin and Fe(III) porphyrin radical cation: New insight into the electronic structure of high-valent iron porphyrin complexes, *Chem. Commun. 49,* 3098-3100.

132. Abu Tarboush, N., Jensen, L. M. R., Feng, M., Tachikawa, H., Wilmot, C. M., and Davidson, V. L. (2010) Functional importance of tyrosine 294 and the catalytic selectivity for the bis-Fe(IV) state of MauG revealed by replacement of this axial heme ligand with histidine, *Biochemistry 49,* 9783-9791.

133. Abu Tarboush, N., Shin, S., Geng, J., Liu, A., and Davidson, V. L. (2012) Effects of the loss of the axial tyrosine ligand of the low-spin heme of MauG on its physical properties and reactivity, *FEBS Lett. 586,* 4339-4343.

134. Feng, M., Jensen, L. M. R., Yukl, E. T., Wei, X., Liu, A., Wilmot, C. M., and Davidson, V. L. (2012) Proline 107 is a major determinant in maintaining the structure of the distal pocket and reactivity of the high-spin heme of MauG, *Biochemistry 51,* 1598-1606.

135. Yukl, E. T., Williamson, H. R., Higgins, L., Davidson, V. L., and Wilmot, C. M. (2013) Oxidative damage in MauG: Implications for the control of high-valent iron species and radical propagation pathways, *Biochemistry 52*, 9447-9455.

136. Dias, J. M., Alves, T., Bonifácio, C., Pereira, A. S., Trincão, J., Bourgeois, D., Moura, I., and Romão, M. J. (2004) Structural basis for the mechanism of Ca^{2+} activation of the di-heme cytochrome *c* peroxidase from *Pseudomonas nautica* 617, *Structure 12*, 961-973.

137. Prazeres, S., Moura, J. J. G., Moura, I., Gilmour, R., Goodhew, C. F., Pettigrew, G. W., Ravi, N., and Huynh, B. H. (1995) Mossbauer characterization of *Paracoccus denitrificans* cytochrome *c* peroxidase - further evidence for redox and calcium binding-induced heme-heme interaction, *J. Biol. Chem. 270*, 24264-24269.

138. Chen, Y., Naik, S. G., Krzystek, J., Shin, S., Nelson, W. H., Xue, S., Yang, J. J., Davidson, V. L., and Liu, A. (2012) Role of calcium in metalloenzymes: Effects of calcium removal on the axial ligation geometry and magnetic properties of the catalytic diheme center in MauG, *Biochemistry 51*, 1586-1597.

139. Shin, S., Feng, M., Chen, Y., Jensen, L. M., Tachikawa, H., Wilmot, C. M., Liu, A., and Davidson, V. L. (2011) The tightly bound calcium of MauG is required for tryptophan tryptophylquinone cofactor biosynthesis, *Biochemistry 50*, 144-150.

140. Barry, S. M., and Challis, G. L. (2013) Mechanism and catalytic diversity of Rieske non-heme iron-dependent oxygenases, *ACS Catal. 3*, 2362-2370.

141. Bugg, T. D., and Ramaswamy, S. (2008) Non-heme iron-dependent dioxygenases: Unravelling catalytic mechanisms for complex enzymatic oxidations, *Curr. Opin. Chem. Biol. 12*, 134-140.

142. Wackett, L. P. (2002) Mechanism and applications of Rieske non-heme iron dioxygenases, *Enzyme Microb. Technol. 31*, 577-587.

143. Kovaleva, E. G., Neibergall, M. B., Chakrabarty, S., and Lipscomb, J. D. (2007) Finding intermediates in the O_2 activation pathways of non-heme iron oxygenases, *Acc. Chem. Res. 40*, 475-483.

144. Chakrabarty, S., Austin, R. N., Deng, D., Groves, J. T., and Lipscomb, J. D. (2007) Radical intermediates in monooxygenase reactions of rieske dioxygenases, *J. Am. Chem. Soc. 129*, 3514-3515.

145. Tiago de Oliveira, F., Chanda, A., Banerjee, D., Shan, X., Mondal, S., Que, L., Jr, Bominaar, E. L., Münck, E., and Collins, T. J. (2007) Chemical and spectroscopic evidence for an Fe^{V}-oxo complex, *Science 315*, 835-838.

146. Prat, I., Mathieson, J. S., Guell, M., Ribas, X., Luis, J. M., Cronin, L., and Costas, M. (2011) Observation of Fe(V)=O using variable-temperature mass spectrometry and its enzyme-like C-H and C=C oxidation reactions, *Nat. Chem. 3*, 788-793.

147. Torres-Alacan, J., Das, U., Filippou, A. C., and Vohringer, P. (2013) Observing the formation and the reactivity of an octahedral iron(V) nitrido complex in real time, *Angew. Chem. Int. Ed. 52*, 12833-12837.

148. Lang, G., Spartalian, K., and Yonetani, T. (1976) Mössbauer spectroscopic study of compound ES of cytochrome *c* peroxidase, *Biochim. Biophys. Acta. 451*, 250-258.

149. Ho, P. S., Hoffman, B. M., Kang, C. H., and Margoliash, E. (1983) Control of the transfer of oxidizing equivalents between heme iron and free radical site in yeast cytochrome *c* peroxidase, *J. Biol. Chem. 258*, 4356-4363.

150. Lee, S. K., Nesheim, J. C., and Lipscomb, J. D. (1993) Transient intermediates of the methane monooxygenase catalytic cycle, *J. Biol. Chem. 268*, 21569-21577.

151. Shu, L., Nesheim, J. C., Kauffmann, K., Münck, E., Lipscomb, J. D., and Que, L., Jr. (1997) An $Fe_2^{IV}O_2$ diamond core structure for the key intermediate Q of methane monooxygenase, *Science 275*, 515-518.

152. Geng, J., Dornevil, K., Davidson, V. L., and Liu, A. (2013) Tryptophan-mediated charge-resonance stabilization in the *bis*-Fe(IV) redox state of MauG, *Proc. Natl. Acad. Sci. U.S.A. 110*, 9639-9644.

153. Byrdin, M., Villette, S., Eker, A. P., and Brettel, K. (2007) Observation of an intermediate tryptophanyl radical in W306F mutant DNA photolyase from *Escherichia coli* supports electron hopping along the triple tryptophan chain, *Biochemistry 46*, 10072-10077.

154. Li, J. S., Han, Q., Fang, J., Rizzi, M., James, A. A., and Li, J. (2007) Biochemical mechanisms leading to tryptophan 2,3-dioxygenase activation, *Arch. Insect Biochem. Physiol. 64*, 74-87.

155. Brady, F. O., Forman, H. J., and Feigelson, P. (1971) The role of superoxide and hydroperoxide in the reductive activation of tryptophan-2,3-dioxygenase, *J. Biol. Chem. 246*, 7119-7124.

156. Gupta, R., Fu, R., Liu, A., and Hendrich, M. P. (2010) EPR and Mossbauer spectroscopy show inequivalent hemes in tryptophan dioxygenase, *J. Am. Chem. Soc. 132*, 1098-1109.

157. Becke, A. D. (1993) Density-functional thermochemistry. 3. The role of exact exchange, *J. Chem. Phys. 98*, 5648-5652.

158. Wachters, A. J. H. (1970) Gaussian basis set for molecular wavefunctions containing third-row atoms, *J. Chem. Phys. 52*, 1033-1036.

159. Zhang, Y., and Oldfield, E. (2004) Cytochrome P450: An investigation of the Mössbauer spectra of a reaction intermediate and an Fe(IV)=O model system, *J. Am. Chem. Soc. 126*, 4470-4471.

160. Ling, Y., Davidson, V. L., and Zhang, Y. (2010) Unprecedented Fe(IV) species in a diheme protein MauG: A quantum chemical investigation on the unusual Mössbauer spectroscopic properties, *J. Phys. Chem. Lett. 1*, 2936-2939.

161. Becke, A. D. (1988) Density-functional exchange-energy approximation with correct asymptotic behavior, *Phys. Rev. A 38*, 3098-3100.

162. Perdew, J. P., Burke, K., and Wang, Y. (1996) Generalized gradient approximation for the exchange-correlation hole of a many-electron system, *Phys. Rev. B 54*, 16533-16539.

163. Debrunner, P. G. (1989) *Iron Porphyrins*, Vol. 3, VCH Publishers, Inc., NY.

164. Münck, E. (2000) *Aspects of ^{57}Fe Mössbauer Spectroscopy*, University Science Books, Saussalito, CA.

165. Stubbe, J., and van der Donk, W. A. (1998) Protein radicals in enzyme catalysis, *Chem. Rev. 98*, 705-762.

166. Liu, A. (2009) Electron paramagnetic resonance (EPR) in enzymology, In *Wiley Encyclopedia of Chemical Biology*, 591-601, John Wiley and Sons, Inc.

167. Yonetani, T. (1965) Studies on cytochrome *c* peroxidase, *J. Biol. Chem. 240*, 4509-4514.

168. Sivaraja, M., Goodin, D., Smith, M., and Hoffman, B. (1989) Identification by ENDOR of Trp191 as the free-radical site in cytochrome *c* peroxidase compound ES, *Science 245*, 738-740.

169. Yamamoto, S., and Hayaishi, O. (1970) Tryptophan 2,3-dioxygenase (tryptophan pyrrolase), *Methods Enzymol. 17*, 434-438.

170. Mehler, A. H., and Knox, W. E. (1950) The conversion of tryptophan to kynurenine in liver. II. The enzymatic hydrolysis of formylkynurenine, *J. Biol. Chem. 187*, 431-438.

171. Basran, J., Rafice, S. A., Chauhan, N., Efimov, I., Cheesman, M. R., Ghamsari, L., and Raven, E. L. (2008) A kinetic, spectroscopic, and redox study of human tryptophan 2,3-dioxygenase, *Biochemistry 47*, 4752-4760.

172. Dalosto, S. D., Vanderkooi, J. M., and Sharp, K. A. (2004) Vibrational stark effects on carbonyl, nitrile, and nitrosyl compounds including heme ligands, CO, CN, and NO, studied with density functional theory, *J. Phys. Chem. B. 108*, 6450-6457.

173. Pfister, T. D., Ohki, T., Ueno, T., Hara, I., Adachi, S., Makino, Y., Ueyama, N., Lu, Y., and Watanabe, Y. (2005) Monooxygenation of an aromatic ring by F43W/H64D/V68I myoglobin mutant and hydrogen peroxide. Myoglobin mutants as a model for P450 hydroxylation chemistry, *J. Biol. Chem. 280*, 12858-12866.

174. Nagy, J. M., Cass, A. E. G., and Brown, K. A. (1997) Purification and characterization of recombinant catalase-peroxidase, which confers isoniazid sensitivity in *Mycobacterium tuberculosis*, *J. Biol. Chem. 272*, 31265-31271.

175. Claiborne, A., and Fridovich, I. (1979) Purification of the *o*-dianisidine peroxidase from *Escherichia coli* B. Physicochemical characterization and analysis of its dual catalatic and peroxidatic activities, *J. Biol. Chem. 254*, 4245-4252.

176. Johnsson, K., Froland, W. A., and Schultz, P. G. (1997) Overexpression, purification, and characterization of the catalase-peroxidase KatG from *Mycobacterium tuberculosis*, *J. Biol. Chem. 272*, 2834-2840.

177. Varnado, C. L., Hertwig, K. M., Thomas, R., Roberts, J. K., and Goodwin, D. C. (2004) Properties of a novel periplasmic catalase-peroxidase from *Escherichia coli* O157:H7, *Arch. Biochem. Biophys. 421*, 166-174.

178. Jeng, W. Y., Tsai, Y. H., and Chuang, W. J. (2004) The catalase activity of *N*α-acetyl-microperoxidase-8, *J. Pept. Res. 64*, 104-109.

179. Paco, L., Galarneau, A., Drone, J., Fajula, F., Bailly, C., Pulvin, S., and Thomas, D. (2009) Catalase-like activity of bovine met-hemoglobin: Interaction with the pseudo-

catalytic peroxidation of anthracene traces in aqueous medium, *Biotechnol. J. 4*, 1460-1470.

180. Deisseroth, A., and Dounce, A. L. (1970) Catalase: Physical and chemical properties, mechanism of catalysis, and physiological role, *Physiol. Rev. 50*, 319-375.

181. Gouet, P., Jouve, H. M., Williams, P. A., Andersson, I., Andreoletti, P., Nussaume, L., and Hajdu, J. (1996) Ferryl intermediates of catalase captured by time-resolved Weissenberg crystallography and UV-vis spectroscopy, *Nat. Struct. Biol. 3*, 951-956.

182. Schünemann, V., Jung, C., Trautwein, A. X., Mandon, D., and Weiss, R. (2000) Intermediates in the reaction of substrate-free cytochrome $P450_{cam}$ with peroxy acetic acid, *FEBS Lett. 479*, 149-154.

183. Hoffman, B. M., Roberts, J. E., Kang, C. H., and Margoliash, E. (1981) Electron paramagnetic and electron nuclear double resonance of the hydrogen peroxide compound of cytochrome *c* peroxidase, *J. Biol. Chem. 256*, 6556-6564.

184. Schünemann, V., Lendzian, F., Jung, C., Contzen, J., Barra, A.-L., Sligar, S. G., and Trautwein, A. X. (2004) Tyrosine radical formation in the reaction of wild type and mutant cytochrome $P450_{cam}$ with peroxy acids, *J. Biol. Chem. 279*, 10919-10930.

185. Tsai, A. L., and Kulmacz, R. J. (2010) Prostaglandin H synthase: Resolved and unresolved mechanistic issues, *Arch. Biochem. Biophys. 493*, 103-124.

186. Green, M. T., Dawson, J. H., and Gray, H. B. (2004) Oxoiron(IV) in chloroperoxidase compound II is basic: Implications for P450 chemistry, *Science 304*, 1653-1656.

187. Behan, R. K., and Green, M. T. (2006) On the status of ferryl protonation, *J. Inorg. Biochem. 100*, 448-459.

188. Horner, O., Mouesca, J. M., Solari, P. L., Orio, M., Oddou, J. L., Bonville, P., and Jouve, H. M. (2007) Spectroscopic description of an unusual protonated ferryl species in the catalase from *Proteus mirabilis* and density functional theory calculations on related models. Consequences for the ferryl protonation state in catalase, peroxidase and chloroperoxidase, *J. Biol. Inorg. Chem. 12*, 509-525.

189. Schulz, C. E., Rutter, R., Sage, J. T., Debrunner, P. G., and Hager, L. P. (1984) Mössbauer and electron paramagnetic resonance studies of horseradish peroxidase and its catalytic intermediates, *Biochemistry 23*, 4743-4754.

190. Harami, T., Maeda, Y., Morita, Y., Trautwein, A., and Gonser, U. (1977) Mössbauer spectroscopic determination of the electronic structure of highly oxidized iron in hemoproteins, *J. Chem. Phys. 67*, 1164-1169.

191. Maeda, Y., Higashimura, T., and Morita, Y. (1967) Mössbauer effect in peroxidase, *Biochem. Biophys. Res. Commun. 29*, 362-367.

192. Garcia-Serres, R., Davydov, R. M., Matsui, T., Ikeda-Saito, M., Hoffman, B. M., and Huynh, B. H. (2007) Distinct reaction pathways followed upon reduction of oxy-heme oxygenase and oxy-myoglobin as characterized by Mössbauer spectroscopy, *J. Am. Chem. Soc. 129*, 1402-1412.

193. Rutter, R., Hager, L. P., Dhonau, H., Hendrich, M., Valentine, M., and Debrunner, P. (1984) Chloroperoxidase compound I: Electron paramagnetic resonance and Mössbauer studies, *Biochemistry 23*, 6809-6816.

194. Bender, M. L., and Kemp, K. C. (1957) Kinetics of the α-chymotrypsin-catalyzed oxygen exchange of carboxylic acids, *J. Am. Chem. Soc. 79*, 116-120.

195. Byrn, M., and Calvin, M. (1966) Oxygen-18 exchange reactions of aldehydes and ketones, *J. Am. Chem. Soc. 88*, 1916-1922.

196. Poljak, A., Grant, R., Austin, C. J., Jamie, J. F., Willows, R. D., Takikawa, O., Littlejohn, T. K., Truscott, R. J., Walker, M. J., Sachdev, P., and Smythe, G. A. (2006) Inhibition of indoleamine 2,3 dioxygenase activity by H_2O_2, *Arch. Biochem. Biophys. 450*, 9-19.

197. Abu-Soud, H. M., and Hazen, S. L. (2000) Nitric oxide is a physiological substrate for mammalian peroxidases, *J. Biol. Chem. 275*, 37524-37532.

198. De Marinis, E., Casella, L., Ciaccio, C., Coletta, M., Visca, P., and Ascenzi, P. (2009) Catalytic peroxidation of nitrogen monoxide and peroxynitrite by globins, *IUBMB Life 61*, 62-73.

199. Eiserich, J. P., Hristova, M., Cross, C. E., Jones, A. D., Freeman, B. A., Halliwell, B., and van der Vliet, A. (1998) Formation of nitric oxide-derived inflammatory oxidants by myeloperoxidase in neutrophils, *Nature 391*, 393-397.

200. Burner, U., Furtmuller, P. G., Kettle, A. J., Koppenol, W. H., and Obinger, C. (2000) Mechanism of reaction of myeloperoxidase with nitrite, *J. Biol. Chem. 275*, 20597-20601.

201. Kuo, H. H., and Mauk, A. G. (2012) Indole peroxygenase activity of indoleamine 2,3-dioxygenase, *Proc. Natl. Acad. Sci. U.S.A 109*, 13966-13971.

202. Maghzal, G. J., Thomas, S. R., Hunt, N. H., and Stocker, R. (2008) Cytochrome b_5, not superoxide anion radical, is a major reductant of indoleamine 2,3-dioxygenase in human cells, *J. Biol. Chem. 283*, 12014-12025.

203. Vottero, E., Mitchell, D. A., Page, M. J., MacGillivray, R. T. A., Sadowski, I. J., Roberge, M., and Mauk, A. G. (2006) Cytochrome b_5 is a major reductant in vivo of human indoleamine 2,3-dioxygenase expressed in yeast, *FEBS Lett. 580*, 2265-2268.

204. Collman, J. P., Brauman, J. I., Halbert, T. R., and Suslick, K. S. (1976) Nature of O_2 and CO binding to metalloporphyrins and heme proteins, *Proc. Natl. Acad. Sci. U.S.A. 73*, 3333-3337.

205. Tsai, A. L., Kulmacz, R. J., Wang, J. S., Wang, Y., Vanwart, H. E., and Palmer, G. (1993) Heme coordination of prostaglandin H synthase, *J. Biol. Chem. 268*, 8554-8563.

206. Ikeda-Saito, M., and Iizuka, T. (1975) Studies on the heme environment of horse heart ferric cytochrome *c*. Azide and imidazole complexes of ferric cytochrome *c*, *Biochim. Biophys. Acta 393*, 335-342.

207. Gadsby, P. M. A., and Thomson, A. J. (1990) Assignment of the axial ligands of ferric ion in low-spin hemoproteins by near-infrared magnetic circular dichroism and electron paramagnetic resonance spectroscopy, *J. Am. Chem. Soc. 112*, 5003.

208. Walker, F. A. (2004) Models of the bis-histidine-ligated electron-transferring cytochromes. Comparative geometric and electronic structure of low-spin ferro- and ferrihemes, *Chem. Rev. 104*, 589-615.

209. Walker, F. A. (1999) Magnetic spectroscopic (EPR, ESEEM, Mössbauer, MCD and NMR) studies of low-spin ferriheme centers and their corresponding heme proteins, *Coord. Chem. Rev. 185-6*, 471-534.

210. Zoppellaro, G., Bren, K. L., Ensign, A. A., Harbitz, E., Kaur, R., Hersleth, H.-P., Ryde, U., Hederstedt, L., and Andersson, K. K. (2009) Review: Studies of ferric heme proteins with highly anisotropic/highly axial low spin (S = 1/2) electron paramagnetic resonance signals with bis-histidine and histidine-methionine axial iron coordination, *Biopolymers 91*, 1064-1082.

211. Uchida, K., Shimizu, T., Makino, R., Sakaguchi, K., Iizuka, T., Ishimura, Y., Nozawa, T., and Hatano, M. (1983) Magnetic and natural circular dichroism of L-tryptophan 2,3-dioxygenases and indoleamine 2,3-dioxygenase. II. Spectra of their ferric cyanide and ferrous carbon monoxide complexes and an oxygenated form, *J. Biol. Chem. 258*, 2526-2533.

212. Papadopoulou, N. D., Mewies, M., McLean, K. J., Seward, H. E., Svistunenko, D. A., Munro, A. W., and Raven, E. L. (2005) Redox and spectroscopic properties of human

indoleamine 2,3-dioxygenase and a His303Ala variant: Implications for catalysis, *Biochemistry 44*, 14318-14328.

213. Sono, M., and Dawson, J. H. (1984) Extensive studies of the heme coordination structure of indoleamine 2,3-dioxygenase and of tryptophan binding with magnetic and natural circular dichroism and electron paramagnetic resonance spectroscopy, *Biochim. Biophys. Acta 789*, 170-187.

214. Yonetani, T., and Anni, H. (1987) Yeast cytochrome *c* peroxidase. Coordination and spin states of heme prosthetic group, *J. Biol. Chem. 262*, 9547-9554.

215. An, H. Q., Tu, C. K., Duda, D., Montanez-Clemente, I., Math, K., Laipis, P. J., McKenna, R., and Silverman, D. N. (2002) Chemical rescue in catalysis by human carbonic anhydrases II and III, *Biochemistry 41*, 3235-3242.

216. Lehoux, I. E., and Mitra, B. (1999) (*S*)-Mandelate dehydrogenase from *Pseudomonas putida*: Mutations of the catalytic base histidine-274 and chemical rescue of activity, *Biochemistry 38*, 9948-9955.

217. Ghanem, M., and Gadda, G. (2005) On the catalytic role of the conserved active site residue His466 of choline oxidase, *Biochemistry 44*, 893-904.

218. Wilks, A., Sun, J., Loehr, T. M., and Ortiz de Montellano, P. R. (1995) Heme oxygenase His25ala mutant - replacement of the proximal histidine iron ligand by exogenous bases restores catalytic activity, *J. Am. Chem. Soc. 117*, 2925-2926.

219. Newmyer, S. L., and Ortiz de Montellano, P. R. (1996) Rescue of the catalytic activity of an H42A mutant of horseradish peroxidase by exogenous imidazoles, *J. Biol. Chem. 271*, 14891-14896.

220. Salerno, J. C., and Leigh, J. S. (1984) Crystal field of atypical low-spin ferriheme complexes, *J. Am. Chem. Soc. 106*, 2156-2159.

221. Migita, C. T., and Iwaizumi, M. (1981) Low-temperature EPR studies of highly anisotropic low-spin (protoporphyrinato)iron(III) complexes, *J. Am. Chem. Soc. 103*, 4378-4381.

222. Berka, V., Palmer, G., Chen, P. F., and Tsai, A. L. (1998) Effects of various imidazole ligands on heme conformation in endothelial nitric oxide synthase, *Biochemistry 37*, 6136-6144.

223. Silaghi-Dumitrescu, R., Reeder, B. J., Nicholls, P., Cooper, C. E., and Wilson, M. T. (2007) Ferryl haem protonation gates peroxidatic reactivity in globins, *Biochem. J. 403*, 391-395.

224. Davidson, V. L. (2001) Pyrroloquinoline quinone (PQQ) from methanol dehydrogenase and tryptophan tryptophylquinone (TTQ) from methylamine dehydrogenase, *Adv. Protein Chem. 58*, 95-140.

225. Wang, Y., Li, X., Jones, L. H., Pearson, A. R., Wilmot, C. M., and Davidson, V. L. (2005) MauG-dependent in vitro biosynthesis of tryptophan tryptophylquinone in methylamine dehydrogenase, *J. Am. Chem. Soc. 127*, 8258-8259.

226. Choi, M., Shin, S., and Davidson, V. L. (2012) Characterization of electron tunneling and hole hopping reactions between different forms of MauG and methylamine dehydrogenase within a natural protein complex, *Biochemistry 51*, 6942-6949.

227. Davidson, V. L. (1990) Methylamine dehydrogenases from methylotrophic bacteria, *Methods Enzymol. 188*, 241-246.

228. Shin, S., Abu Tarboush, N., and Davidson, V. L. (2010) Long-range electron transfer reactions between hemes of MauG and different forms of tryptophan tryptophylquinone of methylamine dehydrogenase, *Biochemistry 49*, 5810-5816.

229. Berry, E. A., and Trumpower, B. L. (1987) Simultaneous determination of hemes *a*, *b*, and *c* from pyridine hemochrome spectra, *Anal. Biochem. 161*, 1-15.

230. Foote, N., Peterson, J., Gadsby, P. M., Greenwood, C., and Thomson, A. J. (1985) Redox-linked spin-state changes in the di-haem cytochrome *c*-551 peroxidase from *Pseudomonas aeruginosa*, *Biochem. J. 230*, 227-237.

231. Fülöp, V., Watmough, N. J., and Ferguson, S. J. (2000) Structure and enzymology of two bacterial diheme enzymes: Cytochrome cd_1 nitrite reductase and cytochrome *c* peroxidase, *Adv. Inorg. Chem 51*, 163.

232. Lee, S., Shin, S., Li, X., and Davidson, V. L. (2009) Kinetic mechanism for the initial steps in MauG-dependent tryptophan tryptophylquinone biosynthesis, *Biochemistry 48*, 2442-2447.

233. Makris, T. M., von Koenig, K., Schlichting, I., and Sligar, S. G. (2006) The status of high-valent metal oxo complexes in the P450 cytochromes, *J. Inorg. Biochem. 100*, 507-518.

234. Sheng, X., Horner, J. H., and Newcomb, M. (2008) Spectra and kinetic studies of the compound I derivative of cytochrome P450 119, *J. Am. Chem. Soc. 130*, 13310-13320.

235. Dolphin, D., Forman, A., Borg, D. C., Fajer, J., and Felton, R. H. (1971) Compounds I of catalase and horse radish peroxidase: Pi-cation radicals, *Proc. Natl. Acad. Sci. U.S.A. 68*, 614-618.

236. Bell, S. R., and Groves, J. T. (2009) A highly reactive P450 model compound I, *J. Am. Chem. Soc. 131*, 9640-9641.

237. Das, T. K., Couture, M., Lee, H. C., Peisach, J., Rousseau, D. L., Wittenberg, B. A., Wittenberg, J. B., and Guertin, M. (1999) Identification of the ligands to the ferric heme of *Chlamydomonas chloroplast* hemoglobin: Evidence for ligation of tyrosine-63 (B10) to the heme, *Biochemistry 38*, 15360-15368.

238. Page, C. C., Moser, C. C., Chen, X. X., and Dutton, P. L. (1999) Natural engineering principles of electron tunnelling in biological oxidation-reduction, *Nature 402*, 47-52.

239. Davidson, V. L. (2008) Protein control of true, gated, and coupled electron transfer reactions, *Acc. Chem. Res. 41*, 730-738.

240. Beratan, D. N., Skourtis, S. S., Balabin, I. A., Balaeff, A., Keinan, S., Venkatramani, R., and Xiao, D. (2009) Steering electrons on moving pathways, *Acc. Chem. Res. 42,* 1669-1678.

241. Gray, H. B., and Winkler, J. R. (2003) Electron tunneling through proteins, *Q. Rev. Biophys. 36,* 341-372.

242. Davidson, V. L. (1996) Unraveling the kinetic complexity of interprotein electron transfer reactions, *Biochemistry 35,* 14035-14039.

243. Davidson, V. L. (2000) What controls the rates of interprotein electron-transfer reactions, *Acc. Chem. Res. 33,* 87-93.

244. Baldwin, J., Krebs, C., Ley, B. A., Edmondson, D. E., Huynh, B. H., and Bollinger, J. M., Jr. (2000) Mechanism of rapid electron transfer during oxygen activation in the R2 subunit of *Escherichia coli* ribonucleotide reductase. 1. Evidence for a transient tryptophan radical, *J. Am. Chem. Soc. 122,* 12195-12206.

245. Lukacs, A., Eker, A. P. M., Byrdin, M., Brettel, K., and Vos, M. H. (2008) Electron hopping through the 15 angstrom triple tryptophan molecular wire in DNA photolyase occurs within 30 ps, *J. Am. Chem. Soc. 130,* 14394-+.

246. Giese, B., Graber, M., and Cordes, M. (2008) Electron transfer in peptides and proteins, *Curr. Opin. Chem. Biol. 12,* 755-759.

247. Stayton, P. S., and Sligar, S. G. (1991) Structural microheterogeneity of a tryptophan residue required for efficient biological electron transfer between putidaredoxin and cytochrome P-450$_{cam}$, *Biochemistry 30*, 1845-1851.

248. Battistuzzi, G., Bellei, M., Bortolotti, C. A., and Sola, M. (2010) Redox properties of heme peroxidases, *Arch. Biochem. Biophys. 500*, 21-36.

249. Goodin, D. B., and McRee, D. E. (1993) The Asp-His-Fe triad of cytochrome *c* peroxidase controls the reduction potential, electronic structure, and coupling of the tryptophan free radical to the heme, *Biochemistry 32*, 3313-3324.

250. Henry, E. R., and Hochstrasser, R. M. (1987) Molecular dynamics simulations of fluorescence polarization of tryptophans in myoglobin, *Proc. Natl. Acad. Sci. U.S.A. 84*, 6142-6146.

251. Colin, J., Wiseman, B., Switala, J., Loewen, P. C., and Ivancich, A. (2009) Distinct role of specific tryptophans in facilitating electron transfer or as [Fe(IV)=O Trp$^{\bullet}$] intermediates in the peroxidase reaction of *Bulkholderia pseudomallei* catalase-peroxidase: A multifrequency EPR spectroscopy investigation, *J. Am. Chem. Soc. 131*, 8557-8563.

252. Pogni, R., Baratto, M. C., Teutloff, C., Giansanti, S., Ruiz-Dueñas, F. J., Choinowski, T., Piontek, K., Martínez, A. T., Lendzian, F., and Basosi, R. (2006) A tryptophan neutral radical in the oxidized state of versatile peroxidase from *Pleurotus eryngii*: A combined multifrequency EPR and density functional theory study, *J. Biol. Chem 281*, 9517-9526.

253. Graichen, M. E., Jones, L. H., Sharma, B. V., van Spanning, R. J. M., Hosler, J. P., and Davidson, V. L. (1999) Heterologous expression of correctly assembled methylamine dehydrogenase in *Rhodobacter sphaeroides*, *J. Bacteriol. 181*, 4216-4222.

254. Kurnikov, I. V. HARLEM program, Carriegia Mellon University, http://harlem.chem.cmu.edu/index.php/Main_Page#HARLEM_-_Molecular_Modeling_Package.

255. Shin, S., Lee, S., and Davidson, V. L. (2009) Suicide inactivation of MauG during reaction with O_2 or H_2O_2 in the absence of its natural protein substrate, *Biochemistry 48*, 10106-10112.

256. Marcus, R. A., and Sutin, N. (1985) Electron transfers in chemistry and biology, *Biochim. Biophys. Acta 811*, 265-322.

257. Navaratnam, S., and Parsons, B. J. (1998) Reduction potential of histidine free radicals: A pulse radiolysis study, *J. Chem. Soc. Faraday Trans. 94*, 2577-2581.

258. Tommos, C., Skalicky, J. J., Pilloud, D. L., Wand, A. J., and Dutton, P. L. (1999) *De novo* proteins as models of radical enzymes, *Biochemistry 38*, 9495-9507.

259. Milligan, J. R., Aguilera, J. A., Ly, A., Tran, N. Q., Hoang, O., and Ward, J. F. (2003) Repair of oxidative DNA damage by amino acids, *Nucleic Acids Res. 31*, 6258-6263.

260. DeFelippis, M. R., Murthy, C. P., Faraggi, M., and Klapper, M. H. (1989) Pulse radiolytic measurement of redox potentials: The tyrosine and tryptophan radicals, *Biochemistry 28*, 4847-4853.

261. Badger, B., and Brocklehurst, B. (1968) Formation of dimer cations of aromatic hydrocarbons, *Nature 219*, 263.

262. Magueres, P. L., Lindeman, S. V., and Kochi, J. K. (2000) Novel (Heteromolecular) π-complexes of aromatic cation radicals. Isolation and structural characterization, *Org. Lett. 2*, 3567-3570.

263. Sun, D., Rosokha, S. V., Lindeman, S. V., and Kochi, J. K. (2003) Intervalence (charge-resonance) transitions in organic mixed-valence systems. Through-space versus through-bond electron transfer between bridged aromatic (redox) centers, *J. Am. Chem. Soc. 125*, 15950-15963.

264. Rosokha, S. V., Sun, D., and Kochi, J. K. (2002) Conformation, distance, and connectivity effects on intramolecular electron transfer between phenylene-bridged aromatic redox centers, *J. Phys. Chem. A 106*, 2283-2292.

265. Lindeman, S. V., Rosokha, S. V., Sun, D., and Kochi, J. K. (2002) X-ray structure analysis and the intervalent electron transfer in organic mixed-valence crystals with bridged aromatic cation radicals, *J. Am. Chem. Soc. 124*, 843-855.

266. Bloch-Mechkour, A., Bally, T., and Marcinek, A. (2011) Dimer radical cations of indole and indole-3-carbinol: Localized and delocalized radical cations of diindolylmethane, *J. Phys. Chem. A 115*, 7700-7708.

267. Breton, J., Nabedryk, E., and Parson, W. W. (1992) A new infrared electronic transition of the oxidized primary electron donor in bacterial reaction centers - a way to assess resonance interactions between the bacteriochlorophylls, *Biochemistry 31*, 7503-7510.

268. Kanchanawong, P., Dahlbom, M. G., Treynor, T. P., Reimers, J. R., Hush, N. S., and Boxer, S. G. (2006) Charge delocalization in the special-pair radical cation of mutant reaction centers of *Rhodobacter sphaeroides* from Stark spectra and nonadiabatic spectral simulations, *J. Phys. Chem. B 110*, 18688-18702.

269. Que, L., Jr. (2007) The road to non-heme oxoferryls and beyond, *Acc. Chem. Res. 40*, 493-500.

270. Decker, A., Rohde, J. U., Que, L., Jr., and Solomon, E. I. (2004) Spectroscopic and quantum chemical characterization of the electronic structure and bonding in a non-heme Fe^{IV}=O complex, *J. Am. Chem. Soc. 126*, 5378-5379.

271. Orgel, L. E. (1960) *An Introduction to Transition-Metal Chemistry: Ligand-Field Theory*, 2nd Ed., Methuen, London.

272. Wittenberg, B. A., Kampa, L., Wittenberg, J. B., Blumberg, W. E., and Peisach, J. (1968) The electronic structure of protoheme proteins. II. An electron paramagnetic resonance and optical study of cytochrome *c* peroxidase and its derivatives, *J. Biol. Chem. 243*, 1863-1870.

273. Hewson, W. D., and Hager, L. P. (1979) Oxidation of horseradish peroxidase compound II to compound I, *J. Biol. Chem. 254*, 3182-3186.

274. Lardinois, O. M., and Ortiz de Montellano, P. R. (2004) Autoreduction of ferryl myoglobin: Discrimination among the three tyrosine and two tryptophan residues as electron donors, *Biochemistry 43*, 4601-4610.

275. Heckmann, A., and Lambert, C. (2012) Organic mixed-valence compounds: A playground for electrons and holes, *Angew. Chem. Int. Ed. 51*, 326-392.

276. Hausser, K. H., and Murrell, J. N. (1957) Pi complexes between organic free radicals, *J. Chem. Phys. 27*, 500-504.

277. Fajer, J., Borg, D. C., Forman, A., Dolphin, D., and Felton, R. H. (1970) Pi-cation radicals and dications of metalloporphyrins, *J. Am. Chem. Soc. 92*, 3451-3459.

278. Fuhrhop, J. H., Wasser, P., Riesner, D., and Mauzerall, D. (1972) Dimerization and π bonding of a zinc porphyrin cation radical. Thermodynamics and fast reaction kinetics, *J. Am. Chem. Soc. 94*, 7996-8001.

279. Brancato-Buentello, K. E., Kang, S. J., and Scheidt, W. R. (1997) Metalloporphyrin mixed-valence π cation radicals: Solution stability and properties, *J. Am. Chem. Soc. 119*, 2839-2846.

280. Lü, J. M., Rosokha, S. V., and Kochi, J. K. (2003) Stable (long-bonded) dimers via the quantitative self-association of different cationic, anionic, and uncharged π-radicals: Structures, energetics, and optical transitions, *J. Am. Chem. Soc. 125*, 12161-12171.

281. Takai, A., Gros, C. P., Barbe, J. M., Guilard, R., and Fukuzumi, S. (2009) Enhanced electron-transfer properties of cofacial porphyrin dimers through π-π interactions, *Chem. Eur. J. 15*, 3110-3122.

282. Bockman, T. M., and Kochi, J. K. (1990) Isolation and oxidation-reduction of methylviologen cation radicals. Novel disproportionation in charge-transfer salts by X-ray crystallography, *J. Org. Chem. 55*, 4127-4135.

283. Song, H., Orosz, R. D., Reed, C. A., and Scheidt, W. R. (1990) Dimerization of metalloporphyrin π cation radicals. Characterization of two novel dimers: $[Zn(OEP^{\bullet})(OH_2)]_2(ClO_4)_2$ and $[Ni(OEP)]_2(ClO_4)_2$, *Inorg. Chem. 29*, 4274-4282.

284. Kochi, J. K., Rathore, R., and Magueres, P. L. (2000) Stable dimeric aromatic cation-radicals. Structural and spectral characterization of through-space charge delocalization, *J. Org. Chem. 65*, 6826-6836.

285. Viola, F., Aime, S., Coletta, M., Desideri, A., Fasano, M., Paoletti, S., Tarricone, C., and Ascenzi, P. (1996) Azide, cyanide, fluoride, imidazole and pyridine binding to ferric and ferrous native horse heart cytochrome *c* and to its carboxymethylated derivative: A comparative study, *J. Inorg. Biochem. 62*, 213-222.

286. Winkler, W. C., Gonzalez, G., Wittenberg, J. B., Hille, R., Dakappagari, N., Jacob, A., Gonzalez, L. A., and Gilles-Gonzalez, M. A. (1996) Nonsteric factors dominate binding of nitric oxide, azide, imidazole, cyanide, and fluoride to the rhizobial heme-based oxygen sensor FixL, *Chem. Biol. 3*, 841-850.

APPENDICES

Appendix I – Abbreviations

TDO	tryptophan 2,3-dioxygenase
IDO	indoleamine 2,3-dioxygenase
cmTDO	*Cupriavidus metallidurans* TDO
xcTDO	*Xanthomonas campestris* TDO
dmTDO	*Drosophila melanogaster* TDO
hTDO	human TDO
CCP	cytochrome *c* peroxidases
HRP	horse radish peroxidase
JRP	Japanese radish peroxidase
CPO	chloroperoxidase
Mb	myoglobin
IPNS	isopenicilin *N* synthase
MADH	methylamine dehydrogenase
L-Trp	L-tryptophan
1-Me-L-Trp	1-methyl-L-tryptophan
NFK	*N*-formylkynurenine
NAD	nicotinamide adenine dinucleotide
CO	carbon monoxide
NO	nitric oxide
IM	imidazole
2MI	2-methylimidazlole
4MI	4-methylimidazole

ABTS	2,2'-azino-bis(3-ethylbenzothiazoline-6-sulphonic acid)
TTQ	tryptophan tryptophylquinone
WT	wild-type
H-bonding	hydrogen-bonding
EPR	electron paramagnetic resonance
RR	resonance Raman
HALS	highly anisotropic low-spin
MS	mass spectrometry
ESI-MS	electrospray ionization mass spectrometry
LC-MS	liquid chromatography-mass spectrometry
m/z	mass-to-charge ratio
δ	isomer shift
ΔE_Q	quadruple splitting
DFT	density functional theory
MD	molecular dynamics
QM/MM	quantum mechanics/molecular mechanics
ET	electron transfer
H_{AB}	electronic coupling element
CR	charge resonance
MO	molecular orbital

Appendix II – List of publications

1. Geng J, Davis I, Liu F, and Liu A (2014) *Bis*-Fe(IV): Nature's sniper for long-range oxidation. ***J. Biol. Inorg. Chem.***, in press (DOI 10.1007/s00775-014-1123-8)
2. Geng J, and Liu A (2014) Heme-dependent dioxygenases in tryptophan oxidation. ***Arch. Biochem. Biophys.***, 544, 18-26
3. Geng J, Dornevil K, Davidson VL, and Liu A (2013) Tryptophan-mediated charge-resonance stabilization of the *bis*-Fe(IV) redox state of MauG. ***Proc. Natl. Acad. Sci. USA***, 110, 9639-9644
4. Abu Tarboush N, Shin S, Geng J, Liu A, and Davidson VL (2012) Effects of loss of the axial tyrosine ligand of the low-spin heme of MauG on its physical properties and reactivity. ***FEBS Lett.***, 586, 4339-4343
5. Geng J, Dornevil K, and Liu A (2012) Chemical rescue of the distal histidine mutants of tryptophan 2,3-dioxygenase. ***J. Am. Chem. Soc***., 134, 12209-12218
6. Abu Tarboush N, Jensen LMR, Yukl ET, Geng J, Liu A, Wilmot CM, and Davidson VL (2011) Mutagenesis of tryptophan199 suggests that electron hopping is required for MauG-dependent tryptophan tryptophylquinone biosynthesis. ***Proc. Natl. Acad. Sci. USA***, 108, 16956-16961
7. Fu R, Gupta R, Geng J, Dornevil K, Wang S, Zhang Y, Hendrich MP, and Liu A (2011) Enzyme reactivation by hydrogen peroxide in heme-based tryptophan dioxygenase. ***J. Biol. Chem***., 286, 26541-26554